ADVANCED MASTERS IN STRUCTURAL ANALYSIS
OF MONUMENTS AND HISTORICAL CONSTRUCTIONS

Master's Thesis

Alejandro Trujillo Rivas

Stability Analysis of Famagusta Churches: St. George of the Latins

This Masters Course has been funded with support from the European Commission. This publication reflects the views only of the author, and the Commission cannot be held responsible for any use which may be made of the information contained therein.

Portugal I 2009

DECLARATION

Name: Alejandro Trujillo Rivas

Email: alejotrurivas@gmail.com

Title of the Msc Dissertation: Stability Analysis of Famagusta Churches: St. George of the Latins

Supervisor(s): Paulo B. Lourenço

Year: 2008 - 2009

I hereby declare that all information in this document has been obtained and shown in accordance with academic rules and ethical conduct. I also declare that, as required by these rules and conduct, I have fully cited and referenced all material and results that are not original to this work.

I hereby declare that the MSc Consortium responsible for the Advanced Masters in Structural Analysis of Monuments and Historical Constructions is allowed to store and make available electronically the present MSc Dissertation.

University: Universidade de Minho

Date: 15th of July of 2009

Signature:

_____

A mi familia porque gracias a su amor
y paciencia he cumplido mis sueños.

A mi amor por la incondicionalidad,
paciencia y felicidad.

ACKNOWLEDGEMENTS

I want to give a special acknowledgement to the European Commission and the Master Consortium for the Erasmus Mundus scholarship which was given to me. Thanks to the scholarship I was able to live abroad with all the facilities, only worried about studying for the Master.

Special thanks to Professor Pere Roca F. for his hospitality and kind help during the course work in Barcelona at Universitat Politècnica de Catalunya. Also thank you for the nice site visits, especially the one to Mallorca Cathedral. Gracias por todo!!!

I also want to give a special acknowledgement to my thesis supervisor Professor Paulo B. Lourenço, at Universidade de Minho, who was always available for solving my questions and answer my doubts despite of his multiples occupations. Thank you also for your great advises Prof Lourenço; I learned a lot from you. Muito obrigado pela sua ajuda!!!

I want to highlight the huge collaboration received from the PhD student Nuno Mendes, he was always available to help me run the analyses and to solve my doubts about different technical issues; and he prepared the RESUMO. Also special thanks to Prof. Luis Ramos for his valuable advices during the calibration of the model process. Muito obrigado pele seu tempo!!!

Also, I want to thank the helpful collaboration of Maria Teresa for her valuables corrections in my English grammar.

It is important to remark the hard work of Sandra Pereira and Dora Coelho, the old and new Master's Secretariat; thanks for solving our visa, accommodation and payment issues while living abroad, sorry for bother you that much. Muito obrigado e beijinhos!!!

Finally, I would like to say that this experience was a time life one, because I was able to meet people from all over the world during my course work in Barcelona and during my dissertation in Guimarães. It was very important for me to learn from different cultures, their costumes and thoughts, to open my mind and see the different ways in which each of us see the world's reality. I really enjoyed exploring Catalan and Portuguese cultures with my friends, I think something new we learned. Thank you guys for those nice moments, these memories will be always in my mind and in my heart, hope not to lose contact with you and wish you the best for your life!!!

ABSTRACT

This thesis addresses the study of the stability of Saint George of the Latins church, which is located in Famagusta (Cyprus), under self-weight and seismic loading. In the first part of the work, the state of the art is presented, including brief review on Famagusta history, its seismicity and the inspection and diagnosis works carried out on the church. The limit analysis of collapse mechanisms, both force based and displacement based, was used for a first safety assessment. After that, a numerical model was prepared using finite elements and it was updated using the dynamic identification results. The updated model was subjected to non-linear static (pushover) analysis in different directions (global and principal) using two lateral load patterns: proportional to the mass and proportional to the mode shape of the structure in the applicable direction. The results of the pushover analyses were compared with the limit analysis results. As final step, non-linear dynamic analyses with time integration were carried out and the dynamic behavior of the structure was compared with the results of limit analysis and pushover analysis.

By analyzing simplified collapse mechanisms (2D), an absolute lower bound of the structure capacity was obtained. Then by performing pushover analyses in different directions, the plastic hinge distribution assumed for the collapse mechanisms was validated and higher values for the loading capacity of the structure than those obtained from limit analyses were obtained, but all of them are lower than the Eurocode 8 seismic demand. Finally, from the stability seismic assessment of the structure by means of non-linear dynamic analysis was possible to determine that the structure is safe under PGA equal to 0.06g, but it was not possible to analyze the response for higher seismic load (0.07g), leading to the conclusion that the structure is in the limit of its loading capacity or the numerical model should be improved to perform these non-linear dynamic analyses.

RESUMO

Análise de estabilidade de igrejas de Famagusta: Saint George of the Latins

Esta tese tem por objectivo o estudo da estabilidade da igreja de “Saint George of the Latins”, situada em Famagusta (Chipre), sob acção do peso próprio e acção sísmica. Na primeira parte do trabalho é apresentada a revisão dos conhecimentos, incluindo uma breve revisão sobre a história de Famagusta, a sua sismicidade e os trabalhos de diagnóstico e inspecção levados a cabo na igreja. Na primeira verificação da segurança recorreu-se à análise limite, baseada quer em força quer em deslocamento, através da definição dos mecanismos de colapso. Seguidamente, foi preparado um modelo número de elementos finitos, tendo sido calibrado de acordo com os resultados da identificação dinâmica. O modelo calibrado foi utilizado em análises não-lineares estáticas segundo diferentes direcções (globais e principais) e com dois padrões de forças laterais: proporcional à massa e proporcional ao modo de vibração da estrutura na direcção em estudo. Os resultados das análises estáticas não-lineares foram comparados com os resultados da análise limite. Por último, foram feitas análises não-lineares dinâmicas com integração no tempo, tendo sido comparada a resposta dinâmica da estrutura com os resultados obtidos na análise limite e nas análises estáticas não-lineares.

O limite inferior de capacidade de carga da estrutura foi obtido com recurso à análise dos mecanismos simplificados (2D) de colapso. A distribuição das rótulas plásticas assumida na análise limite foi validada através das análises não-lineares estáticas em diferentes direcções, demonstrando que estas análises apresentam valores de capacidade de carga superiores aos obtidos na análise limite, no entanto ambas as análises apresentam capacidades inferiores às exigências definidas no Eurocódigo 8. Por último, através da avaliação da estabilidade sísmica da análise não-linear dinâmica foi possível determinar que a estrutura está estável quando submetida a uma aceleração de pico na base igual a 0.06g,no entanto não foi possível analisar a resposta da estrutura para uma acção sísmica superior (0.07g), sugerindo que a estrutura está no seu limite de capacidade de carga ou que o modelo numérico deve ser melhorado para levar a caco estas análises não-lineares dinâmicas.

RESUMEN

Análisis de Estabilidad de las Iglesias de Famagusta: "St. George of the Latins"

Esta tesis está encaminada al estudio de estabilidad de la iglesia "St. George of the Latins", la cual está localizada en la ciudad de Famagusta (Chipre), bajo la acción de peso propio y acciones sísmicas. En la primera parte del trabajo, el estado del arte fue hecho incluyendo una corta revisión de la historia de Famagusta, su sismicidad así como también la inspección y diagnostico llevados a cabo en la iglesia. Análisis límite de mecanismo de colapso, basados en fuerza y desplazamiento, fueron usados tener un primer estimativo de las condiciones de seguridad. Posteriormente, un modelo numérico de la iglesia fue construido utilizando elementos finitos y fue actualizado utilizando los resultados de la caracterización dinámica de la iglesia. El modelo actualizado fue sometido a análisis estáticos no lineales (pushover) en diferentes direcciones (global y principal) utilizando dos patrones de carga: uno proporcional a la distribución de masa y el otro proporcional a los modos de vibración de la estructura en la dirección de aplicación. Los resultados de los análisis pushover fueron comparados con los resultados obtenidos en los análisis límite. Finalmente, análisis dinámicos no lineales con integración en el tiempo fueron llevados a cabo y el comportamiento dinámico de la estructura fue comparado con los resultados obtenidos en los análisis límite y los análisis estáticos no lineales.

Mediante el análisis de mecanismos de colapso simplificados (2D) fue posible encontrar el menor valor absoluto de la capacidad de la estructura. Después, mediante la aplicación de análisis pushover en diferentes direcciones, la distribución de rotulas plásticas asumida para los mecanismos de colapso fue validada y valores mayores a los encontrados en los análisis limite fueron encontrados para la capacidad de carga de la estructura, pero todos ellos mucho menores que la demanda sísmica estipulada en el Eurocode 8. Finalmente, de la valoración de estabilidad sísmica de la estructura y mediante el uso de análisis dinámicos no lineales, fue posible determinar que la estructura es segura cuando es sometida a una aceleración pico del terreno igual a 0.06g, pero no fue posible analizar la respuesta de la estructura ante carga sísmica mayor (0.07g), llegando a la conclusión que la estructura está en su estado limite de capacidad de carga o que el modelo numérico debe ser mejorado para llevar a cabo estos análisis dinámicos no lineales.

TABLE OF CONTENTS

LIST OF FIGURES

LIST OF TABLES

1. INTRODUCTION

The city of Famagusta, located in Cyprus island, has been since many centuries ago a strategic location for the commercial interchange between the West and the East, and also a religious center for both Islamic and Christian people. All of this is reflected in its historical constructions, which have been built by several communities as Armenian, Jewish, Nestorian, Maronite and Jacobite. The heritage treasures of this city include several impressive examples of gothic style as medieval churches as well as mosques and military buildings with some impressive city walls. Once, Famagusta was known as the most important city in the world, where very rich people used to live, but now the city is completely abandoned and neglected and threatened by earthquakes. Besides, it was place on the 2008 World Monuments Watch List of 100 Most Endangered Sites by the World Monument Fund.

A joint collaboration between University of Minho, Eastern Mediterranean University (EMU) and the Municipality of Famagusta was established with the aim to analyze the stability of the Medieval Churches. A previous work on visual inspection and non-destructive testing was carried out by (Lourenço & Ramos, 2008), which included three churches: (a) St. George of the Latins; (b) St. George of the Greeks and (c) The Carmelite Church. The obtained results of this work provide a basis for the studies regarding the safety assessment of the churches; nevertheless the stability assessment under gravity loads and seismic loads was not carried out. Appealing for the claim of the world to save Famagusta heritage, the stability assessment of Saint George of the Latins church under gravity loading and earthquake loading was performed.

Due to the complex nature of historical constructions a scientific approach is required to understand its behavior and its response to external actions. Therefore structural analysis is one of the four different tools among: history, inspection of the present condition, monitoring and structural modeling, which can be considered to investigate a historical structure. The contribution of structural analysis is essential in combination with the other tools because it contributes with the possibility of simulating the performance of the structure when subjected to past actions and thus conclude about their possible influence on the present condition and existing damage (Roca & Kabele, 2008-2009).

Modeling often takes the form of mathematical formulations, which may be solved by computers, therefore the analysis lose control of the situation. Furthermore, simple models are still needed to check and assess results. This can also be justified by the need to obtain difficult material properties and boundary conditions among the structure. The structural model must take into account all the aspects that influence the structural response such as geometry, material properties, actions, exiting alterations and damages, and the interaction of the structure with the soil (Roca & Kabele, 2008-2009).

As a first approach, the structural model must be built in combination with history, inspections and experiments to furbish data for the model. Then these activities will provide information for validation by applying the calibration (updating) process which is a direct application of the scientific method.

The hypotheses are implicitly formulated by the considerations taken into account during the construction of the structural model. Finally the model is validated by comparing the results with the empirical evidence provided by history, inspection and monitoring. Once the model is validated, it will be used to predict unknown aspects of the structural response such as seismic capacity (Roca & Kabele, 2008-2009).

Within this process important considerations arise and they are: the extension of the validation, the level of validation, the application of different actions from those used in the validation process and the available possibilities to calibrate the models. Those are inherent uncertainties and there is space for subjectivity and they should be based on experience and judgment of the analysts (Roca & Kabele, 2008-2009).

There are several challenges posed by historical heritage: (i) the material characterization is complex and the mechanical properties and strength are variable along the direction; (ii) the geometry usually is rather complex composed by domes, arches, vaults and other slender or massive members; (iii) the morphology and connections are non-homogenous caused by fillings, cavities, insertions; (iv) actions of different nature that act along historical time (centuries), specially characterized by long returned periods; (v) the real condition of the structure require the simulation of damages and deformed and cracked members; (vi) the data acquisition is limited by the respect of the original conditions of the monument and non destructive and minor destructive tests are available with limited scope; (vii) by the history it is possible to know the construction process, later alterations and additions, documented destruction, reported natural actions, etc (Roca & Kabele, 2008-2009)

Applying the scientific approach to analyze the structure; taking into account historical and empirical information and the limitations posed by historical heritage; the assess of stability under gravity and seismic loadings was carried out for Saint George of the Latins church using different levels of approach from the simplest to the complex one in terms of analyses procedures and comparing the results obtained by the different approaches.

First, a very brief state of the art was done including the history of Famagusta, its seismic hazard and the actual conditions of the church as well as some historical facts. In a subsequent step, the safety assessment of the church using collapse mechanism limit analysis was carried out, both force based and displacement based.

A next step was to model the church using finite elements and the available information from the inspection and diagnosis report carried out by (Lourenço & Ramos, 2008). For this purpose, model updating using the available dynamic identification results was carried out. After having the model calibrated, it was subjected to a push-over analysis in using two different load patterns: (1) an uniform pattern based on lateral forces that are proportional to the mass regardless their height distribution among the structure and (2) a modal pattern proportional to lateral forces consistent with the lateral force distribution determined in the modal response. The results were compared with the collapse limit

analysis. A third pushover analysis was performed in the direction of the principal axes and the results were also compared with the previous analyses results.

The final step was to carry out advanced dynamic analysis using time integration non-linear dynamic analysis using two different earthquakes with different peak ground accelerations. The results were compared with the results of the collapse limit analysis and the standard pushover analysis. At the end of the report, several conclusions and recommendations on further works are made based on the experience and inconvenient suffered along the process.

The thesis is organized in 9 chapters as follows:

- **Chapter 1:** Presents the motivation, the aim, the scope and the methodology for approach to the problem.
- **Chapter 2:** Presents a brief review on the state of the art, including a short history of Famagusta, the seismic hazard in Cyprus and Famagusta and the general description of Saint George of the Latins church, its present conditions and the experimental tests carried out on it.
- **Chapter 3:** Presents the limit analysis of the defined collapse mechanism by the kinematic approach; both displacement based and force based.
- **Chapter 4:** Presents the definitions of the model, with all the attempts to represent the real conditions of the structure (damages and deterioration).
- **Chapter 5:** Presents the process to calibrate the modal response of the model based on the results of dynamic identification tests.
- **Chapter 6:** Presents the pushover analyses carried out in the global directions, the principal directions and following the modal pattern distribution.
- **Chapter 7:** Presents the non-linear dynamic analysis which was performed using two different earthquakes with different intensities.
- **Chapter 8:** Presents several conclusions made about the applied process, the results of each analysis approach, the calibration of the model, the numerical procedures and the material properties. Also some recommendation about further works that can be carried out to improve the obtained results and to have a better approach to face the problem.
- **Chapter 9:** Presents all the references that were used for write this thesis.

2. STATE OF THE ART

2.1 LOCATION AND HISTORY FAMAGUSTA

Cyprus Island is located in the Eastern portion of the Mediterranean Sea; south of Turkey, west of Syria, Lebanon, and Israel, east of Greece, and north of Egypt; its location is shown in Figure 2.1. It is the third largest island in the Mediterranean and the world's 81st largest one (Republic of Cyprus, Ministry of Finance, 2006). It is located at a confluence of Western Asia, Southern Europe and Northern Africa and has had periods of influence of several dynasties such as Byzantine, Lusignan, Genoese, Venetian, Ottoman and British. At the same time it has been the home of Armenian, Jewish, Nestorian, Maronite and Jacobite communities (Walsh, 2007). The city of Famagusta is located in North-East Cyprus, it has been over many centuries at the crossroads between the West and the East, and has played a pivotal role between the Christian and Islamic Worlds

Figure 2.1. Location of Cyprus Island and Famagusta (Google, 2009)

The first city that appeared in the East coast of Cyprus was Enkomi, around 16th century B.C. This small town was dependant on the exportation of copper, which was easily commercialized thanks to the port located nearby the town. The city became an important center of distribution because of the greater demand of copper, but after natural catastrophes around 12th century B. C., the city declined and its population moved more to the east of the island and founded a new centre known as Salamis (Municipality of Famagusta, 2009).

Salamis was the capital of the Island for more than one thousand years and was considered one of the most important sites in the Mediterranean. During the 13th century B.C, the Greek colonists established themselves and introduced the Western culture to the island; hence it was open to commercial and cultural exchanges between the Western World and the Near East. At the end of the 8th century, the island was a bastion of the Hellenic culture but later on during year 525 B.C., Cyprus surrendered to the Persians and became a tributary province of Persian Empire. After several years of Persian rules, the Island control went back to the Greeks during year 411 B.C., and the Island became an independent kingdom. The Greeks established the peace with the Persians by paying them an annual tribute. They were able to accumulate health and embark, by means of several works including fortification of the walls of the city, which elevated Salamis to the wondrous splendor (Municipality of Famagusta, 2009).

In year 294 B.C., Ptolemy I conquered Cyprus and incorporated into his kingdom. Later on, his son founded three cities with the name of his sister Arsinoe, one of them was located next to Salamis. Arsinoe and the harbor were built during year 274 B.C. since Salamis had been destroyed by earthquakes. In fact, the complete destruction of Salamis came about in 332 and 342 A.D after consecutive earthquakes stroke the city. Emperor Constantios II took control of the Eastern Roman state and assisted in the reconstruction of the city under the Christian name of Constantia. The city became a religious and administrative metropolis, and recovers its forms size and grandeur, as that of Salamis. Constantia played an important role for the Christianity; as Apostles Paul and Barnabas embarked on their first missionary enterprise and preached in the synagogues of the city. After Barnabas death and from year 396 on, Cyprus was part of the Eastern Byzantine Empire, hereby the Patriarch decided to grant autonomy to Cyprus church because he offered to the Emperor the original of St Matthew's hand written gospel that he found on Barnabas chest. (Municipality of Famagusta, 2009).

The Arabs' sudden incursion started at the middle of 7th century finished with the destruction of Constantia and Arsinoe; which were permanent abandoned. Arabs gained the complete command of the Eastern Mediterranean and the privileged position of Cyprus made it possible that the Island was not affected by the war and, just the opposite, it played an important role. First, the island was proclaimed as neutral territory, but later on the Arabs secured the island for themselves, and they transfered the peoples from Constantia to Asia Minor. The Arabs raids lasted until year 965, when Nicephorous Phocas forced them to leave, being Salamis-Constantia completely abandoned, and Famagusta was established a few kilometers to the south of its original place (Municipality of Famagusta, 2009).

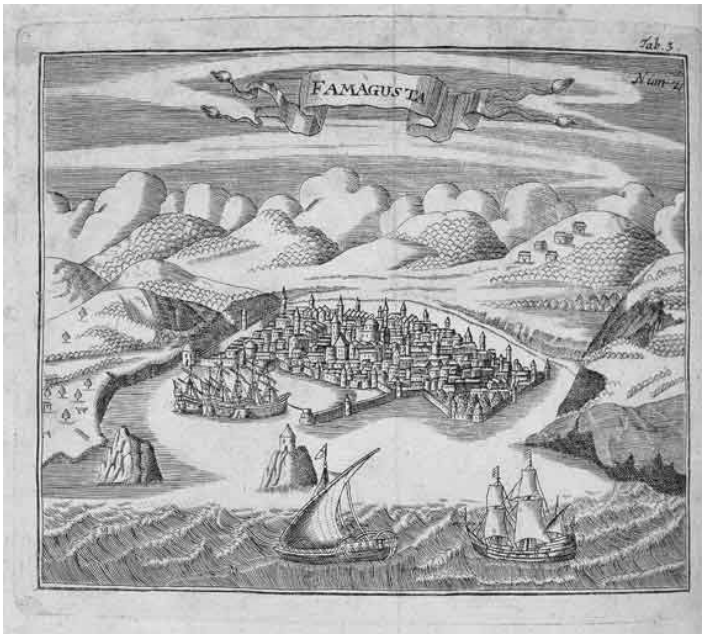

Figure 2.2. Famagusta city by (Miller, 1735)

There is a gap in the history of Famagusta from the 3rd century to year 1200, with no material that could give information on Byzantine Famagusta (Municipality of Famagusta, 2009). There are some written source dated from the end of the 12th century but there is no relevant information regarding the city.

Between years 1191 and 1489, Famagusta played an important role in the Lusignan dynasty becoming the largest distribution center of western products to the east. Also it was the harbor with most activity and the most beautiful city in Cyprus. The most magnificent period of the city occurred after the fall of Acre in 1291 (Walsh, 2007) when Christian refugees settled in Famagusta. During this time, the great fortification works were undertaken; the harbor, the castle, the bastions and the tower were built to protect the inner part of the harbor. The city was divided in two quarters; the Latin Quarter in the north-east part of the city and the Orthodox quarter located in the south-east part

Between 1300 and 1370 Famagusta was a most glamorous city due to the presence of powerful merchants; it became the most important port for eastern trade in the Mediterranean. Around 300 churches were built during this period, including The Cathedral of St. Nicholas where the crusader kings were crowned (Walsh, 2007) and St George of the Greeks, which are two examples of Orthodox cathedrals. They were surrounded by many churches and houses built in the finest Gothic style (Walsh, 2007). The splendor came down during the middle of the 14th century after the epidemic Black Death, and also when a conflict of interest arose between Genoese and Venetian (Municipality of Famagusta, 2009).

In 1374, the Genoese sent their troops to Famagusta and destroyed a huge part of the city. They arrested the King and forced him to pay a huge indemnity. This was the beginning of the fall of Famagusta; hence all the economical and commercial activity was gradually disappearing. During the subsequent 90 years, the City and the harbor were under Genoese rules (Municipality of Famagusta, 2009). After four years of blockade, the Lusignans were able to get rid from the Genoese and due to the marriage between King of Cyprus with the “daughter of St. Mark”, patron saint of Venice, Cyprus lead Venice to consolidate its position in the Eastern Mediterranean. After this king’s death, the Queen was forced to concede the power to the Vice Admiral of the Venetian Republic, in a ceremony that took place in the Cathedral of St Nicolas (Municipality of Famagusta, 2009).

The Venetian took over the island which was strategically important for its war against the Ottomans, especially after the fall of Constantinople. The domination of Cyprus lead Venice to gain commercial, economic and political power in the Eastern Mediterranean; but the city itself was completely abandoned and people was living in miserable conditions. In order to safeguard the city from the Ottomans, the Venetian decided to strength the defensive structures of Famagusta. They brought expert masons and engineers to restructure the walls of the city and the Othello tower (Walsh, 2007) and to build another important structures, such as the castle of the harbor, new bastions (the Ravelin, the Tower of the Arsenal and Martinengo) and a string of islets and rocks and two towers to protect the inner harbor (Municipality of Famagusta, 2009).

Despite the restoration and improvement works to make the city safe, the Ottomans took control in 1571 after a long period of attacks that ended in the defeat of the city. The Venetians negotiated an agreement that allowed the Christian Greeks to stay in the city under Ottoman control. However they did not keep up their promise and they destroyed almost everything they found. Then, the Greeks went southwards and take refuge in fields where they founded the New Famagusta. From 1571 on, Ottoman occupation began and no Christian was allowed within the walls, neither Christian ships could approach the harbor; the situation led the city to an inevitable decline (Municipality of Famagusta, 2009).

Four and a half centuries of neglect combined with exposure to hard environmental conditions and natural phenomena such as earthquakes, plague and flooding left the city almost ruined by the time the British arrived in 1878 (Walsh, 2007); the historical sites and treasures of the city were completely destroyed. Despite the ambitious British’ plan for restoration of Famagusta, there were only few restoration works carried out and the British gave priority to new prospects that were opened for trading (Municipality of Famagusta, 2009). However, after the Second World War, a new era started in Famagusta, its population increased significantly and the city expanded. The inhabitants start to build their houses again and the sea font started to be filled with hotels, which was a first re-birth for the city in intellectual and economical terms.

Once again, the city was taken apart during 1974, when the Turkish troops entered to the north part of the Island and took control of Famagusta. Nowadays, Cyprus is divided in two different territories; one

is the self-proclaimed Turkish Republic of Northern Cyprus, which is not internationally accepted and the other is the Greek section of the island which is fully recognized internationally and it is part of the European Union. The present conditions have leaded the Northern Cyprus un-funded and un-assisted, with the exception of substantial financial aid from Turkish government. Hence the Cultural heritage of the city has been neglected for over three decades, it serves as politically motivated pawn (Walsh, 2007), and meanwhile there is a big effort to include several Famagusta's cultural sites in an European Foundation in order to fund the conservation of specific monuments.

According to (Walsh, 2007) the sandstone which is the construction material of almost all the historic Monuments in Famagusta (Around 200) is highly deteriorated (see Figure 2.3), and the collapse of domes, arches and ribbed vaults will be inevitable if no action is taken, in particular, the exterior of St Nicolas Cathedral and St George of the Latins; one of the finest Gothic buildings of medieval Christendom. Due to severe state of deterioration, Famagusta was recently placed on the 2008 World Monuments Watch List of 100 Most Endangered Sites by the World Monument Fund (Lourenço & Ramos, 2008).

Numerous natural and man-made threats endangered the old city, mainly geotechnical instability, drainage problems, vegetation growth, presence of water, inappropriate prior conservation, neglect and inadequate maintenance, rapid development and haphazard town planning, and a lack of conservation expertise, and after a decade of continued neglect the result will be a further decline with possible catastrophic structural failures (Walsh, 2007).

(a) **(b)** **(c)**

Figure 2.3. General view of the state of conservation (2008) in (a) St George of the Latins Church, (b) St George of the Greeks Church and (c) Carmelite Church

2.2 FAMAGUSTA SEISMIC HAZARD

2.2.1 Tectonic Hazard

Cyprus is located in a tectonically complex zone where three continental plates assemble; they are the African plate to the south, the Eurasian plate to the north and the Arabian plate to the east. The movements between these three plates are: rifting (the plates separate from each other), collision (the plates move towards each other and collide or crash) and wrenching (the plates move parallel to each other but in different directions). The combination of all these movements has produced features in this region such as the Hellenic Arc to the west and its continuation to the east and Cyprus itself (the Troodos Ophiolite) (Unit of Environmental Studies, 2004).

The Alpine-Himalaya belt is the second most intensive seismic zone of the earth, where the earthquakes that occur represent about 15% of the world seismic activity, and Cyprus is located among this region, in the southern side of the Anatolian Plate. Its seismicity is attributed to the “Cyprus Arc” which is the tectonic boundary between the African and Eurasian plates (it extends from gulf of Antalia, passes from west to south of Cyprus and goes towards the Gulf of Isknedurn; see Figure 2.4). There is subduction of the African Plate under the Eurasian Plate; hereby many epicenters are concentrated along the arc because the tectonic movements are the main cause for earthquakes, some of them are strong. Recently, several active faults inside the island have shown that earthquakes also occur along them (Unit of Environmental Studies, 2004).

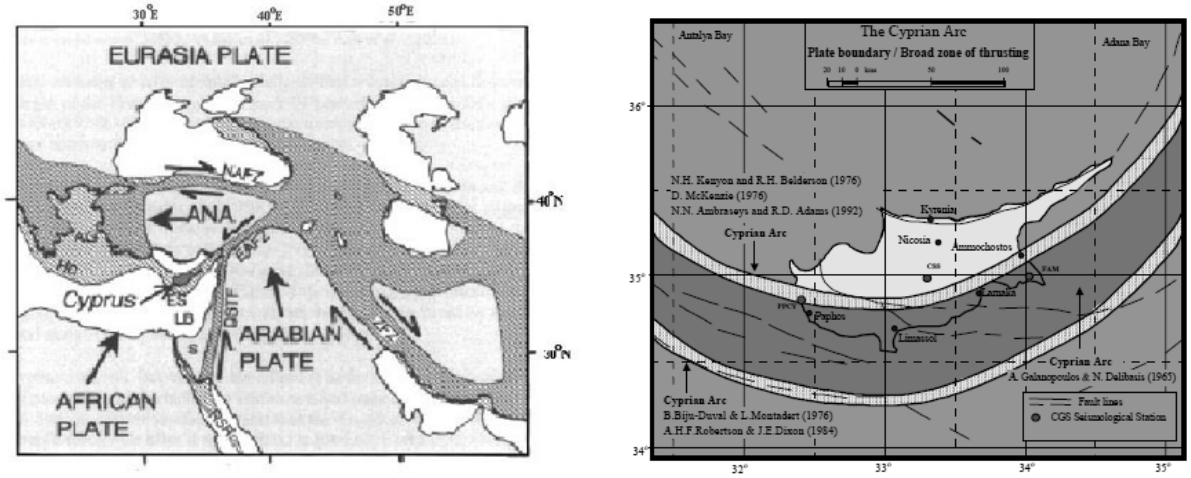

(a) **(b)**

Figure 2.4. (a) Lithospheric plates in the Cyprus region (Unit of Environmental Studies, 2004) and (b) Cyprus Arc estimation (Kythreoti & Pilakoutas, 2000)

2.2.2 Historical Records and Instrumental Records

According to several historical references and archaeological findings, Cyprus was stroke by strong earthquakes in the past, which destroyed and damaged towns such as Salamis (today's Famagusta), Kition, Amathus, Kourion, Pafos and Nicosia. This data indicates that 16 earthquakes with intensities of VIII (on modified Mercalli scale) or higher occurred between years 26 B. C. and 1900 A. D., especially two of them had big impact in Salamis (today's Famagusta) and destroyed the whole town; one occurred in 76 A. D. and the other occurred in 332 A. D. (Unit of Environmental Studies, 2004).

It was only in year 1896 that more accurate data started to be collected when seismological stations started to operate on neighboring countries. Later on 1984, the accuracy and completeness of this data was improved by the establishment of a seismological station in Cyprus, therefore a continued expansion and upgrading began. Hereby the areas with high seismic activity among Cyprus territory were clearly recognized and during this time period (1896-2004) more than 400 earthquakes had epicenters on Cyprus and the surrounding region, with 14 of those causing severe damages as well as victims (Unit of Environmental Studies, 2004) as it is shown in Table 2.1. It is important to highlight that from those 14 strong earthquakes, 2 stroke Famagusta; one in February 18th of 1924 with a magnitude of 6.0 caused small damage in Famagusta and the other stroke in January 20th of 1941 and caused severe damage in the district of Famagusta.

Date	Magnitude	Description of damage
29/6/1896	6.5	Damage in the area of Limassol. Many aftershocks followed.
5/1/1900	5.7	Small damage in Mesaoria.
23/2/1906	5.3	Small damage in Limassol and Kolossi. Felt all over the island.
18/2/1924	6.0	Small damage in Famagusta.
13/12/1927	5.0	Small damage in Limassol and in villages to the north.
9/5/1930	5.4	Damage in Pafos and the surrounding area.
26/6/1937	4.7	Damage in southwest Cyprus.
20/1/1941	5.9	Severe damage in the district of Famagusta, especially at Paralimni, where 24 people were injured and many houses collapsed. Limited damage in the districts of Nicosia, Larnaca and Kyrenia.
10/9/1953	6.1	Destructive earthquake in the district of Pafos with 63 dead, 200 injured and 4000 homeless. Many houses were destroyed in 158 villages.
15/1/1961	5.7	Small damage in Larnaca town and the surrounding area.
28/3/1984	4.5	Small damage in the town and district of Larnaca.
23/2/1995	5.7	Destructive earthquake in the Pafos district with two dead. Many houses collapsed in the nearby villages.
9/10/1996	6.5	Very strong earthquake in the southwest of Cyprus (Pafos, Limassol, Nicosia, Larnaca and Paralimni). Twenty people were slightly injured and two lost their lives from indirect causes. Limited damage in Pafos and Limassol.
11/8/1999	5.6	Strong earthquake close to Gerasa caused damage to buildings in Limassol and the villages to the north of the town. Felt all over Cyprus. Forty people were slightly injured. Many aftershocks followed.

Table 2.1. Catastrophic and Damaging Earthquakes on Cyprus 1896-2000 (Unit of Environmental Studies, 2004)

Regarding all the earthquakes within the island, the most catastrophic earthquakes were those of 1941, 1953, 1995, 1996 and 1999. The study of these records has shown that the distribution along time of Cyprus seismic activity is not regular, with intense periods following by calm periods. For instance, there was an important increase in seismic activity between years 1995 and 1999, when several strong earthquakes stroke the island with magnitudes ranging from 5.6 to 6.5 (Unit of Environmental Studies, 2004). A spatial distribution of catastrophic and damaging earthquakes is shown in Figure 2.5 where it is important to highlight the presence of one earthquake near Famagusta region with magnitude between 5.3 and 6.0.

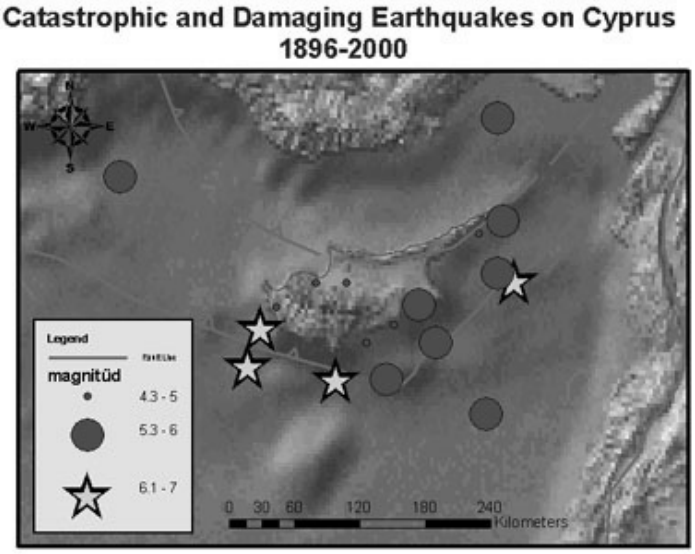

Figure 2.5. Distribution of catastrophic and damaging earthquakes on Cyprus between 1896 and 2000 (Unit of Environmental Studies, 2004)

2.2.3 Earthquake Vulnerable Areas

Notwithstanding that Cyprus lies in high activity seismic zone, the area where most number of historical records and instrumental data has been recorded is the coastal zone that extends from Pafos through Limassol and Larnaca and then to Famagusta. Large number of medium to strong earthquakes have epicenters in the sea, which may cause small to negligible damage, but many other earthquakes have epicenter in the west and south regions of the island, affecting more these areas of the country rather than the others (Unit of Environmental Studies, 2004). According to the Seismic Hazard Map of Cyprus (shown in Figure 2.6), the maximum peak ground acceleration (PGA) on rock for the south and west regions, where Famagusta is included, is about 0.25g. This value is the highest within the whole territory compared with the minimum PGA of 0.15g, which is shown in the north and center regions.

Figure 2.6. Definition of reference peak ground acceleration (PGA) on rock among Cyprus territory (CYS EN 1998-1:2005, 2007)

Another important parameter that increases the vulnerability of a region is the ground condition. In this manner, areas covered with loose deposit, mainly coast areas are more vulnerable than areas that are wholesale covered of rock, such as the center of the territory (Unit of Environmental Studies, 2004), meaning that Famagusta is more prone to have strong impact of earthquakes. According to Figure 2.7, Famagusta is located over Terrace deposits which are mainly formed by Calcarenites, sands and gravels.

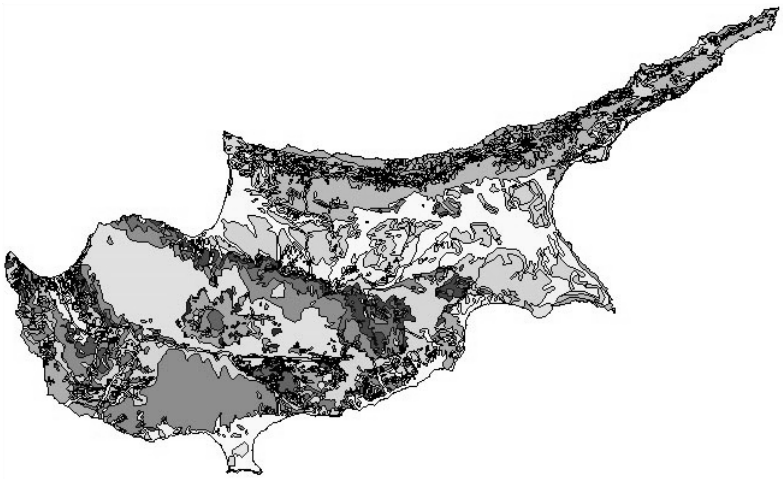

Figure 2.7. Geological map of Cyprus from Geological Survey Department (Unit of Environmental Studies, 2004)

2.3 SAINT GEORGE OF THE LATINS CHURCH

2.3.1 General description

The Church of Saint George of the Latins is located inside the city walls, in front of Citadel Othello's tower, in Kapou Street, however, it seems that it was built before the city was walled because it has been a fortified church (Supporting Activities that Value the enviroment, 2008); its location within the city is circled and it is shown in Figure 2.8. Although is in a ruinous state of preservation, there is enough evidence to demonstrate that this building is an impressive example of Gothic architecture with excellent masonry because all the church was built with three-leaf masonry, with ruble masonry inside and carved sandstone blocks joined together with thinner course of lime mortar as a veneer. It has compact proportions and rich stone carving decoration, hereby the superb quality of the masonry and workmanship suggests that it was built by master masons of the Cathedral workshop (Supporting Activities that Value the enviroment, 2008). The church however still preserves its northern half, the lower section of the apse and a part of its south side (Lourenço & Ramos, 2008).

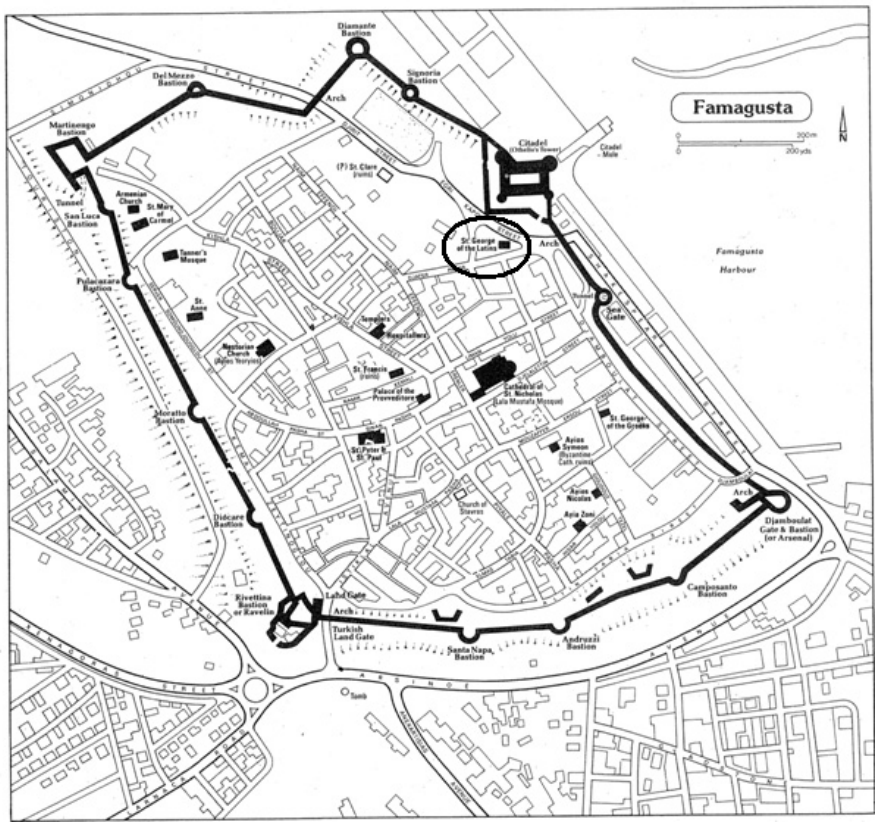

Figure 2.8. Map of Famagusta with St. George of the Latins location (Enlart, 1913)

The church is dated to the end of the 13th century, and it is recorded to be the oldest building in Famagusta. Also it is recorded as one of the most picturesque because it is built in the best French style of the 13th century (Supporting Activities that Value the enviroment, 2008). Its layout is quite

simple because it is a single-aisled building with four groin vaults which are supported by a grouping of three thin columns located in the north and south walls. Like in most Gothic churches, it has large and high windows, which used to have carved stone decoration. The church has some impressive gargoyles depicting human figures and winged dragons. A small conch adorned with richly decorated pediments is formed in the church's apse and was probably used to receive a sculpture (Lourenço & Ramos, 2008);

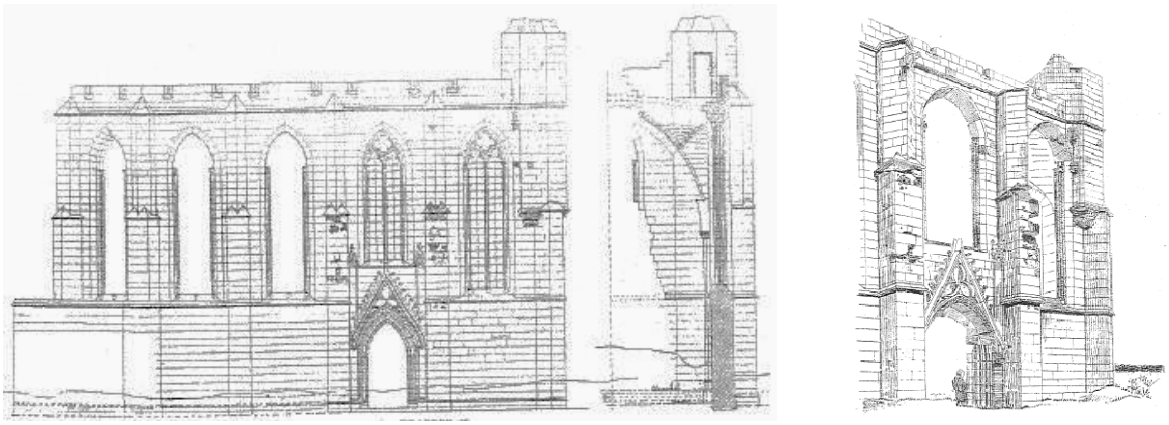

(a) **(b)**

Figure 2.9. Drawings carried out of (a) Front view of north Façade and (b) details on façade's door (Kell, 1982)

A geometrical survey of the church was carried out by (Lourenço & Ramos, 2008) using a laser distance meter and drawings obtained from (Kell, 1982). The church has 20.00 meters long and 8.91 meters of internal width, the separation inside two consecutive buttresses is about 3.52 meters, it has a lateral chapel which perimeter measures are 3.84, 5.43 and 4.89 meters and the width of the walls varies according to the element of the church. The Buttresses thickness is between 0.90 and 0.96 meters, the North façade and Apse thickness is about 1.02 meters and the West façade thickness is about 1.29 meters; with its plan arrangement shown in Figure 2.10-a. The height from the ground to the windows cornice is ranging from 4.55 to 4.87 meters, the height from the ground to the second cornice is about 13.60 meters, the mean height of the tower located in the connection between the West and the North façades is about 3.87 meters, the height of the windows is variable with values close to 7.24 meters and their width is between 1.80 and 1.85 meters; its height distribution is shown in Figure 2.10-b.

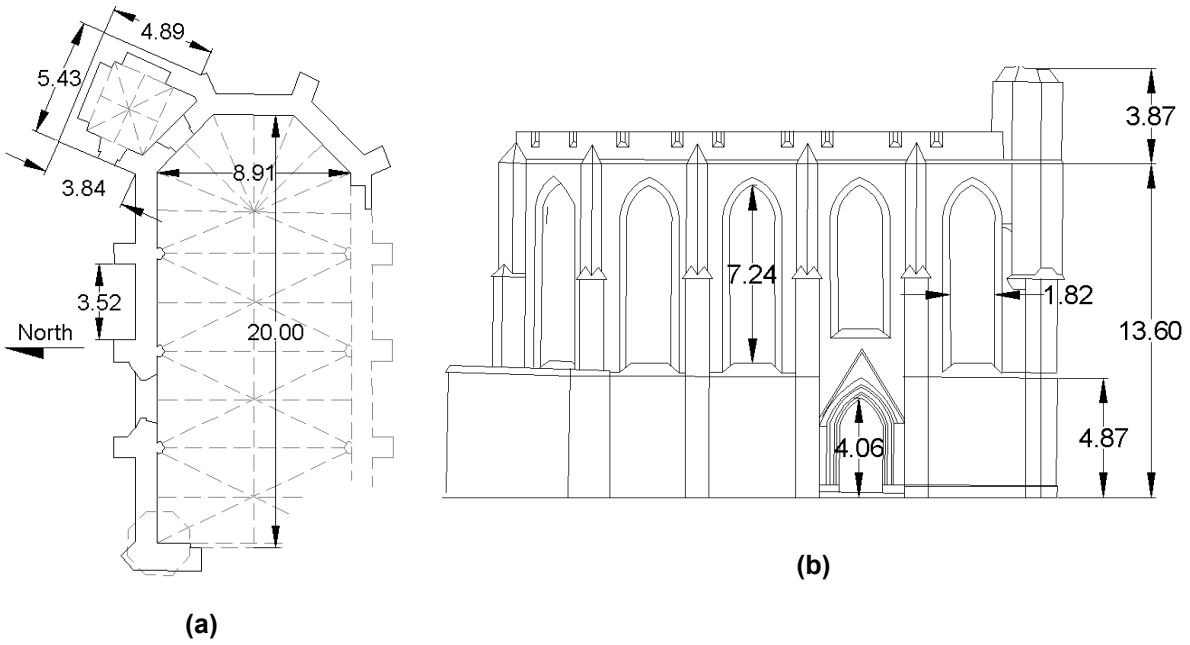

Figure 2.10. Geometrical survey of (a) church's plane and (b) church's height

2.3.2 Results from the Visual Inspection

According to the inspection works carried out by (Lourenço & Ramos, 2008), the present condition of the church seems not to differ significantly from the condition around 1940 (See Figure 2.11-a). Severe deterioration of the stones is reported in drawings from 1882 and several stones have been replaced in the conservation works around 1940 (see Figure 2.11-b)

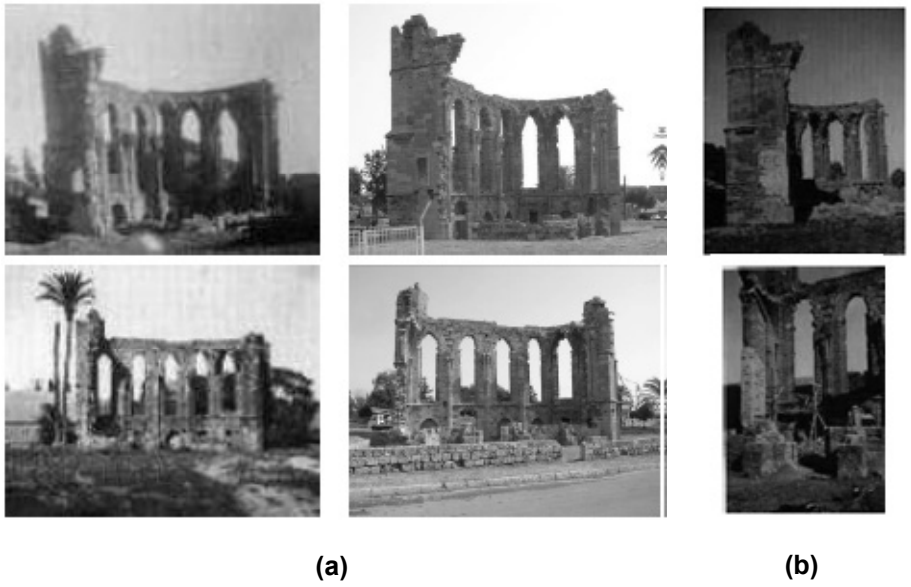

Figure 2.11. Historical photographs: (a) 1940 situation vs. current condition and (b) presence of new (lighter) stone (Lourenço & Ramos, 2008)

The present condition, shown in Figure 2.12, is characterized by: (a) & (b) lack of cleaning / possible misuse of one room (sacristy); (c) severe stone deterioration; (d) loose stone elements, which must be consolidated or removed; (e) highly corroded reinforced concrete lintel in main door; (f) inefficient buttresses due to stone deterioration; (g) & (h) a crack / rotation of the tower, possibly due to a previous earthquake / foundation problems (Lourenço & Ramos, 2008).

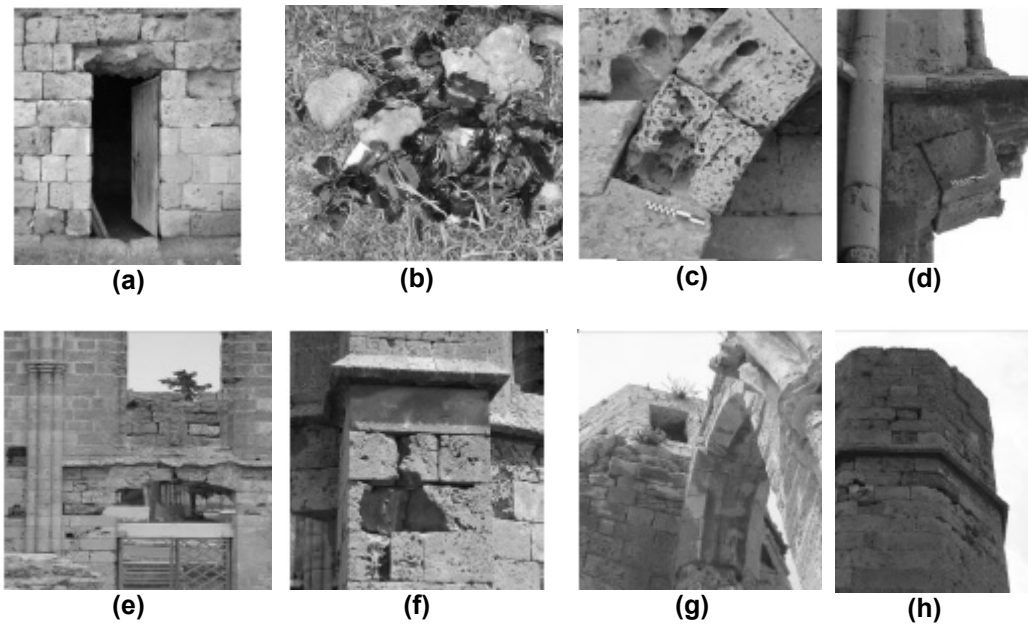

Figure 2.12. Details of current condition of the church from the inspection carried out by (Lourenço & Ramos, 2008)

2.3.3 Experimental results from dynamic Identification test

The dynamic identification analysis is a procedure that combines vibration testing techniques and analytical methods to determine modal parameters of structures, such as frequencies, mode shapes and damping coefficients. Those parameters are helpful to understand how a structure responds to dynamic excitations, such as earthquakes or winds, and to calibrate the computational model of a structure. With this purpose, output-only modal identification techniques were applied and the structure was excited with ambient vibration.

During the inspection on St. George of the Latins church in Famagusta city carried out by (Lourenço & Ramos, 2008), three accelerometers with 10 V/g sensitivity, able to measure 0.07mg (g is gravity acceleration), were used to measure accelerations and they were connected to a laptop by a 24-bit resolution data acquisition system using USB cable connection. All the measurements were carried out using natural vibration of the structure, where long periods of 10 minutes were recorded with a

sample rate of 200 Hz, and the data was processed using Stochastic Subspace Identification (SSI) methods. The ambient temperature and relative humidity were also measured while the dynamic test was performed but variations were small. Here, it is assumed that these parameters will not affect significantly the dynamic response of the church.

In St. George of the Latins church the measurements were carried out mainly in three points in the North façade, close to the top of three buttresses, which are indicated in Figure 2.13 with the letter A.

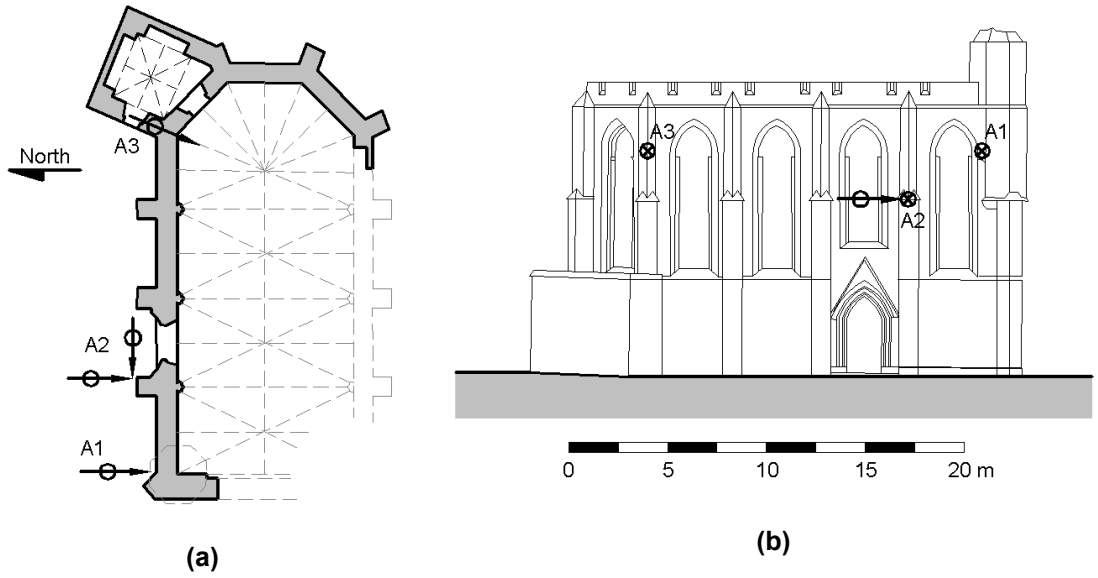

Figure 2.13. Test measurements in St. George of the Latins church: (a) top plan and (b) North façade (Lourenço & Ramos, 2008)

According to the results shown by (Lourenço & Ramos, 2008), natural frequencies are well spaced and their values are ranging between 2.6 to 18.0 Hz; the standard deviation is low, indicating that they were well estimated. Regarding mode shapes, as only three points were measured, the mode configurations are mainly out-of-plane modes, as expected, due to the unconstrained walls of the church ruins (Lourenço & Ramos, 2008). Concerning the damping coefficients, higher variations were observed for the estimated values and the obtained average damping value is equal to 1.26% which is low because ambient vibrations were used to excite the structure (Lourenço & Ramos, 2008). For this particular case of study only the first six modes were taken into account because they are out-of-plane modes which are more probable to occur and the measured frequencies and damping coefficients are shown in Figure 2.14. Also the mode shapes were estimated by (Lourenço & Ramos, 2008) using a specialized software and they are shown in Figure 2.15

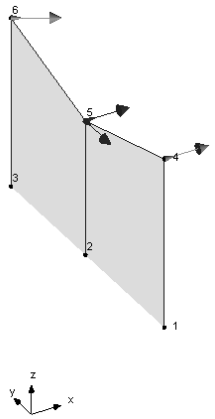

(a)

Modes	Frequency Values [Hz]	Frequency Standard Deviation [Hz]	Damping Values [%]	Damping Standard Deviation [%]
1	2.57	<0.01	1.04	0.38
2	3.14	0.01	1.05	1.02
3	3.95	0.06	0.55	0.57
4	4.06	0.02	0.58	0.14
5	5.26	0.02	0.85	0.16
6	5.61	0.02	0.77	0.21

(b)

Figure 2.14. Results of dynamic test: (a) Setup configuration and (b) measured frequencies and damping coefficients for the first six modes (Lourenço & Ramos, 2008)

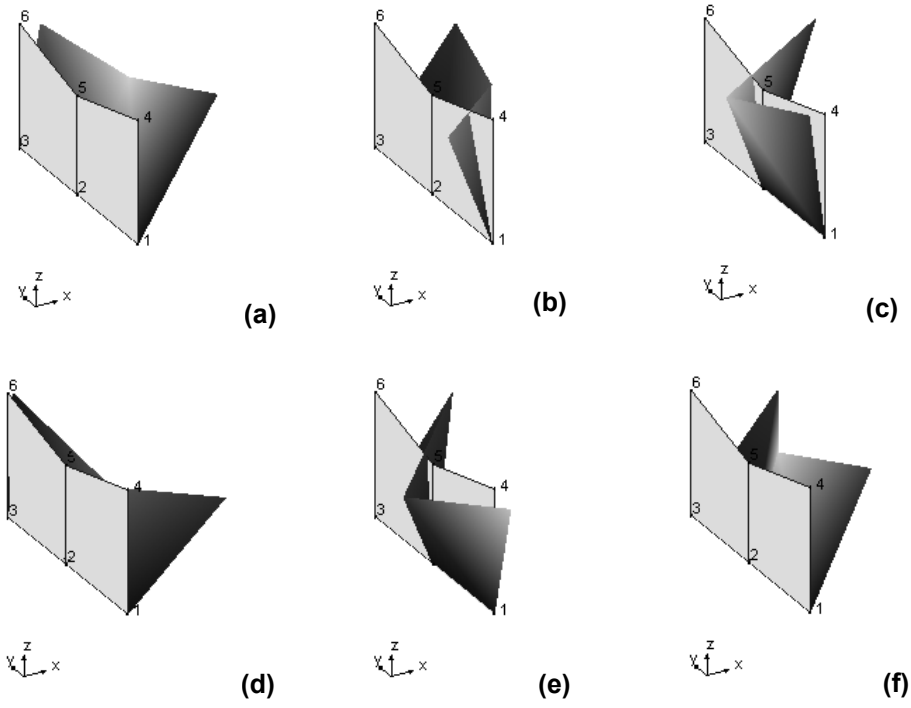

Figure 2.15. Mode shapes calculated with the experimental data: (a) 1st Mode shape configuration; (b) 2nd Mode shape configuration; (c) 3rd Mode shape configuration; (d) 4th Mode shape configuration, (e) 5th Mode shape configuration and (f) 6th Mode shape configuration

2.3.4 Experimental Results from Sonic Tests

The sonic tests are based on the propagation properties of elastic waves across solid mediums. These waves usually cross the medium in frequencies ranging from 0.4 to 10 kHz. Hence, knowing the distance between two points in the medium (the wall) and by measuring the travel time, it is possible to calculate the sonic velocity (elastic waves' velocity); there are several references for sonic velocities in different type of materials. Mainly two types of sensors are used, the hammer for impact transmission and the receiver (can be an accelerometer), both of them are connected to a data acquisition system that measures quantities, are stores them in a laptop. This technique is used to locate potential areas in the structure with damage, control the efficiency of injection works for walls consolidation and qualitatively assess wall's morphology by correlating its results with other types of non destructive tests (NDT).

In the tests carried out by (Lourenço & Ramos, 2008) in St. George of the Latins church one stone block with 1.12 m length and two buttresses with 0.97 m thickness were tested. The stone block was selected to measure the sonic velocity of the sandstone used in the construction. The two buttresses, one in the North façade and one in the South façade, were chosen with the aim to evaluate the internal condition, mainly if there are internal voids, different density materials or if repair works occurred in the recent past. Figure 2.16 shows the location of testing.

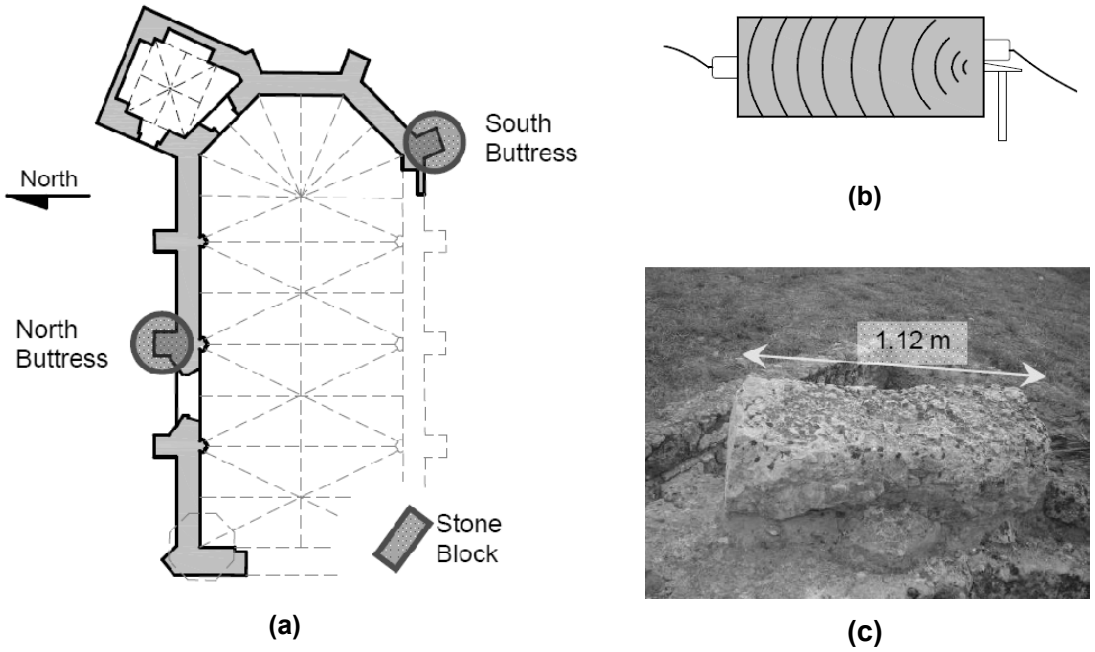

Figure 2.16. Sonic tests in St. George of the Latins church: (a) selected buttresses and block stone; (b) test setup for the stone block; and (c) image of the stone block (Lourenço & Ramos, 2008)

Starting with the stone block, shown in Figure 2.16-c, the average value for the sonic velocity of ten measurements was equal to 3033 m/s, with a Coefficient of Variation (CV) equal to 5%. This value is relatively low, possibly indicating that the stones used for the construction are porous. On the buttresses two vertical columns (A and B) and five horizontal levels were tested (10 points per column). The tested points in the North buttress are shown in Figure 2.17-a, and the velocity results are illustrated in Figure 2.17-b, where the sonic velocity ranges from 1400 to 2400 m/s and the average value for column A and B is 1597 and 2249 m/s, respectively. Observing the scale for the velocities in Figure 2.17-b, it is possible to see that the outer points of the buttress (column B) have higher velocity than the inner points (column A). The results indicate that the stones in the outer column were probably replaced by new ones in the recent past, while the internal part of the buttresses are in worse condition (Lourenço & Ramos, 2008).

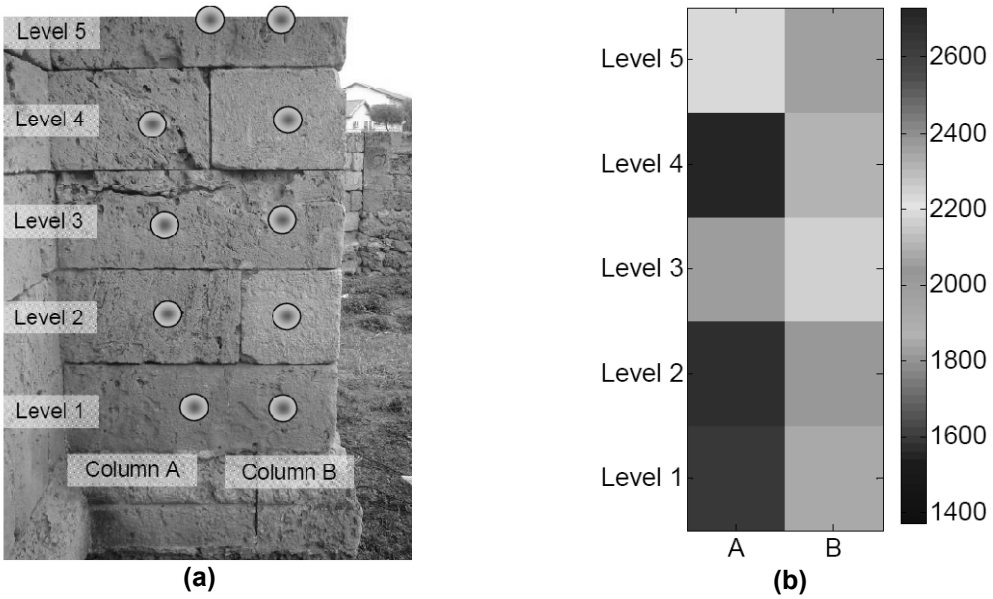

Figure 2.17. Sonic tests in North buttresses: (a) location of measured points and (b) velocity map (Lourenço & Ramos, 2008)

Concerning the South buttress, Figure 2.18 presents the measured points and the sonic velocity map. In this buttress small differences were found between the velocity values. Ranging from 1400 to 2600 m/s, the average values for A and B were 1923 and 1996 m/s, respectively. The values indicate that the internal condition of the buttress in the two columns (internal and external) is similar, with similar distribution of voids (Lourenço & Ramos, 2008).

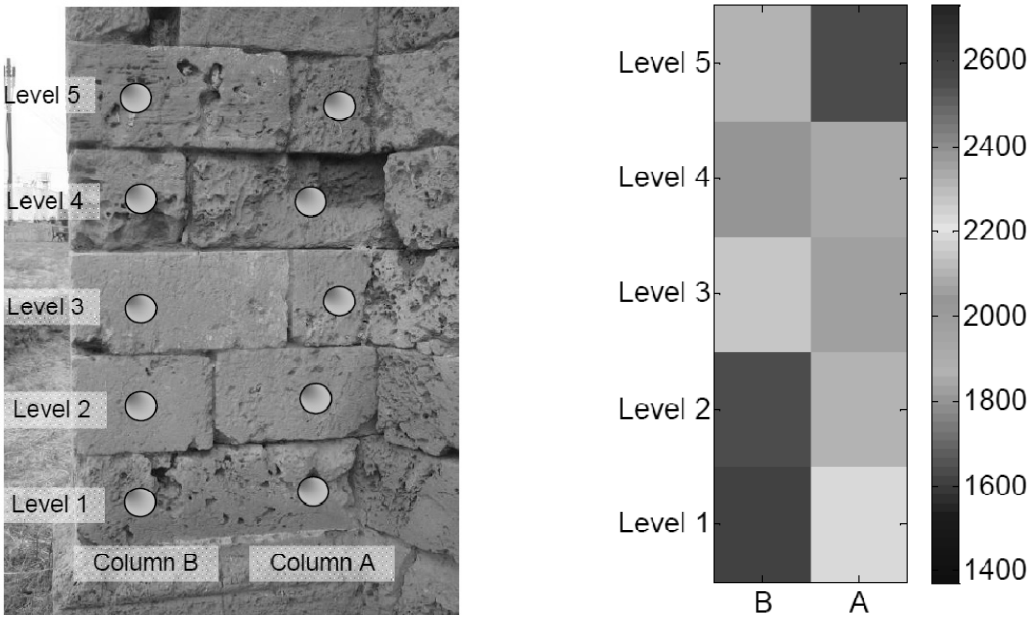

Figure 2.18. Sonic tests in South buttresses: (a) location of measured points and (b) velocity map (Lourenço & Ramos, 2008)

3. LIMIT ANALYSIS OF COLLAPSE MECHANISM

3.1 INTRODUCTION

During the 19th and the 20th centuries, the modern theory of elasticity and plasticity arise, including the limit analysis approach. It was (Heyman, 1966) who applied the modern formulation of limit analysis theory relaying on the rigid-perfectly plastic material model. To evaluate the load capacity and failure mechanism of masonry arches (known today as macro-elements). He considered three main hypotheses: (i) Masonry has null tensile stress, (ii) The compressive strength of masonry is infinite and (iii) Sliding between stone blocks is impossible, hence the failure should occur under small displacements. This author applied the following theorems: (i) The structure is safe, meaning that the collapse will not occur, if a statically admissible state of equilibrium can be found (Lower bound) and (ii) If a kinematically admissible mechanism can be found, for which the work developed by external forces is positive or zero, then the structure will collapse (Upper bound). Thus, the limit condition of the macro-element, or collapsing configuration, will be reached if both statically and kinematically admissible collapsing mechanism can be found. When this occurs, the load is the true ultimate load, the mechanism is the true ultimate mechanism and the thrust line is the only one possible (Roca, 2008-2009).

The use of limit analysis to analyze more complex and articulated masonry structures arose in Italy, where several experimental and theoretical studies, carried out after several important earthquakes, demonstrated that the behavior of historical constructions was out of range of the usual analysis approach (box behavior) and it was necessary to apply new analysis techniques, which result from a series of information deduced from the observation, namely for the evaluation of seismic response (Franchetti, 2008-2009). Hence, significant work of classification was developed for several cases of study finding common collapsing configuration for structures with the same typology, and they were joined together in a set of abacus shown in (O. P. C. M. 3431, 2005). This abacus represents local failure (loss of equilibrium) in different parts of the structure that for several reasons are not able to develop a global response, and it takes into account 28 different local failure modes for religious and civilian constructions, mainly two-stories houses, churches and bell towers. Among the local mechanisms, the most common recorded were: out-of-plane rotation of load-bearing masonry due to lack of orthogonal connections (see Figure 3.1-a), rotation out-of-plane of the top part of the walls (see Figure 3.1-b), masonry disaggregation or expulsion depending on wall's typology (see Figure 3.1-c) and in-plane mechanism for shear stresses with diagonal cracks (see Figure 3.1-d) (Franchetti, 2008-2009).

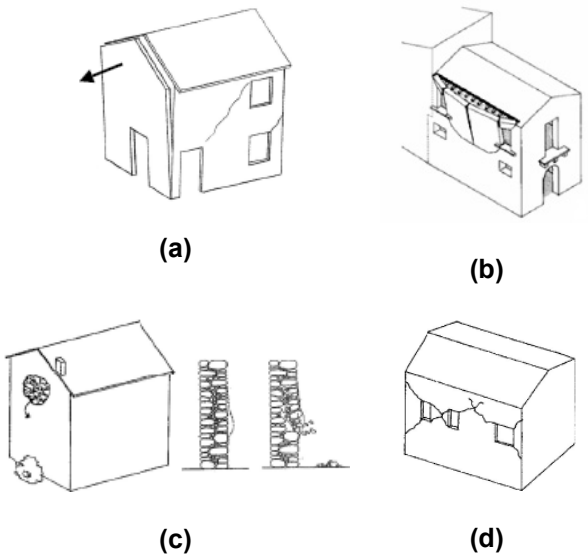

Figure 3.1. Most common local collapse mechanisms: (a) Out-of-plane rotation of external wall, (b) Out-of-plane rotation of upper part, (c) expulsion or disaggregation and (d) in-plane shear stresses

Following the principles abovementioned, the ultimate capacity of the structure depends on the stability of its macro-elements, which are portions of the structure bounded by potential damage patterns that can behave as a whole, following a kinematic mechanism (Giuffrè, 1993). For this particular case, these macro-elements were defined according to the damage reported in photographs taken during the inspection works carried out by (Lourenço & Ramos, 2008) and the photographs of the restoration project carried out during 1940, where same structural components were taken into account for each portion of the structure. In order to define the different macro-elements, the structure was divided in three different parts: its West façade, the Apse and its North façade and for each part, the damage was evaluated and subsequent damage patterns were defined. The buttresses and pier walls of the church were numbered for an easy identification and description of the defined collapse mechanisms and as it is shown in Figure 3.2; it is important to highlight the importance of the Global axes definitions because the directions of the defined collapse mechanisms were determined along them.

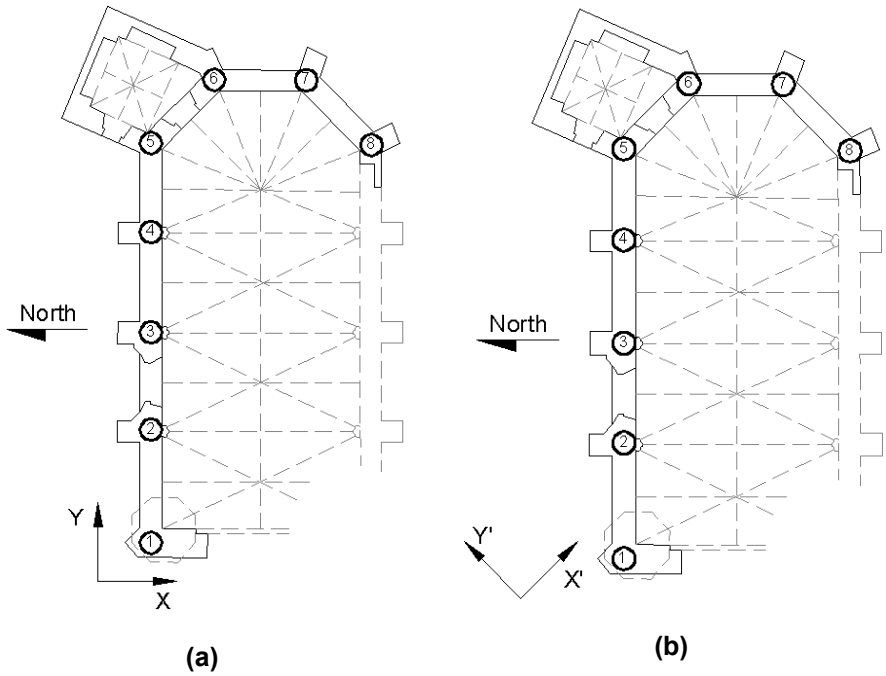

Figure 3.2. Numbering of pier walls and buttresses for two different reference directions: (a) global directions and (b) rotated directions (parallel to the apse's walls)

After defining the different macro-elements that compose the church, the next step was to identify the most probable mechanism that characterize each macro-element, hence out-of-plane collapse mechanisms were defined in each of the structural components of the church in different directions; the in-plane mechanisms were disregarded due to lack of confinement and only out-of-plane mechanisms were taken into account due to unconstrained walls (lack of orthogonal connections). After that, mechanical models reported in (Valluzzi, Cardani, Binda, & Modena, 2004) which described collapse mechanism's specific behavior by kinematic models were applied; it is important to highlight the application of simple models, as those shown in Figure 3.3-a, disregarding the constraints of the connections with orthogonal walls and assuming that the crack region is opened enough so that tensile and shear strengths in the hinges may be neglected. Despite the thickness of the wall, the arch effect was disregarded as well as the bending of the horizontal strips (see Figure 3.3-b) and the macro-element was assumed as a rigid body except in its boundaries where cylindrical hinges are formed following the damage pattern (cracks and openings); thus it is expected that results obtained in this chapter are absolute lower bounds.

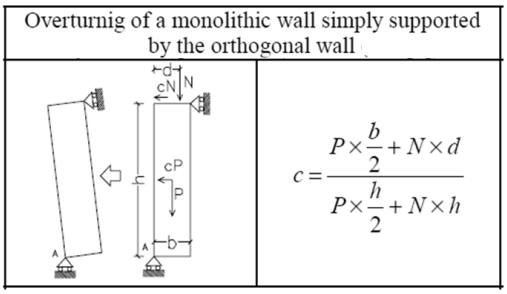

(a)

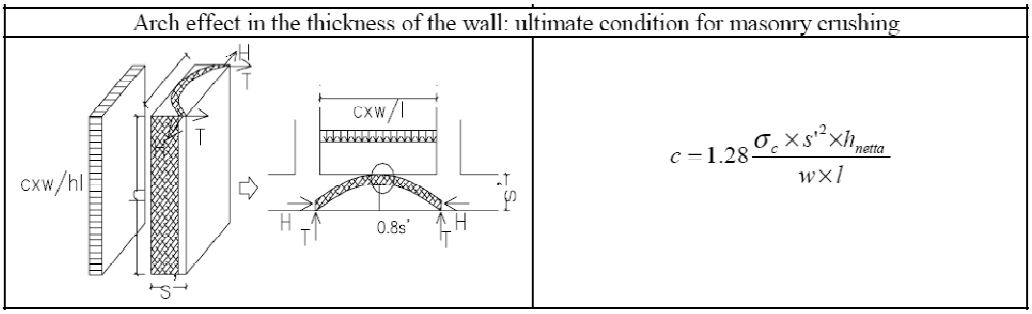

(b)

Figure 3.3. Applied Kinematic Models for out-of-plane mechanisms: (a) Vertical strips (Avorio, Borri, & Corradi, 2002) and (b) Horizontal strips (Bernardini, Gori, & Modena, 1988)

The result obtained from the application of kinematic models is a Load coefficient c (see Equation 3.1) which represents the mass multiplier that activates the local failure mode thus leads the macro-element to collapse. A simplified procedure to assess the seismic response of a structure is to compare the collapse coefficient obtained from the limit analysis of all the possible kinematic collapse mechanisms, and select the lowest coefficient; therefore this mechanism is the weakest one and the most probable to occur during a seismic event. The collapse is due to a loss of equilibrium of its structural configuration instead of exceeding the ultimate strength of the material (Valluzzi, Cardani, Binda, & Modena, 2004).

$$c = a/g \tag{3.1}$$

Where: a: is the ground acceleration

g: is the gravity acceleration (9.81m/s²)

Besides finding the load coefficient that activates the mechanism, the kinematic approach also allows to determine the amount of horizontal force that the macro-element is progressively able to bear in the post-peak, with the developing of the mechanism until total collapse which occurs when the collapse coefficient is equal to zero and the structural element fully overturns. Hereby it is possible to obtain the path of a specific point (reference control point) which in this case is its center of mass. Such curve represents the capacity of the macro-element to bear horizontal force until the collapse and it is

expressed by the collapse coefficient c plotted versus the total displacement of the control point $d_{k,o}$; this procedure was applied for each defined collapse mechanism following the recommendations of (O. P. C. M. 3431, 2005).

3.2 WEST FAÇADE AREA

This façade is only composed by small portion of wall of about 5.00 meters long, and its height is about 18.00 meters, with a tower with a box structure (void inside) at the top (see Figure 3.4-a). The tower seems to have suffered rotation due to settlement or earthquake problems according to (Lourenço & Ramos, 2008) and crack opening is shown in Figure 3.4-b . Despite restoration works carried out during 1940 (see Figure 3.4-d) where several stone replacements were done, stone deterioration concentrated in the lower part at the corner is still found (see Figure 3.4-d). Also there is a stone deteriorated region in the lower part of the connection between North and West façades (see Figure 3.4-c), which could be a possible sign of weakness in this connection. According to this damage patterns the mechanism selected is shown in following sections and its overturning was taken into account along two different directions.

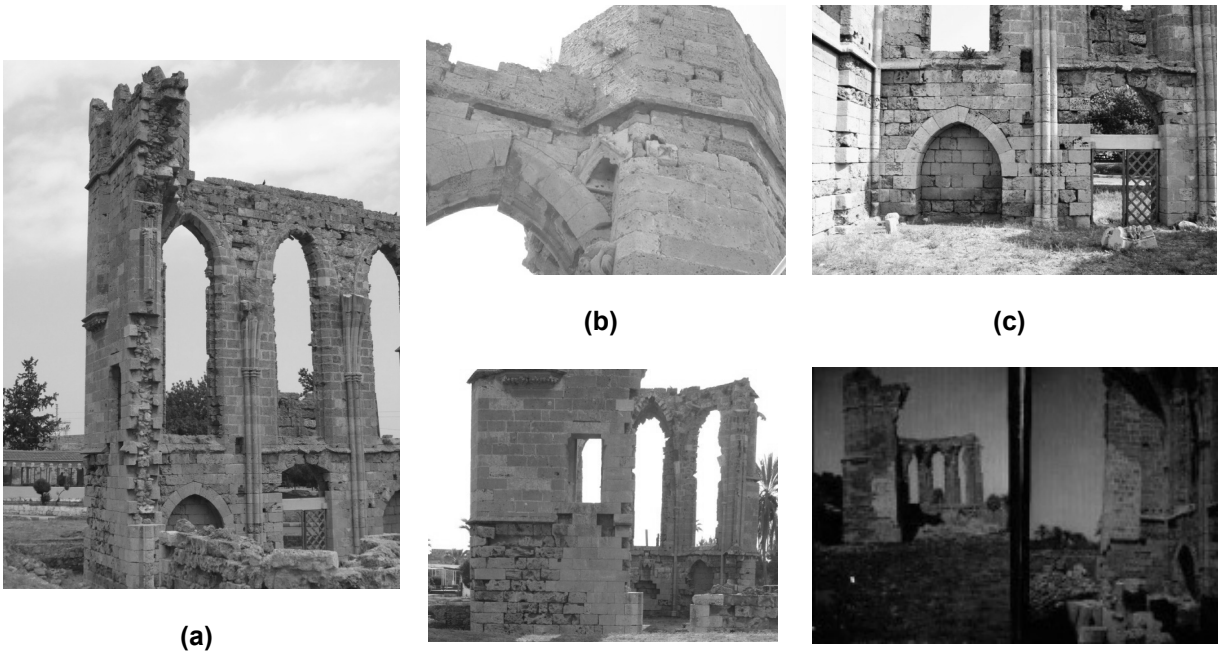

Figure 3.4. West façade: (a) general view, (b) upper part disconnection due to tower rotation, (c) severe deterioration of stones in the connection with North façade, (d) severe stone deterioration in the lower part and (e) replaced (lighter) stones during conservation works in 1940

3.2.1 Overturning in -X direction (Outwards)

One kinematic mechanism considered is the overturning in –X direction of the macro-element shown in Figure 3.5. This macro-element compromises the whole tower structure and two thirds (in height) of the west façade. The defined hinges follow the damage pattern shown in Section 3.2; thus one is located in the upper part of the connection between North and West façades, and the other one is located at one third (in height) forming a tridimensional wedge. The results obtained from the kinematic analysis of this mechanism are shown in Section 3.2.3.

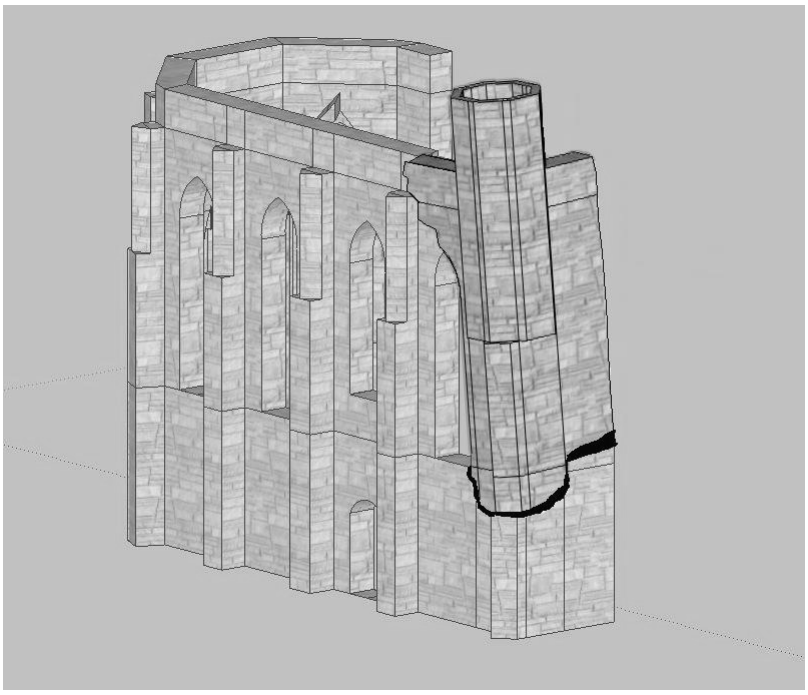

Figure 3.5. Macro-element selected for its overturning in –X direction

3.2.2 Overturning in –Y direction (Outwards)

The other kinematic mechanism considered for this part of the structure is the overturning in –Y direction of the macro-element shown in Figure 3.6. This macro-element was previously described in Section 3.2, the only difference is the direction of its overturning, which in this case is in –Y direction. The results of the kinematic analysis of this mechanism are shown in Section 3.2.3.

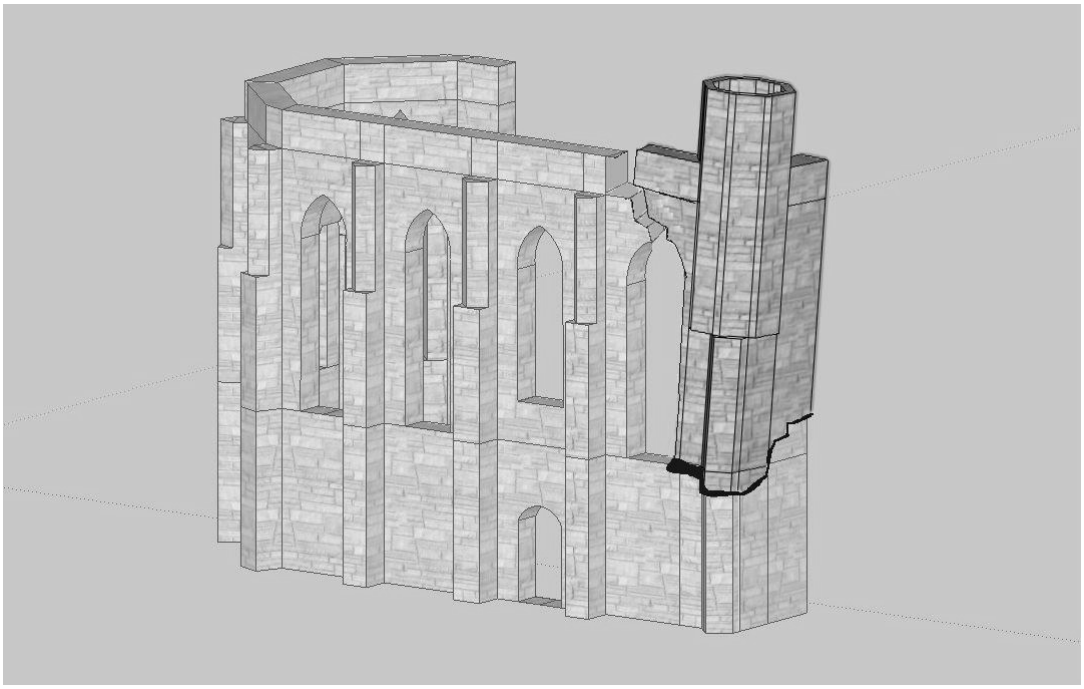

Figure 3.6. Macro-element selected for its overturning in –Y direction

3.2.3 Collapse Mechanisms Results

In order to evaluate its stability, the mechanical model shown Figure 3.3-a was used for both mechanisms, overturning in –X direction (CM_W_X) and overturning in –Y direction (CM_W_Y), obtaining the load coefficient for each of them, which represents the amount of lateral acceleration that is necessary to activate the mechanism (see Table 3.1). Then, the capacity curve was obtained following the recommendations exposed in (O. P. C. M. 3431, 2005), in order to find the lateral load evolution until the structure's collapse, and it is reported in Figure 3.7.

Mechanism	Load Coefficient (c)	Total displacement ($d_{k,o}$) [m]
CM_W_X	0.136	1.94
CM_W_Y	0.109	1.56

Table 3.1. Results from the kinematic analysis of the collapse mechanism CM_W_X and CM_W_Y

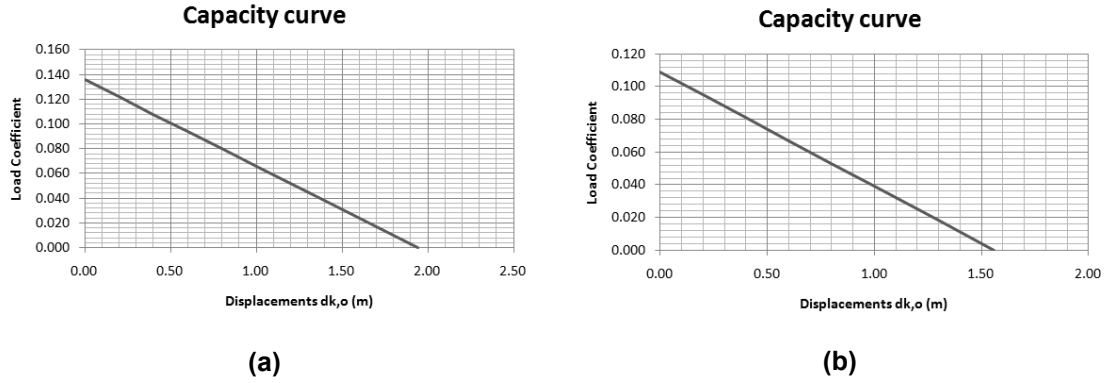

Figure 3.7. Capacity curves of mechanism: (a) CM_W_X and (b) CM_W_Y

The results indicate that the collapse mechanism most probable to occur in this portion of the structure is the overturning in –Y direction of the macro-element. Also it is important to remark that excessive displacements obtained from the capacity curves of both mechanisms should be limited in the reality due to previous local damages or three dimensional collapse mechanisms which were simplified in terms of planar mechanisms.

3.3 NORTH FAÇADE AREA

This façade is composed by four large windows of about 7.00 meters high, and three pier walls (number 2, 3 & 4; see Figure 3.2) which are located in the middle of the windows, alternating with each other (see Figure 3.8-a). Its lower part is completely massive; except for one door located between piers 2 and 3 (see Figure 3.2). Regarding its present conditions, there were several stone replacements in both sides of the walls, especially in the outer side of the wall (Figure 3.8-d) where the stone are less porous. Also it is possible to see that buttresses show loss of stone elements and severe stone deterioration, and according to (Lourenço & Ramos, 2008) their structural function is possibly very limited. In the upper part of the inner face, the stones are deteriorated and some of them have been detached (see Figure 3.8-b & Figure 3.8-c); this also occurs in some areas of the wall lower part. Some stones of the buttresses were replaced during 1940's restoration works; nevertheless their internal conditions are damaged (Lourenço & Ramos, 2008). The assumed failure mechanism for this part of the structure includes three pier walls (number 2, 3 & 4) from the cornice to the top part of the wall and the assumed plastic hinges for its development are shown in Figure 3.8-e and Figure 3.8-f, where cracks are clearly defined (opening and sliding). The only overturning direction considered for this macro-element was its rotation coming inwards; its kinematic analysis is shown in following Sections.

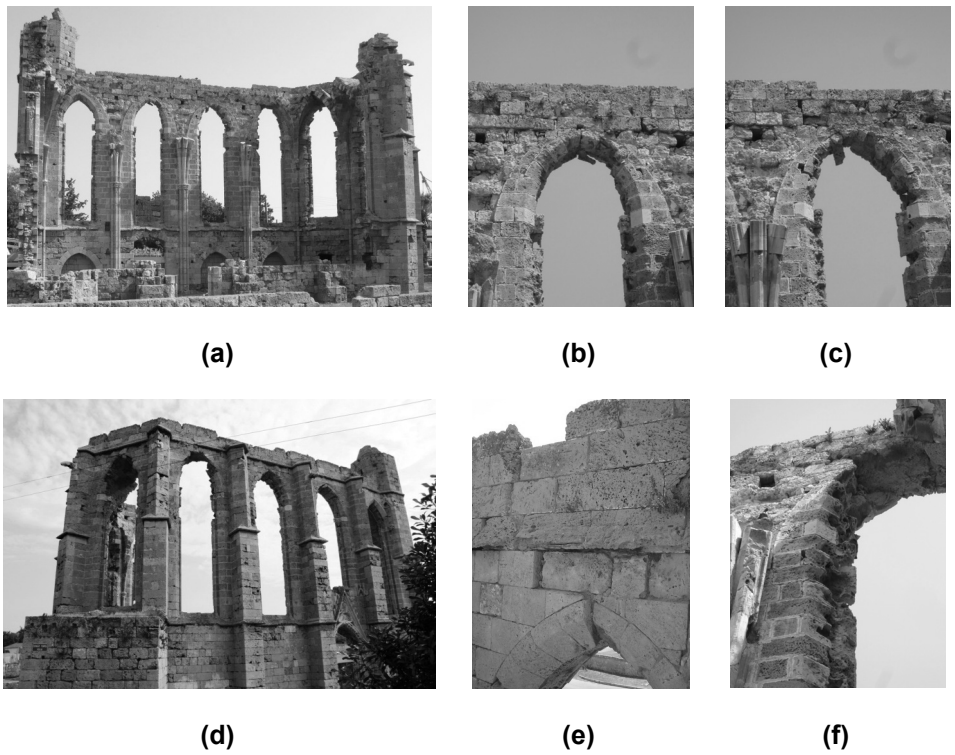

Figure 3.8. North façade: (a) interior view, (b) upper part of the second window (from left to right), (c) upper part of the third window (from left to right), (d) exterior view, (e) crack opening and sliding in the connection with West façade and (f) crack opening and sliding in the connection with the Apse

3.3.1 Overturning in X direction (Inwards)

This collapse mechanism was defined following the damage conditions previously exposed in Section 3.3 and it involves three pier walls (number 2, 3 & 4) which behave as a rigid body meaning that three of them rotate at the same time along the cornice located just below windows (see Figure 3.9), which is the first defined plastic hinge. The other two hinges are located in the connection between North and West façades and North façade and Apse, as it was previously discussed. The results of the kinematic analysis of the macro-element's collapse mechanism are shown in Section 3.3.2.

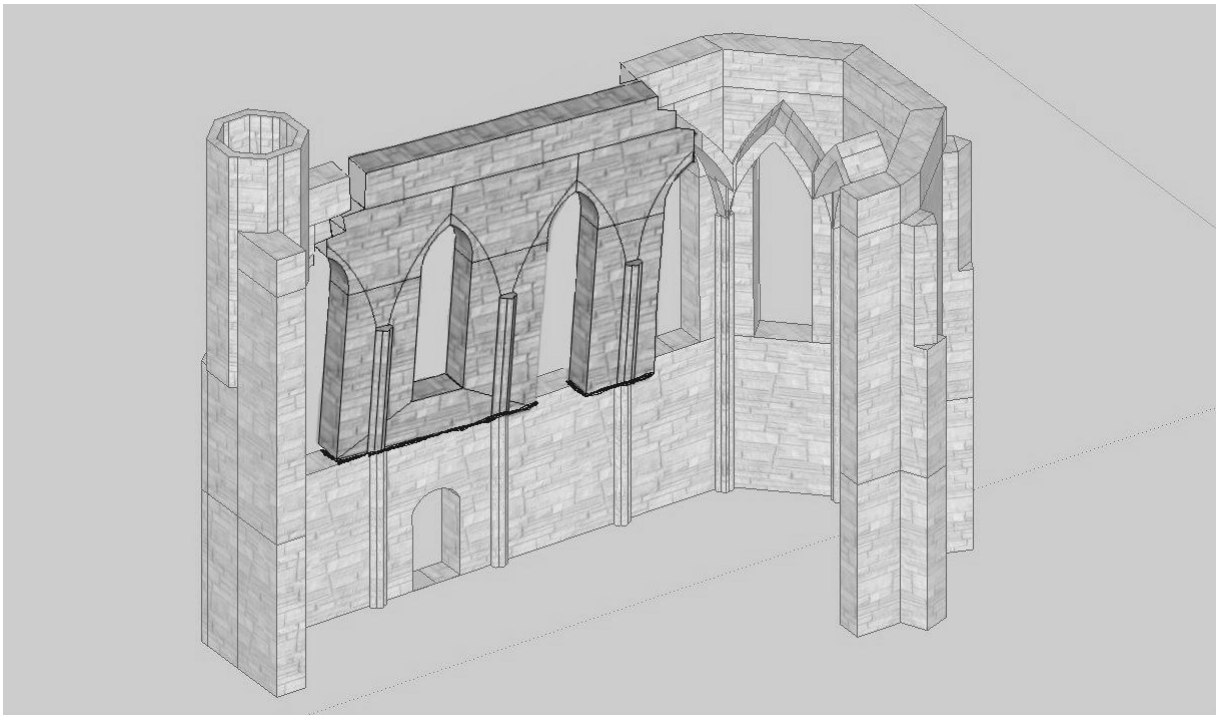

Figure 3.9. Selected macro-element (CM_N_X) for its overturning in X direction

3.3.2 Collapse Mechanism Results

The collapse mechanism (CM_N_X) stability was evaluated by means of the mechanical model shown Figure 3.3-a; this mechanism involves the overturning of the macro-element previously defined in X direction (inwards). The obtained load coefficient, which represents amount of lateral acceleration that is necessary to activate the mechanism and the ultimate displacement where the mechanism is fully activated (load coefficient is zero) are shown in Table 3.2. Also its capacity curve was calculated following the recommendations exposed in (O. P. C. M. 3431, 2005), and it represents the lateral load evolution until the macro-element reaches collapse; it is reported in Figure 3.10.

Mechanism	Load Coefficient (c)	Total displacement ($d_{k,o}$) [m]
CM_N_X	0.097	0.96

Table 3.2. Results from the kinematic analysis of the collapse mechanism CM_N_X

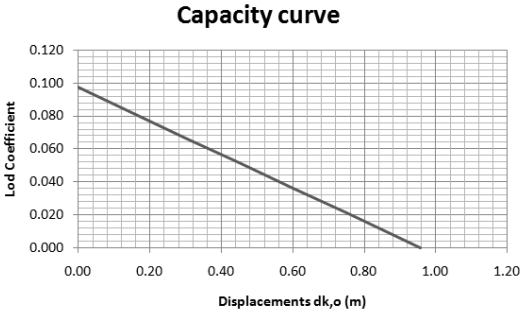

Figure 3.10. Capacity curve of mechanism CM_N_X

The results indicate that the amount of horizontal acceleration that activates the collapse mechanism is about 10% of the gravity acceleration and the mechanism reach its collapse after 0.96 meters of displacement in its control point (center of mass of the macro-element). It is important to highlight that these results are the lower bound of the solution because several simplifications were done. Also it is important to remark that excessive displacement obtained from the capacity curve should be limited in the reality due to possible local damages meanwhile the horizontal acceleration is increasing.

3.4 APSE AREA

The apse of the church is composed by three windows and four pier walls (number 5, 6, 7 & 8; see Figure 3.2) and the lower portion of the wall is mainly solid (no openings) except the lower portion of the wall located between pier walls 5 and 6 which has a door opening in order to connect the church with the Sacristy (see Figure 3.11-a). The apse buttresses (see Figure 3.11-d) are also deteriorated, but in contrast with North buttresses, they present similar void distribution, in their external and internal portions (Lourenço & Ramos, 2008), thus their structural function is in doubt. The explicit damages in the buttresses according to the photographs obtained from the inspection carried out by (Lourenço & Ramos, 2008) are similar to stone damages in other parts of the church; porosity, loss of material and severe decay (see Figure 3.11-b and Figure 3.11-c).

This part of the church is the only one that still has a part of the vaults, although they are deteriorated, mainly the stone on them has the same problems as those arising in the rest of the church: loss of material and unconfined portions of material (see Figure 3.11-f). In almost all of them, there is a plastic hinge formed in the vertex of the vault, where two pointed arches converge; this hinge is formed by sliding crack (see Figure 3.11-e).

The bottom part of the façade is made by a solid wall with pointed arches located below the windows which thickness is equal to about half of the total thickness of the wall. Its condition of deterioration is also the same as in other parts; loss of material, porosity and lack of confinement (see Figure 3.11-e).

Three different collapse mechanisms were defined involving three different macro-elements which were defined following the abovementioned damage pattern and structural arrangement of the apse. Several directions were taken into account for the overturning of each one of the macro-elements, and the kinematic analysis was performed for each different condition and the results were compared in order to estimate the most probable collapse mechanism of the portion of the structure.

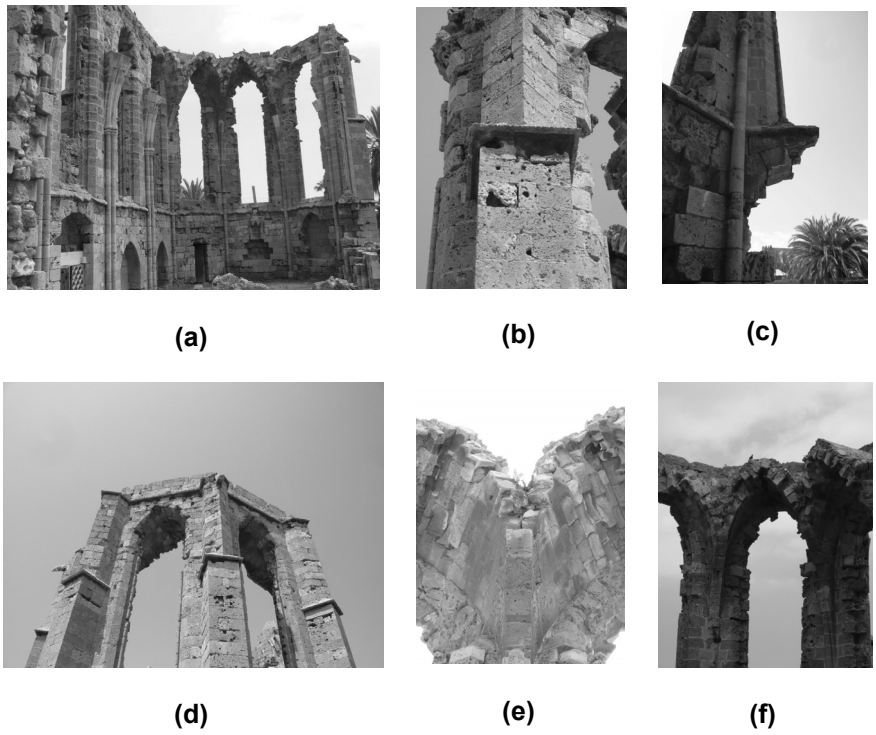

Figure 3.11. Apse region: (a) internal view, (b) external view of buttress number 8, (c) internal view of lower portion of buttress number 8, (d) external view, (e) plastic hinge in the top point of the vault (sliding) and (f) general view of the vaults

3.4.1 Overturning of Pier Wall 5 Outwards

The first collapse mechanism includes the pier wall number 5 that overturns around the cornice located in the lower part of the windows, which is also the first hinge; the second hinge is located in the upper part of the window where the apse connects with the North façade and the third hinge is a straight axis along the vault vertex where two pointed arches meet together between pier walls number 5 and 6 (see Figure 3.12). Two different directions for the overturning were considered based on the structural configuration of the apse; one is the overturning of the macro-element in –X direction (CM_A5_X) (see Figure 3.2-a) and the other is the overturning of the macro-element in Y' (rotated Y) direction (CM_A5_RY) (see Figure 3.2-b). The mechanisms were analyzed using the kinematical approach and the results are shown in Section 3.4.4.

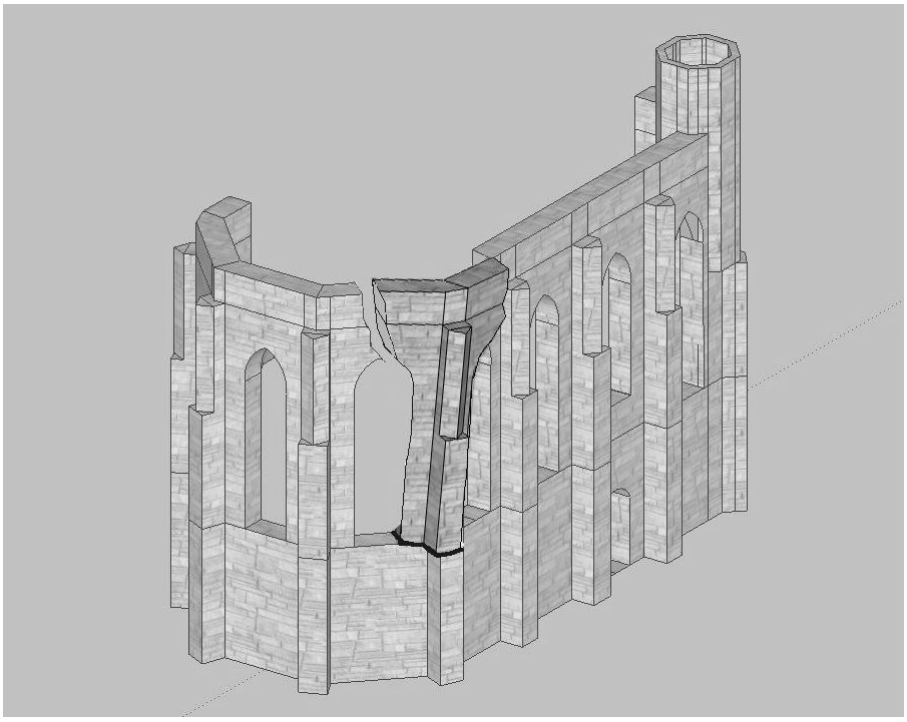

Figure 3.12. Macro-element selected for its overturning in -X direction (CM_A5_X) and Y' direction (CM_A5_RY)

3.4.2 Overturning of Pier Walls 6 and 7 Outwards

The macro-element defined for this collapse mechanism includes pier walls number 6 and number 7 (see Figure 3.13). It is assumed that both pier walls will behave as a rigid body and they will rotate at the same time with the same rate and the lower plastic hinge will simultaneously appear in both of them at the same time; this hypothesis is based on the restriction that vaults give to the movement along certain directions. The other two plastic hinges are the following; one is located along the vault vertex where two pointed arches meet together between pier walls number 5 and 6 (is the same as that for the overturning of pier wall 5); the other one is located in the upper portion of the wall that is between pier walls number 7 and 8 which boundary occurs the end of the vault. The overturning of this macro-element was only analyzed in the only possible direction, Y direction (CM_A67_Y) and the results are shown in Section 3.4.4.

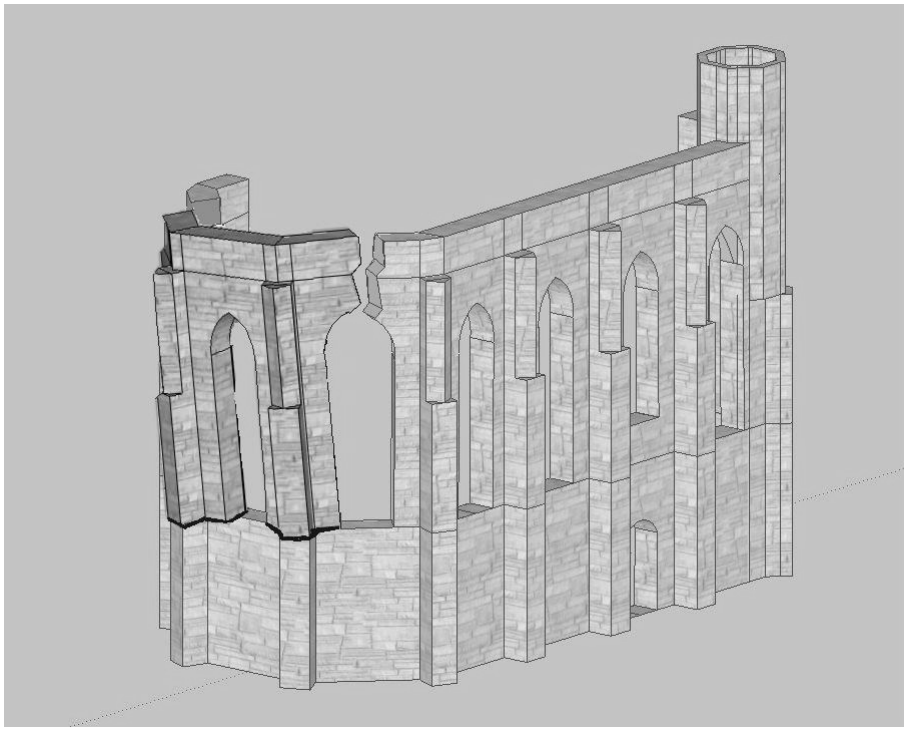

Figure 3.13. Selected macro-element for its overturning in Y direction (CM_A67_Y)

3.4.3 Overturning of Pier Wall 8 Outwards

The definition of the selected macro-element only includes the pier wall number 8 (see Figure 3.14). This pier wall is connected with pier wall number 7, in the upper portion of the window located between them where the first plastic hinge was defined; it follows the same path as that of the vault end. The other side of the pier wall is released; in the past it was connected with the south façade which collapsed. The rotation hinge is located in the lower cornice, just below the window and two different directions were considered for its overturning, X direction (CM_A8_X) and X' (CM_A8_RX), and the kinematic approach was applied obtaining the results shown in Section 3.4.4.

Figure 3.14. Selected macro-element for its overturning in X direction (CM_A8_X) and X' (CM_A8_RX)

3.4.4 Collapse Mechanism Results

The collapse mechanisms (CM_A5_X), (CM_A5_RY), (CM_A67_Y), (CM_A8_X) and (CM_A8_RX) stabilities were assessed by means of the mechanical model shown Figure 3.3-a; this mechanism involves the overturning of the macro-elements previously defined. The obtained load coefficient for each of the mechanisms, which represents the amount of lateral acceleration that is necessary to activate the mechanism and the ultimate displacement of each of the mechanisms where the mechanism is fully collapse (load coefficient is null) are reported in Table 3.3. Also their capacity curves were calculated following the recommendations exposed in (O. P. C. M. 3431, 2005), and they represent the lateral load evolution until the macro-element reaches collapse; the results are reported in Figure 3.15.

Mechanism	Load Coefficient (c)	Total displacement ($d_{k,o}$) [m]
CM_A5_X	0.213	2.01
CM_A5_RY	0.163	1.54
CM_A67_Y	0.170	1.61
CM_A8_X	0.195	1.92
CM_A8_RX	0.120	1.18

Table 3.3. Results from the kinematic analysis of the collapse mechanisms (CM_A5_X), (CM_A5_RY), (CM_A67_Y), (CM_A8_X) and (CM_A8_RX)

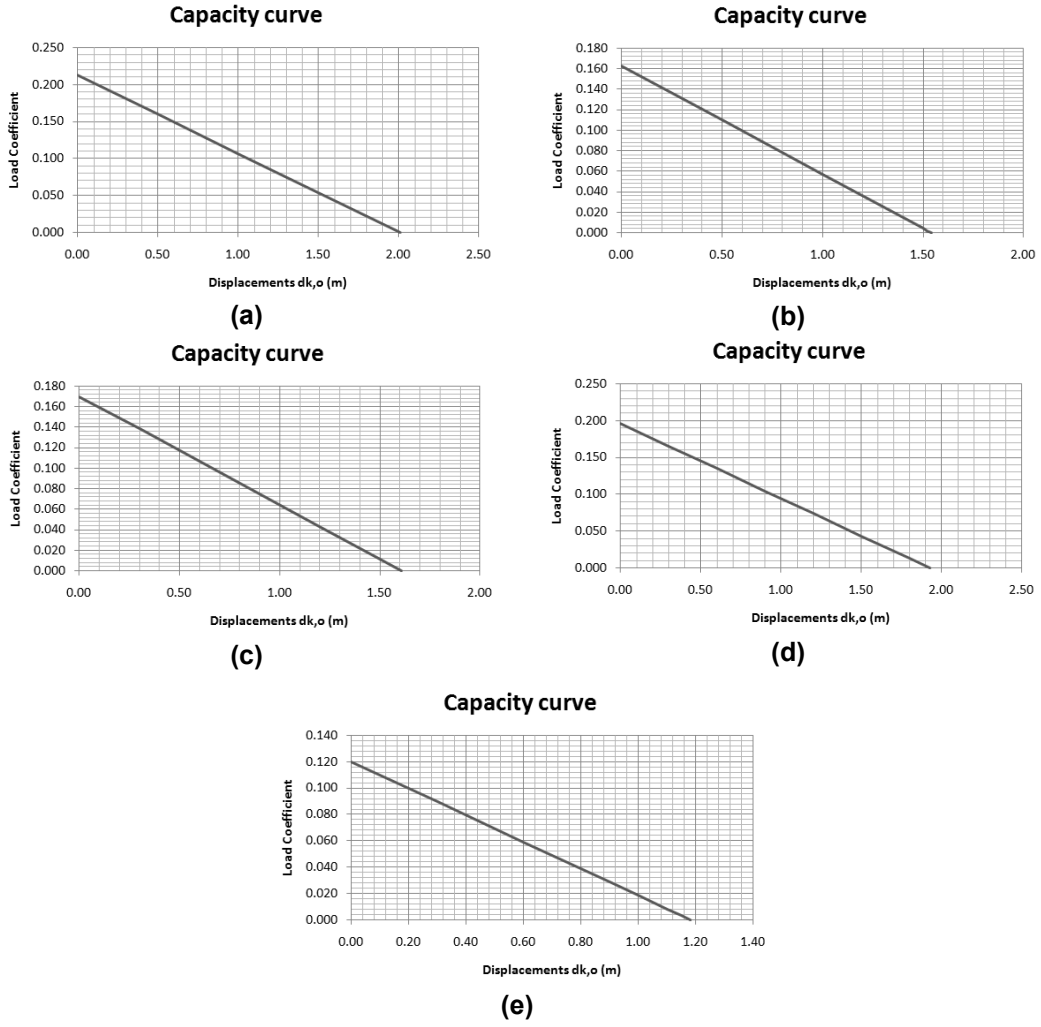

Figure 3.15. Capacity curve of mechanism: (a) CM_A5_X, (b) CM_A5_RY, (c) CM_A67_Y, (d) CM_A8_X and (e) CM_A8_RX

The results indicate that the collapse mechanism that will occur (the one with the minimum load coefficient in each direction), in this portion of the structure, is the overturning of pier wall number 8 in Y' direction with a load coefficient of 0.120 (12% of gravity acceleration). Also it is important to remark that excessive displacements obtained from the capacity curves of all mechanisms should be limited in the reality due to previous local damages or three dimensional collapse mechanisms which were simplified in terms of planar mechanisms

3.5 ANALYSIS OF THE RESULTS

The histograms with all the results obtained from the kinematic analysis of the collapse mechanism are reported in Figure 3.16 for X direction and in Figure 3.17 for Y direction. The minimum load coefficient in X direction (0.097) shows that the mechanism CM_N_X is the most probable of occurrence. This mechanism compromises the stability of the north façade. In Y direction, the minimum load coefficient was about 0.109 for mechanism CM_W_Y which compromises the stability of the west façade. Therefore according to the limit analysis approach the most vulnerable parts of the structure are the North and the West façades.

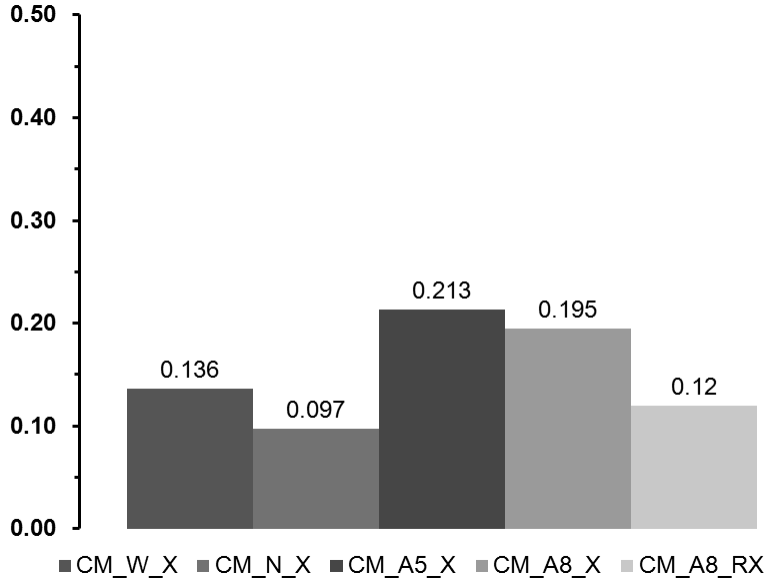

Figure 3.16. Histogram with the load coefficients obtained from the kinematic analysis in X direction of collapse mechanism

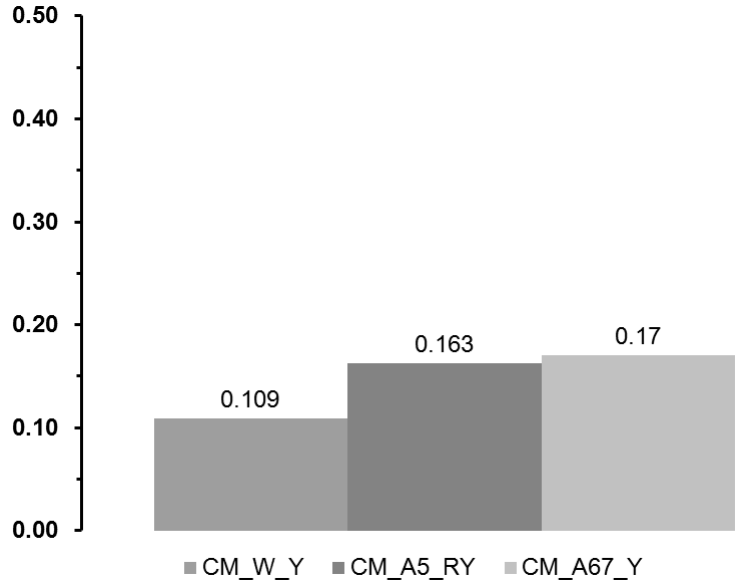

Figure 3.17. Histogram with the load coefficients obtained from the kinematic analysis in Y direction of collapse mechanism

4. DEFINITION OF THE NUMERICAL MODEL

4.1 INTRODUCTION

The Finite Element method was applied in order to analyze the model, as this method is suitable for modeling massive structures like Historical Constructions built in masonry. Several linear static analyses and modal response analyses were run in (DIANA, 2008), by changing different geometrical properties and material properties in the model, such as elastic modulus or material thickness, also by modeling the presence of damage. The main purpose of running different numerical analyses was to analyze the influence of each parameter in the behavior of the structural model by measuring the principal stresses, natural frequencies and mode shapes and comparing them with the experimental and historical data.

The main goal in the linear static analysis is to solve the equilibrium conditions and compatibility assuming that the response of the structure is linear and proportional to the actions applied on it because the structure is idealized as if it was made of an elastic material (Equation 4.1). In these preliminary analyses, the action is the gravity, and the task is to analyze the structure reactions, stresses, strains and displacements when it is subjected to its own weight.

$$\sigma = D \cdot \varepsilon \qquad 4.1$$

Where:

σ: is the stress vector

D: is the Elastic stiffness matrix

ε: is the strain vector

The principal stresses are a relevant result of interest in this task because they give the distribution of tensile and compressive stresses among the structure, and they can be compared with masonry compressive and tensile strengths. The principal stresses are calculated solving the characteristic equation (Equation 4.2), which has three invariants that are independent of the coordinate system, and whose real roots are the principal stresses.

$$\sigma^3 - I_1 \cdot \sigma^2 + I_2 \cdot \sigma - I_3 = 0 \qquad 4.2$$

Where:

σ: is the stress tensor

$I_1,\ I_2,\ I_3$: are the invariants of the stress tensor

The main objective in the modal response analysis is to determine the vibration modes and their contribution to the dynamic response of the structures. The Eurocode 8 (EN 1998-1, 2004) state that several modes of vibration should be determined until the total mass participation factor reaches 90%. It is important to remark that this is an ancient construction dated to the end of 13th century, which is out of the scope of the Eurocode rules and this parameter is only mentioned as a reference. For this structure only the first 6 modes were calculated in order to compare them with the first six measured modes of vibration in the dynamic identification test reported in (Lourenço & Ramos, 2008).

As a first approach to the modal response problem, the eigenvalue problem shown in Equation 4.3 should be solved and therefore angular frequencies of the structure are estimated. Later on, the mode shape vectors are estimated using Equation 4.4, which are proportional to the mass matrix, the stiffness matrix and its respective angular frequency.

$$\det\left(k - \omega_i^2 . m\right) = 0 \qquad 4.3$$

Where:

k: is the stiffness matrix

ω_i: is each one of the angular frequencies

m: is the mass matrix

$$\left(k - \omega_i^2 \cdot m\right) \cdot \phi_i = \underline{0} \qquad 4.4$$

Where: ϕ_i: is each one of the mode shapes

In order to know the mass participation factor for each mode, several variables should be calculated according to the following equations:

$$m_i = \phi_i^T \cdot m \cdot \phi_i \qquad 4.5$$

Where: m_i: is the excited mass of the i mode

$$L_i = \phi_i^T \cdot m \cdot r \qquad 4.6.$$

Where: r: influence vector of the resultant mass to an unitary displacement at the base

$$\Gamma_i = \frac{L_i}{m_i} \qquad 4.7$$

Where: Γ_i : is the modal participation factor of the i mode

$$m_{eff,i} = \frac{L_i^2}{m_i} \qquad 4.8$$

Where: $m_{eff,i}$: is the modal mass per vibration mode and direction

After solving the eigenvalue problem, the obtained frequencies were compared with the frequencies measure in the dynamic tests, and the error of the numerical estimation was computed using Equation 4.9.

$$error = \frac{\omega_i - \omega_{EXP}}{\omega_{EXP}} \cdot 100\% \qquad 4.9$$

Where: ω_i : is the i-th numerical angular frequencies

ω_{EXP} : is the measured experimental frequencies

The computed numerical mode shapes were correlated with those obtained from the experimental results by means of the Modal Assurance Criteria (MAC) value, which is the most well known procedure to study the numerical correlation between two sets of mode shape vectors (Ramos, 2007). It gives one for perfect correlation while returning a value of zero for uncorrelated mode shapes. It is defined by Equation 4.10.

$$MAC\left(\phi_{NUM,i}, \phi_{EXP,j}\right) = \frac{\left(\phi_{NUM,i}^T \phi_{EXP,j}\right)^2}{\left(\phi_{NUM,i}^T \phi_{NUM,i}\right)\left(\phi_{EXP,j}^T \phi_{EXP,j}\right)} \cdot 100\% \qquad 4.10$$

Where: $\phi_{NUM,i}$: is the i-th mode of numerical model

$\phi_{EXP,j}$: is the j-th mode of experimental measurement

At the end, two models were selected according to the frequency estimation error and the MAC values between the obtained numerical data and the measured experimental data; these models were those with results that better approach the experimental measurements and predicted data, and they were used to perform a model updating procedure.

4.2 GENERAL DESCRIPTION OF THE NUMERICAL MODEL

The numerical model was prepared using (DIANA, 2008), which is a specialized software for analyses using the Finite Element method (FEM). The model was prepared according to the geometrical information gathered from the historical documents and by the measurement of the actual conditions of the structure and it is shown in Figure 4.1-b . In order to model the structure, solid elements were disregarded because they have higher computation cost than shell elements, which have been adopted. These elements follow two shell hypotheses: shear deformation is included according to the *Mindlin-Reissner* theory and the normal stress component perpendicular to the surface of the element is zero (DIANA, 2008).

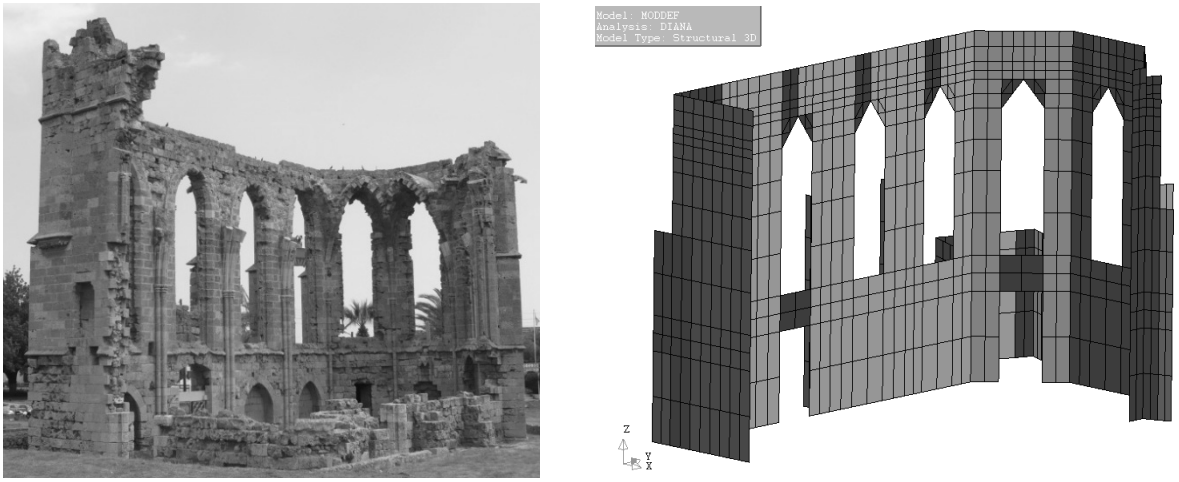

Figure 4.1. (a) General view of the church and (b) numerical model definition with (DIANA, 2008)

Two different types of shell elements were used to generate the mesh: quadrilateral elements with eight nodes (CQ40S-four nodes in the vertices and four mid-side nodes) to mesh the surfaces composed by four sides and triangular elements with six nodes (CT30S-three nodes in the vertices and three mid-side nodes) to mesh three-sided surfaces. Each node has five degrees of freedom: three translations and two rotations as it is shown in Figure 4.2-a and the elements include quadratic displacement fields. Also some special elements were used to model concentrated masses (PT3T); these elements allow translation in three global directions in one particular node.

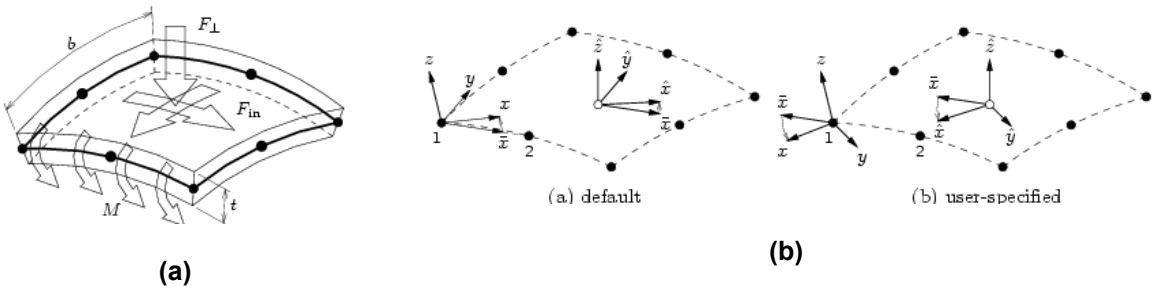

Figure 4.2. (a) Shell elements characteristics and (b) local axes convention (DIANA, 2008)

The shell elements should be thin, hereby their thickness should be much less than its in-plane dimensions (DIANA, 2008), otherwise the bending stiffness of the walls will be much less than in reality and the model will not be able to represent the stiffness of the connection between two orthogonal walls, as the out-of-plane bending stiffness of walls seems to become incorrect (Lourenço, Krakowiak, Fernandes, & Ramos, 2007). The mesh was generated using iDIANA-9.3 (DIANA, 2008) and there were obtained 3589 nodes, 1104 elements (56 CT30S and 1048 CQ40S) for a total number of 17945 degrees of freedom (DOF) were obtained.

Due to the lack of information regarding the physical and mechanical properties of masonry, typical values were adopted. For non-linear analyses, the material non linearity was taken into account and its properties are shown further in Section 6.2. In order to model the boundary conditions, it was supposed that the translation in the three global directions of the base nodes is fixed; no springs were used to model the interaction between the soil and the structure because of the limited information in local conditions of the soil.

4.3 DEFINITION OF DIFFERENT NUMERICAL MODELS AND RESULTS OF LINEAR STATIC AND MODAL RESPONSE ANALYSES

4.3.1 Model MODDEF

This model is the simplest one; its geometrical representation is simplified by using different thicknesses for each one of the façades, the buttresses, the blind arches, the top wall and the sacristy, but their thickness is constant along them. For this first approximation, only one material with its properties was definied and it is representing all the masonry of the structure. It is important to note that after a carefully review of the photos taken during the inspection and diagnosis works reported on (Lourenço & Ramos, 2008), the distribution of the material seems to be constant, and only some

regions can be identified that have suffered more damage rather. The physical and mechanical properties used to model the masonry are shown in Table 4.1.

Parameter	Unit	Value
Thickness of North façade	Meter [m]	1.02
Thickness of Apse & Sacristy	Meter [m]	1.02
Thickness of West façade	Meter [m]	1.29
Thickness of Buttresses	Meter [m]	0.95
Thickness of Top wall	Meter [m]	0.60
Thickness of Blind arches walls	Meter [m]	0.60
Unit weight of masonry	Kilo Newton / Meter³ [KN/m³]	16
Elastic Modulus	Mega Pascal [MPa]	5000
Poisson's ratio	Dimensionless [-]	0.2

Table 4.1. Physical and material properties used in models MODDEF and MODDEF (VAULTS)

After the definition of the model, the same was submitted to gravity loads and a linear static analysis was performed. The maximum principal stresses distribution is shown in Figure 4.3-a, these are tensile stresses lower than 0.12 MPa, which is an acceptable value for the tensile strength of the masonry, and they are located below the windows. Also the minimum principal stresses distribution is shown in Figure 4.3-b and the lowest value is located at the base of the structure, which is around 0.24 MPa and it is the expected value using a maximum height of 14.95m and specific weight of the masonry of 16KN/m³.

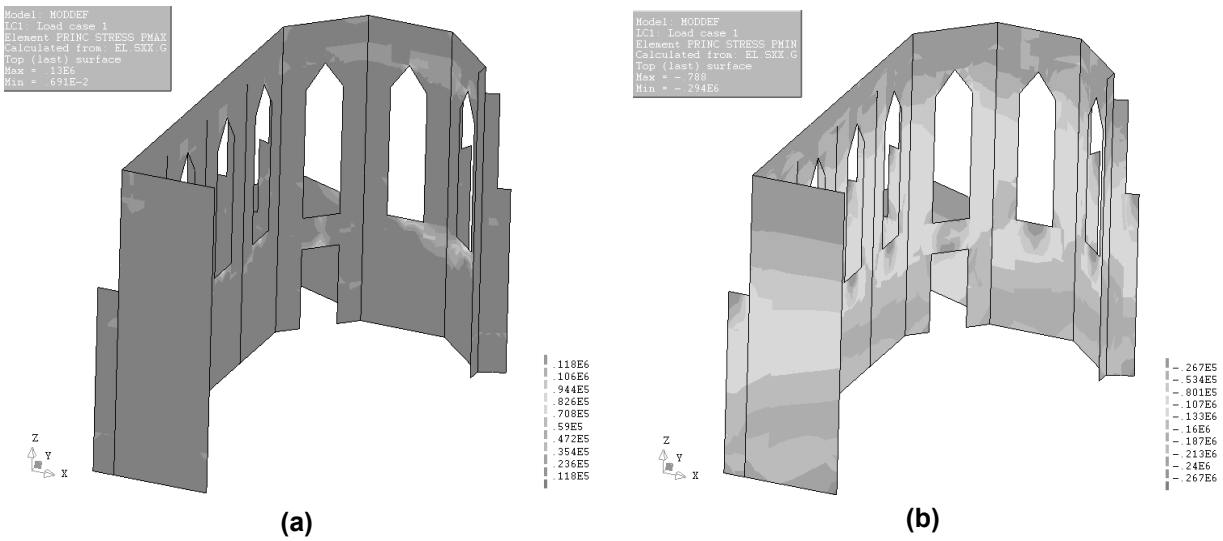

Figure 4.3. Maximum (a) and minimum (b) principal stresses of model MODDEF

After the linear static analysis, a modal response analysis was carried out. The results of the first six modes are shown in Figure 4.4. The first six natural frequencies are ranging between 3 Hz and 9 Hz and some of them are very close to each other. By a qualitative comparison between the experimental

mode shapes shown in Figure 2.15 and the results shown in Figure 4.4, it can be noted that the 1st numerical and experimental mode shapes are similar, but the 2nd numerical mode shape does not match with 2nd experimental mode shape, and from there on, the mode shapes do not match.

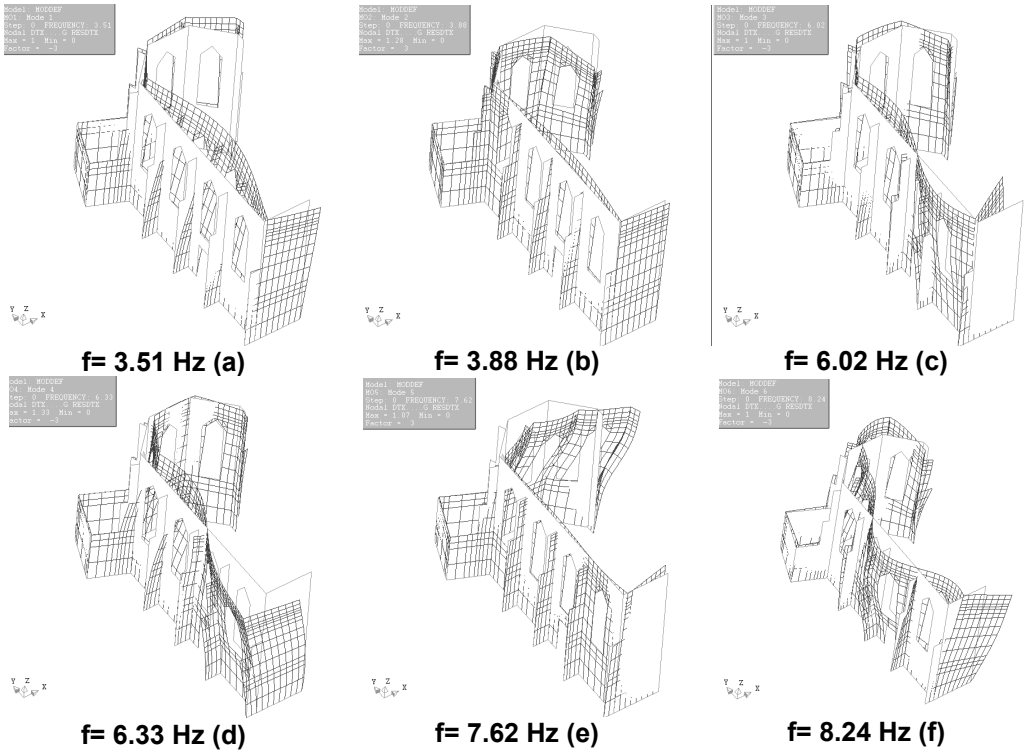

Figure 4.4. First (a), second (b), third (c), fourth (d), fifth (e) and sixth (f) mode shapes of model MODDEF

Although the qualitative differences, the numerical results were compared with the experimental results and they are reported in Table 4.2. The average error in the estimation of the frequencies is 43.4% and the error estimation for each single frequency mode is inside the range between 20% and 55%, which is high and it means that still some properties and parameters of the model should be changed to obtain more accurate results. Only the 1st mode presents a MAC value higher than 80% and the MAC of 2nd mode, 3rd mode and 4th are below 30%, but it is important to state that if the mode shapes are not qualitative similar this comparison is meaningless. Some properties should be modified in the model and different characteristics should be added in order to obtain better results.

Mode Shape	f_{EXP} [Hz]	f_{NUM} [Hz]	Error [%]	MAC [%]	Mass part. in X [%]	Mass part. in Y [%]
1st	2.57	3.51	36.6	81.4	27.95	0.31
2nd	3.14	3.88	23.6	0.3	0.02	7.72
3rd	3.95	6.02	52.4	32.5	0.64	15.42
4th	4.06	6.33	55.9	27.3	2.95	10.17
5th	5.26	7.62	44.9	54.2	12.88	4.69
6th	5.61	8.24	46.9	62.3	7.10	0.01

Table 4.2. Comparison between experimental and numerical results in model MODDEF

It is clear that from the qualitative point of view, the numerical modes do not match with the experimental modes following the same order, this is the reason why a qualitative comparison is needed in order to know which numerical modes should be compared with the experimental modes. As it is shown in Figure 4.5, the 1st experimental mode looks similar to the 1st numerical mode, the 2nd experimental mode looks similar to the 3rd numerical mode, the 3rd experimental mode looks similar to the 4th numerical mode and the 5th experimental mode looks similar to the 6th numerical mode. The 2nd and 5th numerical modes are not similar to any of the first six mode shapes shown in the experimental results (Figure 2.15). This is possible and could be explained due to the fact that in these two modes the large displacements occur in the Apse, which was not taken into account to perform the dynamic identification tests reported in (Lourenço & Ramos, 2008). According to Figure 2.13 the measurements were only carried out in three North-façade points, hereby it is possible that during the record of the dynamic behavior of the structure, the accelerometers did not catch data that involves movement in the Apse, therefore, the numerical 2nd and 5th mode shapes were disregarded in the processing of the measured data. This can be justified due to the small mass participation factors of the 2nd and 5th numerical modes, which is less than 10% in both directions for 2nd mode and less than 13% in both directions for 5th mode, further and these amounts of mass are excited in the Apse. Finally, according to (Doebling, C.R., & Prime, 1998), a large number of measurement locations can be required to accurately characterize the mode shapes and to provide sufficient resolution for the damage identification.

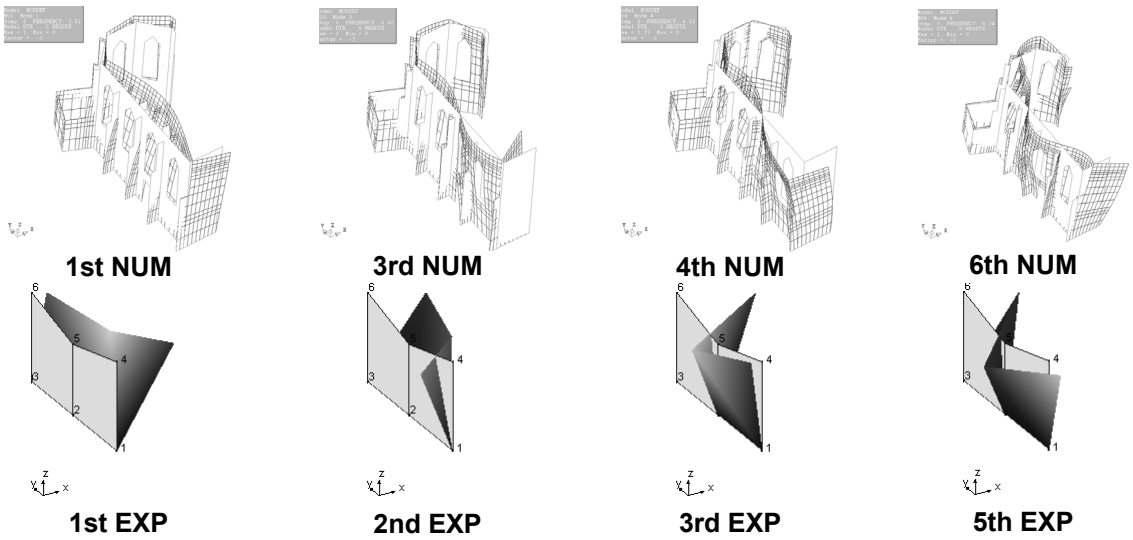

Figure 4.5. Qualitative comparison between model MODDEF and experimental mode shapes

The main idea of showing these results is to have a first approximation on what characteristics should be included in the model and what characteristics and results can be neglected in order to obtain a model as simple as possible but that represents the real structure with enough accuracy to perform further analyses.

4.3.2 Model MODDEF (VAULTS)

The same hypothesis and material properties of the previous section were taken into account for the definition of this model and they are also shown in Table 4.1. The main difference is the inclusion of the geometrical model of the vaults, but with the same material properties. The goal of this analysis is to determine whether the vaults give additional stiffness to the Apse and there is an important shift in the mode shapes, or if the vaults can be modeled as concentrated masses. The definition of the numerical model is shown in Figure 4.6, where curve shell triangular elements (CT30S) were used to model the vaults due to their geometrical complexity. The model has 3754 nodes, 1216 elements (208 CT30S and 1008 CQ40S) for a total number of degrees of freedom of 18770, which is 5% higher of the number of DOF'S from the previous model.

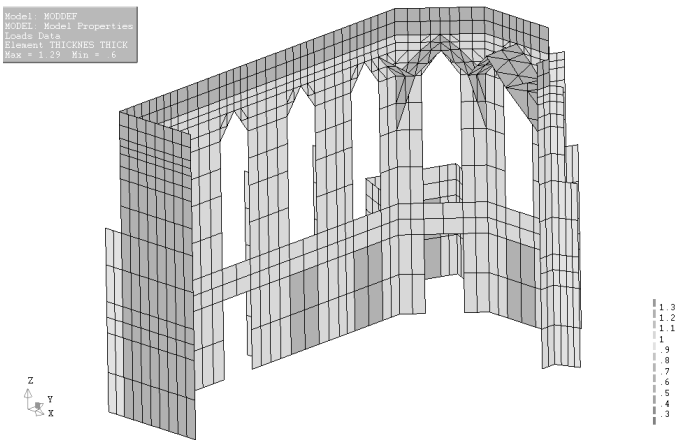

Figure 4.6. Definition of the numerical model MODDEF (VAULTS)

After the definition of the model, the same was submitted to gravity loads by performing a linear static analysis and the results of the distribution of the principal stresses are shown in Figure 4.7. In Figure 4.7-a, the distribution of maximum principal stresses is shown and it is show that the highest values are around 0.14 MPa which is less rather low. These maximum stresses are located in areas such as below the large widows. In Figure 4.7-b, the distribution of the minimum principal stresses is shown and the lowest value is located at the base of the structure, where is around 0.24 MPa. This value is the expected for the height of the structure (14.95 m) and the specific weight of the masonry (16 KN/m³).

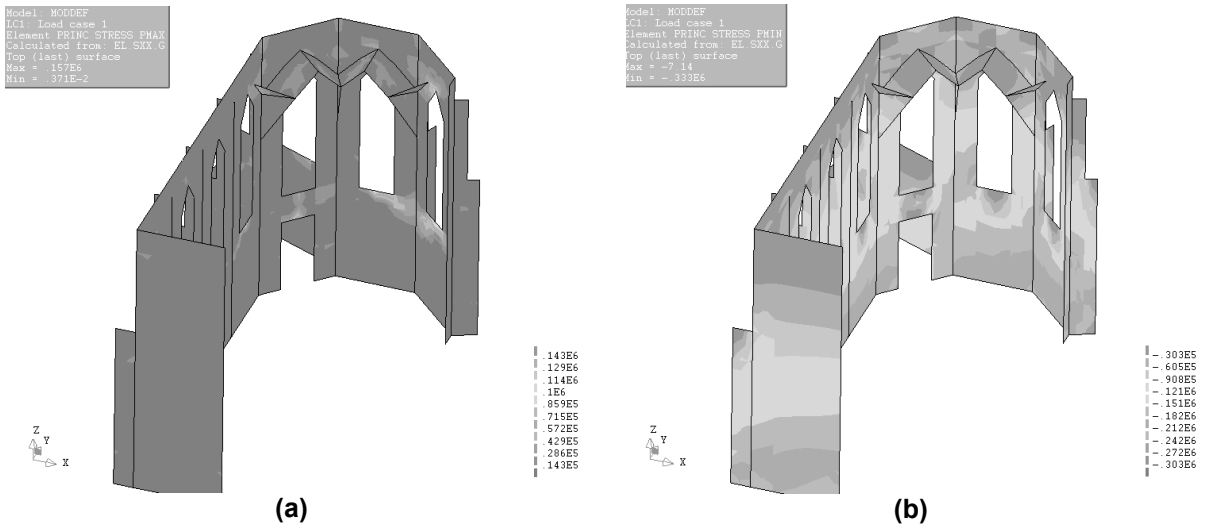

Figure 4.7. Maximum (a) and minimum (b) principal stresses of model MODDEF (VAULTS)

After the linear static analysis, a modal response analysis was performed and the shapes of the first six modes are shown in Figure 4.8. As it was shown in Figure 4.4, from a qualitatively comparison of the experimental and the numerical mode shapes, the 2nd mode shape and the 5th mode shape do

not fit with any of the first six experimental results, so it is needed to compare the experimental results with the numerical results following a different order. Because the main attempt in this model is to determine the influence of the vaults in the model, the abovementioned comparison between the experimental and numerical results will not be done here. The values of the frequencies are between 3 Hz and 9 Hz, but still they are not so close to experimental values as it is shown in Table 4.3.

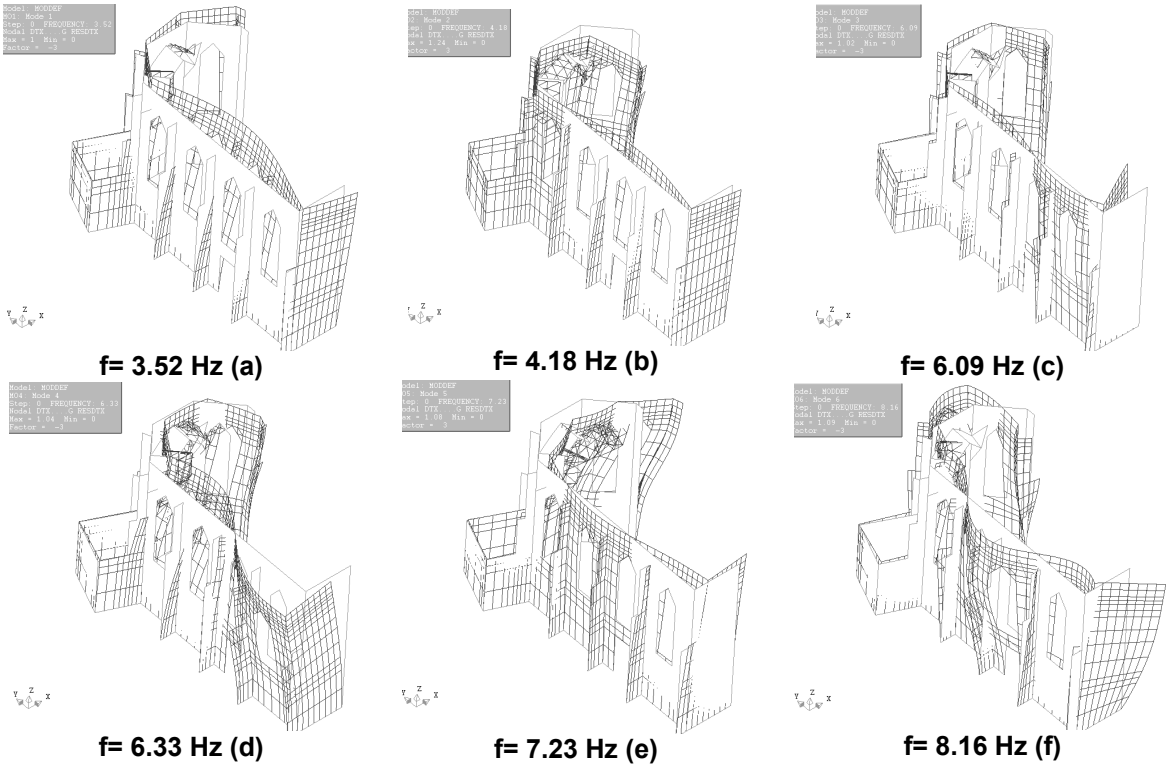

Figure 4.8. First (a), second (b), third (c), fourth (d), fifth (e) and sixth (f) mode shapes of model MODDEF (VAULTS)

The average error in the estimation of the frequencies is 43.8% which is similar to that obtained for the model MODDEF and the MAC values, calculated using as reference the values obtained from the previous model without vaults (MODDEF), are higher than 80%, except for mode shape 4^{th}. Disregarding the abovementioned value, the results are very similar to those obtained in the model MODDEF, but in this case the number of DOF is 5% higher. So it is possible to conclude that the geometrical modeling of the vaults does not affect significantly the frequencies estimation or the mode shapes prediction.

Mode Shape	f_{EXP} [Hz]	f_{NUM} [Hz]	Error [%]	MAC* [%]	Mass part. in X [%]	Mass part. in Y [%]
1st	2.57	3.52	37.0	88.4	28.45	0.90
2nd	3.14	4.18	33.1	99.4	0.26	10.40
3rd	3.95	6.09	54.2	81.6	1.89	20.17
4th	4.06	6.33	55.9	98.1	0.13	6.03
5th	5.26	7.23	37.4	45.8	20.51	2.87
6th	5.61	8.16	45.4	96.9	1.44	0.82

* The reference values for the calculation of MAC were those obtained for the model MODDEF.

Table 4.3. Comparison between experimental and numerical results in model MODDEF (VAULTS)

4.3.3 Model MODTRIAL

As it was demonstrated in Paragraph 4.3.2, the effect of the vaults in the model can be neglected in terms of stiffness, but in terms of mass it is important because it can make several contributions for the mode shapes that involve mainly the Apse. In this attempt, it was consider also important to include the mass of the tower located in the connection between the North and the West façades (Figure 4.9-a) and also the mass of the vaults located in the Apse (Figure 4.9-b).

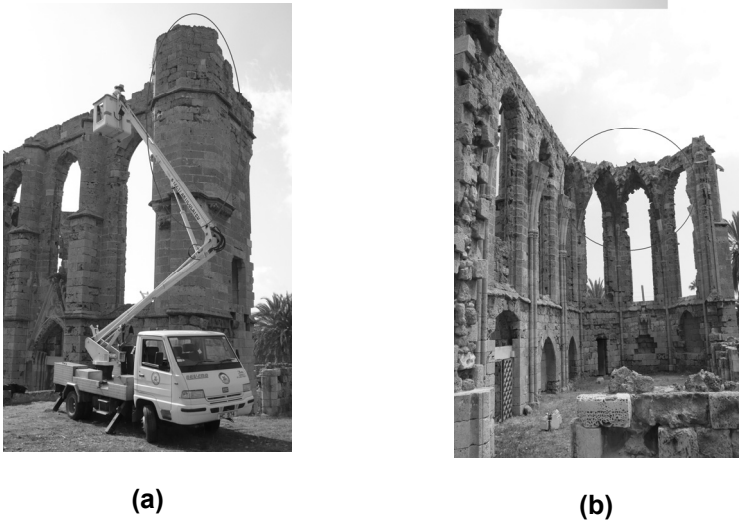

(a) **(b)**

Figure 4.9. Additional mass of the tower (a) and the vaults (b) included in the numerical model

The definition of the masses was done by quantifying the volume of each element and then multiplying it by the specific weight of the masonry. Then, the number of needed punctual masses in the model was defined by superimposing the geometry of the numerical model and the tributary area of the tower and the vaults. Afterwards, the nodes located in that region were selected and the amount of mass corresponding to each one of them was calculated by its influence area. The total amount of the additional masses used in the model is reported in Table 4.4.

Element	Unit	Value
Tower in connection of North and West façades	Kilogram [Kg]	52632
Ruins of the original vaults located in the Apse	Kilogram [Kg]	32752

Table 4.4. Additional masses used in the numerical model MODTRIAL

Another property that was changed for this model was the Elastic modulus. It was noticed from previous Modal response analysis' results from a model that is not reported here, but include the same physical and material properties as those indicated in Table 4.1 and the masses specified in Table 4.4, that the average error of the first 15 frequencies was +15%. As it is know from the Equation 4.11 that relates the natural frequency of the structure with its mass and its stiffness, the square of the natural frequency of the structure is directly proportional to the stiffness. Hereby, by reducing the stiffness by an amount, the frequency will be reduced proportionally to the square of this amount. As a consequence, the elastic modulus was reduced 1.32 times, expecting to obtain very close frequencies to those obtained in the experimental results.

$$f = \frac{1}{2\pi} \cdot \sqrt{\frac{k}{m}} \qquad 4.11$$

An additional characteristic was added in this model and it is the modeling of the actual damage state in North façade. For this propose, several regions within the North façade were identified (Figure 4.10) following the inspection and diagnosis carried out by (Lourenço & Ramos, 2008). In these regions the stiffness should be lower than in other areas that have not appreciable damage. It is possible to reduce the stiffness by reducing either the elastic modulus or the thickness of the elements located in the damaged region. Hereby, the element thickness was reduced to 0.30m in order to make a higher reduction, because as the thickness of the element is reduced, the stiffness of that element is reduced to the cubic power.

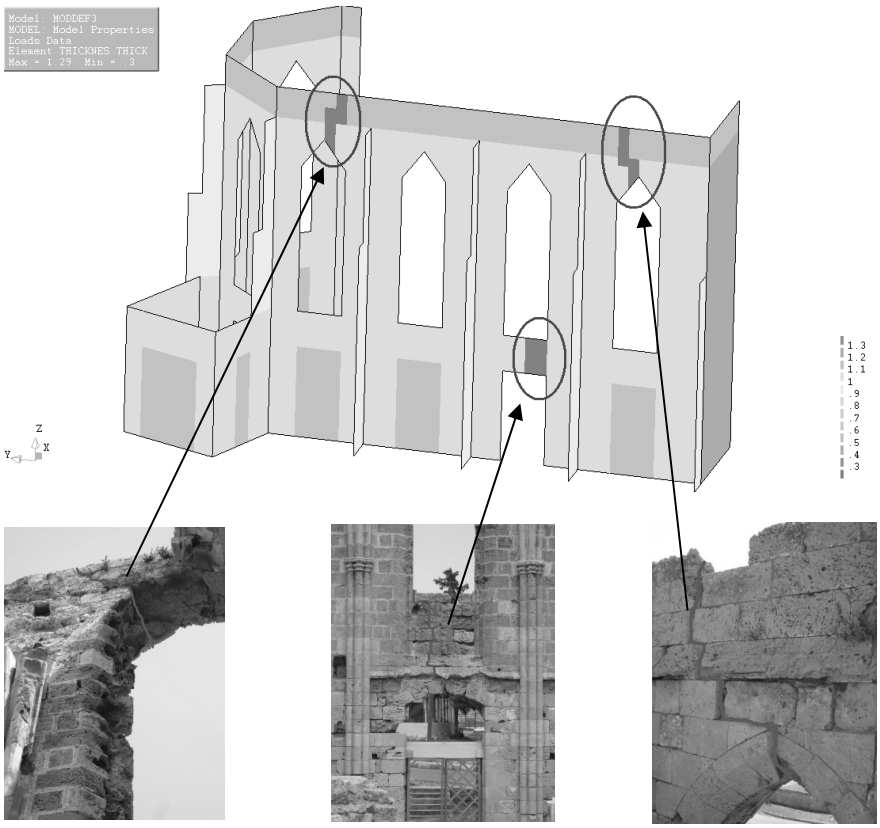

Figure 4.10. Selected regions in North façade with appreciable damage

As a second attempt to model the damaged regions in the structure, some areas located in the Apse were selected. They were identified according to the inspection and diagnosis carried out by (Lourenço & Ramos, 2008), and apparently only one region has explicit damage and it is shown in Figure 4.11. The same principle abovementioned was applied to model the reduction of stiffness in the damaged region and the assumed thickness of the elements located in the damaged region of the Apse was 0.30m.

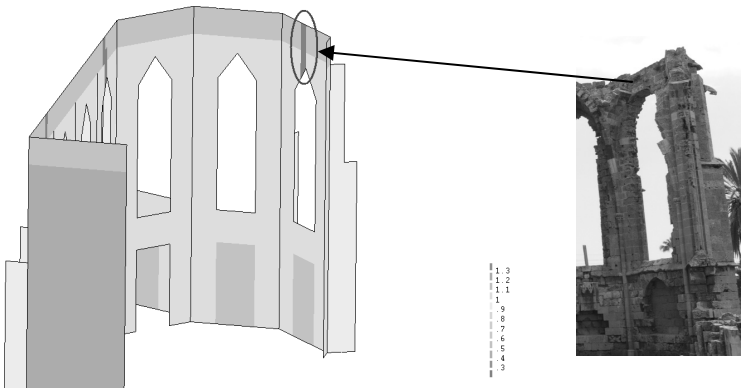

Figure 4.11. Selected region in the Apse with appreciable damage

The final attempt to model damage in this model was the modeling of damage located in West façade, which is shown in Figure 4.12. In order to take into account this damage, the thickness of the elements that are located inside this region was reduced, so that their stiffness is also reduced. According to the figure, there are stones severely damaged and others are simply loose. The assumed thickness for modeling this damage was 0.60m, because it seems that the deterioration is only in the external layer of the masonry.

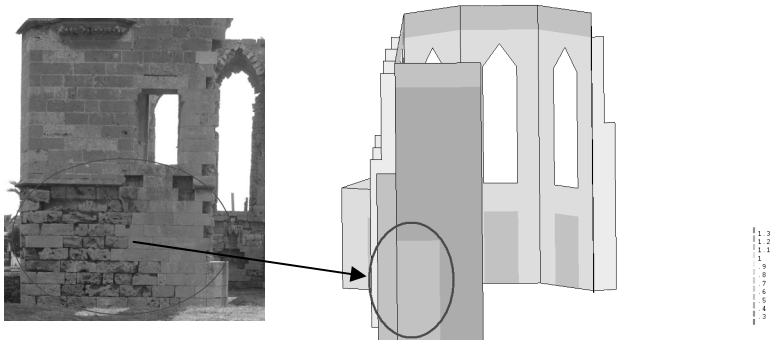

Figure 4.12. Damaged region in west façade due to loss of elements and severe stone deterioration

A summary of the physical and material properties is shown in Table 4.5, which includes the values of the additional masses, the change in elastic modulus and the decrease of the thicknesses in some regions of the Apse, North and West façades in order to represent the existing damages.

Parameter	Unit	Value
Thickness of North façade	Meter [m]	1.02
Thickness of damage (N-façade)	Meter [m]	0.30
Thickness of Apse & Sacristy	Meter [m]	1.02
Thickness of damage (Apse)	Meter [m]	0.30
Thickness of West façade	Meter [m]	1.29
Thickness of damage (W-façade)	Meter [m]	0.60
Thickness of Buttresses	Meter [m]	0.95
Thickness of Top wall	Meter [m]	0.60
Thickness of Blind arches walls	Meter [m]	0.60
Unit weight of masonry	Kilo Newton / Meter³ [KN/m³]	16
Elastic Modulus	Mega Pascal [MPa]	3780
Poisson's ratio	Dimensionless [-]	0.2
Additional mass of the tower	Kilogram [Kg]	52632
Additional mass of the vault	Kilogram [Kg]	32752

Table 4.5. Physical and material properties used in model MODTRIAL

A linear static analysis was carried out to assess the level of stresses due to the gravity load, leading to, the distribution of the maximum and minimum principal stresses shown in Figure 4.13. In Figure 4.13-a, the distribution of the maximum principal stresses (tensile) is shown, where the maximum value is 0.25 MPa, which is higher than the values obtained in previous analyses, but still it can be acceptable because it is located in the areas where the damage was reshown by decreasing the thickness. Regarding the distribution of the minimum principal stresses (compressive), which is shown in Figure 4.13-b, the value at the base of the structure is 0.24 MPa which is the expected value according to the specific weight of the masonry and the height of the structure. The other values of the minimum principal stresses concentrated in the upper and lower parts of the West façade, which are around 0.40 MPa, are due to the concentrated masses in the top of the connection between the North and the West facades.

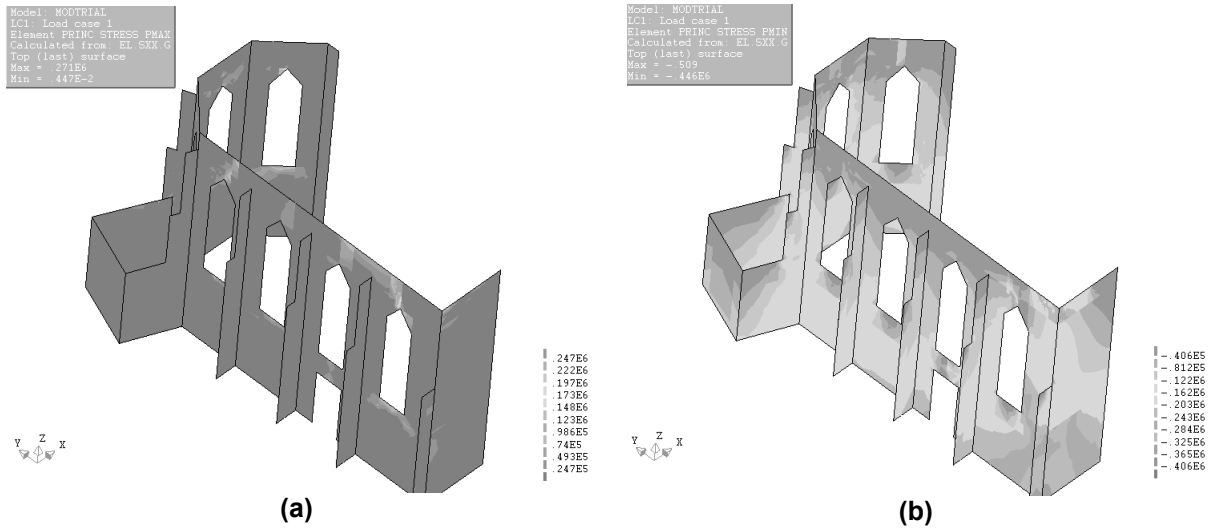

Figure 4.13. Maximum (a) and minimum (b) principal stresses of model MODTRIAL

As mentioned in Paragraph 4.3.1, before making the comparison in terms of frequencies and mode shapes between the experimental and numerical data, a qualitative selection should be done choosing the numerical mode shapes that better approach the experimental measurements. The numerical mode shapes for the model MODTRIAL are shown in Figure 4.14, and by qualitative comparison with the experimental mode shapes shown in Figure 2.15., the 2nd and the 5th numerical mode shapes again do not fit with any of the first six experimental mode shapes. Hereby, these two numerical modes were disregarded and the comparison was done between the modes shown in Figure 4.15.

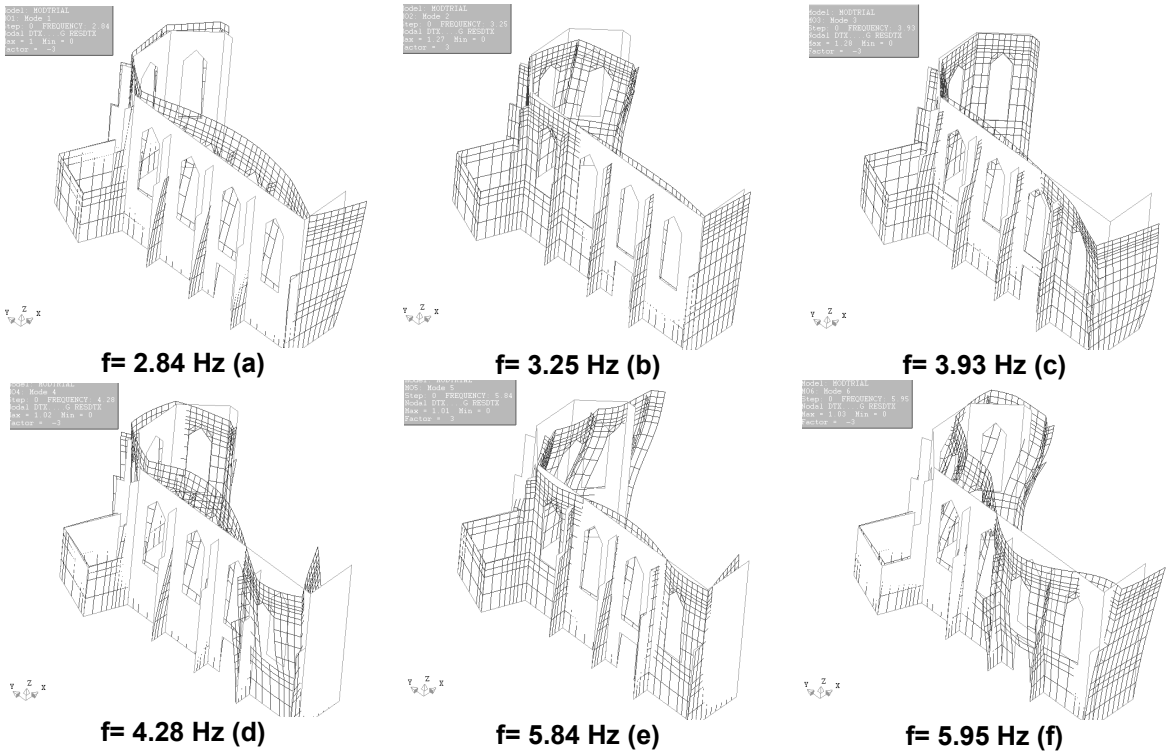

Figure 4.14. First (a), second (b), third (c), fourth (d), fifth (e) and sixth (f) mode shapes of numerical model MODTRIAL

After the qualitative comparison between the numerical modes and the experimental modes, the selected modes to make the comparison in terms of frequencies and MAC values are shown in Figure 4.15. The 1st numerical mode was compared with the 1st experimental mode, the 3rd numerical mode was compared with the 2nd experimental mode, the 4th numerical mode was compared with 3rd experimental mode and the 6th numerical mode was compared with the 5th experimental mode. The comparison was made and the errors in the estimation of the frequencies were computed, as well as the MAC values to quantify the correlation between two mode shapes and the results are shown in Table 4.6.

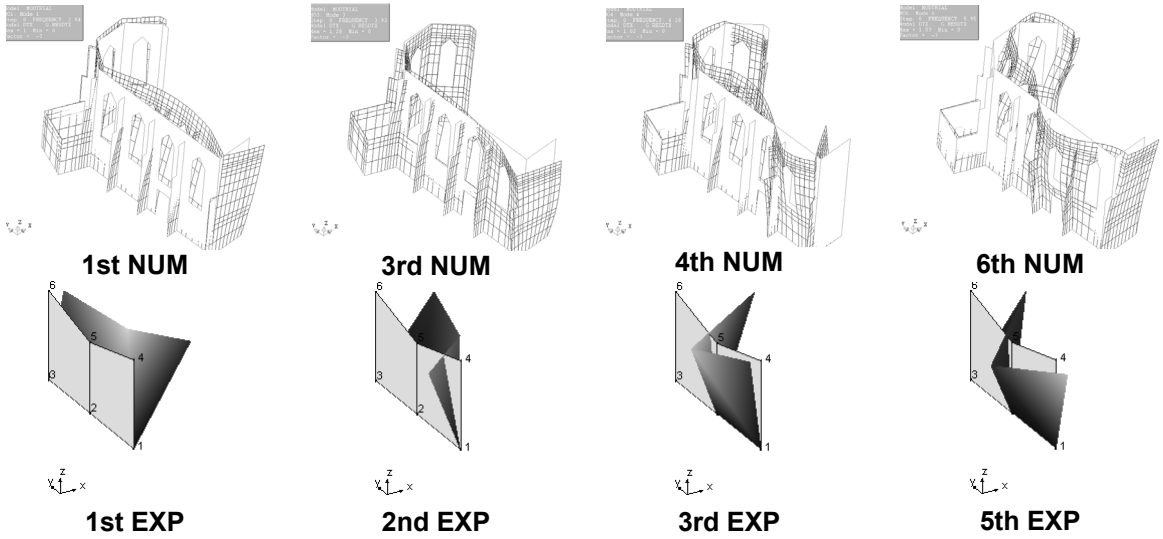

Figure 4.15. Qualitative comparison between model MODTRIAL and experimental mode shapes

The frequency values are now inside the range of the experimental frequencies, which is between 2 Hz and 6 Hz, and the average error is 14.3%, which is much lower than the error obtained for previous models. Also two of the MAC values are higher than 80% which is an acceptable value and show a good correlation between the experimental and numerical mode shapes. In general, the values obtained here with a previous qualitative comparison between the experimental and the numerical mode shapes gives better results than a direct comparison of the modes following the same order.

Mode Shape	f_{EXP} [Hz]	f_{NUM} [Hz]	Error [%]	MAC [%]	Mass part. in X [%]	Mass part. in Y [%]
1^{st}_{NUM}-1^{st}_{EXP}	2.57	2.84	10.5	91.6	29.61	0.04
3^{rd}_{NUM}-2^{nd}_{EXP}	3.14	3.93	25.2	36.3	6.94	13.07
4^{th}_{NUM}-3^{rd}_{EXP}	3.95	4.28	8.3	33.6	0.39	6.65
6^{th}_{NUM}-5^{th}_{EXP}	5.26	5.95	13.1	82.9	11.36	5.94

Table 4.6. Comparison between experimental and numerical results in model MODTRIAL

4.3.4 Model MODDEF (NO APSE)

After having performed the previous analysis (MODTRIAL) and having obtained better results than those obtained from previous analyses, a model without the Apse was performed. The aim of this model is to see the influence of the Apse in the 2^{nd} and 5^{th} numerical modes shown in model MODDEF. For this model, the same properties as those reported in Table 4.5 were used for its definition, except for the modeling of the damage in the Apse which was disregarded because the Apse was completely removed from the model. As it was abovementioned, the main goal is to see the qualitative results from the modal response analysis and understand which the influence of the Apse is in the modal behavior of the structure. The boundary conditions used in this model to simulate the connection between the Apse and the part of the structure that was modeled were to fix the

translations in X and Y global directions. It is important to remark that these boundary conditions do not represent the real connection which should have a real stiffness value and it should be modeled with a pair of springs per node, one in each global direction, but these boundary conditions are suitable for qualitative results as it is shown below.

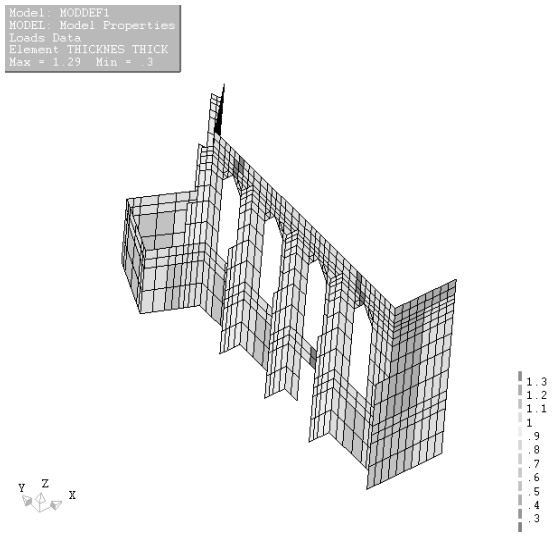

Figure 4.16. Definition of the numerical model MODDEF (NO APSE)

By making a qualitative comparison between the experimental mode shapes (Figure 2.15) and the results of the Modal response analysis (Figure 4.17), the numerical mode shapes are very similar to the shapes obtained from the experimental measurement and they are following the same order. The only difference between this model and the previous model (MODTRIAL) is the removal of the Apse, so it is possible to support the hypothesis done in Paragraph 4.3.1, which explains a possible reason of the presence of the 2nd and 5th modes in models MODDEF, MODDEF (VAULTS) and MODTRIAL. Hereby it is possible to support the hypothesis which stated that the mass of the Apse is excited in the 2nd and the 5th modes shown in the previous numerical models because when the Apse is removed, these modes are not present in the numerical model and they follow the same order as the experimental results. Finally, it is important to underline that no quantitative results are shown for this model, because the main goal is to model the whole structure and calibrate the model in order to analyze future possible scenarios, and if a model without a part of the structure is built, it will not help to understand how the Apse is behaving during possible future scenarios as earthquakes, as well as the possible damages shown and the influence of this part of the structure in its behavior.

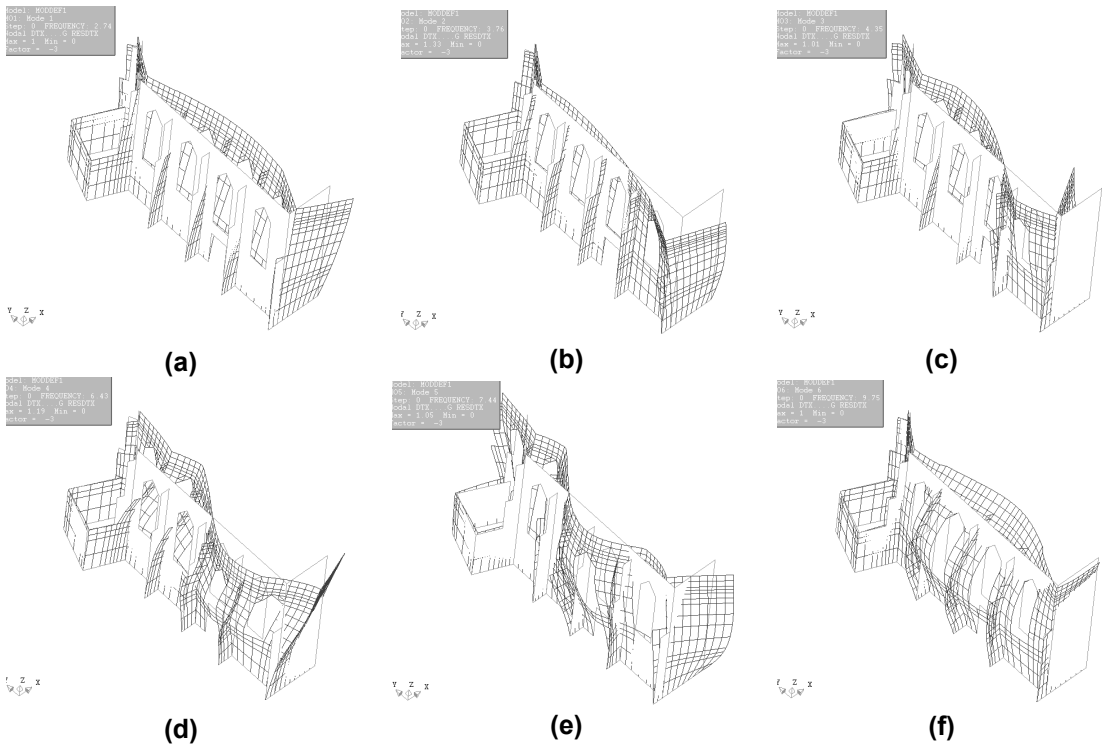

Figure 4.17. First (a), second (b), third (c), fourth (d), fifth (e) and sixth (f) mode shapes of model MODDEF (NO APSE)

4.3.5 Model MODTRIAL1

In this model the main attempt was to change the thickness of the top walls. Up to this model, the used thickness of the top walls is the one that it is stated in the geometrical information that was collected from the 1940s conservation works. But after a carefully review of the photos from the inspection and diagnosis works reported in (Lourenço & Ramos, 2008) it seems that the thickness of the top walls is the same as the bottom walls thickness. In Figure 4.18-a and Figure 4.18-b it can be seen that the thickness of the North façade's walls is constant in both, the interior side and the exterior sides. In the West façade the thickness is also the same through the entire wall from the base to the top as it is shown in Figure 4.18-c.

(a) (b) (c)

Figure 4.18. Interior (a) and exterior (b) views of the walls in the North façade, and cross section view (c) of the walls in the west façade

In order to model this new geometry feature, the thickness of the top part of the walls in the Apse and North façade was changed from 0.60m to 1.02m, and the thickness in the West façade was changed from 0.60m to 1.29m in order to model the constant thickness all over the wall; the physical and material properties used to define this model are shown in Table 4.7.

Parameter	Unit	Value
Thickness of North façade	Meter [m]	1.02
Thickness of damage (N-façade)	Meter [m]	0.30
Thickness of Apse & Sacristy	Meter [m]	1.02
Thickness of damage (Apse)	Meter [m]	0.30
Thickness of West façade	Meter [m]	1.29
Thickness of damage (W-façade)	Meter [m]	0.60
Thickness of Buttresses	Meter [m]	0.95
Thickness of Top wall (North and Apse)	Meter [m]	1.02
Thickness of Top wall (West)	Meter [m]	1.29
Thickness of Blind arches walls	Meter [m]	0.60
Unit weight of masonry	Kilo Newton / Meter³ [KN/m³]	16
Elastic Modulus	Mega Pascal [MPa]	3780
Poisson's ratio	Dimensionless [-]	0.2
Additional mass of the tower	Kilogram [Kg]	52632
Additional mass of the vault	Kilogram [Kg]	32752

Table 4.7. Material and physical properties used for model MODTRIAL1

The definition of the numerical model with the different thicknesses is shown in Figure 4.19. Now after the abovementioned changes, it is noticed that the color of the walls is the same from the base to the top (t= 1.02m) for the North façade and the Apse and it is darker (t= 1.29m) for the West façade.

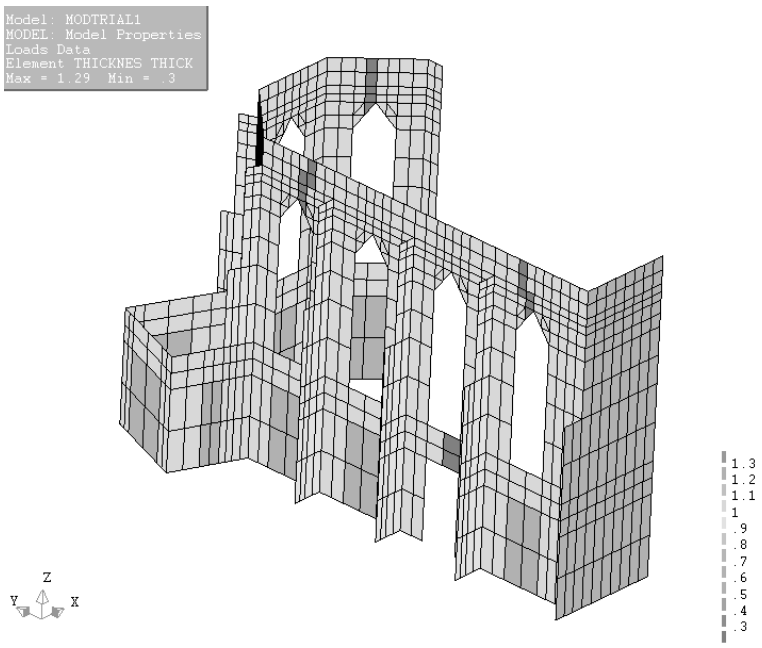

Figure 4.19. Definition of Numerical Model MODTRIAL1

A linear static analysis was performed to the model and the results show the distribution of the principal stresses shown in Figure 4.20. The distribution of the maximum principal stresses (Tensile stresses) along the structure is shown in Figure 4.20-a showing a maximum value of 0.24 MPa which is located in the areas that the damage was modeled by reducing the stiffness of the elements and also it is located below the windows. The minimum principal stresses distribution is shown in Figure 4.20-b and the value at the base is of about 0.25 MPa (Compressive stress) which is the expected value for the height and the specific weight of the masonry, the other areas that have values of about 0.42 MPa, are due to the mass concentration representing tower and vaults.

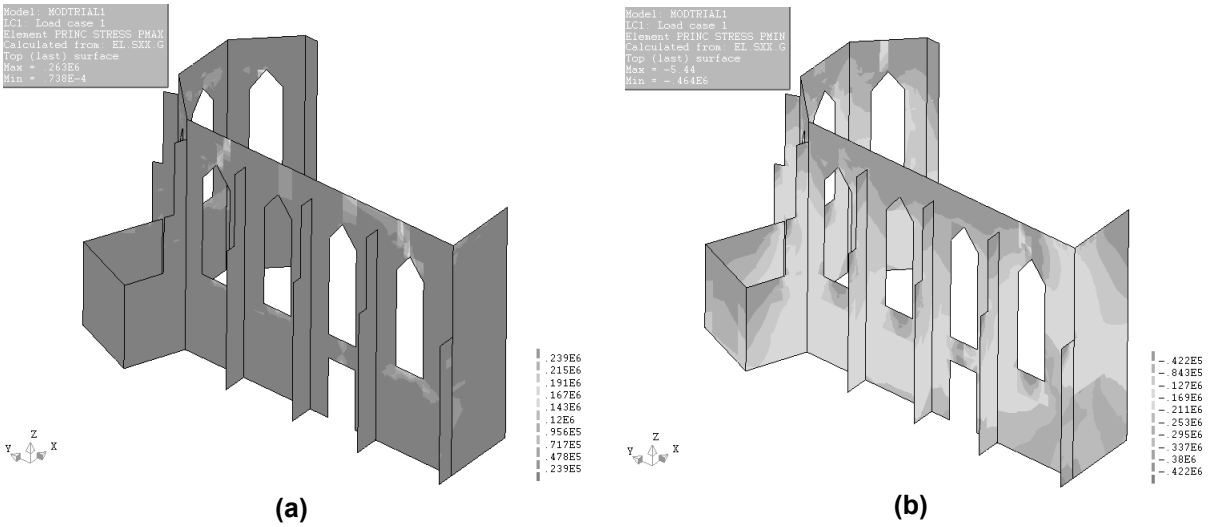

Figure 4.20. Maximum (a) and minimum (b) principal stresses of model MODTRIAL1

After performing the linear static analysis, a modal response analysis was performed to the structure and the resultant frequencies and mode shapes are shown in Figure 4.21. The frequency values are in the same range of the values measure in the dynamic test (2 Hz to 6 Hz), but by making a qualitative comparison between the obtained mode shapes and the experimental modes, it looks like the 2nd and the 5th numerical modes again do not fit with the experimental results. In order to obtain more reliable results in the comparison between the experimental data and the numerical data, the numerical mode shapes were selected according to a qualitatively comparison with the experimental modes and the results are reported in Figure 4.22.

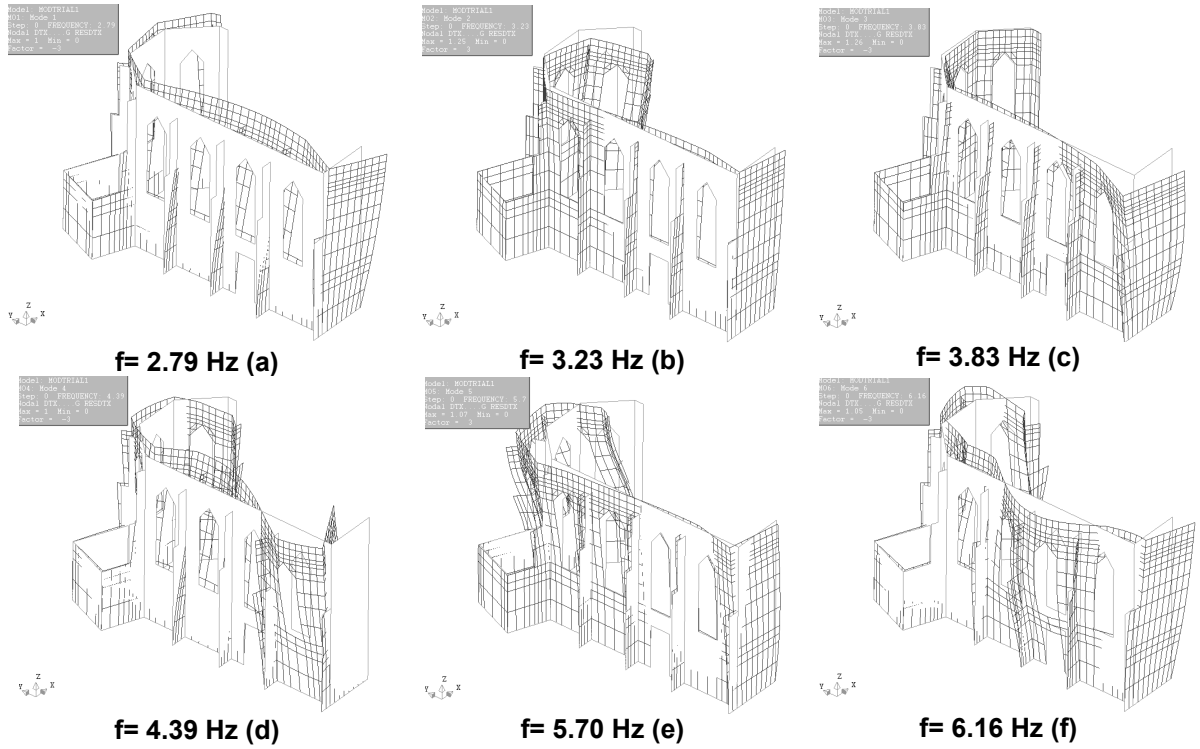

Figure 4.21. First (a), second (b), third (c), fourth (d), fifth (e) and sixth (f) mode shapes of numerical model MODTRIAL1

After a qualitative comparison, the selected numerical modes are the 1st, 3rd, 4th and the 6th mode, which were compared with 1st, 2nd, 3rd and 5th experimental modes respectively. It is shown in the Figure 4.22, that now the experimental and the numerical mode shapes, following an ascendant order, match to each other and the comparisons in terms of frequencies and MAC values are more accurate than in the previous analyses, as it is shown in Table 4.8.

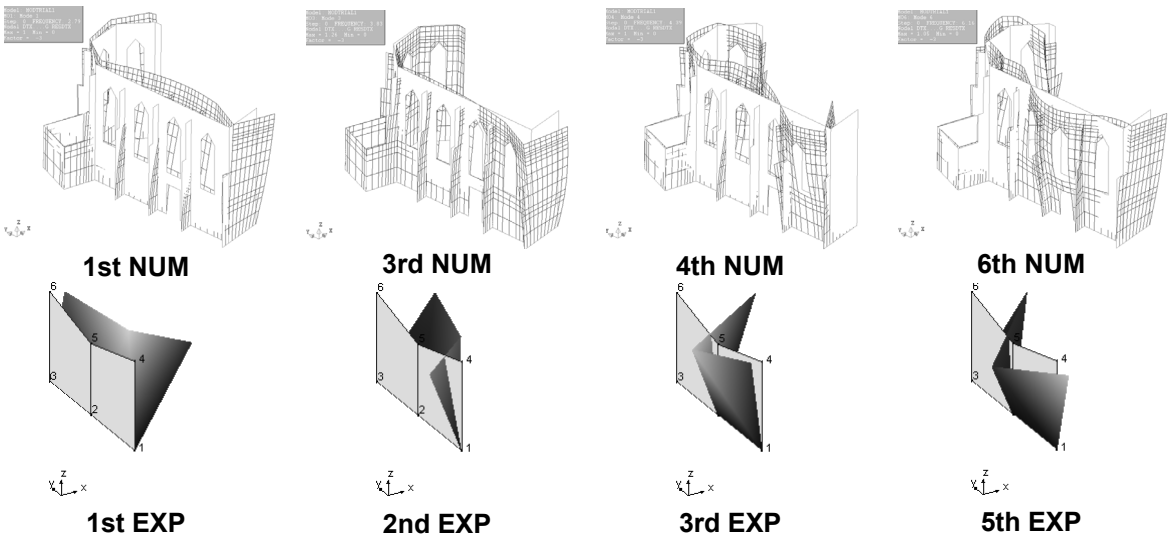

Figure 4.22. Qualitative comparison between model MODTRIAL1 and experimental mode shapes

The comparisons between the measured frequencies and those obtained from the numerical model, and between the experimental and the predicted mode shapes are shown in Table 4.8. In average the error between the experimental frequencies and the frequencies calculated in the model is of 14.7% which is very similar to the error obtained in the previous model (MODTRIAL) but the relation between the experimental and numerical mode shapes in terms of MAC values is better for all modes, because they increase 1% for 1st numerical mode, 2% for 3rd numerical mode, 6% for 4th numerical mode and it decreases 6% for the 6th numerical mode, but still is close to 80%, so it can be acceptable value. But despite the increasing of MAC values, still the model needs improvement

Mode Shape	f_{EXP} [Hz]	f_{NUM} [Hz]	Error [%]	MAC [%]	Mass part. in X [%]	Mass part. in Y [%]
1^{st}_{NUM}-1^{st}_{EXP}	2.57	2.79	8.6	92.2	30.91	0.001
3^{rd}_{NUM}-2^{nd}_{EXP}	3.14	3.83	22.0	38.1	6.99	14.50
4^{th}_{NUM}-3^{rd}_{EXP}	3.95	4.39	11.1	39.0	0.69	4.87
6^{th}_{NUM}-5^{th}_{EXP}	5.26	6.16	17.1	76.2	16.14	0.71

Table 4.8. Comparison between experimental and numerical results in model MODTRIAL1

4.3.6 Model MODTRIAL2

The main attempt of this model was to reproduce a part of an apparent blind arch (Figure 4.23-b) that is located in the West façade. For this purpose, the thickness of the elements located below the top wall was decreased from 1.29m to 1.02m, and this is shown in Figure 4.23-a where the lighter elements in the West façade have 1.02m of thickness and the dark elements have 1.29m of thickness.

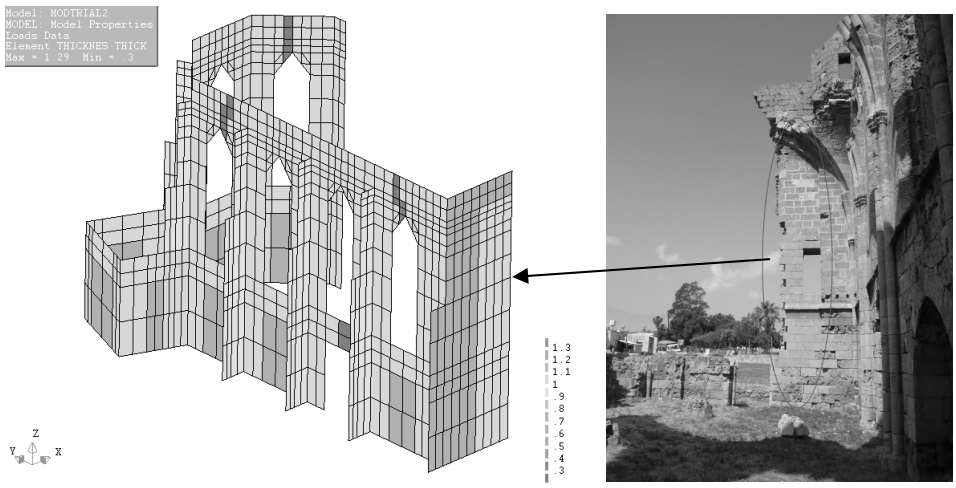

(a) **(b)**

Figure 4.23. Definition of Numerical Model MODTRIAL2 (a) and blind arch located in West façade (b)

The whole set of physical and material properties is the same as that used for the previous model (MODTRIAL1) and it is shown in Table 4.9. The main change in this model is the thickness of half part the West façade that is named as Thickness of blind arch wall (West), which was changed from 1.29m to 1.02m, as it was abovementioned.

Parameter	Unit	Value
Thickness of North façade	Meter [m]	1.02
Thickness of damage (N-façade)	Meter [m]	0.30
Thickness of Apse & Sacristy	Meter [m]	1.02
Thickness of damage (Apse)	Meter [m]	0.30
Thickness of West façade	Meter [m]	1.29
Thickness of damage (W-façade)	Meter [m]	0.60
Thickness of Buttresses	Meter [m]	0.95
Thickness of Top wall (North and Apse)	Meter [m]	1.02
Thickness of Top wall (West)	Meter [m]	1.29
Thickness of Blind arches walls	Meter [m]	0.60
Thickness of Blind arch wall (West)	Meter [m]	1.02
Unit weight of masonry	Kilo Newton / Meter³ [KN/m³]	16
Elastic Modulus	Mega Pascal [MPa]	3780
Poisson's ratio	Dimensionless [-]	0.2
Additional mass of the tower	Kilogram [Kg]	52632
Additional mass of the vault	Kilogram [Kg]	32752

Table 4.9. Material and physical properties used for model MODTRIAL2

After defining the model properties, a linear static analysis was performed and the results of the distribution of the principal stresses are shown in Figure 4.24. In Figure 4.24-a, the distribution of the maximum principal stresses (Tensile) is shown, where the highest value is located below the windows and in the areas where the damage was reshown by reducing the stiffness of the elements and its value is of 0.22 MPa, which is inside the range of acceptable values for tensile strength of the masonry. Regarding the minimum principal stresses distribution (Compression), it is shown in Figure 4.24-b and the value at the base of the structure is 0.26 MPa, which is the expected value for the geometrical and physical distribution of the model. The maximum value for pure compressive stresses is around 0.40 MPa and it is due to the presence of additional concentrated masses that represent the vaults and the tower.

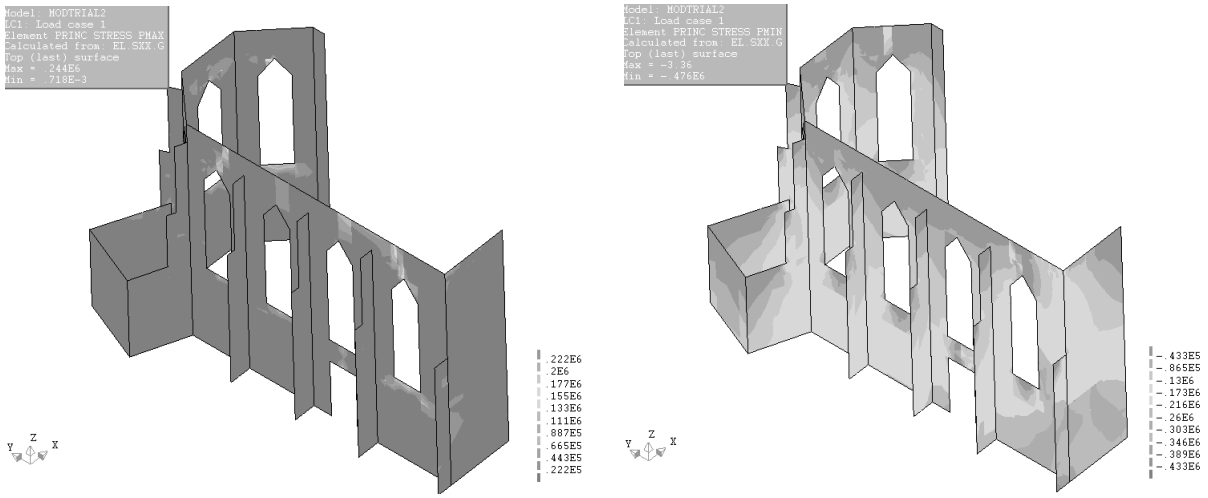

(a) **(b)**

Figure 4.24. Maximum (a) and minimum (b) principal stresses of model MODTRIAL2

After the linear static analysis, a modal response analysis was performed to the structure. The results in terms of frequencies and mode shapes are reported in Figure 4.25. Again, it is noted that the obtained numerical modes do not fit with the experimental modes following the same order, so it was necessary to make a previous qualitative comparison between the mode shapes that help to decide which numerical modes should be compared with the experimental modes and the selected numerical modes are shown in Figure 4.26.

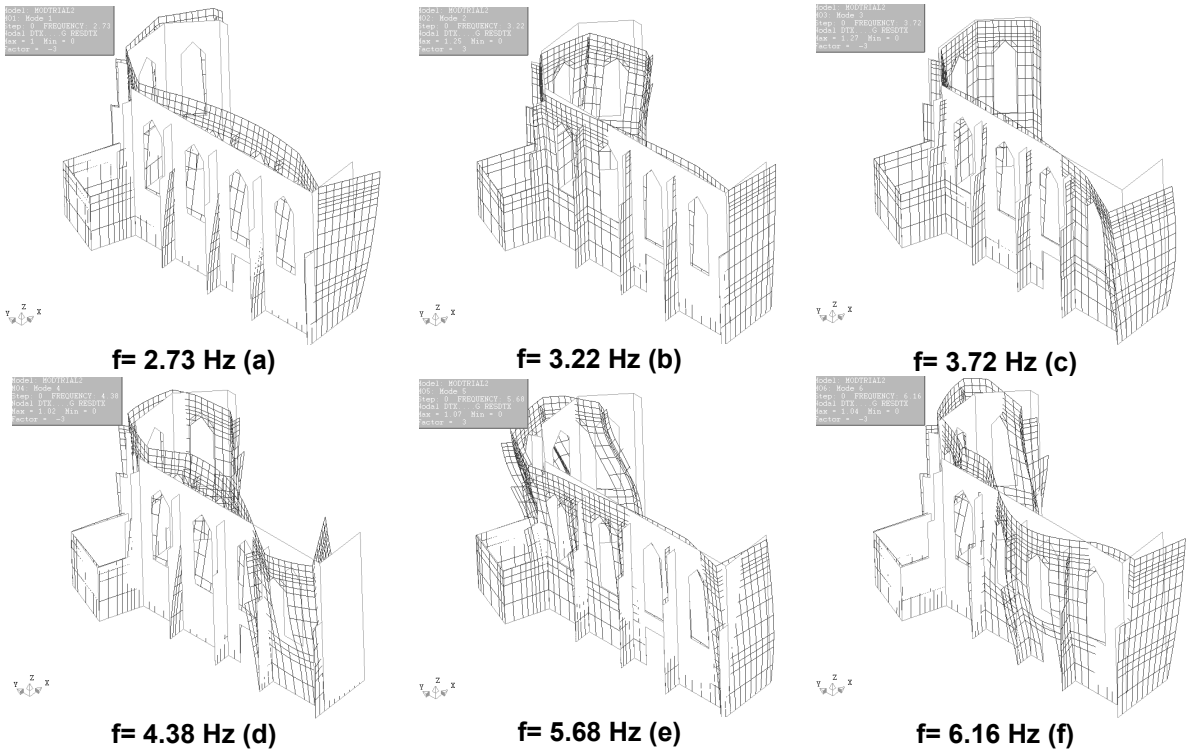

Figure 4.25. First (a), second (b), third (c), fourth (d), fifth (e) and sixth (f) mode shapes of numerical model MODTRIAL2

The selected numerical modes to make the comparison in terms of frequencies and mode shapes are the 1st mode, the 3rd mode, the 4th mode and the 6th mode. They were compared with the 1st, 2nd, 3rd and 5th experimental modes; the experimental and the numerical shapes are shown in Figure 4.26.

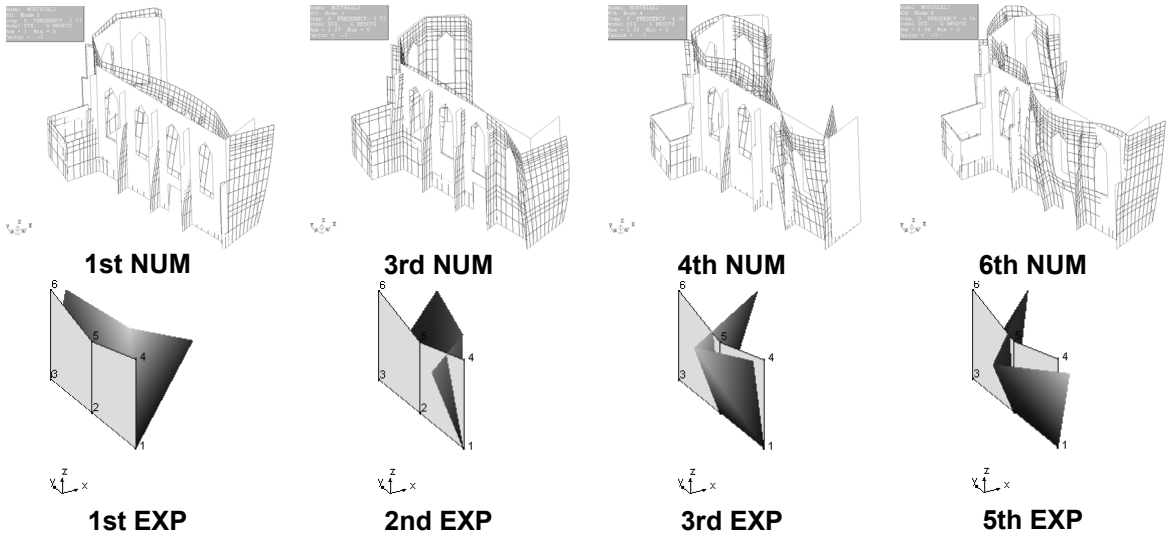

Figure 4.26. Qualitative comparison between model MODTRIAL2 and experimental mode shapes

In this case, the average error for the frequencies is of 13.2%, which is lower than from the value obtained for the previous model (14.7%). Also there is an improving in the comparison between the mode shapes because the MAC values are improving for all the modes; 2% for the 1st mode, 6% for the 3rd mode, for the 4th mode remain equal and the MAC of the 6th mode was improved by almost 3%. These results are shown in Table 4.10, where also the mass participation factors are reported, showing that the 1st mode has the highest mass participation in X global direction and the 3rd mode has the highest mass participation in Y global direction, but still they are very low and there is an important contribution of the higher modes to the dynamic response of the structure.

Mode Shape	f_{EXP} [Hz]	f_{NUM} [Hz]	Error [%]	MAC [%]	Mass part. in X [%]	Mass part. in Y [%]
1^{st}_{NUM}-1^{st}_{EXP}	2.57	2.73	6.2	94.1	31.06	0.01
3^{rd}_{NUM}-2^{nd}_{EXP}	3.14	3.72	18.5	44.2	6.37	12.54
4^{th}_{NUM}-3^{rd}_{EXP}	3.95	4.38	10.9	39.1	1.25	4.96
6^{th}_{NUM}-5^{th}_{EXP}	5.26	6.16	17.1	78.8	0.32	1.01

Table 4.10. Comparison between experimental and numerical results in model MODTRIAL2

4.3.7 Model MODTRIAL3

Similar hypotheses were used for this model as those used for modeling MODTRIAL2 regarding geometrical properties, properties for representing the damages and additional masses. In this trial, the main attempt was to define different material properties, which were changed according to a carefully review of the photos taken during the inspection visit reported on (Lourenço & Ramos, 2008). For this purpose three different zones were defined, each one of them has different material properties. The proposal is supported by the fact that it seems that the damage condition of each one of the three zones is varying among the height of the structure as it is shown in Figure 4.27. It seems that the upper zone, is severely damaged, meaning that it can be modeled as the material with the lowest stiffness. The middle zone and buttresses damage condition seems to be moderate, so it is possible to define the stiffness of this material with middle range values. And finally, it seems that the lower zone of wall, has moderate damage condition, because several stones have been replaced during previous restoration works, meaning that it is possible to assign a stiffer material to this region.

Figure 4.27. Three different zones in the walls of the church with a possible difference in the stiffness

As it was abovementioned, the material properties were changed according to the location of regions among the height of the church. For this purpose the elastic modulus of the material was shift into 3 different values with different stiffness according to previous evaluation of the actual walls conditions. For the upper zone, a value of 1780 MPa was assigned, for the middle zone and the buttresses a value of 2780 MPa was adopted and for the lower zone the value of the elastic modulus remained constant (3780 MPa) as that one used for previous model (MODTRIAL2); the whole set of physical and material properties is reported in Table 4.11.

Parameter	Unit	Value
Thickness of North façade	Meter [m]	1.02
Thickness of damage (N-façade)	Meter [m]	0.30
Thickness of Apse & Sacristy	Meter [m]	1.02
Thickness of damage (Apse)	Meter [m]	0.30
Thickness of West façade	Meter [m]	1.29
Thickness of damage (W-façade)	Meter [m]	0.60
Thickness of Buttresses	Meter [m]	0.95
Thickness of Top wall (North and Apse)	Meter [m]	1.02
Thickness of Top wall (West)	Meter [m]	1.29
Thickness of Blind arches walls	Meter [m]	0.60
Thickness of Blind arch wall (West)	Meter [m]	1.02
Lower zone		
Unit weight of masonry	Kilo Newton / Meter³ [KN/m³]	16
Elastic Modulus	Mega Pascal [MPa]	3780
Poisson's ratio	Dimensionless [-]	0.2
Middle zone and buttresses		
Unit weight of masonry	Kilo Newton / Meter³ [KN/m³]	16
Elastic Modulus	Mega Pascal [MPa]	2780
Poisson's ratio	Dimensionless [-]	0.2

Upper zone		
Unit weight of masonry	Kilo Newton / Meter³ [KN/m³]	16
Elastic Modulus	Mega Pascal [MPa]	1780
Poisson's ratio	Dimensionless [-]	0.2
Additional mass of the tower	Kilogram [Kg]	52632
Additional mass of the vault	Kilogram [Kg]	32752

Table 4.11. Material and physical properties used for model MODTRIAL3

The distribution of the principal stresses among the structure was obtained after performing a linear static analysis in the structure and it is shown in Figure 4.28-a (Maximum) and Figure 4.28-b (Minimum). For the maximum principal stresses (tensile) the maximum value is shown below the windows and in the areas where the damage was modeled, its value is 0.19 MPa, which is acceptable inside the range values of the tensile strength of the masonry. Also the minimum principal stresses (compressive) distribution shows that the highest value is of 0.40 MPa and it is shown in the lower part of the West façade, which is the area of influence off the mass of the tower. The value at the base is of 0.24 MPa, which is the expected value for the specific weight of the masonry used in the model and the height of the structure.

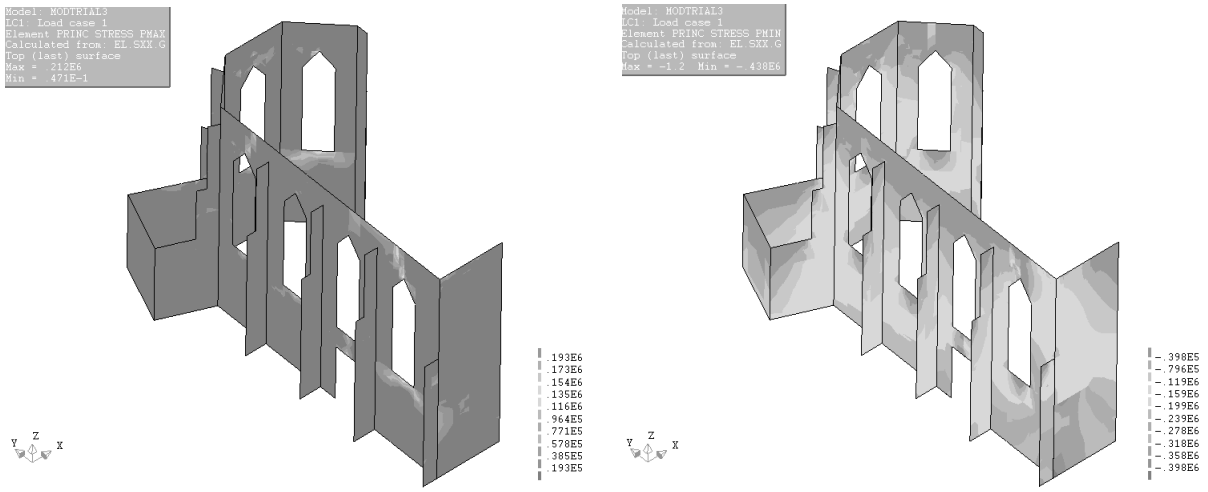

Figure 4.28. Maximum (a) and minimum (b) principal stresses of model MODTRIAL3

After performing the linear static analysis in the structure, a modal response analysis was done and the results in terms of frequencies and mode shapes are reported in Figure 4.29. It can be seen that despite the fact that the material properties were changed dramatically from those used in the previous model (MODTRIAL2), still the 2nd and 5th numerical mode shapes do not fit with any of the first 6 mode shapes obtained by the experimental measurements (Figure 2.15), so a qualitative comparison between the numerical and experimental mode shapes was done before making

quantitative comparison and it is shown in Figure 4.30. In terms of frequencies, they range between 2Hz and 5Hz with many close results to experimental modes as it is shown in Table 4.12.

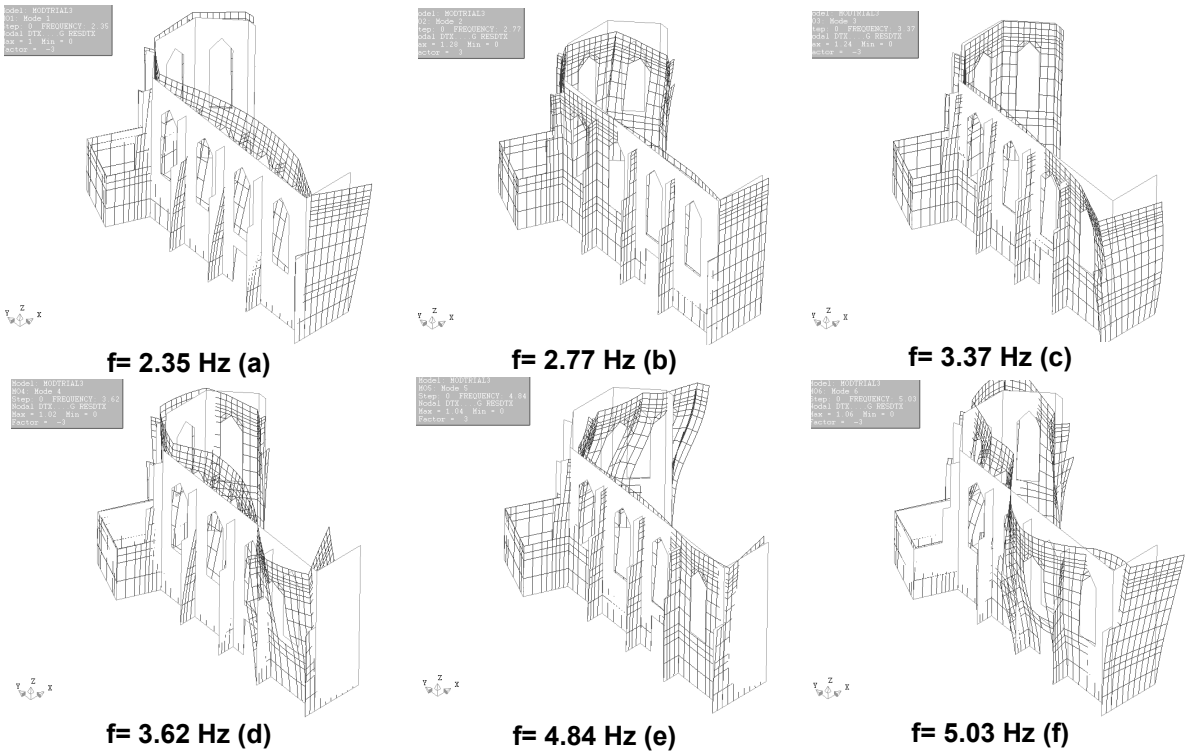

Figure 4.29. First (a), second (b), third (c), fourth (d), fifth (e) and sixth (f) mode shapes of numerical model MODTRIAL3

After making the qualitative comparison the selected numerical mode shapes are the 1st, the 3rd, the 4th and the 6th, and they are shown in Figure 4.30. These modes were compared in terms of frequencies finding the error between the measure value and the estimation of the numerical model. Also these modes were compared in terms of shapes, finding the correlation between the experimental modes shapes and the estimation of the numerical model. This comparison was done using MAC value, which gives a measure of the correlation between the shapes. All the results are reported in Table 4.12.

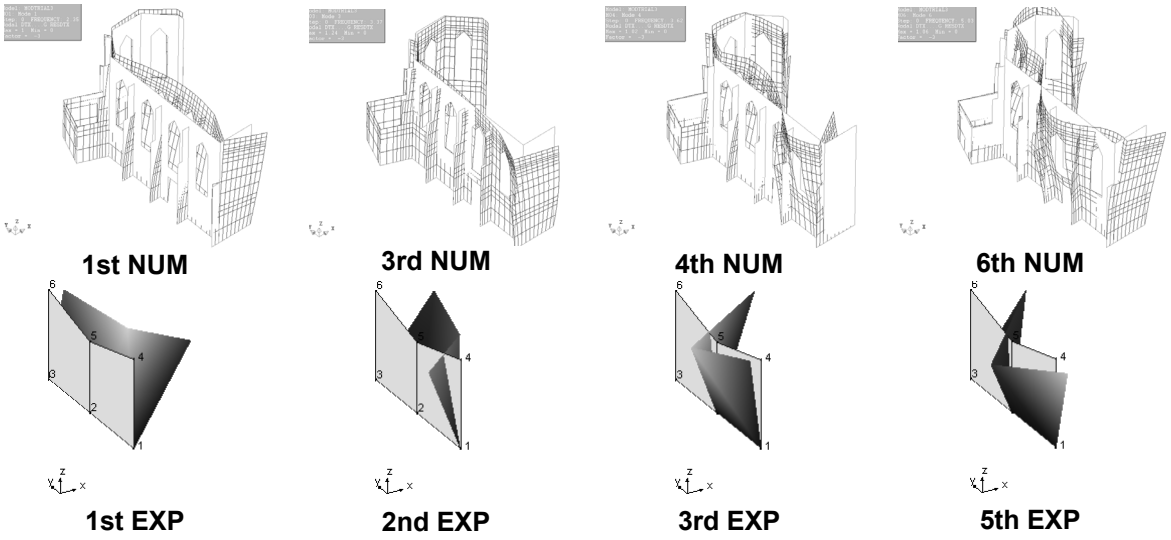

Figure 4.30. Qualitative comparison between model MODTRIAL3 and experimental mode shapes

The frequencies estimated by this model are very close to those measured by the dynamic test, the error estimation is below 10% for all of them and the average is 7.2%, which is an acceptable result. Regarding the mode shapes in terms of MAC estimation, all the values are lower than those obtained for the previous model; for the 1st mode the MAC is 2% lower, for the 3rd mode the MAC is 9% lower, for the 4th mode is 4% lower and for 6th mode is 4% lower, showing that although the frequency estimation error is low, the quality of the estimation of the shapes has decreased, and this model has more complexity than the previous because it has three different materials, with three different set of properties.

Mode Shape	f_{EXP} [Hz]	f_{NUM} [Hz]	Error [%]	MAC [%]	Mass part. in X [%]	Mass part. in Y [%]
1^{st}_{NUM}-1^{st}_{EXP}	2.57	2.35	-8.56	92.4	28.88	0.09
3^{rd}_{NUM}-2^{nd}_{EXP}	3.14	3.37	7.32	35.2	6.90	13.36
4^{th}_{NUM}-3^{rd}_{EXP}	3.95	3.62	-8.35	35.8	0.33	4.71
6^{th}_{NUM}-5^{th}_{EXP}	5.26	5.03	-4.37	74.2	3.77	1.82

Table 4.12. Comparison between experimental and numerical results in model MODTRIAL3

4.3.8 Model MODTRIAL3-A

The main goal in this model was to represent the lack of connection (Figure 4.31-a) that might be present between the North and the West facades. This hypothesis is based on the inspections and diagnosis reported in (Lourenço & Ramos, 2008) where it is stated that the tower located on top of the west façade (Figure 4.31-b) is rotated due to a possible soil settlement or past earthquake event. So it is believed that if this tower suffered rotation in the past, the connection between the North façade and West façade could be weak.

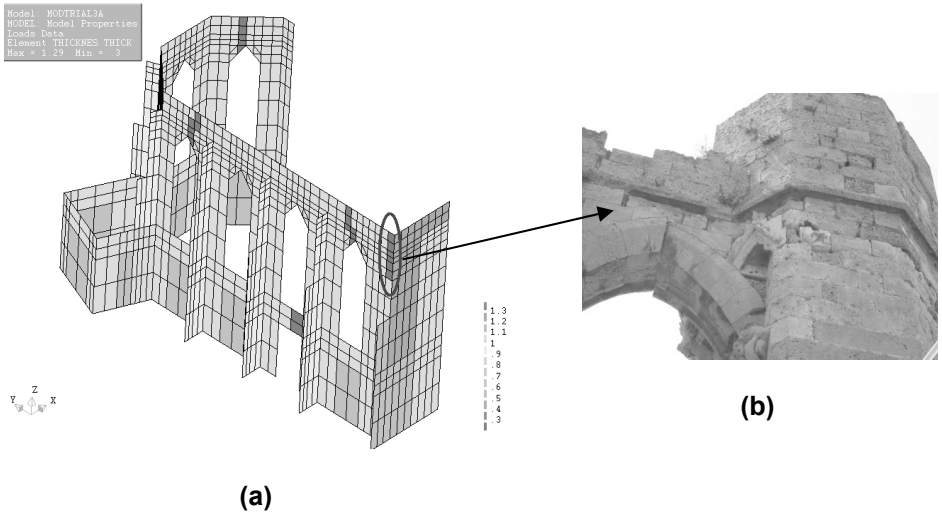

Figure 4.31. Model definition (a) of possible weakness in connection between North and West façades in the upper part of the wall (b)

For the abovementioned purpose, the thickness of the elements located in the upper part of the connection between the North and West façades (circled dark elements in Figure 4.31-a) was reduced from 1.02m to 0.30m, so that the stiffness of these elements is reduced to the cubic power. The other properties used to define this model are the same of those used to define the model MODTRIAL2, with the exception of the inclusion of the new characteristic in the connection named as "Thickness of connection (North-West)"; the whole set of physical and material properties used to define this model are shown in Table 4.13.

Parameter	Unit	Value
Thickness of North façade	Meter [m]	1.02
Thickness of connection (North-West)	Meter [m]	0.30
Thickness of damage (N-façade)	Meter [m]	0.30
Thickness of Apse & Sacristy	Meter [m]	1.02
Thickness of damage (Apse)	Meter [m]	0.30
Thickness of West façade	Meter [m]	1.29
Thickness of damage (W-façade)	Meter [m]	0.60
Thickness of Buttresses	Meter [m]	0.95
Thickness of Top wall (North and Apse)	Meter [m]	1.02
Thickness of Top wall (West)	Meter [m]	1.29
Thickness of Blind arches walls	Meter [m]	0.60
Thickness of Blind arch wall (West)	Meter [m]	1.02
Unit weight of masonry	Kilo Newton / Meter³ [KN/m³]	16
Elastic Modulus	Mega Pascal [MPa]	3780
Poisson's ratio	Dimensionless [-]	0.2
Additional mass of the tower	Kilogram [Kg]	52632
Additional mass of the vault	Kilogram [Kg]	32752

Table 4.13. Material and physical properties used for model MODTRIAL3-A

After the definition of the model, a linear static analysis was done, and the results are shown in Figure 4.32. The main results shown in the figure are the distribution of the maximum and minimum principal stresses, which represent tensile and compressive stresses respectively. The distribution of the maximum stresses in the structure is shown in Figure 4.32-a, and the peaks are located in the areas where the damage was modeled, and below the windows, and the maximum value is 0.20 MPa, which is inside the recommended value of the masonry tensile strength. Regarding the distribution of the minimum principal stresses, they are shown in Figure 4.32-b and the maximum values are shown below the location of the punctual masses that were used to represent the influence of the tower. The values at the base of the structure are about 0.25 MPa, which is the expected value for the geometrical and physical characteristics of the model.

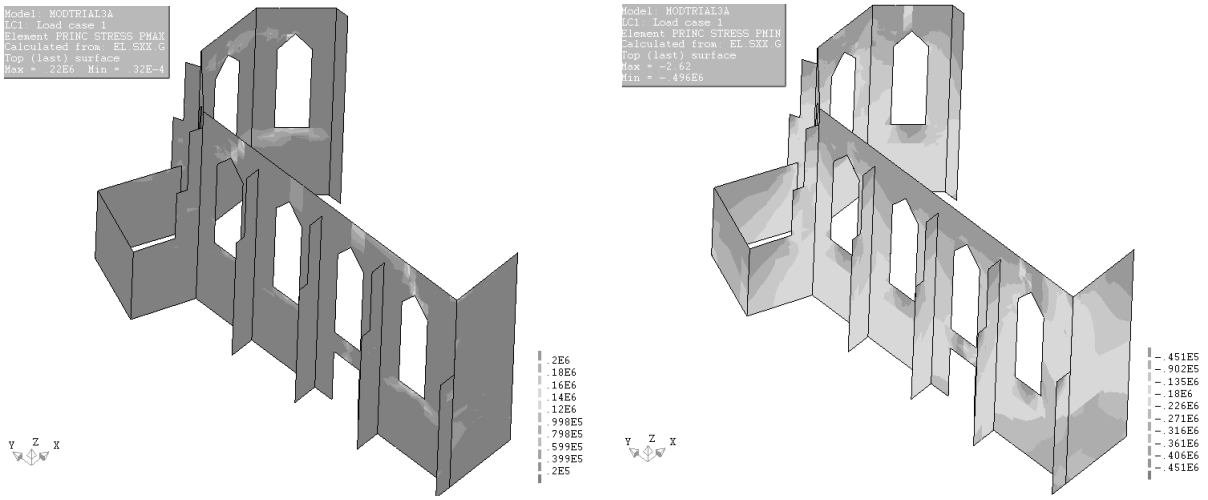

Figure 4.32. Maximum (a) and minimum (b) principal stresses of model MODTRIAL3-A

The next step was to perform a modal response analysis in the model and the results are shown in Figure 4.33. The frequencies range from 2 Hz and 6 Hz, which is the same range of the obtained frequencies by the experimental measurement. Regarding the mode shapes, they do not fit the same order of the experimental mode shapes, so that, it was necessary to make a qualitative comparison before making a quantitative comparison in order to obtain more reliable results, in this manner, this comparison was made and the results are shown in Figure 4.34.

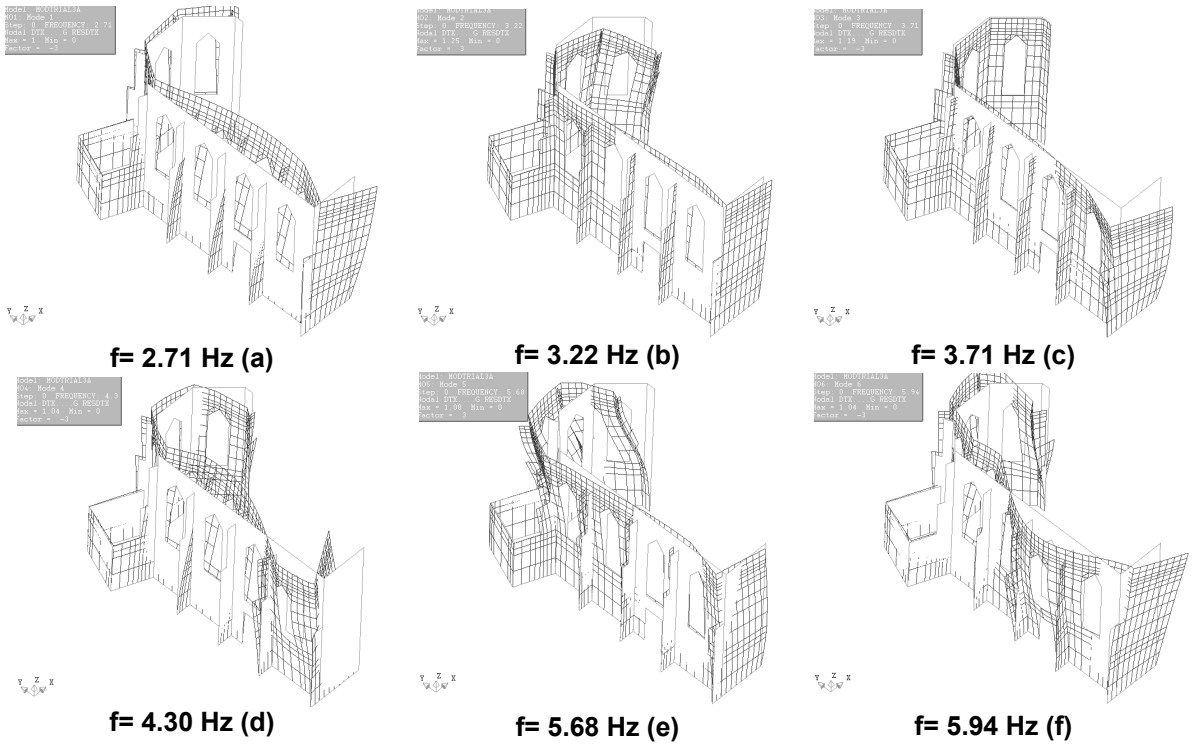

Figure 4.33. First (a), second (b), third (c), fourth (d), fifth (e) and sixth (f) mode shapes of numerical model MODTRIAL3-A

The chosen numerical modes are the 1st mode, the 3rd mode, the 4th mode and the 6th mode, which are compared in terms of frequencies and of mode shapes with the experimental modes following the order shown in Figure 4.34. Just by qualitative appreciation, the obtained numerical shapes are very similar to the experimental shapes. These modes were compared by the calculation of the errors in the estimation of the numerical frequencies and by the correlation of the obtained mode shapes by means of MAC values.

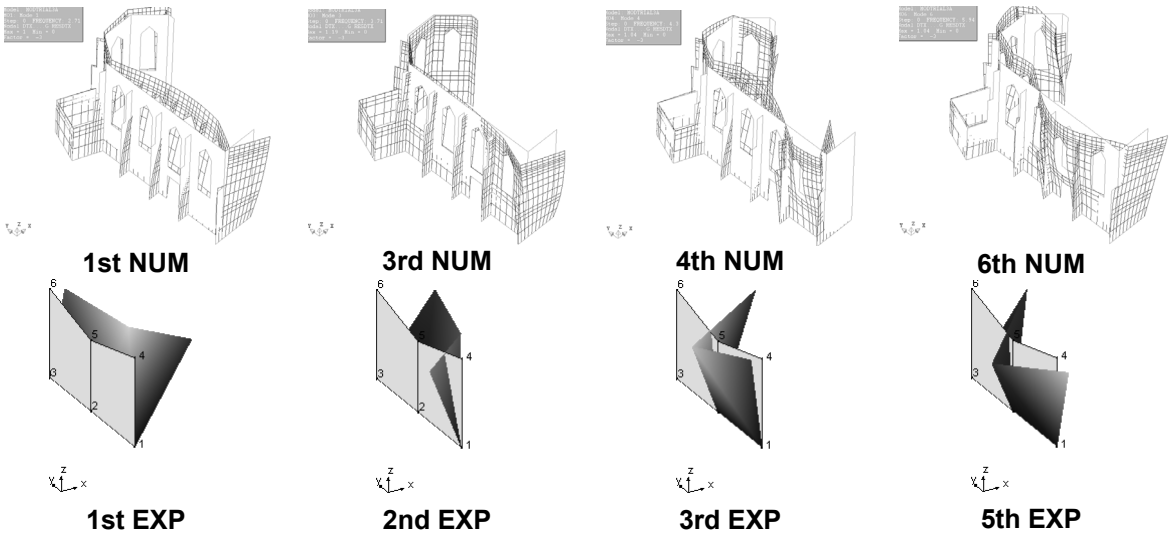

Figure 4.34. Qualitative comparison between model MODTRIAL3-A and experimental mode shapes

The average error between the numerical and experimental frequencies is 11.44%, but not all them, are below the 10% error, in fact one of them is close to 20% of error. Regarding MAC values, the estimation is better for the 6th mode (increased 5% compared with MODTRIAL2), but the other values remain more or less constant. It is important to underline the uncertainty in the stiffness of the connection, and the lack of information to estimate this parameter, as well as its influence in the behavior of the 3rd and the 6th modes. The modes that have higher mass participation factor in each of the global direction are 1st in X direction and 3rd in Y direction; all the above-mentioned facts are shown in Table 4.14.

Mode Shape	f_{EXP} [Hz]	f_{NUM} [Hz]	Error [%]	MAC [%]	Mass part. in X [%]	Mass part. in Y [%]
1^{st}_{NUM}-1^{st}_{EXP}	2.57	2.71	5.84	93.8	31.24	0.003
3^{rd}_{NUM}-2^{nd}_{EXP}	3.14	3.71	18.15	43.4	5.93	13.79
4^{th}_{NUM}-3^{rd}_{EXP}	3.95	4.30	8.86	35.2	0.51	3.88
6^{th}_{NUM}-5^{th}_{EXP}	5.26	5.94	12.96	83.3	0.63	0.29

Table 4.14. Comparison between experimental and numerical results in model MODTRIAL3-A

4.3.9 .Model MODTRIAL3-B

This model is intended to model also the possible weak connection between the North and West facades' walls. In this model the region of the elements that have lower thickness in the connection between the two facades was increased up to the cornice of lower part of the windows and it is shown in Figure 4.35-a. This can be supported because according to the experimental measurements reported by (Lourenço & Ramos, 2008), the point that relates the movement of the West façade (Point 4) in X direction presents large displacements in the entire measurements, so that, this phenomenon

may be possibly caused by the deterioration state of the stones located in the connection between the walls of both façades (Figure 4.35-b).

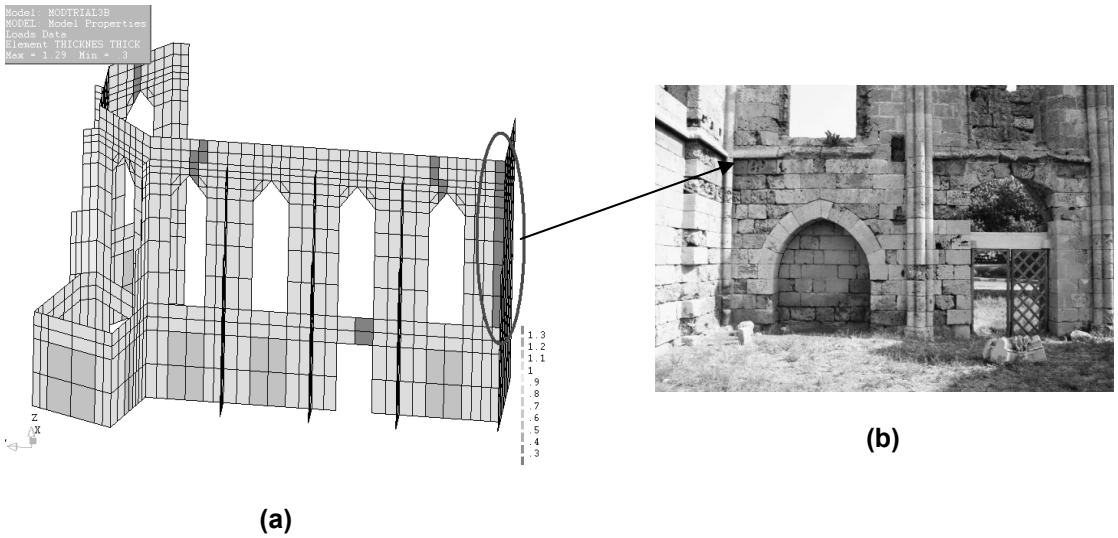

Figure 4.35. Model definition (a) of possible weakness in connection between North and West façades and damage in the lower part of the wall (b)

The thickness of the circled elements was changed from 1.02m to 0.30m in order to decrease their stiffness and make the connection flexible in an attempt to represent the large displacement of the vertex in the connection, as it was mentioned before. The whole set of properties that were used for defining this model is shown in Table 4.15.

Parameter	Unit	Value
Thickness of North façade	Meter [m]	1.02
Thickness of connection (North-West)	Meter [m]	0.30
Thickness of damage (N-façade)	Meter [m]	0.30
Thickness of Apse & Sacristy	Meter [m]	1.02
Thickness of damage (Apse)	Meter [m]	0.30
Thickness of West façade	Meter [m]	1.29
Thickness of damage (W-façade)	Meter [m]	0.60
Thickness of Buttresses	Meter [m]	0.95
Thickness of Top wall (North and Apse)	Meter [m]	1.02
Thickness of Top wall (West)	Meter [m]	1.29
Thickness of Blind arches walls	Meter [m]	0.60
Thickness of Blind arch wall (West)	Meter [m]	1.02
Unit weight of masonry	Kilo Newton / Meter³ [KN/m³]	16
Elastic Modulus	Mega Pascal [MPa]	3780
Poisson's ratio	Dimensionless [-]	0.2
Additional mass of the tower	Kilogram [Kg]	52632
Additional mass of the vault	Kilogram [Kg]	32752

Table 4.15. Material and physical properties used for model MODTRIAL3-B

A linear static analysis was performed in the model, and the results of the tensile and compressive stresses are shown in Figure 4.36-a and Figure 4.36-b respectively. The highest value for tensile stress is 0.20 MPa and it is located in the damaged regions which has lower stiffness. The highest compressive stress is 0.49 MPa and it is located below the area of influence of the punctual masses that represent the tower in the connection of the North and West facades. The value at the base of the structure is 0.25 MPa which is the expected value for the structural configuration and material properties used in this model.

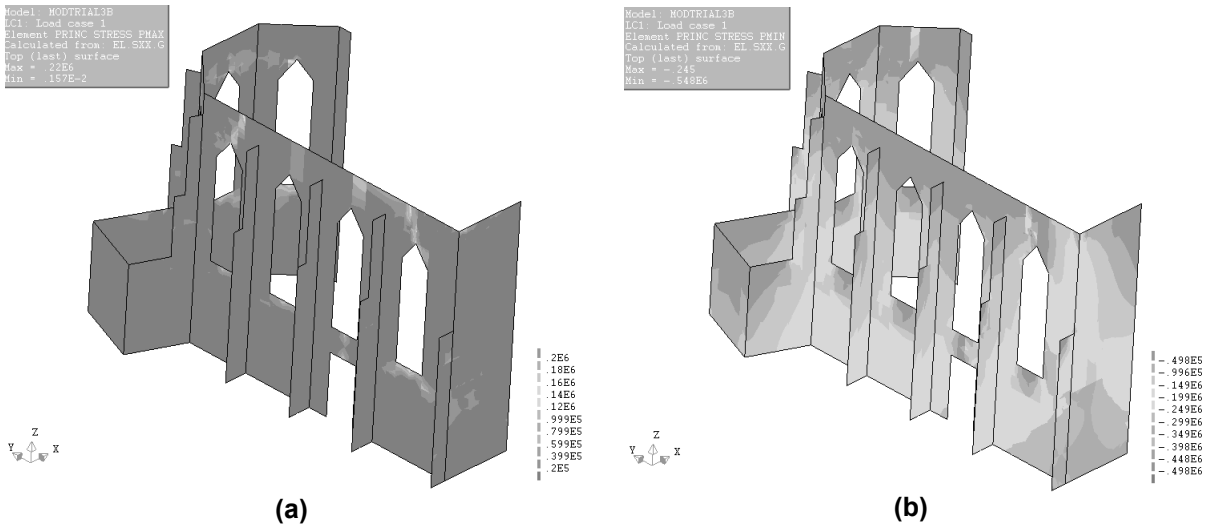

Figure 4.36. Maximum (a) and minimum (b) principal stresses of model MODTRIAL3-B

Also a modal response analysis was performed in order to estimate the response to dynamic events and the results are reported in Figure 4.37. The obtained frequency values are ranging between 2 Hz and 6 Hz which is the same range of the experimental results. The shapes of the first six modes are also shown in Figure 4.37 but the results are not matching the experimental shapes, so it was necessary to perform a qualitative comparison between the experimental and estimated mode shapes in order to choose those modes that better approach the experimental results and then perform the comparison in terms of frequencies and mode shapes.

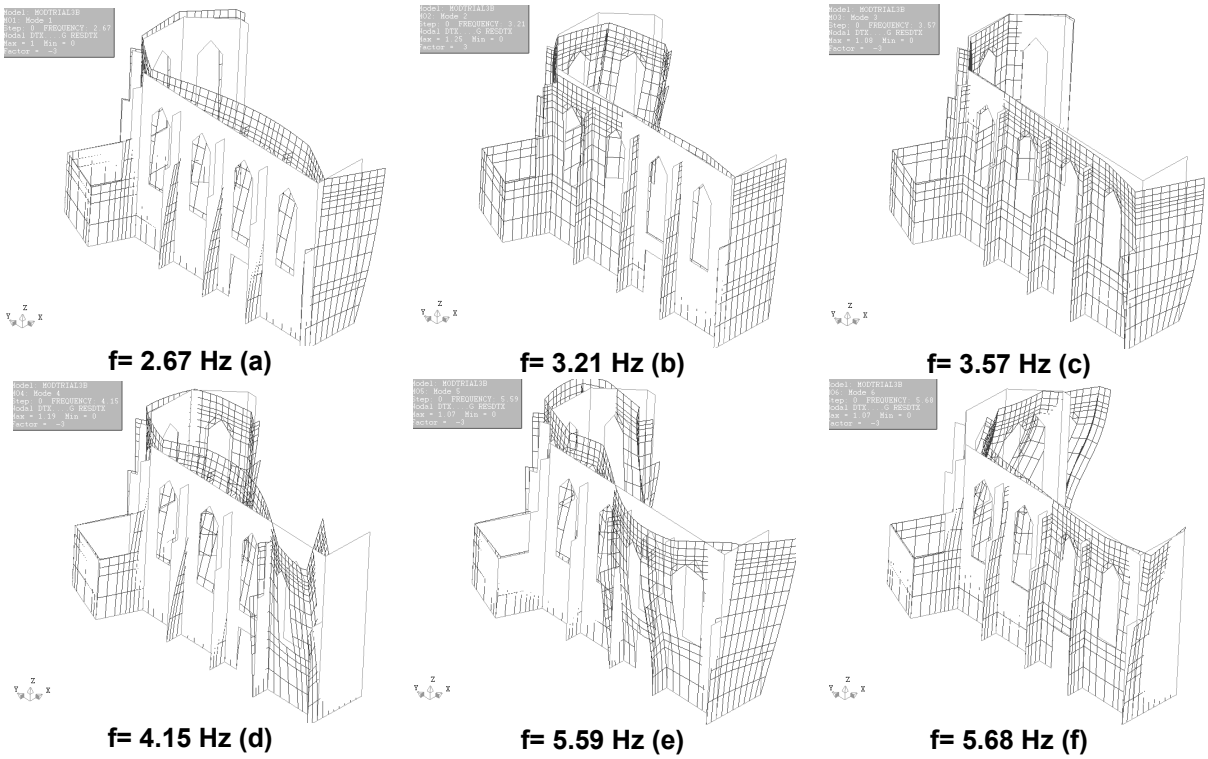

Figure 4.37. First (a), second (b), third (c), fourth (d), fifth (e) and sixth (f) mode shapes of numerical model MODTRIAL3-B

After the qualitative comparison between the experimental and numerical results, the numerical mode shapes that were selected are the 1st mode, the 3rd mode, the 4th mode and the 5th mode and they are shown in Figure 4.38. These modes were compared in terms of frequency values and mode shapes correlation by MAC, and the results are shown in Table 4.16.

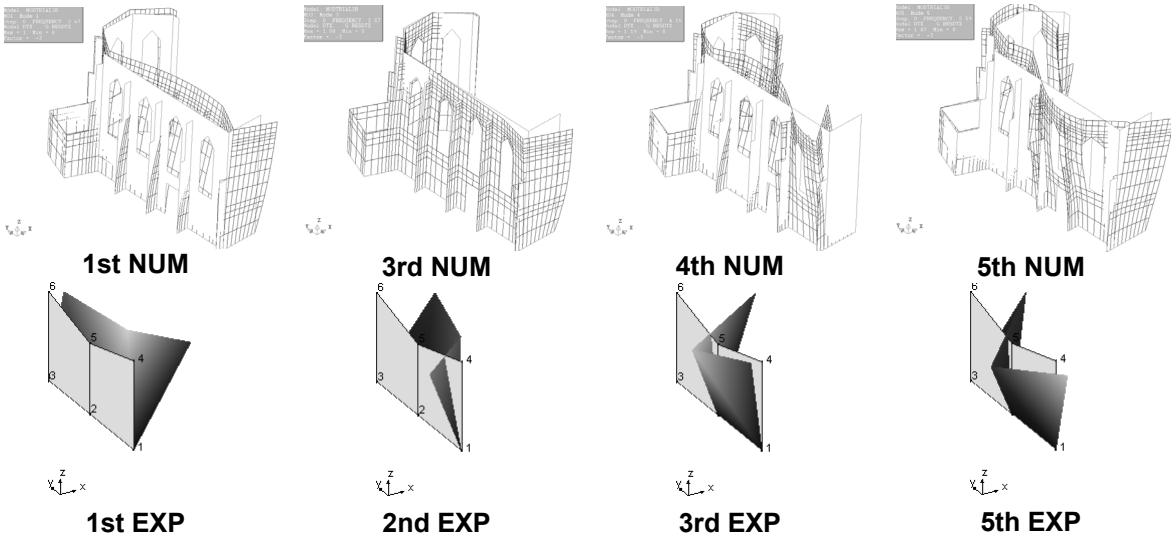

Figure 4.38. Qualitative comparison between model MODTRIAL3-B and experimental mode shapes

The error of the frequency estimation is in average 7.66% which is good, but there is a mode that has an error above 10% which is the 3rd one. Regarding mode shapes, the MAC values decreased from those obtained for model MODTRIAL2, except for th 1st mode, which remained the same and the 5th mode, which increased 2%. It is important to underline that there are several uncertainties in the representation of a possible flexible connection between both facades, and the results are mostly similar to those obtained for previous analyses.

Mode Shape	f_{EXP} [Hz]	f_{NUM} [Hz]	Error [%]	MAC [%]	Mass part. in X [%]	Mass part. in Y [%]
1^{st}_{NUM}-1^{st}_{EXP}	2.57	2.67	3.89	94.6	30.85	0.005
3^{rd}_{NUM}-2^{nd}_{EXP}	3.14	3.57	13.69	25.7	5.66	11.65
4^{th}_{NUM}-3^{rd}_{EXP}	3.95	4.15	5.06	34.1	0.001	14.44
5^{th}_{NUM}-5^{th}_{EXP}	5.26	5.59	7.66	80.9	1.70	0.83

Table 4.16. Comparison between experimental and numerical results in model MODTRIAL3-B

4.3.10 Model MODTRIAL3D

This model is based on the same properties used to define model MODTRIAL2, but the material properties were varied in order to represent sonic test results reported in (Lourenço & Ramos, 2008), which are shown in Section 2.3.4. The main intention in this model was to represent the different stiffness in the buttresses due to the deterioration state in which they were found during the inspection and diagnosis works reported in (Lourenço & Ramos, 2008). In order to take into account this characteristic, the buttresses stiffness was varied according to sonic test results, which divide buttresses in two groups, North buttresses (Figure 4.39-c) and South buttresses (Figure 4.39-b). For this purpose the North buttresses were numbered from 1 to 4 and South buttresses from 5 to 8 and their plane distribution is shown in Figure 4.39-a.

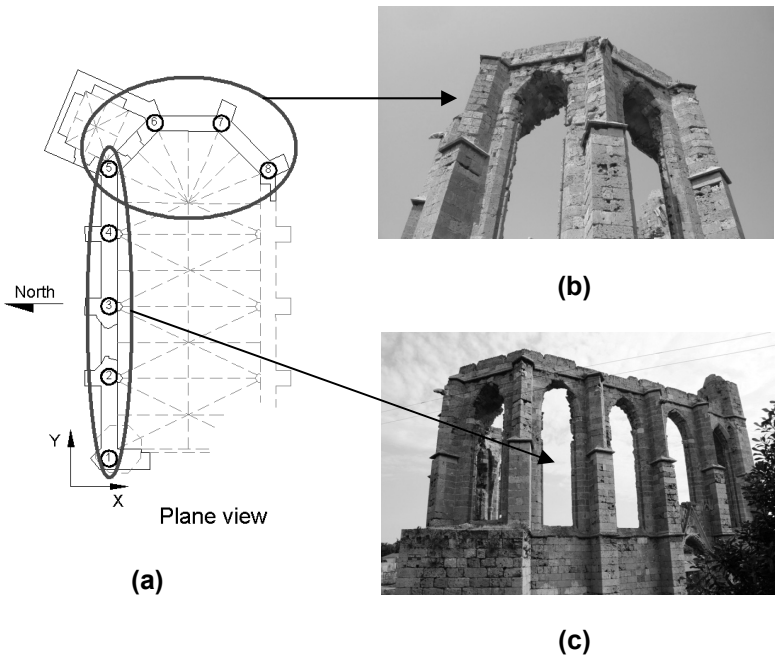

Figure 4.39. Plan view of the church (a) with the numbering of the buttresses. Photos of East façade buttresses (b) and North façade buttresses (c)

The results of sonic tests state that in general the stones in the buttresses are more deteriorated than the reference stone, which was selected by good qualitative conditions. More specifically, the inner part of North buttresses is more deteriorated than the outer part, and regarding South buttresses, the results of the sonic velocity were very similar for the inner and the outer part, so the damage should be moderate in comparison with the reference stone. In order to correlate the sonic velocity with the stiffness of the material, the Equation 4.12 was used, which correlates the velocity of the sound waves in solid material with its elastic modulus and its density.

$$c = \sqrt{\frac{E}{\rho}} \qquad 4.12$$

Where: c: is the wave velocity of the sound in the solid material [m/s]

E: is the elastic modulus of the solid material [Pa]

ρ: is the density of the solid material [Kg/m³]

In order to estimate in which proportion the elastic modulus of the inner and outer parts of the buttresses should be modified, the sonic velocity of the reference stone was correlated with the sonic velocity obtained for the South and North buttresses. If the density of the material is assumed constant, it is possible to correlate the sonic velocity and the elastic modulus of the reference material with the sonic velocity and the elastic modulus of the buttresses using Equation 4.13.

$$\rho = \frac{c_{REF}^2}{E_{REF}} = \frac{c_i^2}{E_i} \qquad 4.13$$

Where: c_{REF} : is the wave velocity of the sound in the reference stone [m/s]

E_{REF} : is the elastic modulus of the reference stone [Pa]

c_i : is the wave velocity of the sound in different buttresses [m/s]

E_i : is the elastic modulus of different buttresses [Pa]

It is possible to leave in one side of the equation, the elastic modulus of the buttresses, which is the unknown, and then obtain the Equation 4.14. In this equation, the elastic modulus of different buttresses depends on the sonic velocity of the reference stone, the sonic velocity measured in the buttresses and the reference elastic modulus, which is the same as used in the previous model (3780 MPa).

$$E_i = \left(\frac{c_i}{c_{REF}} \right)^2 \cdot E_{REF} \qquad 4.14$$

The different values obtained for the elastic modulus in different parts of the structure are reported in Table 4.17 where the different subscripts represent the following parts of the structure: 1 is the reference value which represent the whole structure, 2 represents the values of the inner part of North buttresses (1-4), 3 represents the outer part of the North buttresses and 4 represents the inner and the outer part of the South buttresses.

Subscript [i]	Relation between sonic velocities [C_i/C_{REF}]	Elastic modulus [E_i]
1	---	3.78 GPa
2	0.529	1.05 GPa
3	0.742	2.08 GPa
4	0.648	1.59 GPa

Table 4.17. Values of Elastic modulus according to the equation 4.14

The whole set of properties used in the model MODTRIAL3-D is shown in Table 4.18, including the materials defined according to the sonic test results, which are named as material 1, material 2, material 3 and material 4; the subscripts are representing the different parts of the structure abovementioned. The properties used to define this model are the same of those used for defining the model MODTRIAL2, including physical properties, geometrical dimensions and damage representation.

Parameter	Unit	Value
Thickness of North façade	Meter [m]	1.02
Thickness of damage (N-façade)	Meter [m]	0.30
Thickness of Apse & Sacristy	Meter [m]	1.02
Thickness of damage (Apse)	Meter [m]	0.30
Thickness of West façade	Meter [m]	1.29
Thickness of damage (W-façade)	Meter [m]	0.60
Thickness of Buttresses	Meter [m]	0.95
Thickness of Top wall (North and Apse)	Meter [m]	1.02
Thickness of Top wall (West)	Meter [m]	1.29
Thickness of Blind arches walls	Meter [m]	0.60
Thickness of Blind arch wall (West)	Meter [m]	1.02
Material 1		
Unit weight of masonry	Kilo Newton / Meter³ [KN/m³]	16
Elastic Modulus	Mega Pascal [MPa]	3780
Poisson's ratio	Dimensionless [-]	0.2
Material 2		
Unit weight of masonry	Kilo Newton / Meter³ [KN/m³]	16
Elastic Modulus	Mega Pascal [MPa]	1050
Poisson's ratio	Dimensionless [-]	0.2
Material 3		
Unit weight of masonry	Kilo Newton / Meter³ [KN/m³]	16
Elastic Modulus	Mega Pascal [MPa]	2080
Poisson's ratio	Dimensionless [-]	0.2
Material 4		
Unit weight of masonry	Kilo Newton / Meter³ [KN/m³]	16
Elastic Modulus	Mega Pascal [MPa]	1590
Poisson's ratio	Dimensionless [-]	0.2
Additional mass of the tower	Kilogram [Kg]	52632
Additional mass of the vault	Kilogram [Kg]	32752

Table 4.18. Material and physical properties used for model MODTRIAL3-D

After defining the model, a linear static analysis was done and the results of the principal stresses distribution are reported in Figure 4.40. The distribution of tensile stresses among the structure is shown in Figure 4.40-a, and the maximum tensile stresses are located in the areas where the damage was modeled and their value is of about 0.21 MPa, which is in the range of the recommended range for masonry tensile strength. In Figure 4.40-b the distribution of the compressive stresses is shown, and their peak values are located in the lower part of the West façade, where the punctual masses are concentrated. The value at the base of the structure is of 0.25 MPa, which is the expected value for the structural configuration.

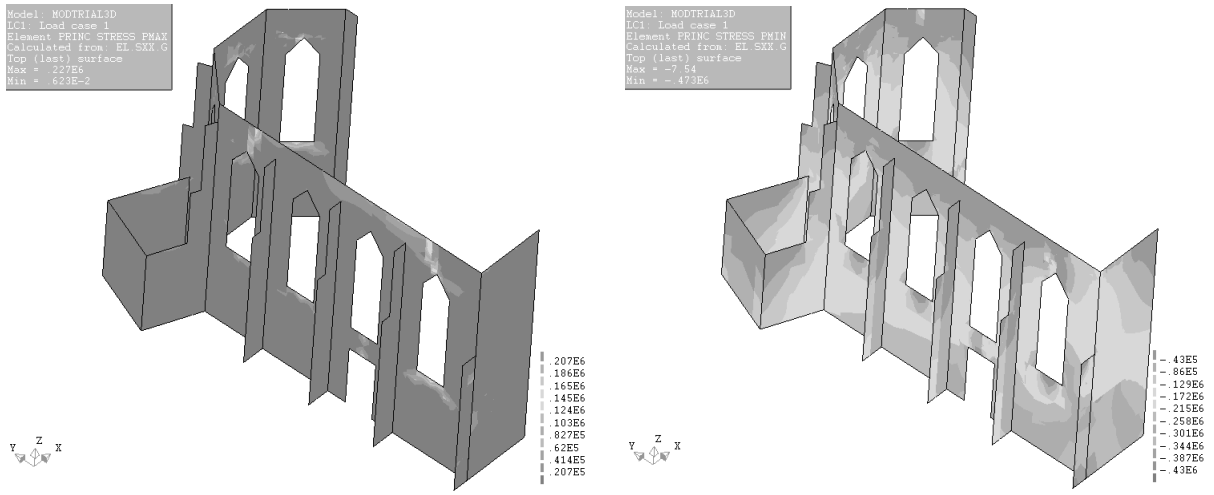

(a) **(b)**

Figure 4.40. Maximum (a) and minimum (b) principal stresses of model MODTRIAL3-D

A modal response analysis was performed and the results are reported in terms of frequencies and mode shapes in Figure 4.41. The frequency values are inside the range of 2 Hz to 6, Hz which is the same range of the measured frequencies, but the mode shapes are not following the same order of the numerical modes. Again, it was necessary to make a previous qualitative comparison between mode shapes because it would improve the results, especially in terms of correlation between shapes which do not match experimental results in the same order; they are shown in Figure 4.42.

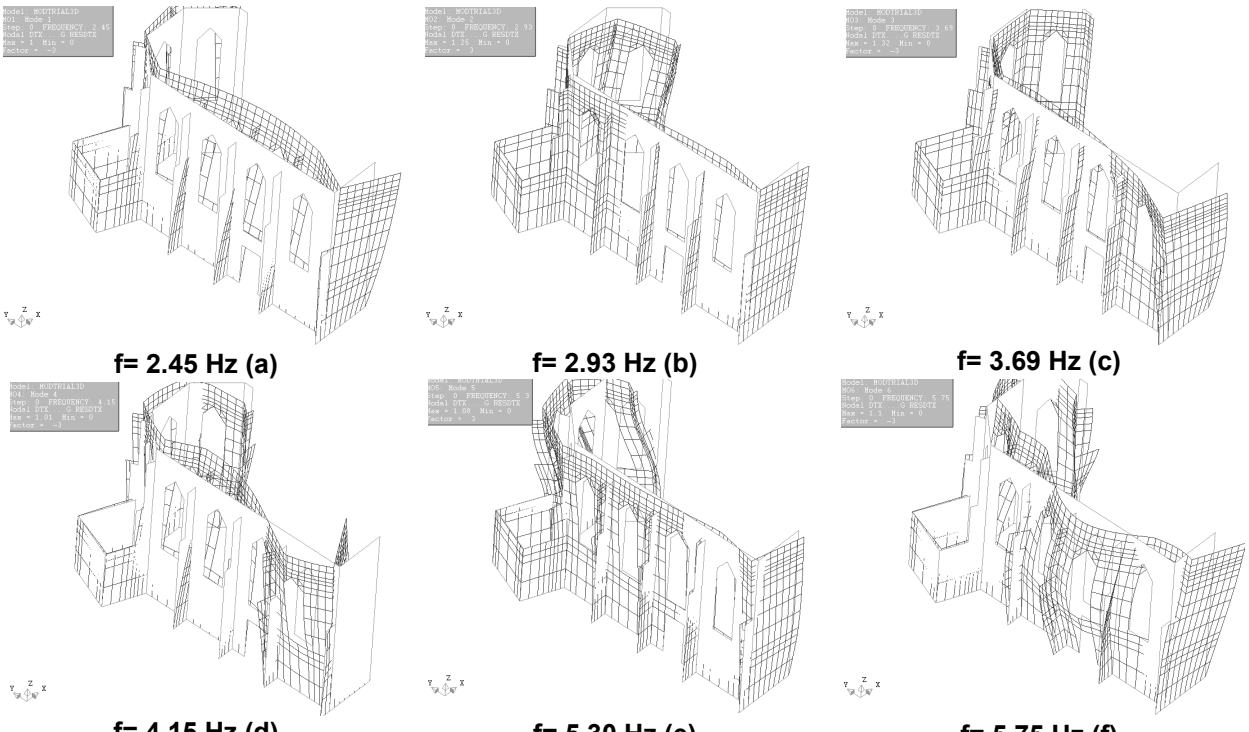

f= 2.45 Hz (a) **f= 2.93 Hz (b)** **f= 3.69 Hz (c)**

f= 4.15 Hz (d) **f= 5.30 Hz (e)** **f= 5.75 Hz (f)**

Figure 4.41. First (a), second (b), third (c), fourth (d), fifth (e) and sixth (f) mode shapes of numerical model MODTRIAL3-D

After the qualitative comparison between the modes, those selected are shown in Figure 4.42. The numerical selected modes are the 1st, the 3rd, the 4th and the 5th mode which were compared with the 1st experimental mode, the 2nd, the 3rd and the 5th experimental modes respectively. After the arrangement of modes in different pairs, each one of the pairs was quantitatively compared in terms of frequencies estimation error and mode shapes correlation using MAC values and the results are shown in Table 4.19.

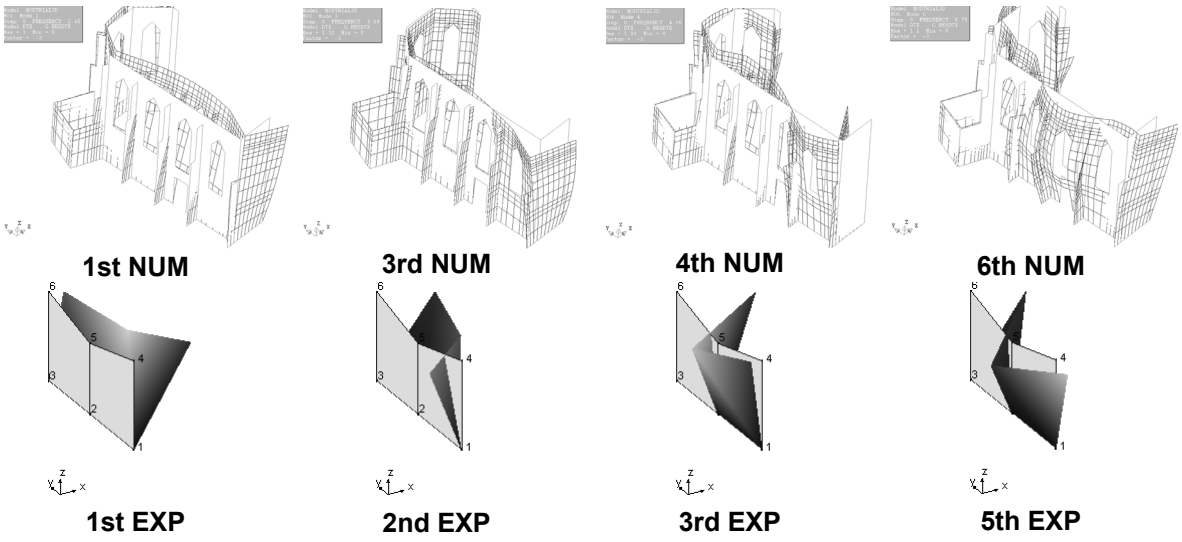

Figure 4.42. Qualitative comparison between model MODTRIAL3-D and experimental mode shapes

The average error in the frequency estimation is 9.14%, which is the lowest value of all the previous models analyzed and almost all the values are below this percentage, except for the estimation of the 3rd numerical frequency (17.52%). Regarding MAC values, they remain similar to those obtained for model MODTRIAL2, specially MAC values for the 1st and 6th numerical modes are equal or higher to 80% which is an acceptable correlation value.

Mode Shape	f_{EXP} [Hz]	f_{NUM} [Hz]	Error [%]	MAC [%]	Mass part. in X [%]	Mass part. in Y [%]
1^{st}_{NUM}-1^{st}_{EXP}	2.57	2.45	-4.67	90.6	32.21	0.05
3^{rd}_{NUM}-2^{nd}_{EXP}	3.14	3.69	17.52	44.2	5.99	11.89
4^{th}_{NUM}-3^{rd}_{EXP}	3.95	4.15	5.06	41.2	0.78	6.36
6^{th}_{NUM}-5^{th}_{EXP}	5.26	5.75	9.32	79.1	0.71	2.72

Table 4.19. Comparison between experimental and numerical results in model MODTRIAL3-D

4.4 COMPARISSON BETWEEN THE MODELS

After performing the several analyses by changing different parameters in the structure, such as physical and material properties, the results of the analyses were compared in order to decide which models are those that better represent the real structure. This task was carried out by making a comparison between the experimental results obtained from the dynamic tests and the numerical estimated data in each model. This comparison was made in terms of percentage of error in the estimation of the frequencies and also in terms of mode shapes correlation using MAC values; the results are reported in Table 4.20.

Model	Mode Shape	f estimation Error [%]	f average Error [%]	MAC [%]	Average MAC [%]
MODTRIAL	1^{st}_{NUM}-1^{st}_{EXP}	10.5	14.27	91.6	61.11
	3^{rd}_{NUM}-2^{nd}_{EXP}	25.2		36.3	
	4^{th}_{NUM}-3^{rd}_{EXP}	8.3		33.6	
	6^{th}_{NUM}-5^{th}_{EXP}	13.1		82.9	
MODTRIAL1	1^{st}_{NUM}-1^{st}_{EXP}	8.6	14.70	92.2	61.38
	3^{rd}_{NUM}-2^{nd}_{EXP}	22.0		38.1	
	4^{th}_{NUM}-3^{rd}_{EXP}	11.1		39.0	
	6^{th}_{NUM}-5^{th}_{EXP}	17.1		76.2	
MODTRIAL2	1^{st}_{NUM}-1^{st}_{EXP}	6.2	13.18	94.1	64.05
	3^{rd}_{NUM}-2^{nd}_{EXP}	18.5		44.2	
	4^{th}_{NUM}-3^{rd}_{EXP}	10.9		39.1	
	6^{th}_{NUM}-5^{th}_{EXP}	17.1		78.8	
MODTRIAL3	1^{st}_{NUM}-1^{st}_{EXP}	-8.56	7.15	92.4	59.40
	3^{rd}_{NUM}-2^{nd}_{EXP}	7.32		35.2	
	4^{th}_{NUM}-3^{rd}_{EXP}	-8.35		35.8	
	6^{th}_{NUM}-5^{th}_{EXP}	-4.37		74.2	
MODTRIAL3-A	1^{st}_{NUM}-1^{st}_{EXP}	5.84	11.45	93.8	63.93
	3^{rd}_{NUM}-2^{nd}_{EXP}	18.15		43.4	
	4^{th}_{NUM}-3^{rd}_{EXP}	8.86		35.2	
	6^{th}_{NUM}-5^{th}_{EXP}	12.96		83.3	
MODTRIAL3-B	1^{st}_{NUM}-1^{st}_{EXP}	3.89	7.58	94.6	58.82
	3^{rd}_{NUM}-2^{nd}_{EXP}	13.69		25.7	
	4^{th}_{NUM}-3^{rd}_{EXP}	5.06		34.1	
	5^{th}_{NUM}-5^{th}_{EXP}	7.66		80.9	
MODTRIAL3-D	1^{st}_{NUM}-1^{st}_{EXP}	-4.67	9.14	90.6	63.78
	3^{rd}_{NUM}-2^{nd}_{EXP}	17.52		44.2	
	4^{th}_{NUM}-3^{rd}_{EXP}	5.06		41.2	
	6^{th}_{NUM}-5^{th}_{EXP}	9.32		79.1	

Table 4.20. Comparison between the different models in terms of frequency estimation error and mode shape correlation (MAC)

The selection criterion was to choose the models that have the higher MAC values, which represents the correlation between the measured shapes and the estimated shapes. The frequency average error was not so important because the experimental frequencies will be fit into the numerical model by

applying the updating method reported later. Following this criteria, the models MODTRIAL2 and MODTRIAL3-D were selected because they have average MAC values of 64.05%, 63.93% and 63.78%, respectively. The results of the updating process applied to the selected models (MODTRIAL2 and MODTRIAL3-D) are reported in the next Chapter.

5. CALIBRATION OF THE NUMERICAL MODELS

5.1 INTRODUCTION

The dynamic behavior of a structure is highly affected by alterations of geometry, variations of the boundary conditions, mass changes and degradation of the mechanical properties of the materials (Ramos, 2007). Aiming at the simulation of the real structure response to dynamic events like earthquakes, the model was calibrated following the procedure shown by (Douglas & Reid, 1982). The approach addressed here is to update modal parameters such as frequencies and/or mode shapes using an optimization process to minimize the residuals between the experimental response and the numerical response. Here, only the frequencies were selected to be updated and the validation of the numerical model was done by making the comparison between the experimental and numerical mode shapes, and comparing the tensile stress distribution with the damage distribution of the actual state of conservation of the structure. The mode shapes should be included in the optimization process but due to the low resolution of modes (Only 5 DOFs), time limitation to carry out this work and the additional complexity, they were disregarded in the optimization process.

According to (Ramos, 2007), the updating parameters should influence the modal data considerably, but not all these parameters should be included in the calibration process. If a parameter can be estimated accurately in the initial FE model by means of experimental tests, or if the geometrical measurement of the structure is detailed, there is no reason to update it. Geometrical changes, variations on the boundary conditions, mass changes and degradation of the mechanical properties of the material may be included in the optimization process. Following the recommendations of (Ramos, 2007), the selected parameters to be updated were the elastic modulus of the masonry and the thickness that represent the reduction of stiffness in damaged areas of the real structure.

After defining which variables will be updated, an initial value for each variable should be defined, as well as a lower and upper bounds. These values should be based on experimental and historical data and engineering judgment, in order to obtain consistent results. At the end of the optimization process, which is the minimization of the error between the experimental and the numerical modal data, the updated values for each selected variable are obtained. These values should be reviewed, in order to see how consistent they are and if they fit with typical results, based on previous experiences in the field of research.

Two models were selected to perform the calibration process, models MODTRIAL2 and MODTRIAL3-D, as it was mentioned in Section 4.4. Both models were updated in terms of eigenfrequencies, by comparing the 1st, the 2nd, the 3rd and the 5th experimental modes with the 1st, the 3rd, the 4th and the 6th numerical modes respectively. At the end, only one model was selected to perform further non-linear analyses.

5.2 MATHEMATIC MODEL FOR THE CALIBRATION PROCESS

In order to define the uncertain structural parameters, the calibration procedure proposed by (Douglas & Reid, 1982) was applied. The frequency *i* can by estimated according to the quasi-structural model shown in Equation 5.1.

$$f_i^D\left(X_1, X_2, ..., X_N\right) = C_i + \sum_{k=1}^{N}\left[A_{ik} \cdot X_k + B_{ik} \cdot X_k^2\right] \qquad 5.1$$

Where: f_i^D : is the approximation of the *i*-th frequency of the FE model

$X_k\left(k = 1,2,..., N\right)$: are the variables to be calibrated

A_{ik}, B_{ik}, C_i : are the calibration constants

According to Equation 5.1, there are $\left(2N+1\right)$ constants A_{ik}, B_{ik}, C_i that should be determined before making the comparison with the experimental results. In order to evaluate these constants, a base value $X_k^B\left(k = 1,2,..., N\right)$, an upper bound $X_k^U\left(k = 1,2,..., N\right)$ and a lower bound $X_k^L\left(k = 1,2,..., N\right)$ for each of the selected variables should be defined based on engineering judgment; this is the definition of the range of variation for each structural variable. Then, those constants are determined by computing the *i*-th natural frequency f_i^C of the numerical model for each of the $\left(2N+1\right)$ choices of the unknown variables following the expressions shown in Equation 5.2, starting with the initial values and then ranging from the lower to the upper bound of each variable, one at time.

$$\begin{aligned}
&f_i^D\left(X_1^B, X_2^B, ..., X_N^B\right) = f_i^C\left(X_1^B, X_2^B, ..., X_N^B\right)\\
&f_i^D\left(X_1^L, X_2^B, ..., X_N^B\right) = f_i^C\left(X_1^L, X_2^B, ..., X_N^B\right)\\
&f_i^D\left(X_1^U, X_2^B, ..., X_N^B\right) = f_i^C\left(X_1^U, X_2^B, ..., X_N^B\right)\\
&\qquad\qquad \dots\\
&f_i^D\left(X_1^B, X_2^B, ..., X_N^L\right) = f_i^C\left(X_1^B, X_2^B, ..., X_N^L\right)\\
&f_i^D\left(X_1^B, X_2^B, ..., X_N^U\right) = f_i^C\left(X_1^B, X_2^B, ..., X_N^U\right)
\end{aligned} \qquad 5.2$$

Where: f_i^C : is the *i*-th frequency calculated through the numerical model

After obtaining the constants, the quasi-structural model shown in Equation 5.1 is already defined and the optimization process is carried out by several iterations of the Equation 5.3, where the error shown in Equation 5.4 is minimized.

$$J = \sum_{i=1}^{m} w_i \cdot \varepsilon_i^2 \qquad 5.3$$

Where: J : is the objective function to be calibrated

$$\varepsilon_i = f_i^{EMA} - f_i^{D}\left(X_1, X_2, ..., X_N\right) \qquad 5.4$$

Where: f_i^{EMA} : is the *i*-th experimental frequency

w_i : weighing factors

5.3 CALIBRATION OF MODEL MODTRIAL2

The selected variables to be calibrated, $X_k^B\left(k = 1,2,...,N\right)$, and their base values are shown in Table 5.1. These are: (1) the material elastic modulus, (2) the thickness of damaged area in the North façade, (3) the thickness of damaged area in the Apse and (4) the thickness of damaged area in the West façade. Also the upper and lower bounds of the range for each variable are shown. For the elastic modulus, 30% of excess was allowed for the upper bound and the lower bound value was obtained by a 30% of decreasing of the initial value. Regarding the element thicknesses, an upper bound of 66.67% exceeding the initial value was adopted and a lower bound of 66.67% of initial value reduction was supposed.

The values of the obtained numerical frequencies using the nine different combinations given in Equation 5.2 are shown in Table 5.2 and the obtained values of the calibration constants are given in Table 5.3.

Variable	Parameter	Base Value	Lower Bound	Upper Bound	Unit
1	Elastic Modulus	3780	2646	4914	MPa
2	Thickness (Damage in N-façade)	0.30	0.10	0.50	m
3	Thickness (Damage in Apse)	0.30	0.10	0.50	m
4	Thickness (Damage in W-façade)	0.60	0.20	1.00	m

Table 5.1. Base values, upper and lower bounds of the calibration variables of model MODTRIAL2

Variable combination	F1 [Hz]	F2 [Hz]	F3 [Hz]	F5 [Hz]
(1b, 2b, 3b, 4b, 5b, 6b, 7b)	2.73	3.72	4.38	6.16
(1lower, 2b, 3b, 4b, 5b, 6b, 7b)	2.28	3.12	3.66	5.16
(1upper, 2b, 3b, 4b, 5b, 6b, 7b)	3.11	4.25	4.99	7.03
(1b, 2lower, 3b, 4b, 5b, 6b, 7b)	2.64	3.66	4.12	5.91
(1b, 2upper, 3b, 4b, 5b, 6b, 7b)	2.78	3.76	4.60	6.29
(1b, 2b, 3lower, 4b, 5b, 6b, 7b)	2.72	3.72	4.32	5.90
(1b, 2b, 3upper, 4b, 5b, 6b, 7b)	2.73	3.73	4.40	6.34
(1b, 2b, 3b, 4lower, 5b, 6b, 7b)	2.67	3.43	4.32	6.14
(1b, 2b, 3b, 4upper, 5b, 6b, 7b)	2.80	3.95	4.47	6.19

Table 5.2. Frequency values for the different combination of variables model MODTRIAL2 calibration MODTRIAL2 (b: base value, lower: lower bound and upper: upper bound)

Constant	F1	F2	F3	F5
C_i	7.557E-01	7.852E-01	1.041E+00	1.352E+00
A_{i1}	5.508E-01	7.524E-01	8.838E-01	1.245E+00
B_{i1}	-2.457E-02	-3.359E-02	-3.943E-02	-5.552E-02
A_{i2}	6.385E-01	4.270E-01	1.475E+00	1.933E+00
B_{i2}	-4.937E-01	-2.875E-01	-4.350E-01	-1.654E+00
A_{i3}	3.450E-02	1.350E-02	4.320E-01	1.783E+00
B_{i3}	-4.125E-02	-1.250E-02	-4.250E-01	-1.124E+00
A_{i4}	1.183E-01	9.170E-01	2.225E-02	6.225E-02
B_{i4}	4.500E-02	-2.228E-01	1.381E-01	-5.938E-03

Table 5.3. Calibration constants for model MODTRIAL2

After the determination of the calibration constants, following the method shown by (Douglas & Reid, 1982), the objective function (Equation 5.3) was minimized using GAMS software (GAMS, 1998), which has different algebraic solvers, and the weighing factors were all kept as one. After the optimization process the minimum value of the objective function was 0.025 and the updated parameters are shown in Table 5.4 marked with (*), among with the other material and physical properties used to analyze the model MODTRIAL2 after calibration process. The obtained results for the calibrated variables show that the elastic modulus was reduced 20.18% from its base value, the thickness representing damaged elements in North façade was increased 60%, the thickness representing the damaged area in Apse was decreased 66.67% from its base value reaching its lower bound and the thickness representing the damaged region of the West façade was reduced 43.33%.

Parameter	Unit	Value
Thickness of North façade	Meter [m]	1.02
Thickness of damage (N-façade)	Meter [m]	0.418*
Thickness of Apse & Sacristy	Meter [m]	1.02
Thickness of damage (Apse)	Meter [m]	0.100*
Thickness of West façade	Meter [m]	1.29
Thickness of damage (W-façade)	Meter [m]	0.340*
Thickness of Buttresses	Meter [m]	0.95
Thickness of Top wall (North and Apse)	Meter [m]	1.02
Thickness of Top wall (West)	Meter [m]	1.29
Thickness of Blind arches walls	Meter [m]	0.60
Thickness of Blind arch wall (West)	Meter [m]	1.02
Unit weight of masonry	Kilo Newton / Meter³ [KN/m³]	16
Elastic Modulus	Mega Pascal [MPa]	3017*
Poisson's ratio	Dimensionless [-]	0.2
Additional mass of the tower	Kilogram [Kg]	52632
Additional mass of the vault	Kilogram [Kg]	32752

Table 5.4. Material and physical properties of model MODTRIAL2 after calibration process

After performing the calibration process of the uncertain structural variables, a linear static analysis was done and the results are shown in Figure 5.1. The distribution of the tensile stresses among the structure is shown in Figure 5.1-a, where the maximum tensile stress is of 0.33 MPa, which is moderately large value but it is located in the areas where the damage is more concentrated according to the visual inspection carried out by (Lourenço & Ramos, 2008). The distribution of compressive stresses is shown in Figure 5.1-b, where the highest value is of 0.48MPa and it is located below the mass concentration that represents the tower. The compressive stress value at the base of the structure is 0.24MPa, which is the expected value for the structural configuration.

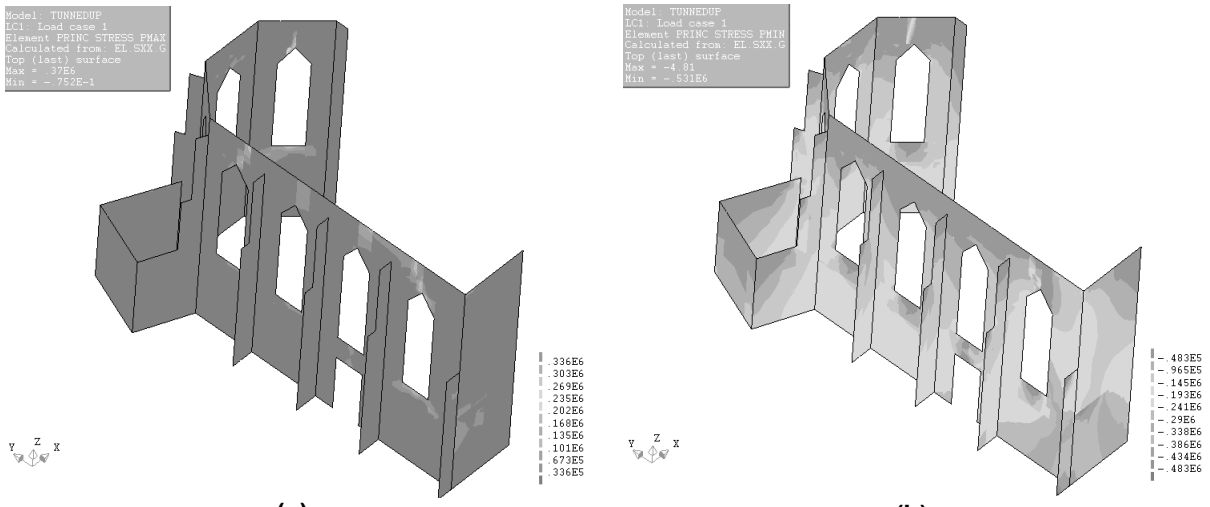

(a) **(b)**

Figure 5.1. Maximum (a) and minimum (b) principal stresses of model MODTRIAL2 after calibration

After the linear static analysis, a modal response analysis was performed in order to determine the eigenfrequencies and the mode shapes displacements. The deformed shapes for the selected numerical modes are shown in Figure 5.2. The results in terms of frequencies and mode shapes are shown in Table 5.5, as well as their comparison with experimental data in terms of average frequency estimation and MAC values.

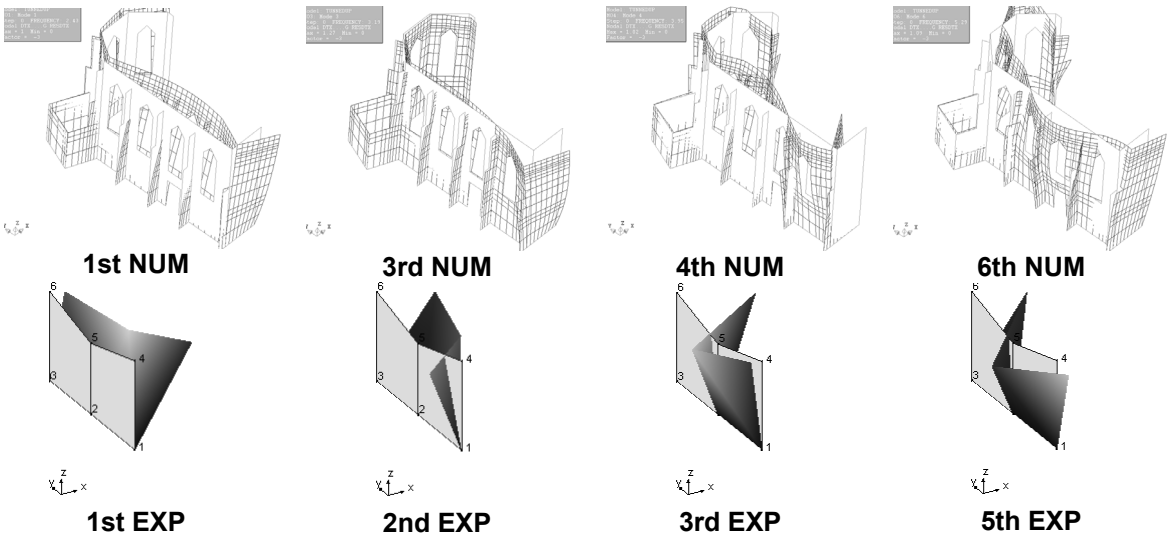

Figure 5.2. Qualitative comparison between model MODTRIAL2 (After calibration) and experimental mode shapes

Mode Shape	f_{EXP} [Hz]	f_{NUM} [Hz]	Error [%]	MAC [%]	Mass part. in X [%]	Mass part. in Y [%]
1^{st}_{NUM}-1^{st}_{EXP}	2.57	2.43	-5.45	94.2	32.49	0.01
3^{rd}_{NUM}-2^{nd}_{EXP}	3.14	3.19	1.59	49.8	5.47	12.34
4^{th}_{NUM}-3^{rd}_{EXP}	3.95	3.95	0.00	40.8	1.21	7.83
6^{th}_{NUM}-5^{th}_{EXP}	5.26	5.29	0.57	76.5	2.96	3.41

Table 5.5. Comparison between experimental and numerical results in model MODTRIAL2 after calibration

The obtained averages of the error in frequency estimation are very low; all of them are below 5%. The MAC values have a different distribution: for the 1st mode, the MAC is very good because it is higher than 90%, for the 5th mode the MAC value is acceptable because is near 80%. But the MAC values for modes 2nd and 3rd are still low. While they improve with respect to the model without calibration, ideally more changes in the model should be made in order to increase these values up to more acceptable levels.

5.4 CALIBRATION OF MODEL MODTRIAL3-D

The selected variables to be calibrated in this model were seven (N=7), $X_k^B\left(k=1,2,...,N\right)$, and their initial values are shown in Table 5.6. These are: (1) the material 1 elastic modulus, (2) the material 2 elastic modulus, (3) the material 3 elastic modulus, (4) the material 4 elastic modulus, (5) the thickness of damaged area in the North façade, (6) the thickness of damaged area in the Apse and (7) the thickness of damaged area in the West façade. Also the upper and lower bounds for each variable are given, which are the same as in the previous model.

The values of the obtained numerical frequencies using the fifteen different combinations of Equation 5.2 are shown in Table 5.7, and the obtained values of the calibration constants are shown in Table 5.8.

Variable	Parameter	Base Value	Lower Bound	Upper Bound	Unit
1	Elastic Modulus (Mat 1)	3780	2646	4914	MPa
2	Elastic Modulus (Mat 2)	1050	735	1365	MPa
3	Elastic Modulus (Mat 3)	2080	1456	2704	MPa
4	Elastic Modulus (Mat 4)	1590	1113	2067	MPa
5	Thickness (Damage in N-façade)	0.30	0.10	0.50	m
6	Thickness (Damage in Apse)	0.30	0.10	0.50	m
7	Thickness (Damage in W- façade)	0.60	0.20	1.00	m

Table 5.6. Base, upper and lower values of the calibration variables of model MODTRIAL3-D

Variable combination	F1 [Hz]	F2 [Hz]	F3 [Hz]	F5 [Hz]
(1b, 2b, 3b, 4b, 5b, 6b, 7b)	2.45	3.69	4.15	5.75
(1lower, 2b, 3b, 4b, 5b, 6b, 7b)	2.15	3.10	3.55	4.94
(1upper, 2b, 3b, 4b, 5b, 6b, 7b)	2.71	4.20	4.67	6.43
(1b, 2lower, 3b, 4b, 5b, 6b, 7b)	2.43	3.69	4.14	5.71
(1b, 2upper, 3b, 4b, 5b, 6b, 7b)	2.47	3.70	4.16	5.78
(1b, 2b, 3lower, 4b, 5b, 6b, 7b)	2.40	3.69	4.13	5.71
(1b, 2b, 3upper, 4b, 5b, 6b, 7b)	2.52	3.70	4.19	5.84
(1b, 2b, 3b, 4lower, 5b, 6b, 7b)	2.43	3.69	4.11	5.67
(1b, 2b, 3b, 4upper, 5b, 6b, 7b)	2.47	3.70	4.18	5.81
(1b, 2b, 3b, 4b, 5lower, 6b, 7b)	2.38	3.64	3.88	5.54
(1b, 2b, 3b, 4b, 5upper, 6b, 7b)	2.49	3.72	4.39	5.87
(1b, 2b, 3b, 4b, 5b, 6lower, 7b)	2.45	3.69	4.07	5.53
(1b, 2b, 3b, 4b, 5b, 6upper, 7b)	2.45	3.69	4.18	5.92
(1b, 2b, 3b, 4b, 5b, 6b, 7lower)	2.40	3.40	4.10	5.73
(1b, 2b, 3b, 4b, 5b, 6b,7upper)	2.52	3.90	4.26	5.77

Table 5.7. Frequency values for the different combination of variables in the calibration of model MODTRIAL3-D (b: base value, lower: lower bound and upper: upper bound)

Constant	F1	F2	F3	F5
C_i	7.256E-01	1.046E+00	9.488E-01	1.526E+00
A_{i1}	3.823E-01	7.365E-01	7.503E-01	1.026E+00
B_{i1}	-1.785E-02	-3.317E-02	-3.390E-02	-4.880E-02
A_{i2}	5.155E-01	5.148E-02	2.482E-01	8.342E-01
B_{i2}	-4.768E-01	-4.097E-02	-1.981E-01	-8.265E-01
A_{i3}	1.842E-01	-7.727E-02	-1.193E-01	-6.817E-01
B_{i3}	1.653E-01	1.047E-01	2.883E-01	9.605E-01
A_{i4}	3.734E-01	6.540E-02	5.489E-01	8.810E-01
B_{i4}	-2.447E-01	-3.641E-02	-3.161E-01	-3.985E-01
A_{i5}	2.885E-01	2.030E-01	1.274E+00	8.157E-01
B_{i5}	2.463E-01	1.575E-01	1.725E-01	5.794E-01
A_{i6}	4.150E-02	2.750E-02	6.545E-01	1.308E+00
B_{i6}	-5.000E-02	-2.750E-02	-6.287E-01	-5.562E-01
A_{i7}	-4.950E-02	-4.766E-01	1.250E-03	-3.300E-02
B_{i7}	1.669E-01	9.169E-01	1.734E-01	7.687E-02

Table 5.8. Calibration constants for model MODTRIAL3-D

After the application of the optimization method exposed by (Douglas & Reid, 1982) to the calibration constants, the numerical frequencies were estimated and the objective function (see Equation 5.3) was minimized using (GAMS, 1998). The weighing factors shown in Equation 5.4 were all kept as one. After the optimization process the minimum value of the objective function was 0.033 and the updated parameters are shown in Table 5.9 marked with (*), among with the other material and physical properties used to analyze the model MODTRIAL3-D after calibration process.

Parameter	**Unit**	**Value**
Thickness of North façade	Meter [m]	1.02
Thickness of damage (N-façade)	Meter [m]	0.50*
Thickness of Apse & Sacristy	Meter [m]	1.02
Thickness of damage (Apse)	Meter [m]	0.10*
Thickness of West façade	Meter [m]	1.29
Thickness of damage (W-façade)	Meter [m]	0.715*
Thickness of Buttresses	Meter [m]	0.95
Thickness of Top wall (North and Apse)	Meter [m]	1.02
Thickness of Top wall (West)	Meter [m]	1.29
Thickness of Blind arches walls	Meter [m]	0.60
Thickness of Blind arch wall (West)	Meter [m]	1.02
Material 1		
Unit weight of masonry	Kilo Newton / Meter³ [KN/m³]	16
Elastic Modulus	Mega Pascal [MPa]	2831*
Poisson's ratio	Dimensionless [-]	0.2
Material 2		
Unit weight of masonry	Kilo Newton / Meter³ [KN/m³]	16
Elastic Modulus	Mega Pascal [MPa]	1364.58*
Poisson's ratio	Dimensionless [-]	0.2

Material 3		
Unit weight of masonry	Kilo Newton / Meter³ [KN/m³]	16
Elastic Modulus	Mega Pascal [MPa]	2702.70*
Poisson's ratio	Dimensionless [-]	0.2
Material 4		
Unit weight of masonry	Kilo Newton / Meter³ [KN/m³]	16
Elastic Modulus	Mega Pascal [MPa]	2067.66*
Poisson's ratio	Dimensionless [-]	0.2
Additional mass of the tower	Kilogram [Kg]	52632
Additional mass of the vault	Kilogram [Kg]	32752

Table 5.9. Material and physical properties for model MODTRIAL3-D after model calibration

The obtained results for the calibrated variables shown that the elastic modulus of material 1 was reduced 25.10% from its base value, the elastic modulus of material 2 was increased 30% from its base value reaching the upper bound, the elastic modulus of material 3 was increased 29.9% from its base value, the elastic modulus of material 4 was increased 30% from its base value reaching the upper bound, the thickness representing damaged elements in the North façade was increased 66.67% reaching its upper bound, the thickness representing the damaged area in the Apse was decreased 66.67% from its base value reaching its lower bound and the thickness representing the damaged region of the West façade was increased 19.17%. In this case, five of the seven variables reached the limit bounds, meaning that they should be increased in order to obtain better results, but the changes of the percentage of variation may induce some meaningless values according to engineering judgment.

After performing the optimization process, a linear static analysis was performed in the model and the results are reported in Figure 5.3. The pure tensile stress distribution among the structure is shown in Figure 5.3-a, and the peak value is of 0.28 MPa, and it is located below the apse windows and in the upper part of the North façade, where the damage is concentrated according to (Lourenço & Ramos, 2008). Regarding the compressive stress distribution, it is shown in Figure 5.3-b, and the peak values are shown at the base of the West façade, just below the concentrated mass that represent the tower. The values at the base of the other walls of the structure are of about 0.24 MPa which is expected for the structural configuration and the density of the material.

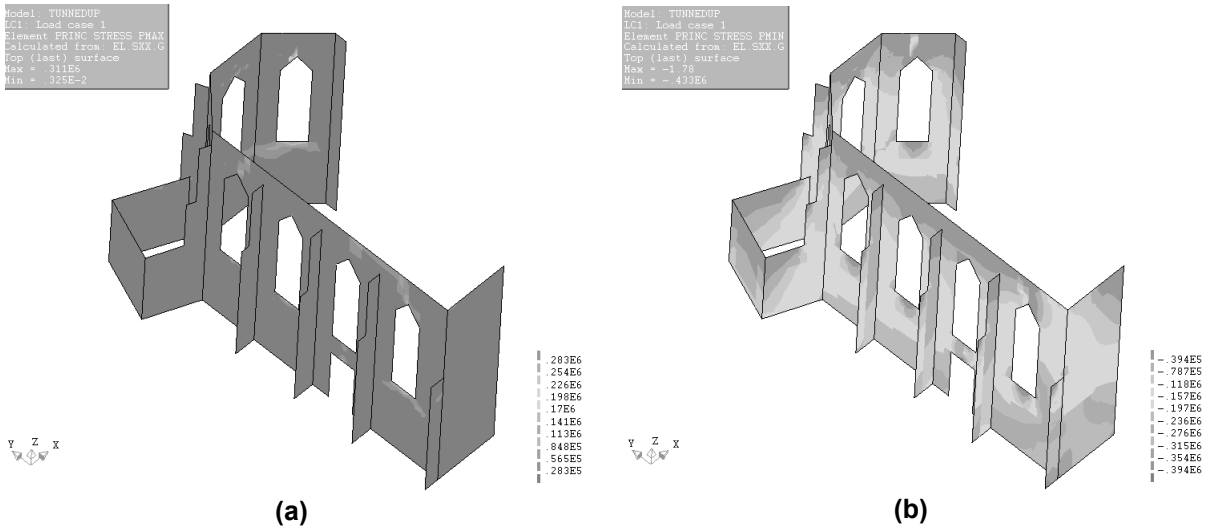

Figure 5.3. Maximum (a) and minimum (b) principal stresses of model MODTRIAL3-D after calibration

A modal response analysis was carried out in the calibrated model and the results in terms of frequencies and mode shapes as shown in Table 5.10. The selected structural modes in the calibration process are shown in terms of mode shapes, and they are qualitatively compare with the experimental mode shapes in Figure 5.4.

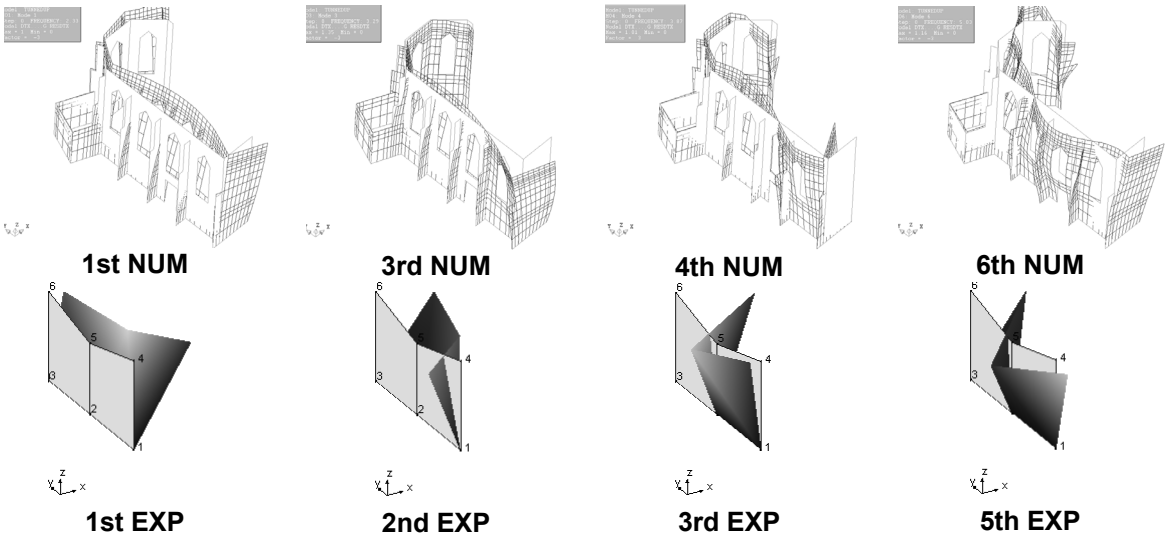

Figure 5.4. Qualitative comparison between model MODTRIAL3-D after calibration and experimental mode shapes

Mode Shape	f_{EXP} [Hz]	f_{NUM} [Hz]	Error [%]	MAC [%]	Mass part. in X [%]	Mass part. in Y [%]
1^{st}_{NUM}-1^{st}_{EXP}	2.57	2.33	-9.34	90.0	32.66	0.39
3^{rd}_{NUM}-2^{nd}_{EXP}	3.14	3.29	4.78	49.8	4.56	10.64
4^{th}_{NUM}-3^{rd}_{EXP}	3.95	3.87	-2.03	39.7	0.62	12.25
6^{th}_{NUM}-5^{th}_{EXP}	5.26	5.03	-4.37	74.5	3.06	4.66

Table 5.10. Comparison between experimental and numerical results in model MODTRIAL3-D after calibration

The results obtained of the modal response analysis in terms of frequencies and mode shapes are shown in Table 5.10, where the frequency estimation error was calculated and the MAC values were computed for each selected mode. After the calibration process, the results in terms of frequency estimation error show that the estimation for all the modes is below 10%, which is much higher than the frequency estimation error of model MODTRIAL2 after calibration. In terms of MAC values, only the 1st mode value shows a good relation because is 90%, for 5th mode the value is acceptable because is near the 80% but the results for the 2nd and the 3rd modes are not good because they remained lower than 50%, meaning that still some improvements should be done to the model in order to obtain better results.

5.5 COMPARISSON BETWEEN CALIBRATED MODELS

After making the calibration of the two selected models, a comparison is needed to determine how much was the improvement or aggravation of the calibrated models, and which model is representing more accurate the real structure. This comparison was performed in terms of the modal data; the eigenfrequencies and the mode shape displacements, by means of the frequency estimation error and the MAC values between the mode shapes; the results are reported in Table 5.11.

According to the results reported in Table 5.11, after the calibration of model MODTRIAL2, the average frequency estimation error decreased more than 11% until reaching the value of 1.9%. Equaly the frequency estimation error for each structural mode individually decreased and all of them are below 5% difference. Regarding the mode shapes information in terms of MAC values, there was an increase of 1% of the average MAC after the calibration process, which is not so significant, because almost all the values remained the same as before the calibration process except for the 2nd mode which had an important improvement of the MAC value because increased almost 6%.

The results for model MODTRIAL3-D before and after the calibration process are also reported in Table 5.11. For this case the average frequency estimation error was decreased by 4% obtaining an average error of 5.13%, but not all the frequencies individually decreased, and their error estimation values after calibration are mostly above 4% except for 4th mode which error is 2%. Regarding the

mode shapes data in terms of average MAC value, this value remained almost the same because an increase of 5% of the 3rd mode was compensated with a decreased of 5% of the 5th mode value.

Model	Mode Shape	f estimation Error [%]	f average Error [%]	MAC [%]	Average MAC [%]
MODTRIAL2 (Before updating)	1^{st}_{NUM}-1^{st}_{EXP}	6.2	13.18	94.1	64.05
	3^{rd}_{NUM}-2^{nd}_{EXP}	18.5		44.2	
	4^{th}_{NUM}-3^{rd}_{EXP}	10.9		39.1	
	6^{th}_{NUM}-5^{th}_{EXP}	17.1		78.8	
MODTRIAL2 (After updating)	1^{st}_{NUM}-1^{st}_{EXP}	-5.45	1.90	94.2	65.32
	3^{rd}_{NUM}-2^{nd}_{EXP}	1.59		49.8	
	4^{th}_{NUM}-3^{rd}_{EXP}	0.00		40.8	
	6^{th}_{NUM}-5^{th}_{EXP}	0.57		76.5	
MODTRIAL3-D (Before updating)	1^{st}_{NUM}-1^{st}_{EXP}	-4.67	9.14	90.6	63.78
	3^{rd}_{NUM}-2^{nd}_{EXP}	17.52		44.2	
	4^{th}_{NUM}-3^{rd}_{EXP}	5.06		41.2	
	6^{th}_{NUM}-5^{th}_{EXP}	9.32		79.1	
MODTRIAL3-D (After updating)	1^{st}_{NUM}-1^{st}_{EXP}	-9.34	5.13	90.0	63.50
	3^{rd}_{NUM}-2^{nd}_{EXP}	4.78		49.8	
	4^{th}_{NUM}-3^{rd}_{EXP}	-2.03		39.7	
	6^{th}_{NUM}-5^{th}_{EXP}	-4.37		74.5	

Table 5.11. Comparison between the different models in terms of frequency estimation error and mode shape correlation (MAC)

Finally making the comparison between the two models after calibration, their modal parameters were improved in terms of average values, but the model that has more improvement in terms of frequencies and MAC values was MODTRIAL2, despite the fact that it is simple when compared to MODTRIAL3-D; it only has been modeled with one material property for masonry.

In Figure 5.5 a graphical comparison between the mode shapes displacements in both models after the calibration process is shown. The amplitude of the displacements is very similar for each mode in both models because they have similar MAC values except for the 1st mode. Hereby, the model MODTRIAL2 was chosen to perform further non-linear analyses, despite the fact that MAC values are similar in both models. In terms of frequencies this model present numerical results closer to the experimental data.

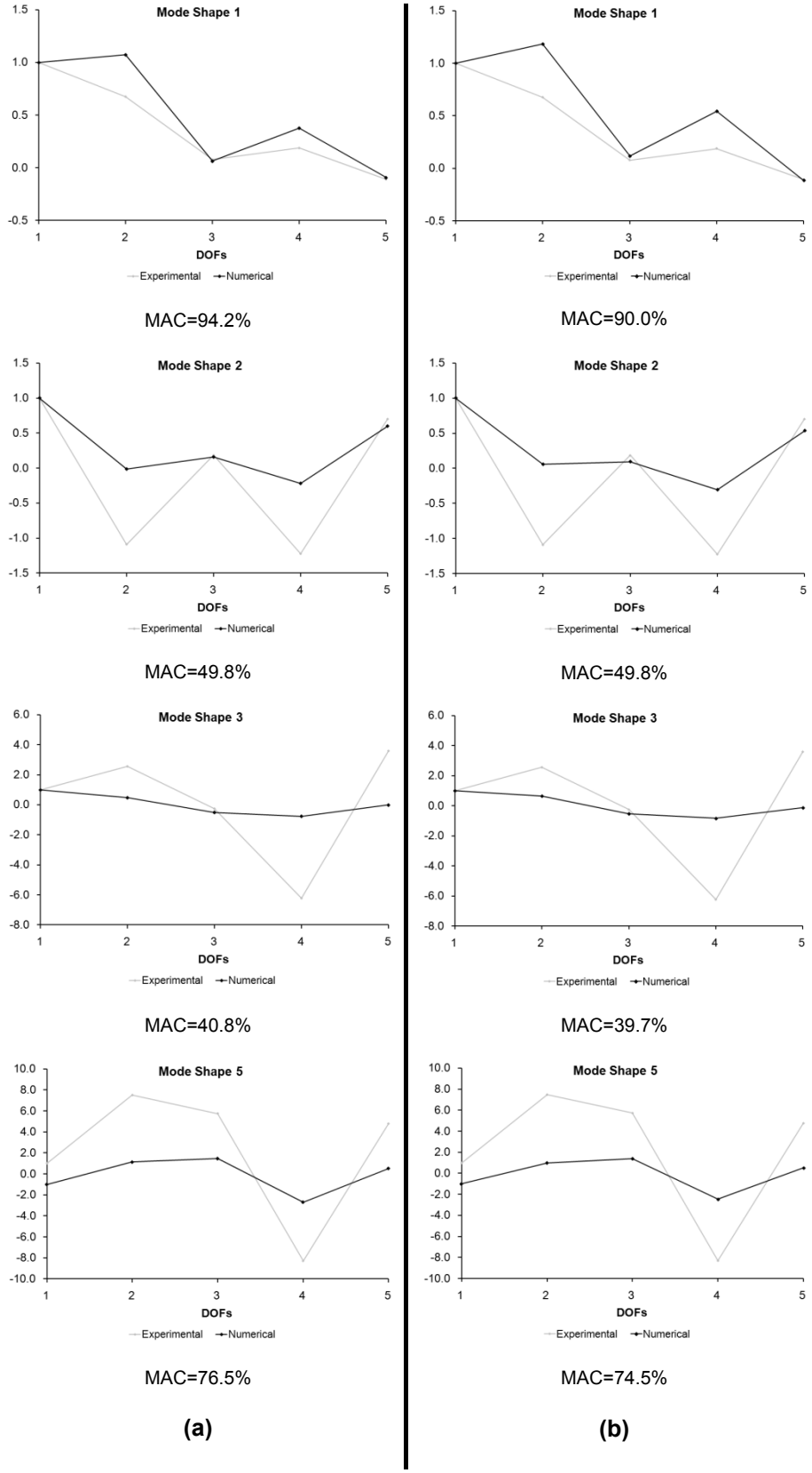

Figure 5.5. Graphical comparison of mode shapes displacements between the experimental and numerical data for models MODTRIAL2 (a) and MODTRIAL3-D (b) after calibration process

6. NON LINEAR STATIC (PUSHOVER) ANALYSES

6.1 INTRODUCTION

Non-linear static analysis with horizontal forces adopted to represent the seismic action, also known as pushover analysis, is an alternative method of analysis to estimate the seismic response of the structure. It is carried out under conditions of constant gravity loads and monotonically increasing horizontal loads that should have at least two vertical distributions: (1) An uniform pattern based on lateral forces that are proportional to the mass regardless their height distribution among the structure and (2) a modal pattern proportional to lateral forces consistent with the lateral force distribution determined in the modal response analysis (EN 1998-1, 2004).

Pushover analysis can be applied in order to verify the structural performance of existing buildings by means of the verification of base shear ratios and the estimation of expected plastic mechanism with its damage distribution. Hereby this analysis was adopted to analyze the actual condition state of the church, in terms of damage distribution and its resistance to lateral actions such as earthquakes. In order to validate the results of those analyses, the damage distribution was taken into account in terms of the maximum principal strains (Strains cause by pure tensile stresses). In order to validate the results in terms of over base shear ratios, a load coefficient was defined by means of Equation 6.1, which relates the total horizontal forces that are applied to the structure in each load increment and the total vertical loads (Its own weight and the weight of the additional masses) of the structure; during the analyses the summation of the applied horizontal forces was extracted from the reactions of the fixed nodes at the base of the structure (Mendes & Lourenço, 2008).

$$\alpha = \frac{\sum F_{Horizontal}}{\sum F_{Vertical}} \qquad 6.1$$

Where:

$\sum F_{Horizontal}$: is the summation of the acting horizontal forces

$\sum F_{Vertical}$: is the summation of the acting vertical forces

In order to evaluate the worst scenario for the structure when is subjected to horizontal loads, two different load patterns were defined according to (EN 1998-1, 2004). Also different directions of the load application were taken into account due to the planar irregularity of the structure. According to (EN 1998-1, 2004), the structures that do not comply with the regularity in plan criteria should be analyzed applying one configuration of lateral loads per direction, one at a time. This means that the seismic action shall be applied in both, positive and negative directions of global axes, with the orientation among the structure is shown in Figure 6.1-a.

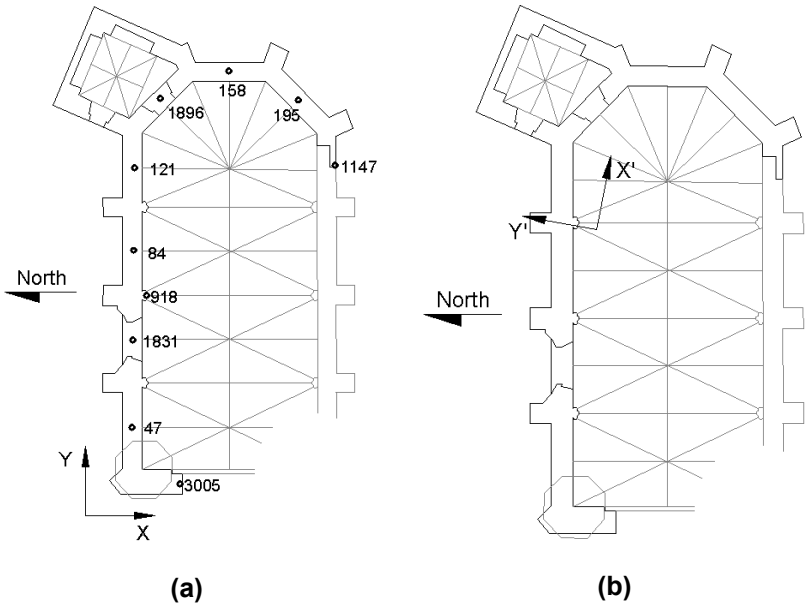

Figure 6.1. (a) Orientation of the axes in global direction and selected top nodes to measure displacement and (b) plan view of principal axes orientation located in the center of mass

It is important to highlight the in plan irregularity of the structure. For this reason, different pushover analyses were performed all of them varying the direction of the load application. First, the "uniform" load pattern proportional to the mass was used to perform four different pushover analyses, two per each global direction (X and Y), one in the positive direction and another in the negative direction. Then a second load pattern was used, the "modal" pattern, and two pushover analyses were performed, each of them is proportional to the first mode with the highest mass participation factor in each global direction. Finally, four pushover analyses were performed in the principal axes directions shown in Figure 6.1-b; one in the positive direction and one in the negative direction per each of the principal axes directions (X' and Y').

At the end, the obtained results were compared in terms of damage and load coefficient ratio with the results of similar collapse mechanisms obtained from the kinematic analyses shown in Chapter 3. Finally, all the results were compared in order to determine the maximum seismic effects in the structure and the worst scenario for damage.

The non linearity of the material was always taken into account following the material constitutive law shown later in this chapter. Also, the geometrical non linearity was taken into account in this problem.

The regular Newton-Raphson method was used to assess the equilibrium of the system of equations with the equilibrium and compatibility conditions, except that the stiffness matrix is variable; the convergence of the analysis was defined in terms of energy with a tolerance of 10^{-3}. The arc-length method was used to control the solution of the system of non-linear equations.

6.2 DEFINITION OF MASONRY CONSITUTIVE LAW AND NON-LINEAR MATERIAL PROPERTIES

The non-linear behavior of the masonry was modeled by the adoption of a constitutive model based on total strain, called Total Strain Fixed Crack model. This model describes the tensile and compressive behavior of the masonry with one stress-strain relationship (DIANA, 2008). In this model the cracks are fixed according to the directions of the principal strains vector, and remain invariable during the loading process of the structure. According to (Mendes & Lourenço, 2008) the selection of the constitutive law should be done by making a balance between the accuracy, possibility to provide reasonable material parameters and computer cost of the calculation process. This model was selected because it provides good stability in the opening crack control and moderate computer cost.

Different strain-stress relationships were defined for tensile and compressive behavior of the material. It is known that the masonry has a linear hardening behavior up to its tensile strength, and the post peak tensile behavior is exponential softening (Roca & Lourenço, 2008-2009) (see Figure 6.2-a). Regarding its compressive behavior a model with parabolic hardening up to its compressive strength was adopted, followed by compressive post peak behavior idealized with a parabolic softening function (see Figure 6.2-b). The post-cracked shear behavior was modeled using a retention factor of its linear behavior (see Figure 6.2-c) which reduces its shear capacity according to Equation 6.2.

$$G^{cr} = \beta \cdot G \qquad 6.2$$

Where:

- β: is the retention factor which varies between 1 and 0
- G: is shear modulus of the uncracked material

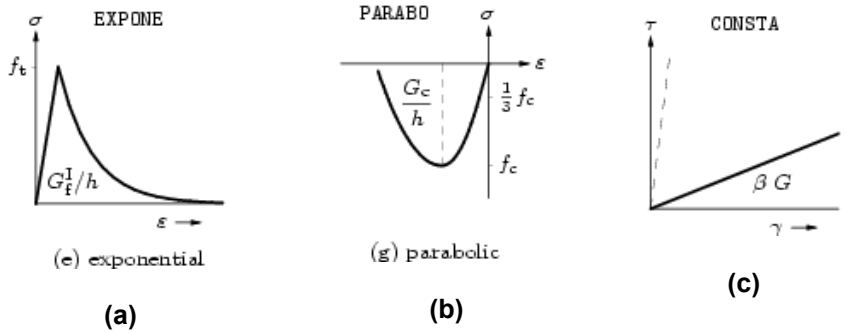

Figure 6.2. (a) Tensile behavior, (b) compressive behavior and (c) shear behavior adopted for masonry (DIANA, 2008)

Finally, the crack bandwidth of each element was defined according to the Equation 6.3, as a function of the area of each element.

$$h = \sqrt{A} \qquad 6.3$$

Where:

A: is the area of each Finite Element

After defining the constitutive law of the material and its compressive and tensile behavior, non-linear properties of the material were defined following the recommendations shown by (Roca & Lourenço, 2008-2009). After the calibration of the selected model (MODTRIAL2), its material and physical properties were determined and they are shown in Table 5.4, from this table, the Elastic Modulus was used to estimate the other parameters which are needed for the Non-linear analyses. The masonry compressive strength was calculated according to the Equation 6.4 and the compressive fracture energy was calculated using the expression shown in Equation 6.5, where the ductility index is equal to 1.6 mm; the adopted values are shown in Table 6.1.

$$f_c = \frac{E}{500} \qquad 6.4$$

Where:

E: is the Elastic Modulus of the material

$$G_c = d \cdot f_c \qquad 6.5$$

Where:

d: is the ductility index

The masonry tensile strength was adopted as the 0.6% of its compressive strength, and the Tensile Fracture Energy used was 50 N/m; these results were adopted according to the results of the linear static analysis and preliminary non-linear analyses following the recommendations of (Roca & Lourenço, 2008-2009) and the experience reported in (Mendes & Lourenço, 2008). The whole set of non-linear material properties used in the pushover and dynamic analyses are shown in Table 6.1.

Parameter	Symbol	Unit	Value
Tensile strength	$[f_t]$	Mega Pascal [MPa]	0.300
Tensile Fracture Energy	$[G_f^I]$	Newton/ meter [N/m]	50
Compressive strength	$[f_c]$	Mega Pascal [MPa]	6.034
Compressive Fracture Energy	$[G_c]$	Newton/ meter [N/m]	9654
Shear Retention Factor	$[\beta]$	Dimensionless [---]	0.01

Table 6.1. Non linear properties used in the pushover and dynamic analyses

6.3 INTEGRATION SCHEME

In order to find the stiffness matrix of the element (see Equation 6.6) it is necessary to apply either an analytical integration method or a numerical one. In most of the cases, it is difficult to apply analytical solutions to find the integrals for the elements, therefore is necessary to apply numerical integration methods which are based on the integration of a function in a number of specific points, so called integration points. The function values are weighted and summed in those points to obtain the value of the integral; the weight function depends on the integration method which usually is Gauss integration method (DIANA, 2008).

$$K_e = \int_{V_e} B^T DB dV = \iiint_{-1}^{+1} B^T DB|J| d\xi \, d\eta \, d\zeta \qquad 6.6$$

Where:

B: is the matrix with the derivative of shape functions

D: is the material stiffness matrix

$|J|$: is the Jacobian matrix

$d\xi, d\eta, d\zeta$: are the differentials of each parametrical coordinate

For linear elastic problems, some high order terms of the polynomial can be ignored safely and it is showed that the position of Gauss integration points coincide with the optimal stress points (DIANA, 2008). However for non-linear problems, the process is complex and there should also define integration points through the thickness of the elements when tridimensional shell elements are used in the analysis. Following the recommendations shown in (Chiumenti & Cervera, 2008-2009) for fulfill the Rank sufficiency for numerically integrated finite elements, which establishes that for 6-node triangular elements 3 mid-side nodes should be used and for 8-node quadrilateral elements an arrangement of 3x3 in side nodes should be used, the in-plane integration scheme was defined for both, triangular (CT30S) and quadrilateral (CQ40S) and they are shown in Figure 6.3-a and Figure 6.3-b. The thickness integration scheme was also defined looking for avoid linear variation in the bending diagram through the thickness and looking for a reasonable computational cost for further non-linear analyses; therefore 5 integration points were defined for both elements (CT30S and CQ40S) and their integration scheme is shown in Figure 6.3-c. It is important to highlight that according to (DIANA, 2008), triangular and quadrilateral elements should be integrated in-plane using Gauss method and in thickness direction using Simpson method.

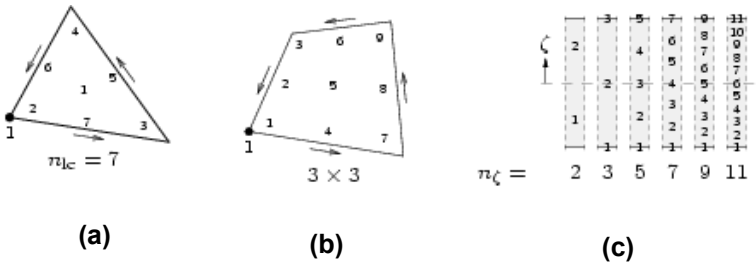

Figure 6.3. Integration Scheme: (a) in-plane for triangular element CT30S, (b) in-plane for quadrilateral element CQ40S and (c) in thickness direction for both element types (DIANA, 2008)

6.4 DESCRIPTION OF ITERATION METHOD

If the non linear analysis only uses incremental steps for the applied load, the solution may be inaccurate and drift to the corresponding truncation error, hereby the great advantage of the implicit procedure is that despite the fact that the allowable load step size is higher, the errors that occur during the calculation process are reduced successively in an iterative process (Chiumenti, Cervera, Kabele, & Roca, 2008-2009). The Regular Newton-Raphson method is an iterative method in which the total displacement increment is adapted iteratively according to Equation 6.7 until the equilibrium is reached with a prescribe tolerance.

$$\Delta u_{i+1} = \Delta u_i + \partial u_{i+1} \qquad 6.7$$

Where:

Δu_i: is the *i-th* displacement increment

Δu_{i+1}: is the *i+1-th* iterative increment

The iterative increments are calculated by means of a stiffness matrix that represents the relation between the force vector and the displacement vector (Equation 6.8). The stiffness matrix is evaluated every iteration as it is shown in Figure 6.4, and it represents the tangential stiffness of the structure. Compared with other methods, it has the advantage of convergence with lesser iterations, but each iteration is time consuming.

$$\Delta\partial u_i = K_i^{-1} \cdot g_i \qquad 6.8$$

Where:

K_i^{-1}: is the inverse of the stiffness matrix used in *i-th* iteration

g_i: is the out of balance force vector at the start of *i-th* iteration

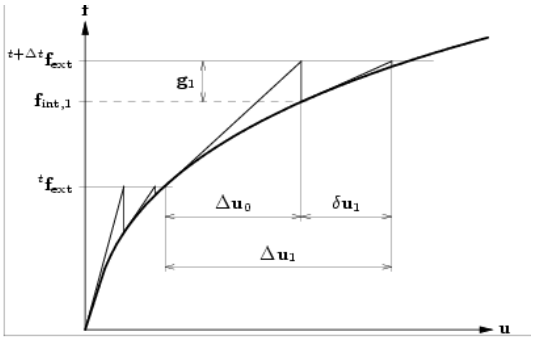

Figure 6.4. Scheme of Regular Newton-Raphson iteration method (DIANA, 2008)

Simultaneously with the Regular Newton-Raphson method, the Arc-length method was used to determine the snap-through behavior of the Load-Displacement relation in the structure (Chiumenti, Cervera, Kabele, & Roca, 2008-2009). This method overcomes the problem of predicting a large displacement for a given force increment.

6.5 PUSHOVER ANALYSES PROPORTIONAL TO MASS IN GLOBAL DIRECTIONS

6.5.1 Pushover analysis in X global direction

For this analysis, a horizontal acceleration was applied by small increments so that the horizontal load acting on the elements was increased proportional to each element mass; the used load direction is shown in Figure 6.5-b. In order to plot the capacity curve of the structure, the node that had the maximum displacement during the analysis was selected, and it is node 1831 with the location shown in Figure 6.5-c. The resultant capacity curve for this analysis is plotted in Figure 6.5-a, where a maximum load coefficient of 0.13g was reached, with highly non linear behavior exhibited in the structure by the saw-tooth diagram. This phenomenon is possibly due to the combination of using a

relatively coarse mesh in the damaged regions, the number of integration points through the thickness and the opening process of several cracks (Softening behavior); besides numerical problems, this phenomenon can be related with the appearance of damage patterns along loading stages as it is discuss later on. The load coefficient obtained for similar collapse mechanism previously analyzed in Section 3.3 (named as CM_N_X) is shown in the same figure and its value is 0.097g. It is clear that the resultant value obtained from limit analysis of the collapse mechanism is much smaller (38% lower) than the value obtained for the pushover analysis because the failure mechanism is 3D and not 2D as it was adopted in the simplified kinematic analysis, but it seems that the structure starts its non-linear behavior from that value on.

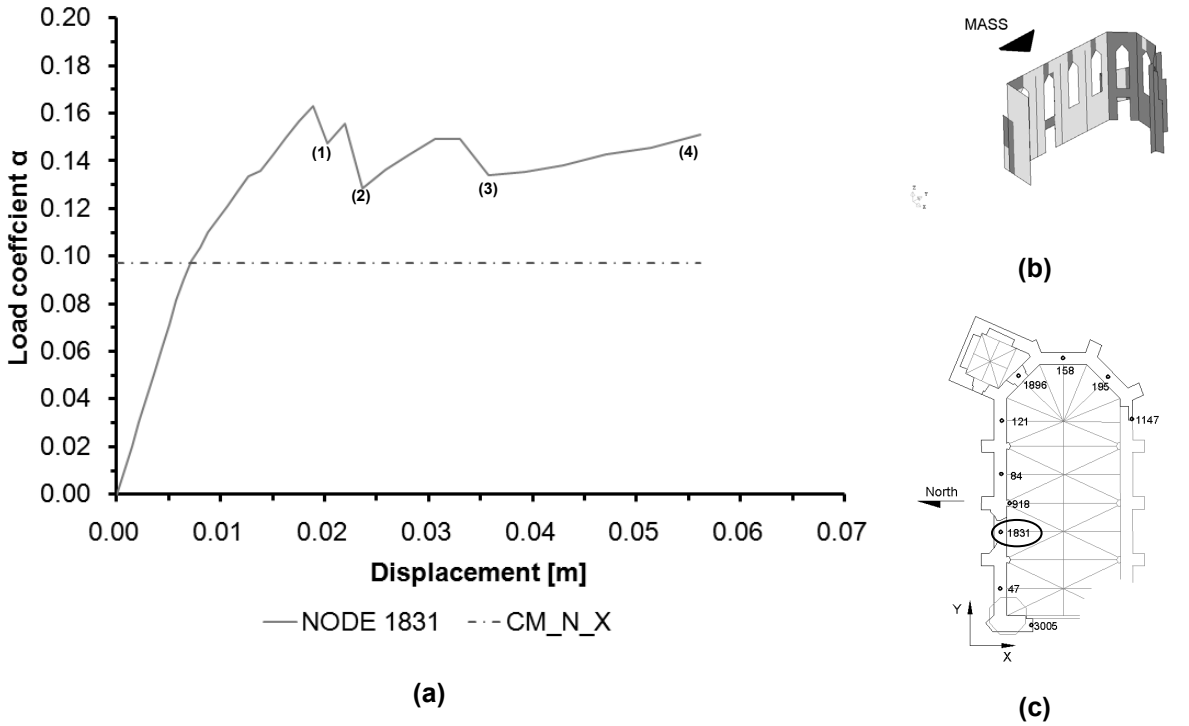

Figure 6.5. (a) Capacity curve of pushover analysis in X global direction, (b) applied load direction and (c) selected control point

For a better understanding of the non-linear behavior of the structure, four load stages were selected in the capacity curve (see Figure 6.5-a) and the principal tensile strains at those stages were plotted in the following figures (see Figure 6.6. to Figure 6.9). The principal tensile strain distribution of stage (1) is shown in Figure 6.6, where two cracks are clearly identified, one in the upper part of the center of the North façade and the other in the lower part of the buttress that connects the North façade with the Sacristy wall; also there is some damage concentration at the base of the buttresses.

After stage (1), the structure suffered an increase of its capacity reaching a small peak and then its capacity decreased; reaching stage (2). At this stage two cracks appear in the structure; one is located along the connection between the North and the West facades and the other one is located in the upper part of the North façade, above the first window to the right this (see in Figure 6.7). It is important to highlight that the strain distribution of the damaged regions in stage (1) remained constant.

After stage (2), the structure suffered an increase of its capacity and after reaching a peak, its capacity decreased up to reach stage (3), which principal tensile strain distribution is plotted in Figure 6.8. This softening branch of the behavior may be caused by the appearance of damage in the lower part of the first window to the right, and large deformation shown in the first buttress to the right possible cause by the loose of horizontal stability.

Finally the structure reaches stage (4), which principal tensile strain distribution is given in Figure 6.9. By looking to the principal tensile strain distribution calculated at the top surface it is clear that the damage in the lower part of the first window to the right has increased compared to the damage from the previous stage (number 3), and it has also increased along the connection between the North and West façades.

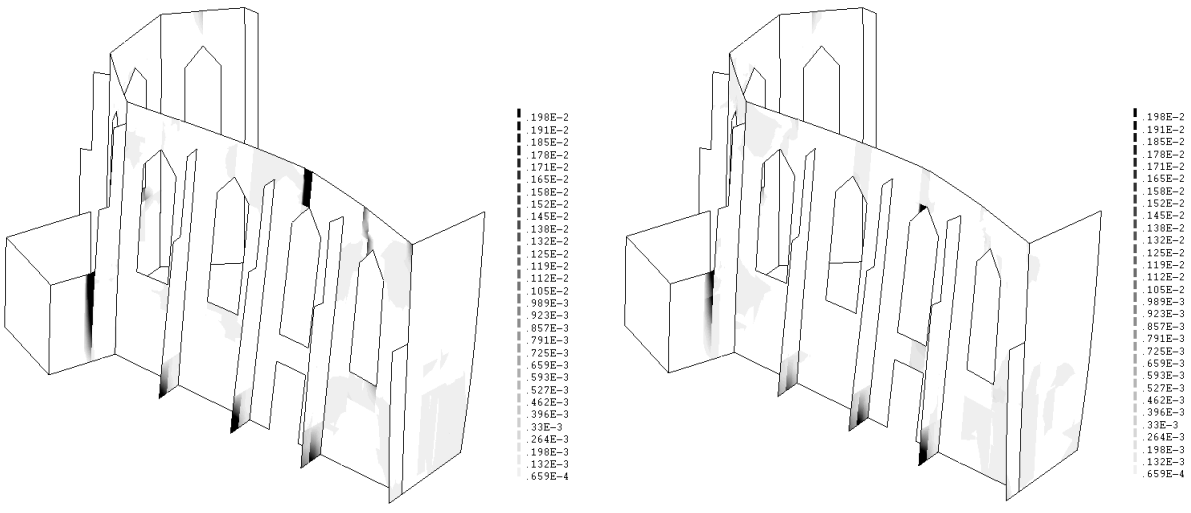

Figure 6.6. Principal tensile strains at stage (1) of the capacity curve calculated at (a) bottom and (b) top surfaces of the shell elements for pushover in X global direction

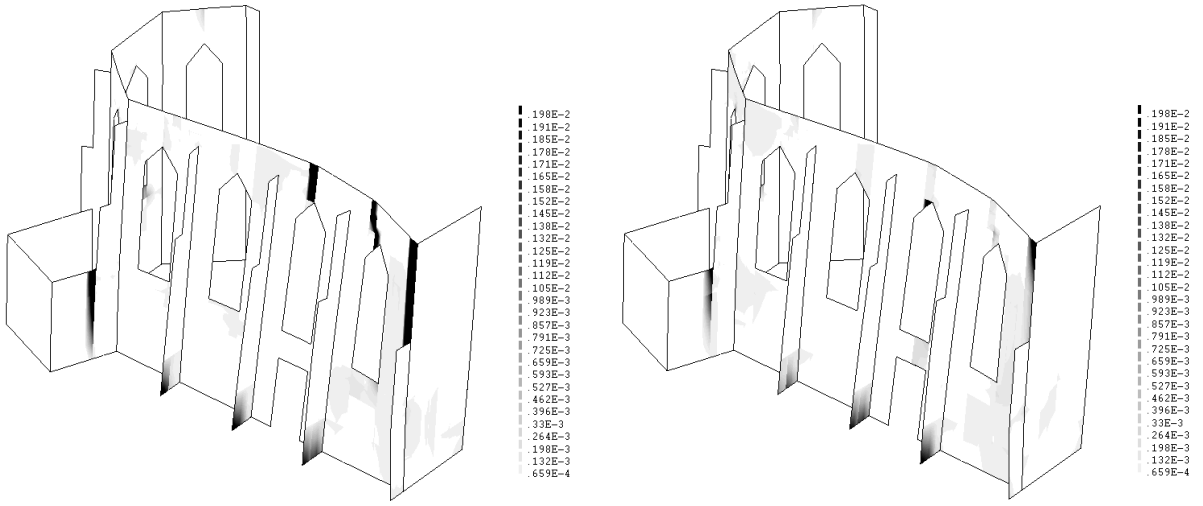

(a) **(b)**

Figure 6.7. Principal tensile strains at stage (2) of the capacity curve calculated at (a) bottom and (b) top surfaces of the shell elements for pushover in X global direction

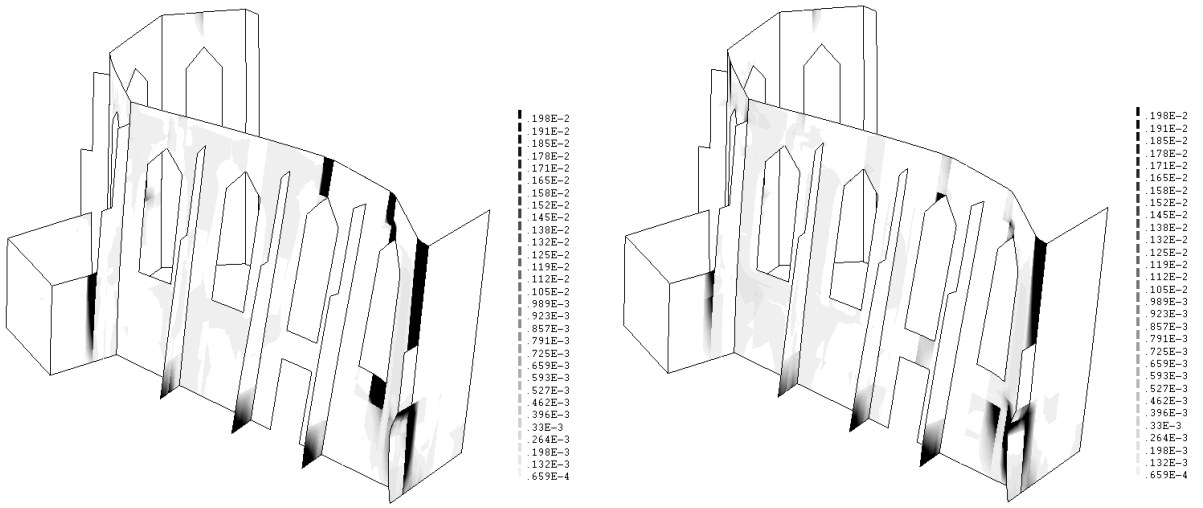

(a) **(b)**

Figure 6.8. Principal tensile strains at stage (3) of the capacity curve calculated at (a) bottom and (b) top surfaces of the shell elements for pushover in X global direction

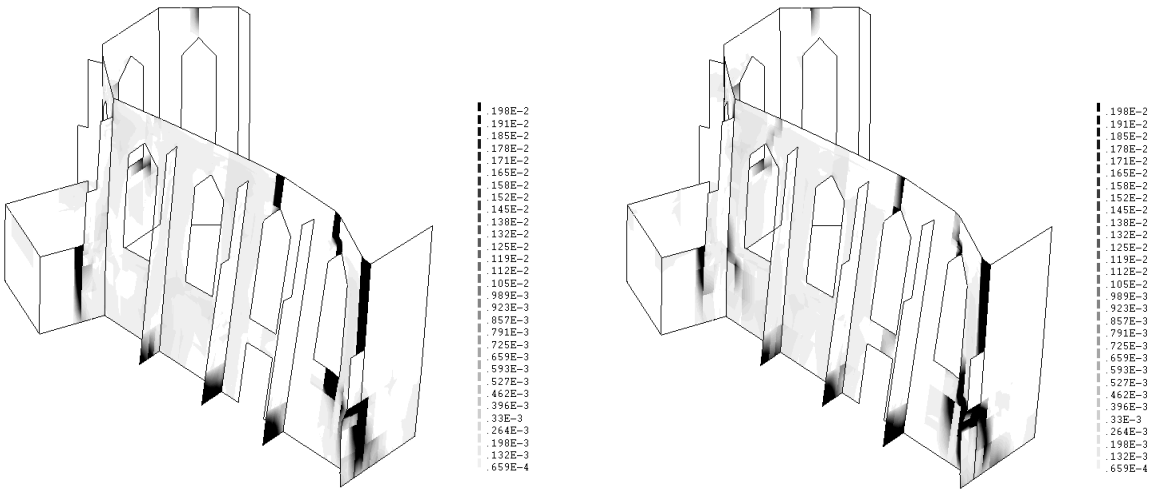

Figure 6.9. Principal tensile strains at stage (4) of the capacity curve calculated at (a) bottom and (b) top surfaces of the shell elements for pushover in X global direction

At the end of the analysis is clear that the damage pattern does not represent the plastic hinges distribution assumed in the kinematic analysis of the selected collapse mechanism (see Figure 3.9) because the assumed collapse mechanism is a 2D simplified version of the real 3D mechanism in which is present the capacity to bending of the horizontal strip.

6.5.2 Pushover analysis in –X global direction

For this analysis, the horizontal acceleration was increased by several increments in the negative X global direction, so that the horizontal force is also increased by several increments proportional to the structure's mass following the same direction of the acceleration; this load direction is shown in Figure 6.10-b. For this analysis, the node 3005 (see Figure 6.10-c) had the highest displacement after performing the whole pushover analysis in the structure, and the capacity curve at this node was plotted in Figure 6.10-a. The structure reaches a maximum load coefficient of 0.15g (small softening peak) after passes the linear range, at the end its behavior seems to stabilize. The obtained value from the pushover analysis is smaller than the load coefficient obtained for the limit analysis of collapse mechanism (named as CM_W_X), which was calculated in Section 3.2, and its value is 0.136g. Nevertheless, it seems that near this value, the non-linear behavior of the structure starts and the slope of the capacity curve changes dramatically being less stiff. For a better understanding of the developing of damage pattern among the structure during the pushover analysis, four load stages were defined in the loading path and the principal tensile strain distribution was calculated for the bottom and the top surfaces of the shell elements at these stages. The results were plotted for each point and they are shown later on this Section.

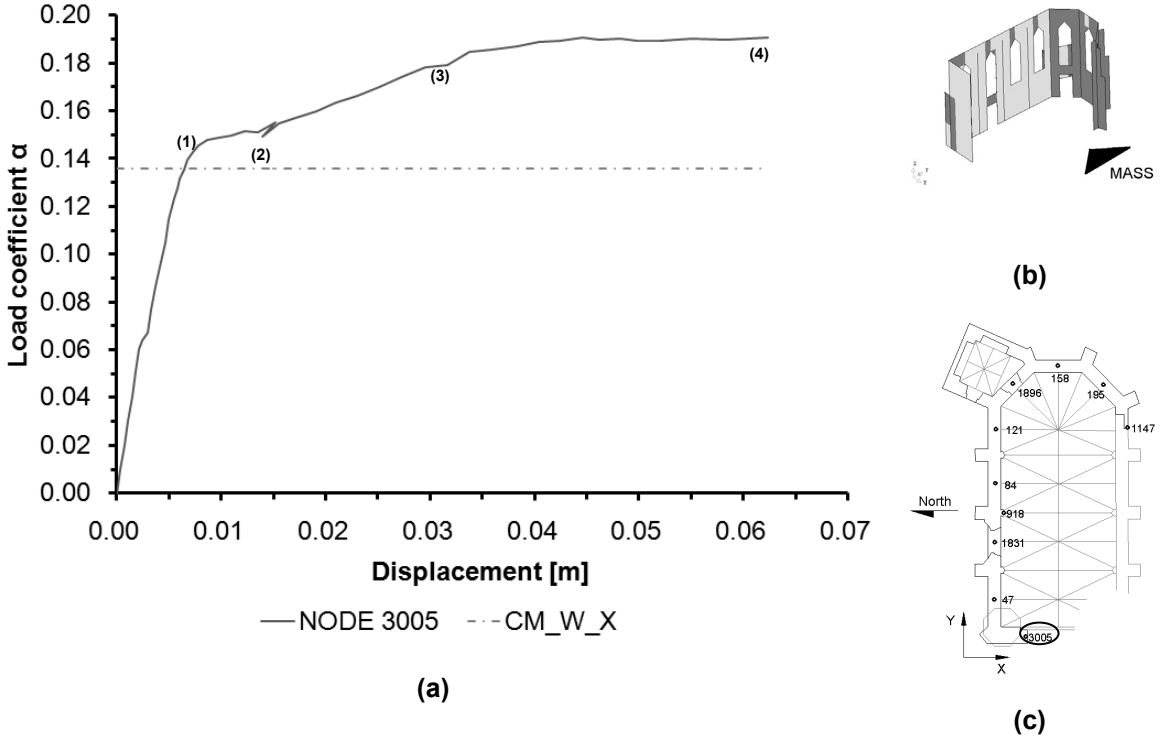

Figure 6.10. (a) Capacity curve of pushover analysis in -X global direction, (b) applied load direction and (c) selected control point

The stage (1) of the curve is located near the point where the structure's behavior is changing from linear response to non-linear one. The principal tensile strain distribution among the structure is plotted in Figure 6.11 where is clear the appearance of damage at the top of the first window to the left in the North façade. This local damage may explain the changing in the response of the structure to a non-linear response.

After stage (1), the structure has an explicit non-linear behavior and it suffers a small decrease of its capacity until it reaches stage (2), which principal tensile strain distribution is plotted in Figure 6.12. The damaged region in the lower part of the West façade is increase and also in the lower part of the first window to the right in the North façade, meanwhile, the previous damages seem to remain constant because the principal tensile strain distribution in that area remains very similar to the values reached in stage (1).

After passing stage (2), the structure increases its capacity with a smoother slope until it reaches stage (3), which principal tensile strain distribution is shown in Figure 6.13. The small decrement of capacity at stage (3) may be caused by the appearance of damage in the middle height of the first window to the left in the North façade and in the lower part of the second window to the right in the North façade. It can be seen that this damage intensity, in terms of principal tensile strain, is small compare to the other damages intensity, but it is enough to affect the structure's capacity. The

extension of previous damages seems to have increased, especially in the lower part of the West façade.

After passing stage (3) in the capacity curve, there is a small increase in the structure's capacity up to 0.19g, and then it seems to stabilize until the end of the analysis (stage 4), which principal tensile strain distribution is shown in Figure 6.14. According to the results, the damage intensity, in terms of principal tensile strains, has increased from the previous stage (number 3) and some other damages appear in along the lower part of the North façade and in the upper part of the first window to the left in the North façade.

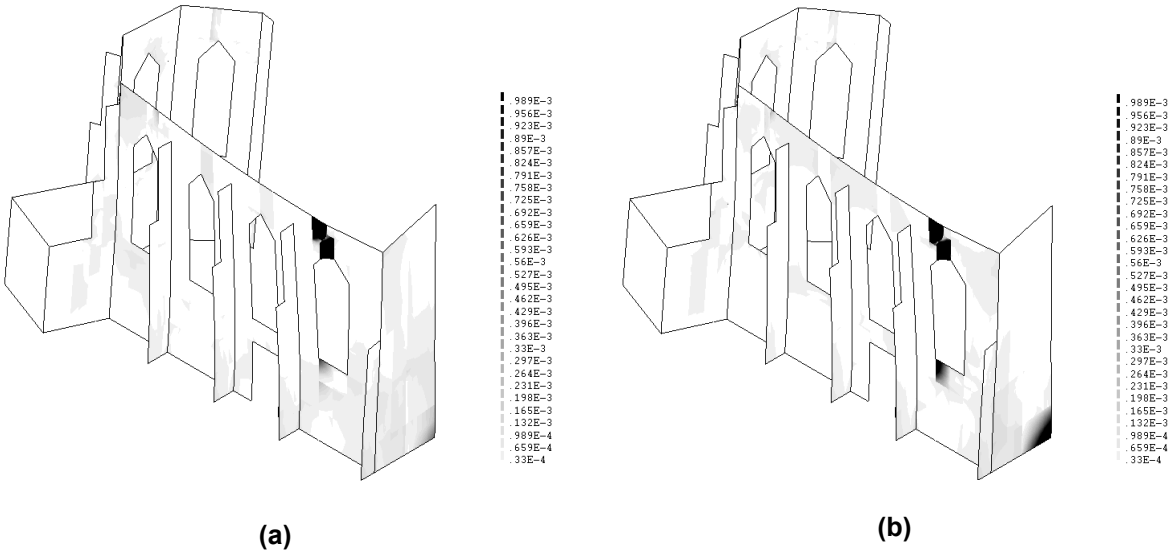

Figure 6.11. Principal tensile strains at stage (1) of the capacity curve calculated at (a) bottom and (b) top surfaces of the shell elements for pushover in -X global direction

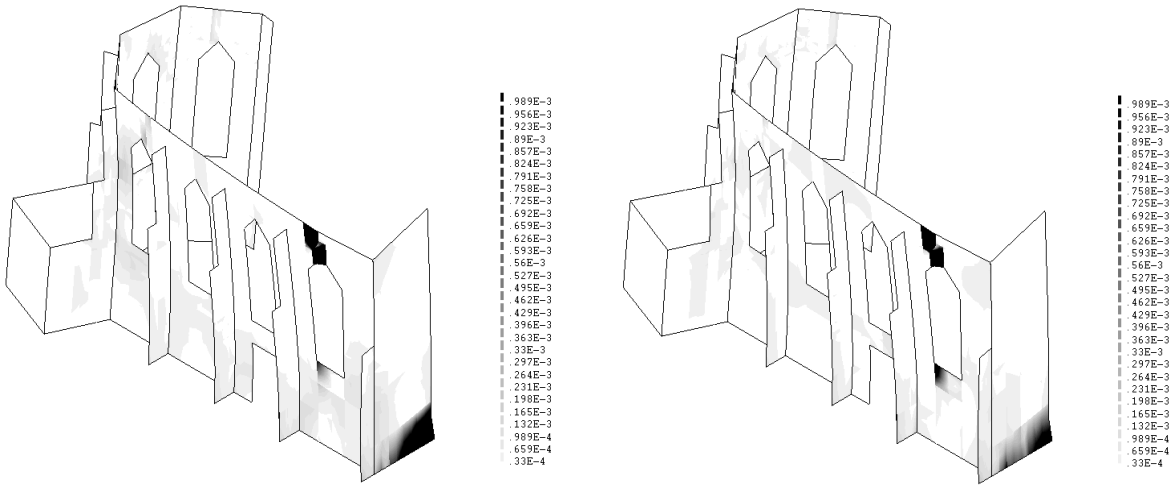

Figure 6.12. Principal tensile strains at stage (2) of the capacity curve calculated at (a) bottom and (b) top surfaces of the shell elements for pushover in -X global direction

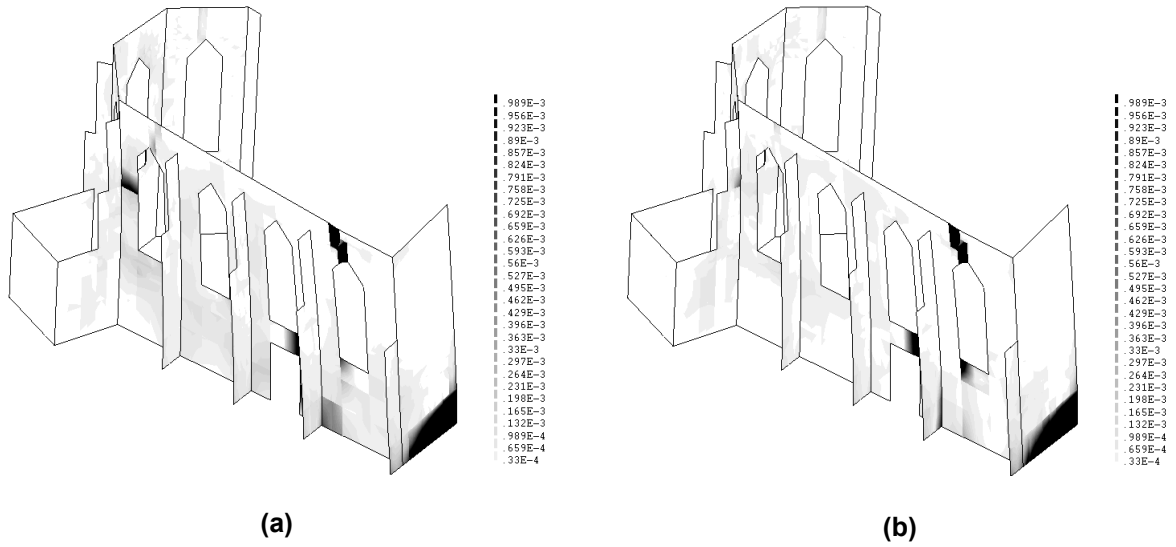

Figure 6.13. Principal tensile strains at stage (3) of the capacity curve calculated at (a) bottom and (b) top surfaces of the shell elements for pushover in -X global direction

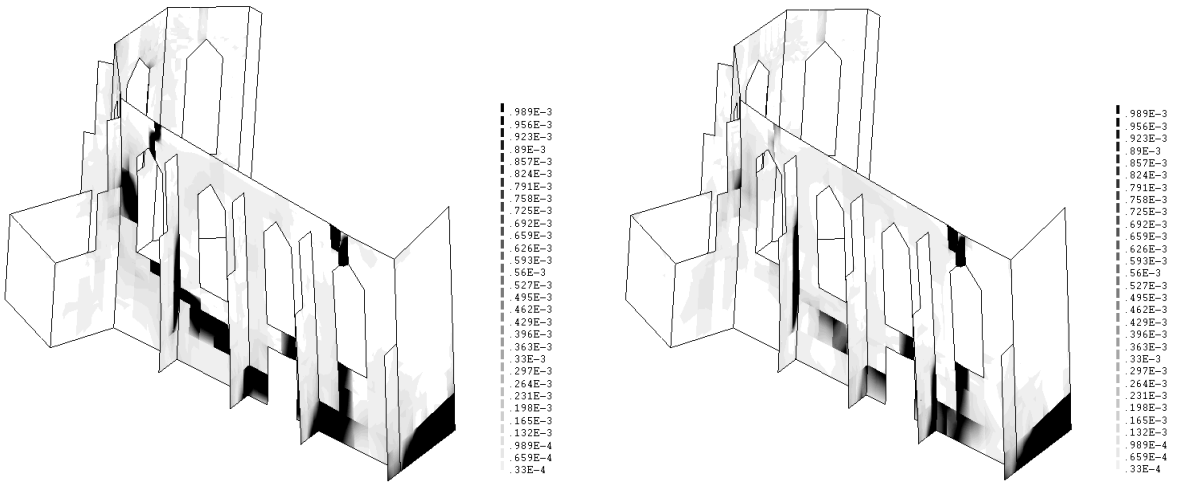

Figure 6.14. Principal tensile strains at stage (4) of the capacity curve calculated at (a) bottom and (b) top surfaces of the shell elements for pushover in -X global direction

At the end of the analysis, the damage evolution shows a pattern which coincides with the assumed collapse mechanism in this direction for this part of the structure (see Figure 3.5). The damages located in the lower part of the West façade and in the connection with the North façade, also in the upper part of the first window to the right in the North façade, represent the assumed hinges of the collapse mechanism.

6.5.3 Pushover analysis in Y global direction

In this attempt, an incremental horizontal acceleration was applied in Y global direction, which direct consequence is that horizontal load increases proportional to the structure's mass, following the same direction of the applied acceleration; the used load direction is shown in Figure 6.15-b. The node 195, which location is plotted in Figure 6.15-c, had the maximum displacement at the end of the analysis, and hereby it was selected for plotting the capacity curve of the structure shown in Figure 6.15-a. In this analysis, the structure reaches a maximum capacity, in terms of Load coefficient, equal to 0.09g, but this value is lower (25%) than the obtained Load coefficient calculated by limit analysis of collapse mechanism in Section 3.4 named as CM_A8_RX (see Figure 6.15-a), which was equal to 0.120g. It is important to highlight that this mechanism was calculated along the direction that gives the lowest capacity but if the same macro-element was used to calculate the kinematic mechanism along the same direction of the pushover analysis, the resultant Load coefficient would be equal to 0.195g. The curve path has three softening peaks which may be explained by numerical problems (see Section 6.5.1) or also by crack opening or local damage concentration at a specific part of the structure, as it is

reported in this section, therefore three load stages were selected to calculate the principal tensile strain distribution.

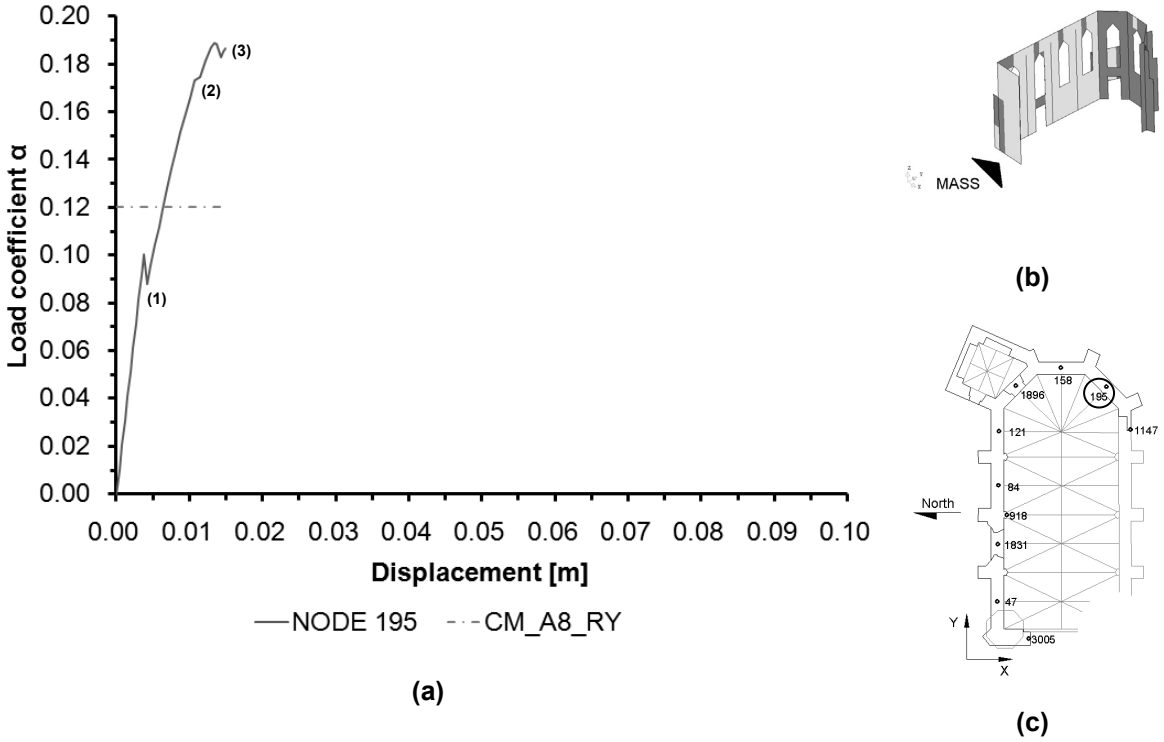

Figure 6.15. (a) Capacity curve of pushover analysis in Y global direction, (b) applied load direction and (c) selected control point

The stage (1) represents the first softening peak in capacity curve, and its damage distribution in terms of principal tensile strain is plotted in Figure 6.16. The damage with the highest intensity at this load stage is located in the upper part of the right window in the Apse. Other damages with less intensity are located in the upper part of the first window to the right and the first window to the left, both in the North façade.

After stage (1), the capacity increases with a constant rate up to reaching stage (2), where the second softening path of the curve is located. The damage distribution among the structure, in terms of principal tensile strains, is shown in Figure 6.17. In this stage, the intensity of the damage located in the upper part of the first window to the right and the first window to the left the upper part of the first window to the right in the North façade is increased in principal strain scale. Also the pier wall number 8 suffers plastic deformation is in the damaged area located above the window of the Apse.

Finally the structure's capacity increases up to reach a Load coefficient of 0.19g, and it seems to be stabilized around that value (stage 3). The principal tensile strain distribution is plotted in Figure 6.18.,

at this stage the intensity of the previous damages is increase and damage with lesser intensity is distributed among several regions within the structure.

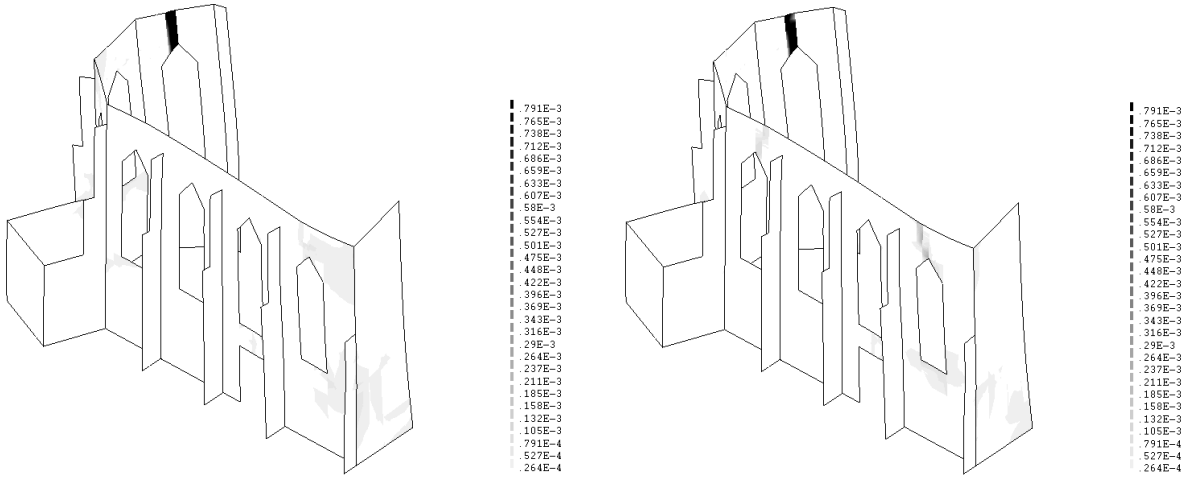

Figure 6.16. Principal tensile strains at stage (1) of the capacity curve calculated at (a) bottom and (b) top surfaces of the shell elements for pushover in Y global direction

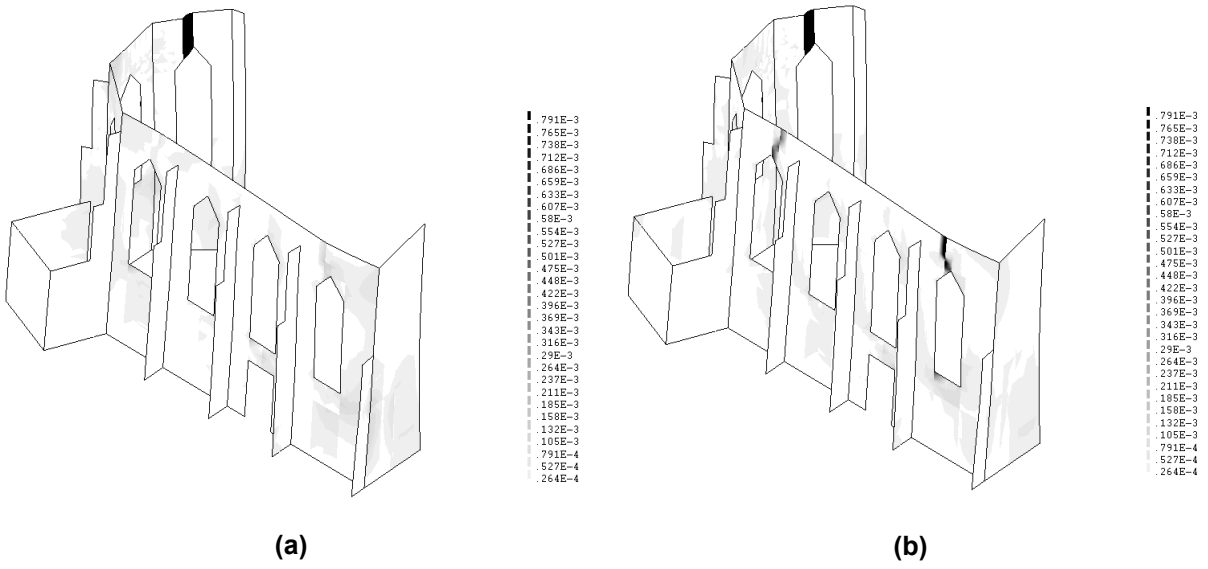

Figure 6.17. Principal tensile strains at stage (2) of the capacity curve calculated at (a) bottom and (b) top surfaces of the shell elements for pushover in Y global direction

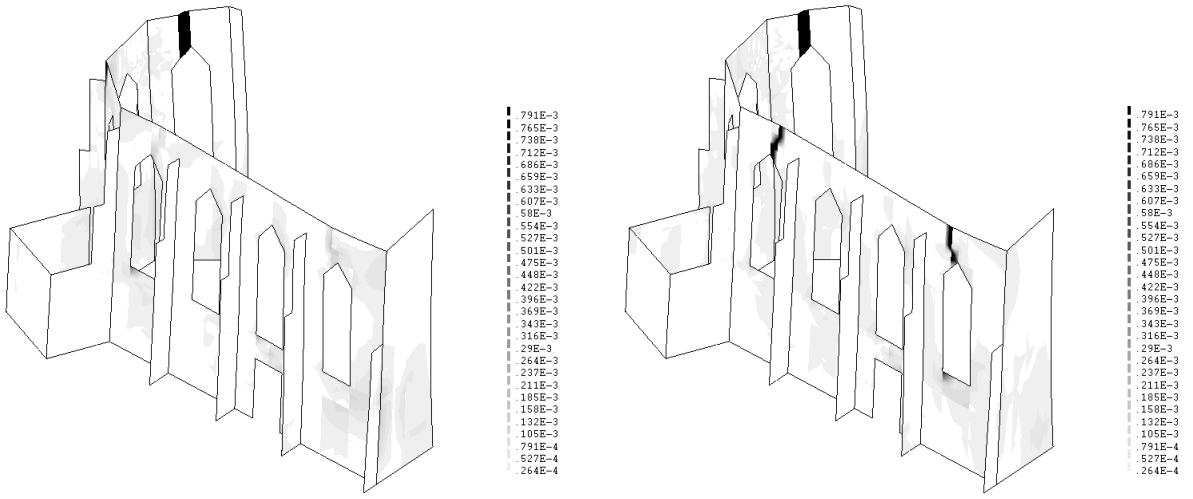

Figure 6.18. Principal tensile strains at stage (3) of the capacity curve calculated at (a) bottom and (b) top surfaces of the shell elements for pushover in Y global direction

The final damage pattern shows that the assumed collapse mechanism is valid for this portion of the structure (see Figure 3.14) in the same direction of the application of the load. The assumed hinges for the mechanism are clearly defined in the last load stage; therefore the comparison is completely validated.

6.5.4 Pushover analysis in –Y global direction

The last direction for the application of the acceleration was in –Y global. The acceleration was increased by small steps in order to obtain convergence during the analysis, so that the applied horizontal force was increasing proportional to the structure's mass regardless its height; the direction of the load is shown in Figure 6.19-b. The node 3005 had the maximum displacement during the whole analysis hereby it was selected to plot the capacity curve of the structure; the location of this node among the structure is reported in Figure 6.19-c. The capacity curve is shown in Figure 6.19-a, where several softening peaks are shown, and possible correlations with local damages are reported further. The maximum Load coefficient was of about 0.03g possibly influenced by the presence of local damages. But the behavior of the structure seems to stabilized after a tooth-saw path in the capacity curve when reaches a Load coefficient of about 0.10g which is similar to the Load coefficient of 0.109g obtained from the limit analysis of the collapse mechanism named as CM_W_Y (see Section 3.2). In order to have a better understanding of the damage condition progress during the loading process, five load stages were selected in the capacity curve (Figure 6.19-a) and the principal tensile strain distribution was calculated for the bottom and top face of the shell elements and the results are reported.

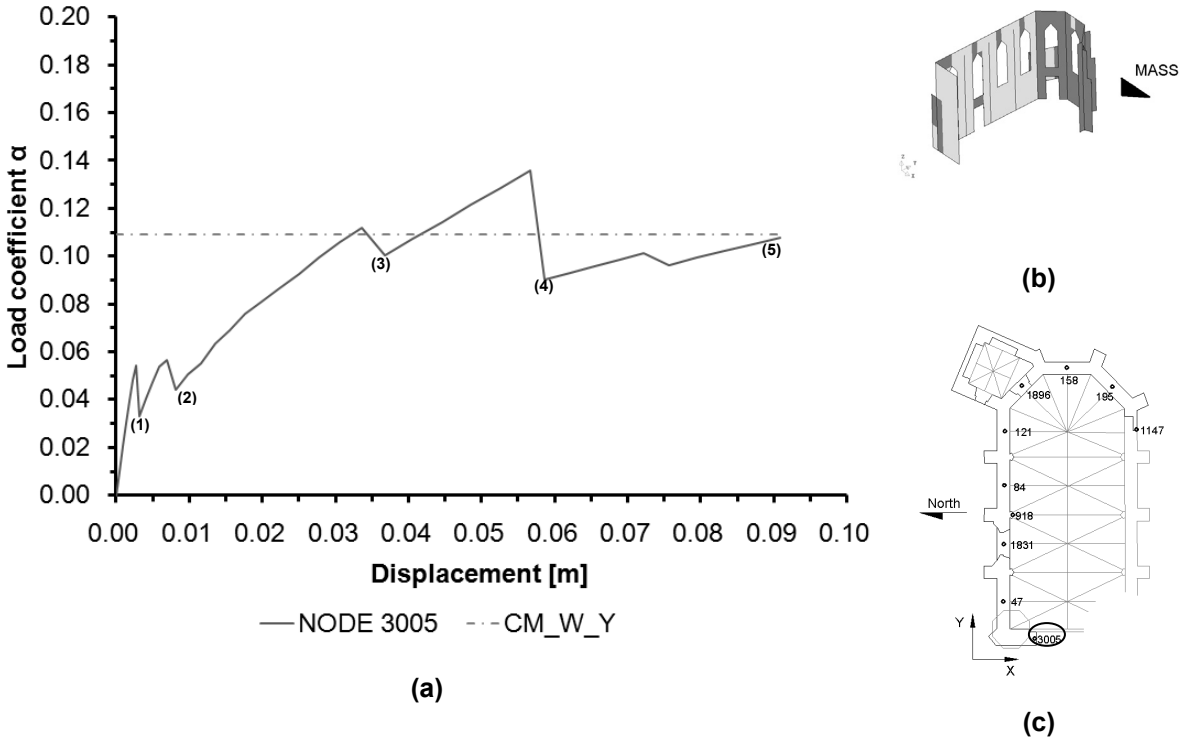

Figure 6.19. (a) Capacity curve of pushover analysis in -Y global direction, (b) applied load direction and (c) selected control point

The load stage (1) of the capacity curve is located after the first softening branch, which Load coefficient decreased from 0.055g to almost 0.035g. This important decreasing of the horizontal capacity of the structure may be explained by some local damage conditions shown at this stage; therefore the principal tensile strain distribution was plotted in Figure 6.20. One damaged region may be identified, in terms of principal tensile strain, and it is located above the first window to the right in the North façade.

After stage (1), the structure gains capacity until reaching a peak of 0.055g, when a second softening path of the curve appears up to stage (2). The previous damage area is increase and the structure suffered plastic deformation. A new damage area appear below the first window to the right in the North façade (see Figure 6.21).

Then, the structure suffers a rapid increment of its capacity up to reach a Load coefficient of 0.11g, but later it loses capacity until stage (3). The damage condition of the structure, in terms of principal tensile strains, is shown in Figure 6.22, where the damage regions increased and a new damage appear above the first window to the right in the Apse.

The structure reaches its maximum capacity of 0.14g but later on it decreases until stage (4). The principal tensile strain distribution is plotted in Figure 6.23, where the previous damaged regions are increase up to severe conditions, especially in the upper part of the first window to the right in the North façade. Light damage appear in the lower part of the West façade.

The last stage is number (5), which capacity in terms of Load coefficient is the same as that obtained from the limit analysis of the collapse mechanism. The principal tensile strain distribution is reported in Figure 6.24, where the damaged regions are highly deformed.

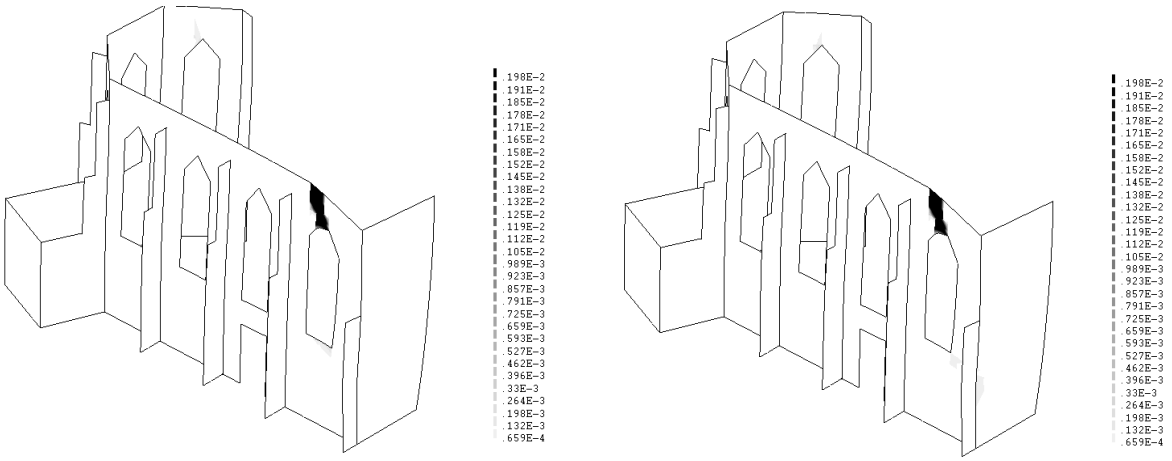

(a) **(b)**

Figure 6.20. Principal tensile strains at stage (1) of the capacity curve calculated at (a) bottom and (b) top surfaces of the shell elements for pushover in -Y global direction

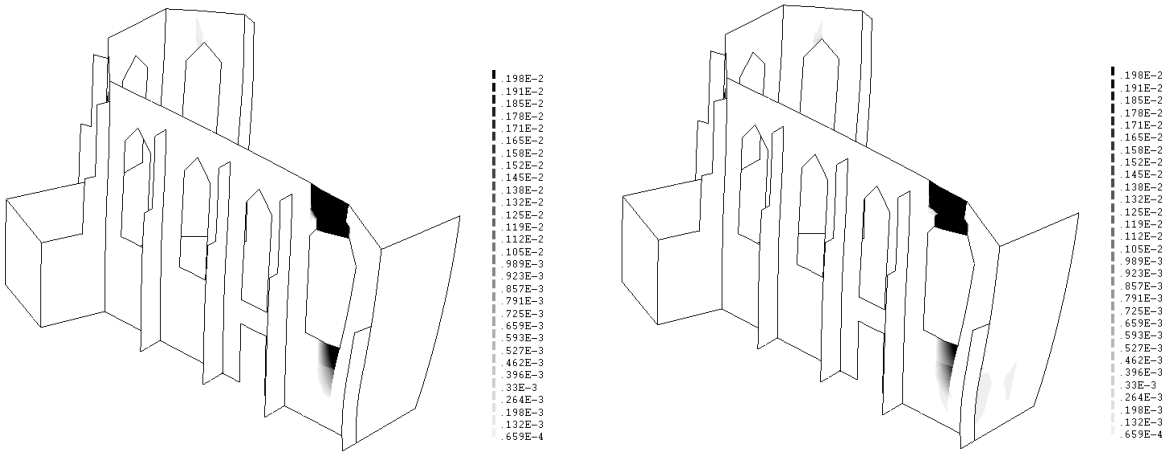

(a) **(b)**

Figure 6.21. Principal tensile strains at stage (2) of the capacity curve calculated at (a) bottom and (b) top surfaces of the shell elements for pushover in -Y global direction

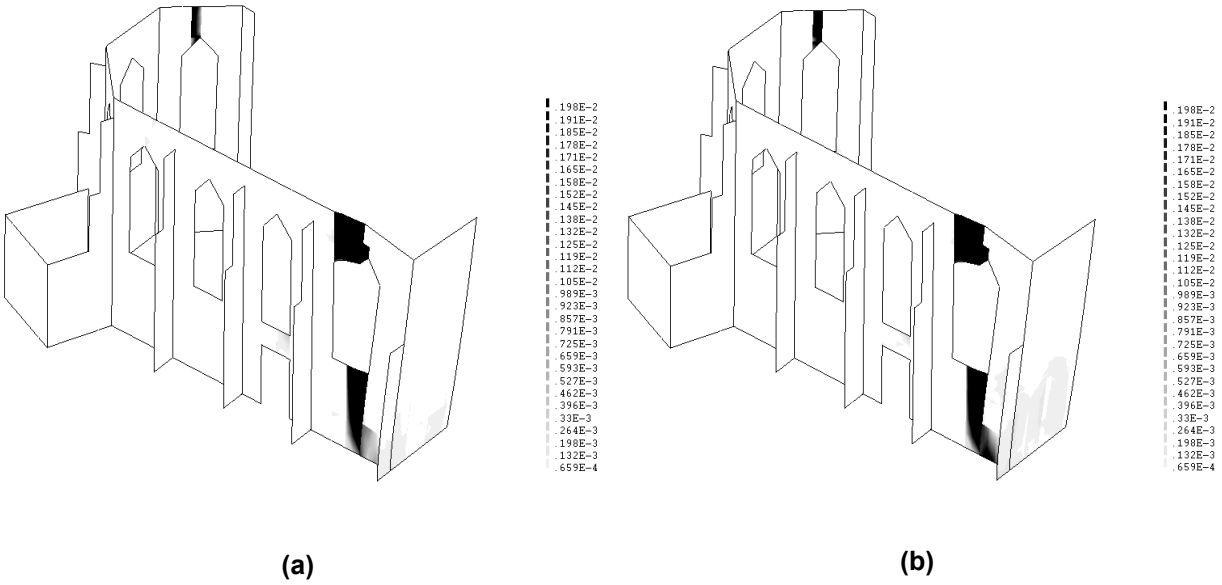

(a) **(b)**

Figure 6.22. Principal tensile strains at stage (3) of the capacity curve calculated at (a) bottom and (b) top surfaces of the shell elements for pushover in -Y global direction

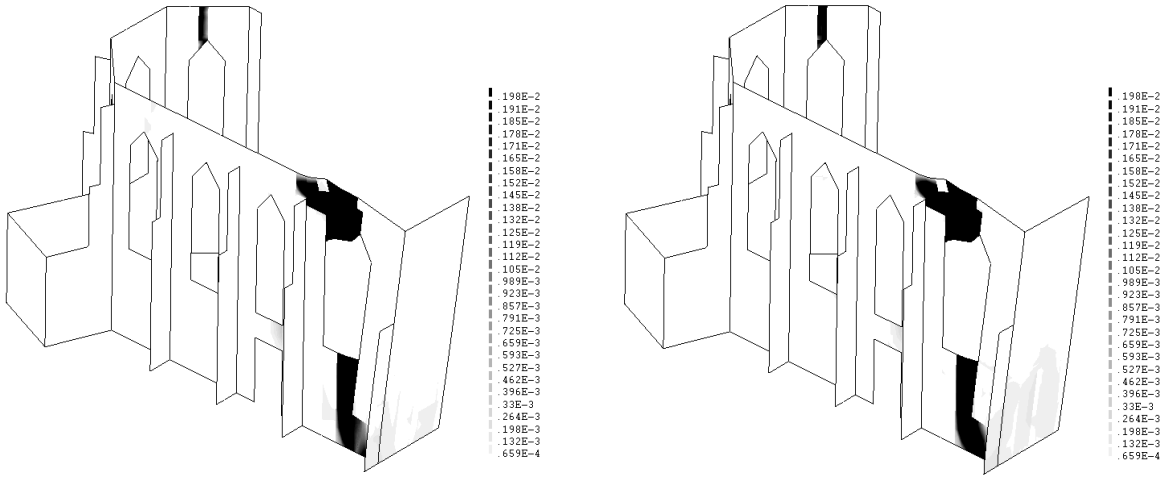

(a) **(b)**

Figure 6.23. Principal tensile strains at stage (4) of the capacity curve calculated at (a) bottom and (b) top surfaces of the shell elements for pushover in -Y global direction

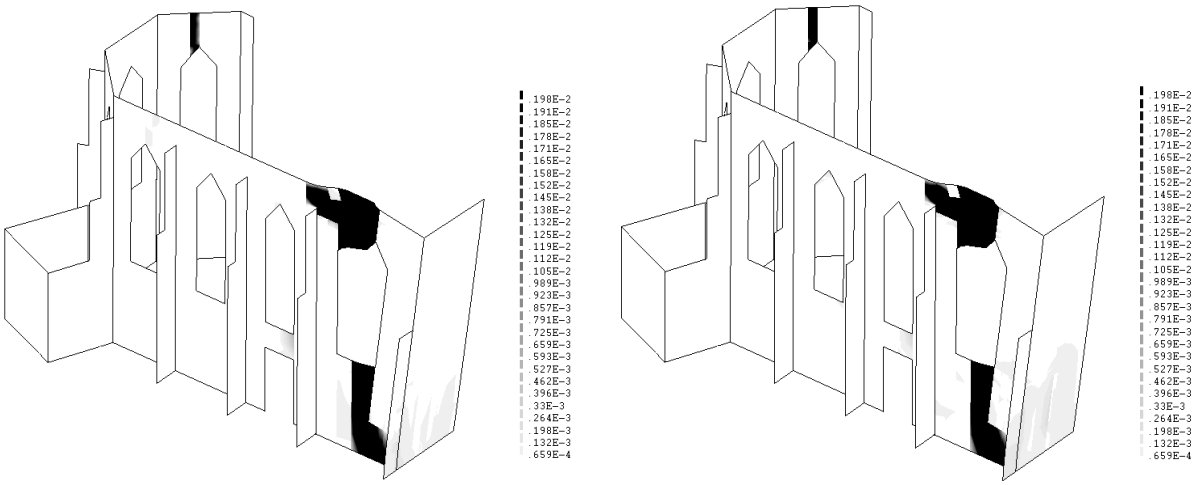

Figure 6.24. Principal tensile strains at stage (5) of the capacity curve calculated at (a) bottom and (b) top surfaces of the shell elements for pushover in Pushover in -Y global direction

The damage pattern at the last stage shows damages along the connection between West and North façades which represent the assumed plastic hinges for the collapse mechanism that was used to compared the results (see Figure 3.6). Also the deformed shape of the assumed macro-element coincides with the deformed shape of the structure at the final load stage.

6.6 PUSHOVER ANALYSES PROPORTIONAL TO MODE SHAPES CONFIGURATION

6.6.1 Selection of structural modes for the pushover analyses

For this analyses the first mode in each global direction with the highest mass participation factor was selected, hence the information of Table 5.5 was extracted in order to define the modes that fulfill that condition. The table has the results of the modal analysis response, where the 1st mode has the highest participation factor in the X global direction (32.49%) and the 3rd mode has the highest participation factor in the Y global direction (12.34%). The displacement pattern for each mode was extracted from the modal response analysis (see Figure 6.25), then a linear static analysis was performed for each mode configuration, by fixing the horizontal displacements (In X and Y directions) in all the nodes, except those at the base of the structure which are fixed in the three global directions and do not have any prescribed displacement, and the displacement from the modal response analysis for each node was prescribed, obtaining the reaction forces at each node that will produce the same displacement in the structure (Mendes & Lourenço, 2008). Then, these forces were applied

to the structure using small increments in order to capture its non-linear behavior and the capacity curve was obtained for the maximum displacement node. Finally, the damage distribution was plotted in terms of principal tensile strains and the results are shown for several stages; this procedure was applied twice for both modes in each global direction.

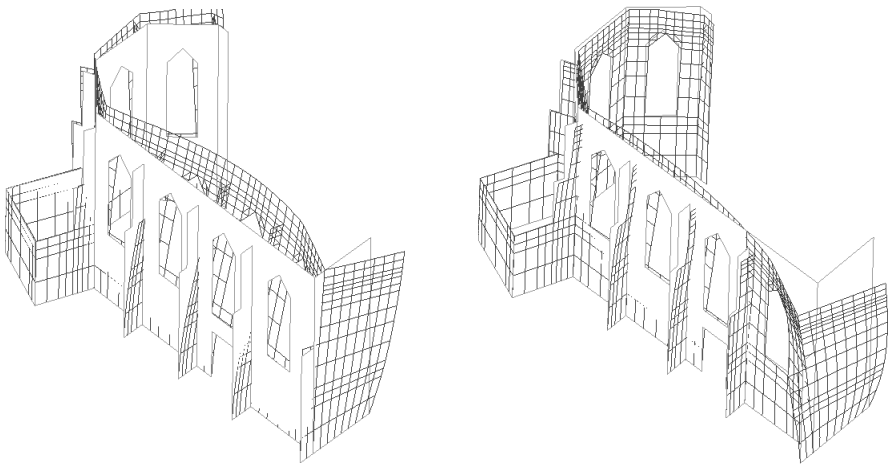

(a) **(b)**

Figure 6.25. Deformed shape for: (a) first mode shape and (b) third mode shape

6.6.2 Pushover analysis proportional to 1st mode

The applied load direction of the pushover analysis proportional to the 1st mode is the X global (see Figure 6.26-b). After performing the linear static analysis described in Section 6.6.1, a load pattern which generates the same displacements as those obtained from the modal response analysis was obtained and then applied to the structure by small increments in order to obtain its non-linear reponse. After finishing the pushover analysis, the node which had the maximum displacement was 1831 (see Figure 6.26-c) and it was selected to plot the capacity curve of the structure (see in Figure 6.26-a). Along the loading path several load stages were defined in order to follow the damage pattern progress. The maximum Load coefficient was about 0.04g (it occurs at stage number 2) which is lesser than the obtained value of 0.097g in the limit analysis of collapse mechanism named as CM_N_X (see Figure 3.9). When the structure is subjected to this load pattern, the capacity is lower than the capacity obtained when the structure is subjected to pushover analysis with the application of a load pattern porpotrtional to the mass. Nevertheless, the structure response also present a saw-tooth behavior in its non-linear range, which can be partially explained by local damages, hereby the principal tensile strains distribution was plotted for the selected load stages.

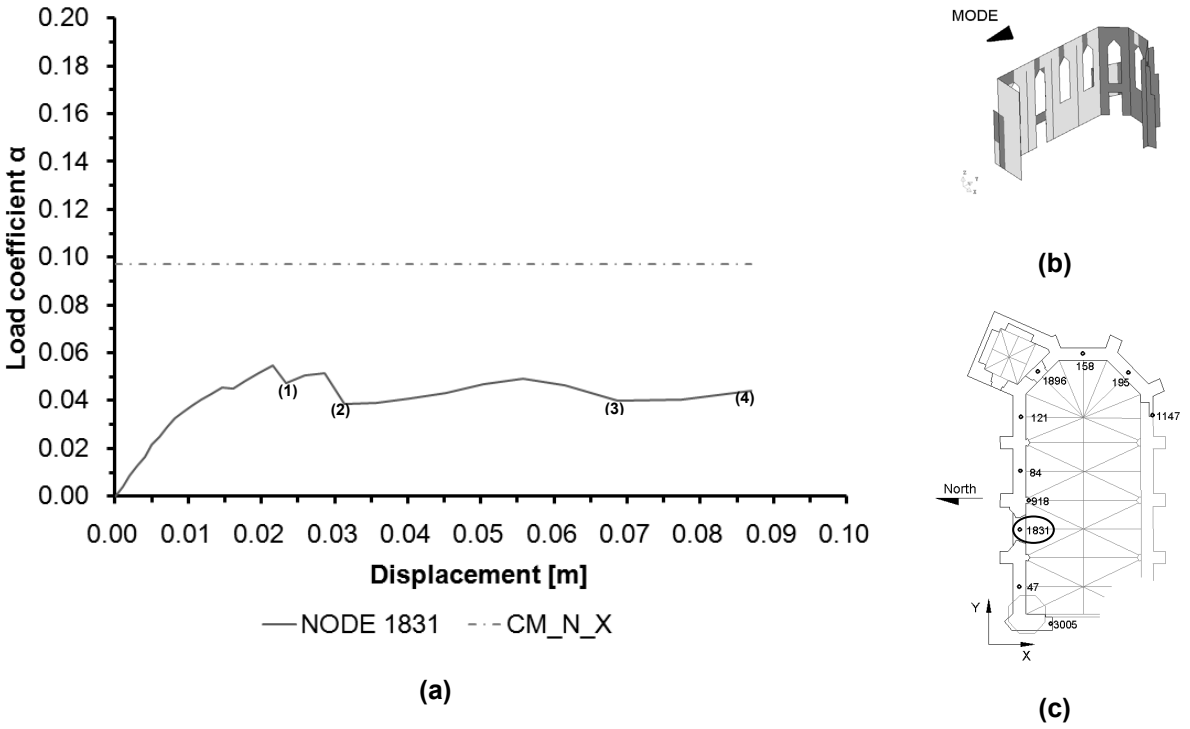

Figure 6.26. (a) Capacity curve of pushover analysis proportional to 1st mode, (b) applied load direction and (c) selected control point

First the capacity of the structure reaches a peak and then suffers softening until stage (1). There are three clear damaged regions in the structure; the first one is located above the first window to the right in the Apse, the second damaged region is located above the first window to the right in North façade and the last damaged region is located above the second window to the right in the North façade (see in Figure 6.27).

After reach stage (1), the structure gains little capacity until reaches load stage (2). The damage condition of the structure at this stage is plotted in Figure 6.28, in which a new damage region appears in the connection between North and West facades. The extension of this damaged region is much higher than in the other regions, and also includes light intensity damage below the first window to the right in the North façade.

At stage (3), new damage conditions appear on the structure mainly in the upper part of the connection between the Apse and the North façade (see Figure 6.29). It is clear the increasing in extension of the damage in the connection between the North and the West facades and the appearance of damage above the first window to the left in the North façade.

Finally at stage (4), the damage intensity all over the regions increased especially at the lower part of the North façade but it is important that the nodes at the base of the structure are fixed in three global

directions, which in reality does not occur, hereby the lower region is stiff and takes more loda during the loading process (see Figure 6.30).

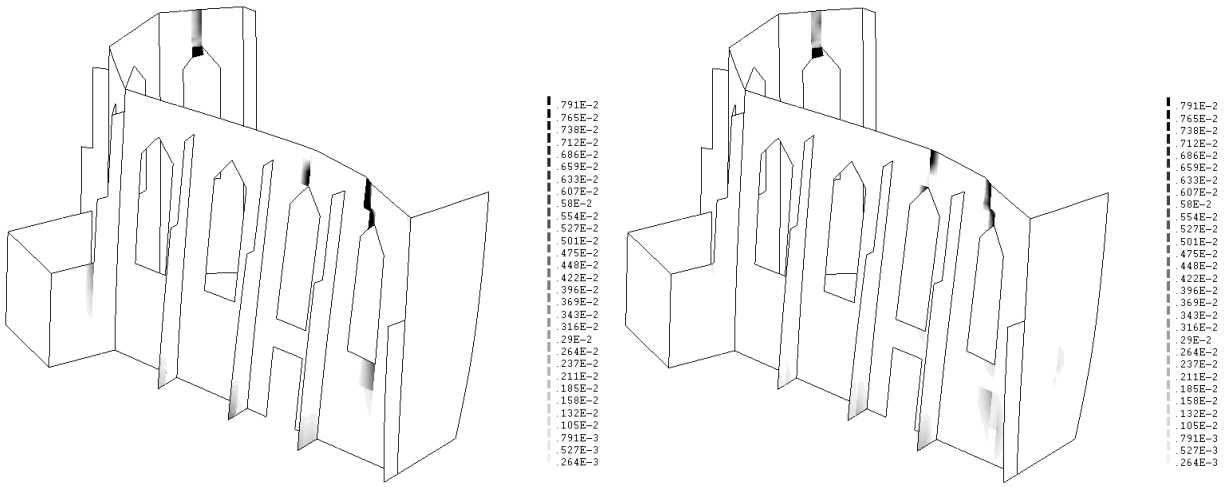

(a) **(b)**

Figure 6.27. Principal tensile strains at stage (1) of the capacity curve calculated at (a) bottom and (b) top surfaces of the shell elements for pushover proportional to 1st mode

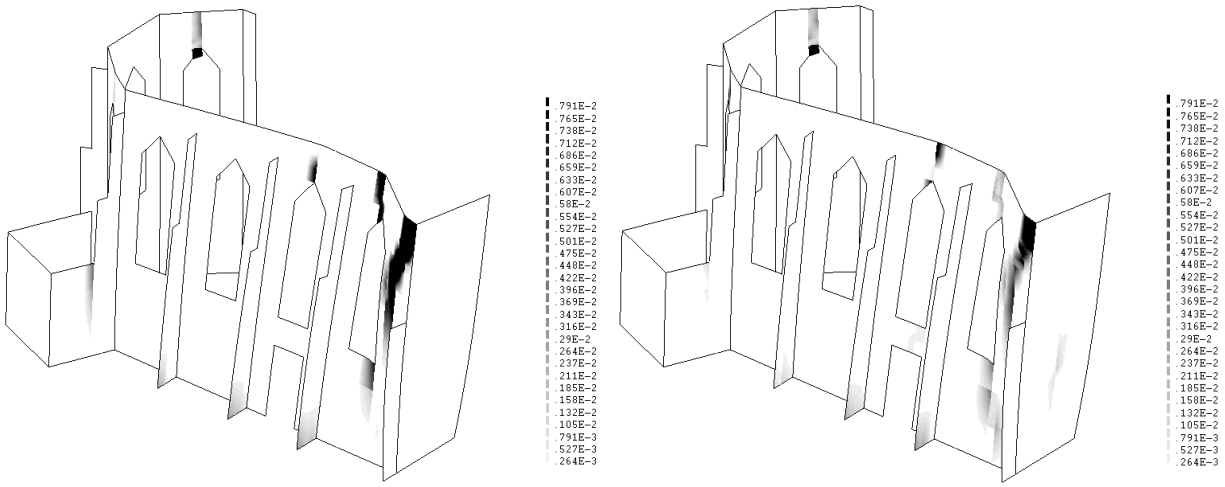

(a) **(b)**

Figure 6.28. Principal tensile strains at stage (2) of the capacity curve calculated at (a) bottom and (b) top surfaces of the shell elements for pushover proportional to 1st mode

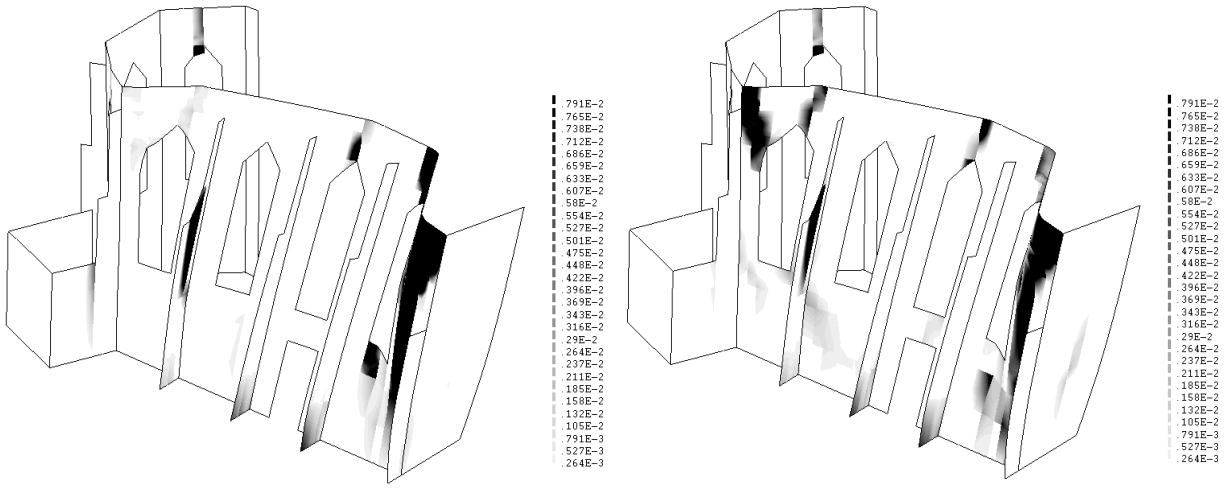

(a) **(b)**

Figure 6.29. Principal tensile strains at stage (3) of the capacity curve calculated at (a) bottom and (b) top surfaces of the shell elements for pushover proportional to 1st mode

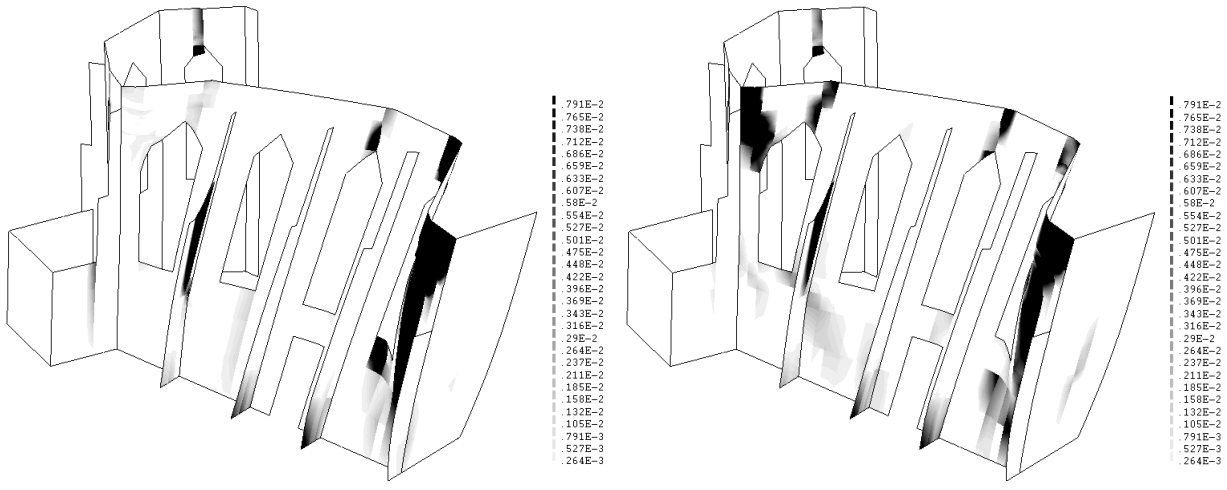

(a) **(b)**

Figure 6.30. Principal tensile strains at stage (4) of the capacity curve calculated at (a) bottom and (b) top surfaces of the shell elements for pushover proportional to 1st mode

The final damage pattern configuration represents with high accuracy the formation of the plastic hinges supposed of the limit analysis of the collapse mechanism (CM_N_X) in Section 3.3., the hinges are located at the connections of the North façade with the Apse and the West façade.

6.6.3 Pushover analysis proportional to 3rd mode

The same procedure described in Paragraph 6.6.2 was used to perform this pushover analysis which load pattern follows the displacement configuration of the 3rd mode. The only difference is the Load pattern, which causes the same displacements as those obtained from the response analysis results for the 3rd mode; the direction of the application of this load pattern is shown in Figure 6.31-b. After run the analysis, the node with the maximum displacement was node number 3005 (see Figure 6.31-c) and it was selected to plot the capacity curve of the structure (see Figure 6.31-a). The maximum Load coefficient obtained from this analysis was about 0.01g (softening peak) which is rather small compared with the results of the previous analyses. The capacity of the structure reach a peak of 0.03g but the resistance is governing by any of the numerical problems discussed in Section 6.5.1 or the appearance of local damages. In this manner, three different stages were defined along the curve's path in order to analyze the progress of the damage pattern, therefore the principal tensile strains distribution was plotted for each stage.

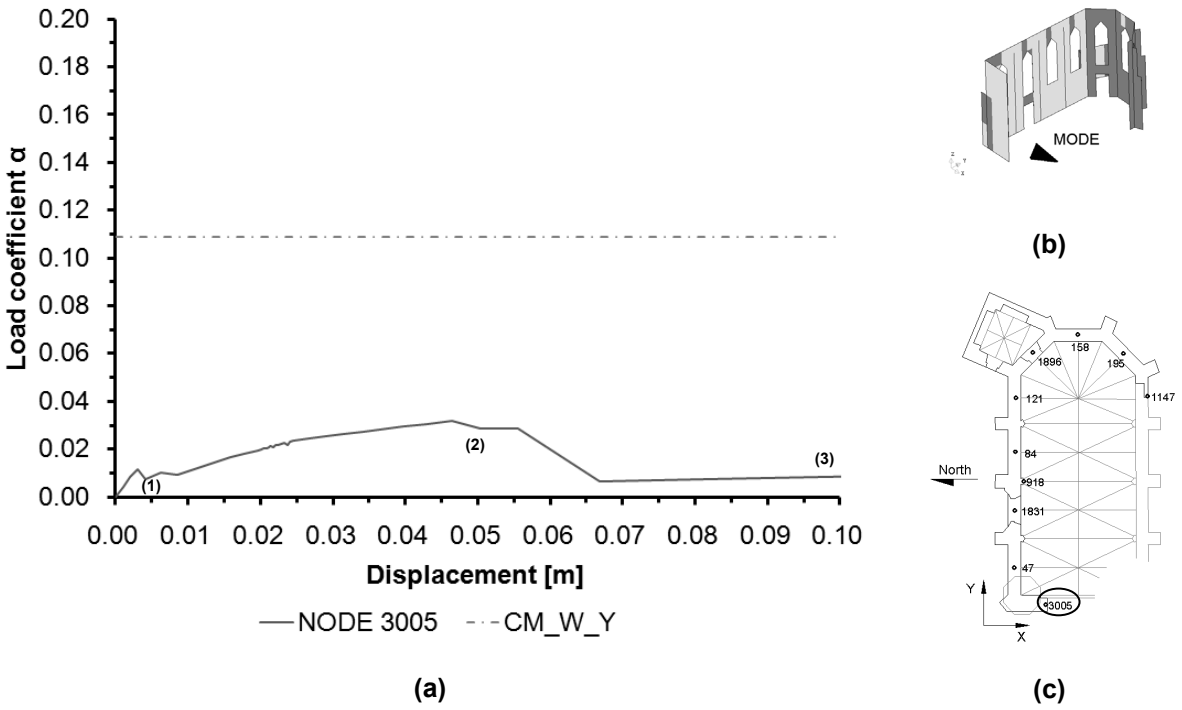

Figure 6.31. (a) Capacity curve of pushover analysis proportional to 3rd mode, (b) applied load direction and (c) selected control point

The structure's capacity increases up to stage (1) in which reaches a softening peak. In this stage the damage condition of the structure was estimated in terms of principal tensile strains and its distribution is shown in Figure 6.32. The only damaged area is located above the first window to the right in the North façade.

Then the structure reaches stage (2), in which reaches the highest Load coefficient (0.05g). During this load stage, new damaged regions appear in the lower part of the West façade and also below the first window to the right in the North façade, just in the connection with the West façade (see Figure 6.33).

Finally stage (3) is reached and the structure shows severe damage condition in the corner that connects the North and the West façades. In addition, the previous damaged areas seems to extend to more zones; the structure also presents high deformation state which can be also interpreted as its collapse (see Figure 6.38).

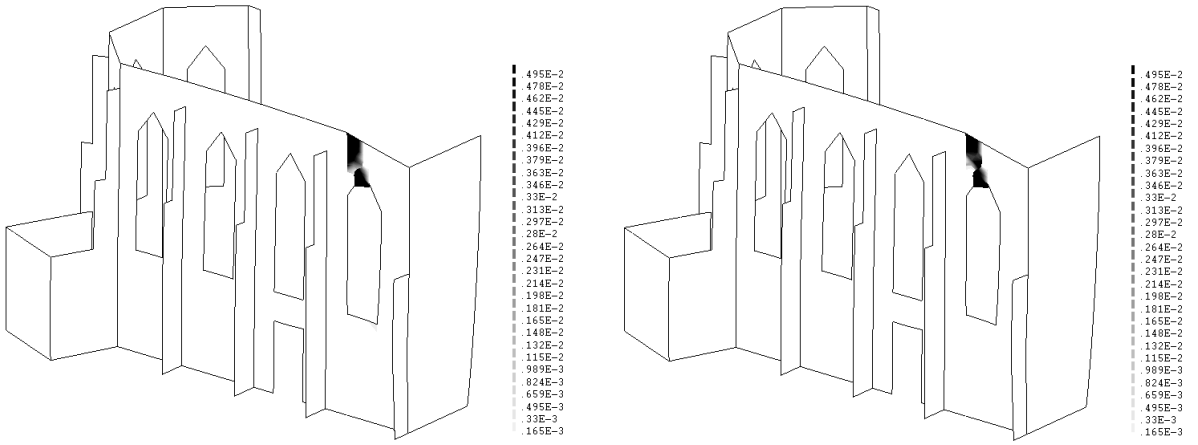

Figure 6.32. Principal tensile strains at stage (1) of the capacity curve calculated at (a) bottom and (b) top surfaces of the shell elements for pushover proportional to 3rd mode

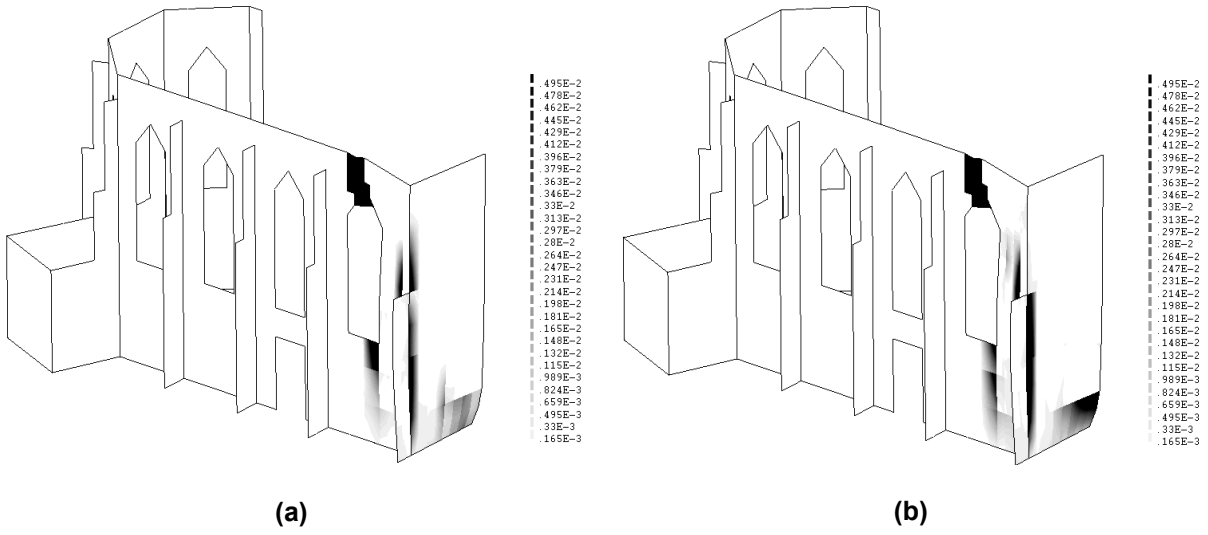

Figure 6.33. Principal tensile strains at stage (2) of the capacity curve calculated at (a) bottom and (b) top surfaces of the shell elements for pushover proportional to 3rd mode

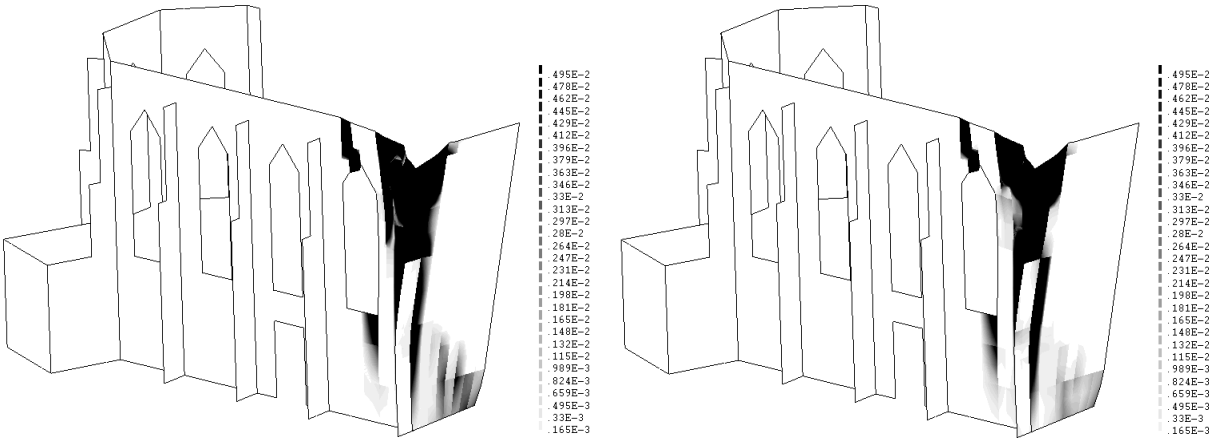

(a) **(b)**

Figure 6.34. Principal tensile strains at stage (3) of the capacity curve calculated at (a) bottom and (b) top surfaces of the shell elements for pushover proportional to 3rd mode

After finishing the loading process of the structure, the final damage pattern shows the presence of two hinges that were also defined for the collapse mechanism analyzed in Section 3.2; those are located above the first window to the right in the North façade and the other is located in the lower part of the corner that connects North and West facades. But there is one damage region that does not coincide with the defined mechanism which is the severe damage present in the upper corner of the connection between North and West facades; one explanation for this severe damage is the presence of concentrated masses that represent the tower.

6.7 PUSHOVER ANALYSES PROPORTIONAL TO MASS IN PRINCIPAL AXES DIRECTION

6.7.1 Definition of the principal axes in plan of the structure

Due to structure in plan irregularity, another attempt to assess the stability of the structure was made by performing several pushover analysis with the load applied in four different directions following the principal axes orientation. The main goal in this analysis was to find a direction for the application of the load in which the structure has a critical response (lowest capacity). Therefore the principal axes orientation was calculated and selected for perform four different analyses. It is important to remark that along the principal axes the structure has its maximum and minimum inertia moments; which are determinant parameters in the calculation of the structure stiffness, hereby in its capacity.

In order to find the principal axes orientation is necessary to find a set of eigenvectors that diagonalize the inertia tensor. Hereby is possible to solve Equation 6.9 and obtain those values (known as eigenvalues), and then replace them into the Equation 6.10 to obtain the eigenvectors which are unitary vectors in the direction of each principal axe.

$$\begin{vmatrix} I_{XX} - \lambda_1 & I_{XY} \\ I_{XY} & I_{YY} - \lambda_2 \end{vmatrix} = 0 \qquad 6.9$$

Where:

I_{XX}: is the moment of inertia along X global direction in the center of mass

I_{YY}: is the moment of inertia along Y global direction in the center of mass

I_{XY}: is the product of inertia along the global axes in the center of mass

λ_i: is the *i-th* eigenvalue (moment of inertia along principal axes)

$$(I - \lambda_i 1) e_i = 0 \qquad 6.10$$

Where:

I: is the inertia tensor

e_i: is the *i-th* eigenvector (vector with principal axes direction)

1: is the unitary tensor (its diagonal contains 1 and the rest is 0)

The moments of inertia were found and they were replaced obtaining the results reported in Table 6.2, in which X' and Y' represent the principal axes (see Figure 6.1-b)

$\boldsymbol{I_{XX}}$ $[\boldsymbol{m^4}]$	$\boldsymbol{I_{YY}}$ $[\boldsymbol{m^4}]$	$\boldsymbol{I_{XY}}$ $[\boldsymbol{m^4}]$	$\boldsymbol{I_{X'}}$ $[\boldsymbol{m^4}]$	$\boldsymbol{I_{Y'}}$ $[\boldsymbol{m^4}]$	$\boldsymbol{e_{X'}}$	$\boldsymbol{e_{Y'}}$
2746.84	598.82	415.97	521.08	2824.58	$\begin{bmatrix} 1.8065 \cdot 10^{-1} \\ 9.8355 \cdot 10^{-1} \end{bmatrix}$	$\begin{bmatrix} -9.8355 \cdot 10^{-1} \\ 1.8065 \cdot 10^{-1} \end{bmatrix}$

Table 6.2. Moment of inertia along the principal axes and principal axes orientation

6.7.2 Pushover analysis in X' direction

The load was applied along X' direction (see Figure 6.35-b) using a pattern which is proportional to the mass. After performing the analysis, the node which had the maximum displacement in the same direction of the load application was 195 (see Figure 6.35-c). This node was selected for plot the capacity curve of the structure (see Figure 6.35-a) in which the maximum capacity obtained was of about 0.08g. The capacity obtained in this analysis is similar to the capacity obtained for the pushover analysis in the global directions. Three load stages were defined to plot the damage progress along the loading process and the principal tensile strains were calculated for each of them.

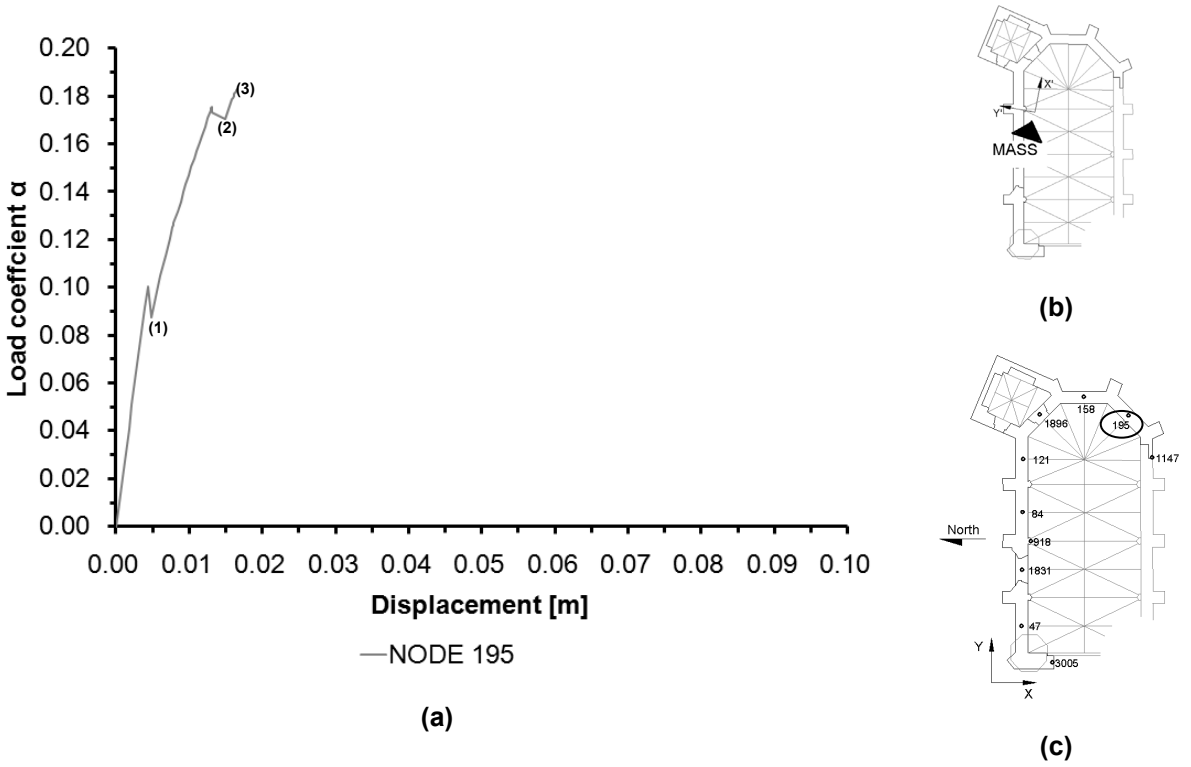

Figure 6.35. (a) Capacity curve of pushover analysis in X' direction, (b) applied load direction and (c) selected control point

The first damage appearance occurs at stage (1), located above the first window to the right in the Apse (see Figure 6.36). Later, on stage (2) new damage appear above the first window to the right and first window to the left in the North façade (see Figure 6.37). Finally at stage (3), the damaged areas remained constant and the deformation seems to be increased (see Figure 6.38).

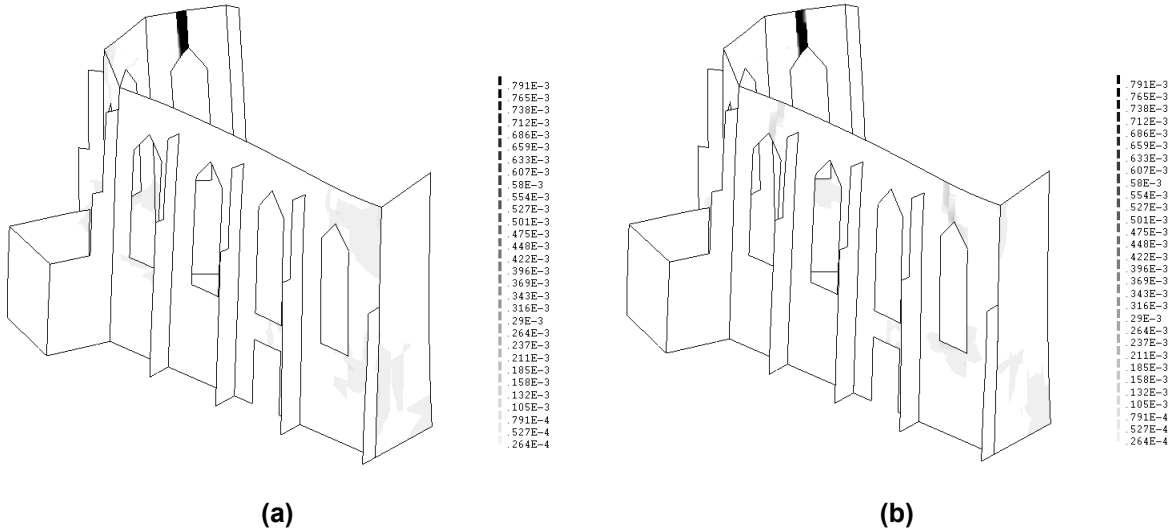

Figure 6.36. Principal tensile strains at stage (1) of the capacity curve calculated at (a) bottom and (b) top surfaces of the shell elements for pushover in X' direction

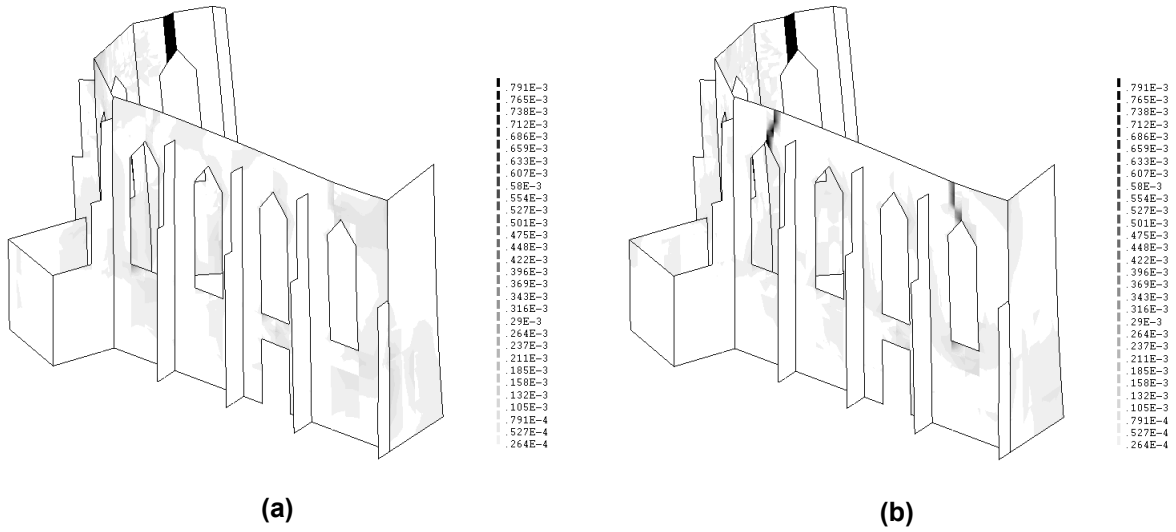

Figure 6.37. Principal tensile strains at stage (2) of the capacity curve calculated at (a) bottom and (b) top surfaces of the shell elements for pushover in X' direction

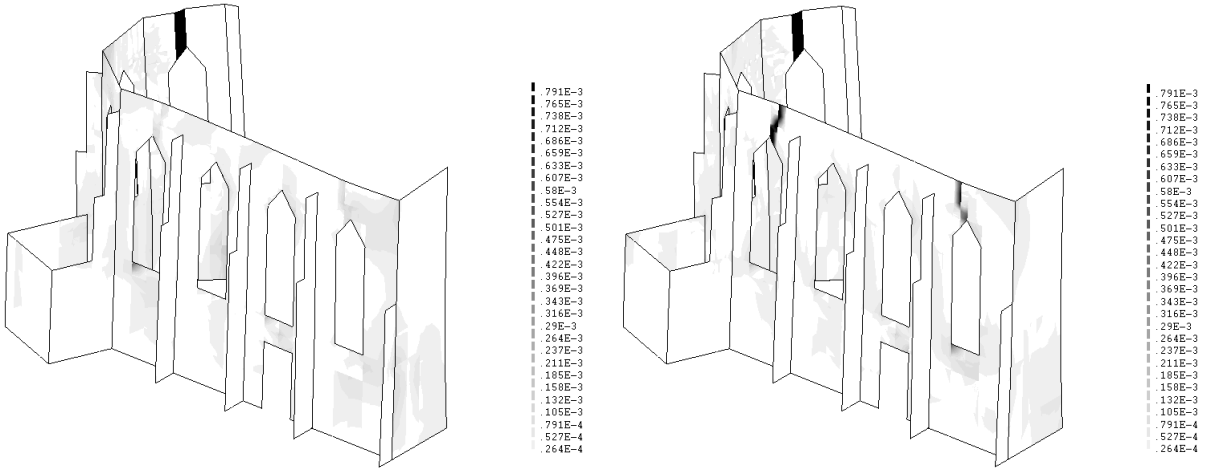

Figure 6.38. Principal tensile strains at stage (3) of the capacity curve calculated at (a) bottom and (b) top surfaces of the shell elements for pushover in X' direction

6.7.3 Pushover analysis in -X' direction

The direction of the application of the load is shown in Figure 6.39-b. The node with the maximum displacement was node 3005 (see Figure 6.39-c) and it was selected to plot the capacity curve of the structure for this analysis which is shown in Figure 6.39-a. The lowest softening peak indicates the maximum capacity of the structure which was about 0.03g, but it seems to be explained even by numerical errors (see Section 6.5.1) or as is discussed, by local damage conditions. The path of the curve seems to be stabilized when the structure reaches values between 0.08g and 0.10g, which are similar to the maximum capacity obtained for the pushover analysis in the global directions. Three different load stages were selected to calculate the damage pattern in terms of principal tensile strains and they were plotted.

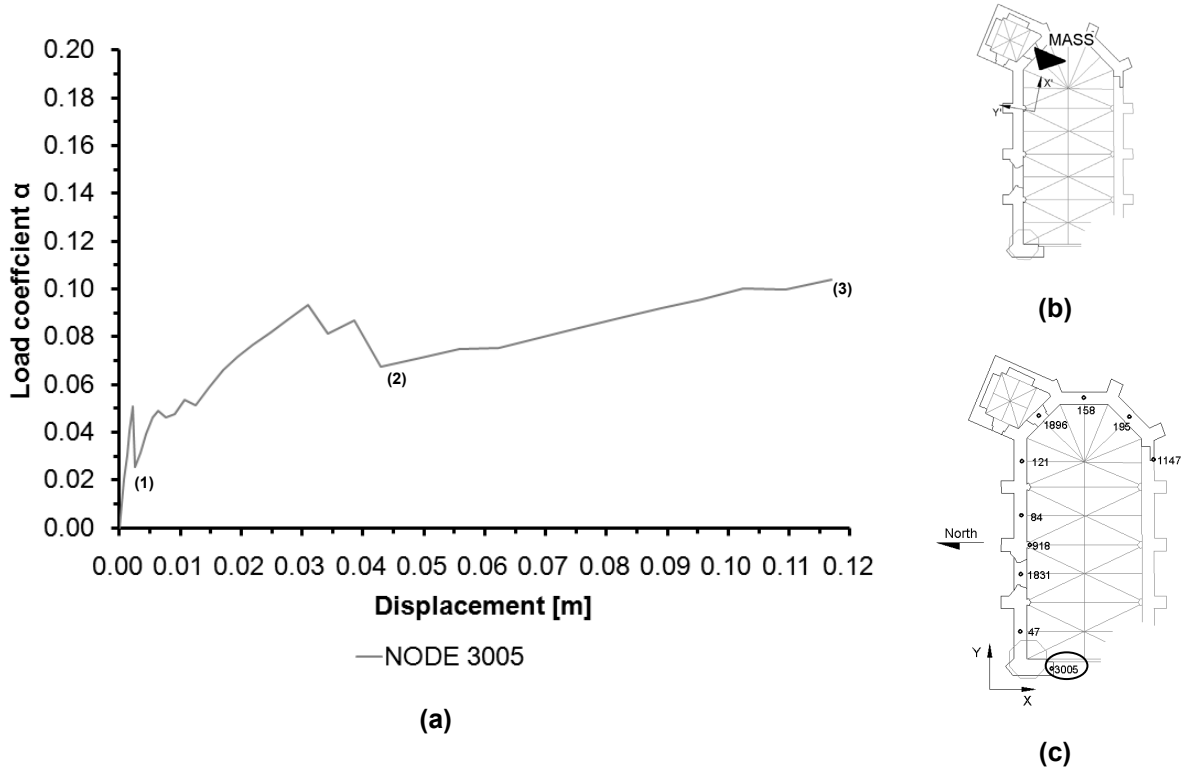

Figure 6.39. (a) Capacity curve of pushover analysis in –X' direction , (b) applied load direction and (c) selected control point

At stage (1) the structure suffered damage above the first window to the right in the North façade (see Figure 6.40). In the following stage (number 2), the structure suffered several damage conditions which are located above the Apse window and below the first window to the right in the North façade (see Figure 6.41). At the final stage the structure is highly deformed and the damage pattern is located all along the connection between the North and West façade, which may indicate the detachment of these two parts of the structure (see Figure 6.42).

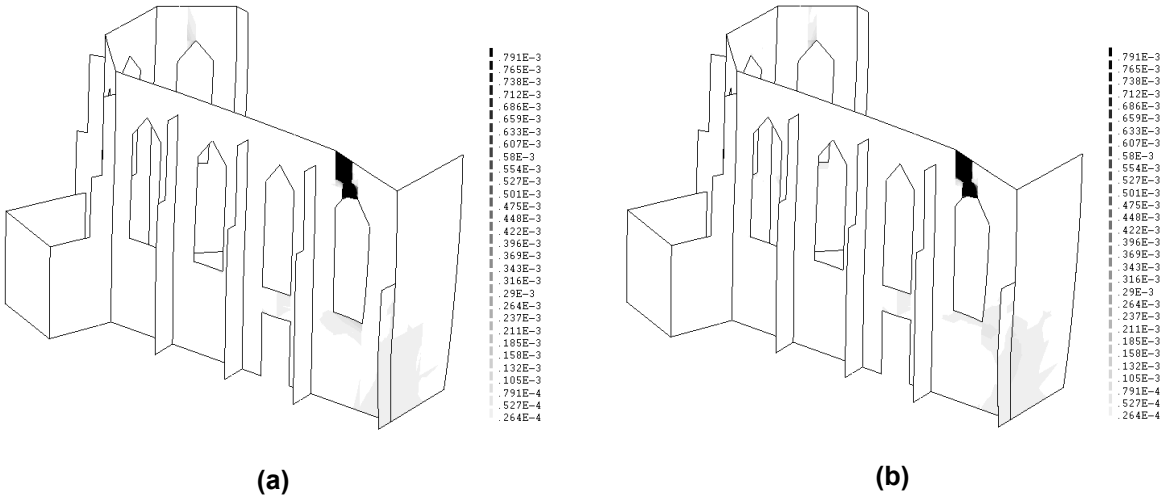

Figure 6.40. Principal tensile strains at stage (1) of the capacity curve calculated at (a) bottom and (b) top surfaces of the shell elements for pushover in –X' direction

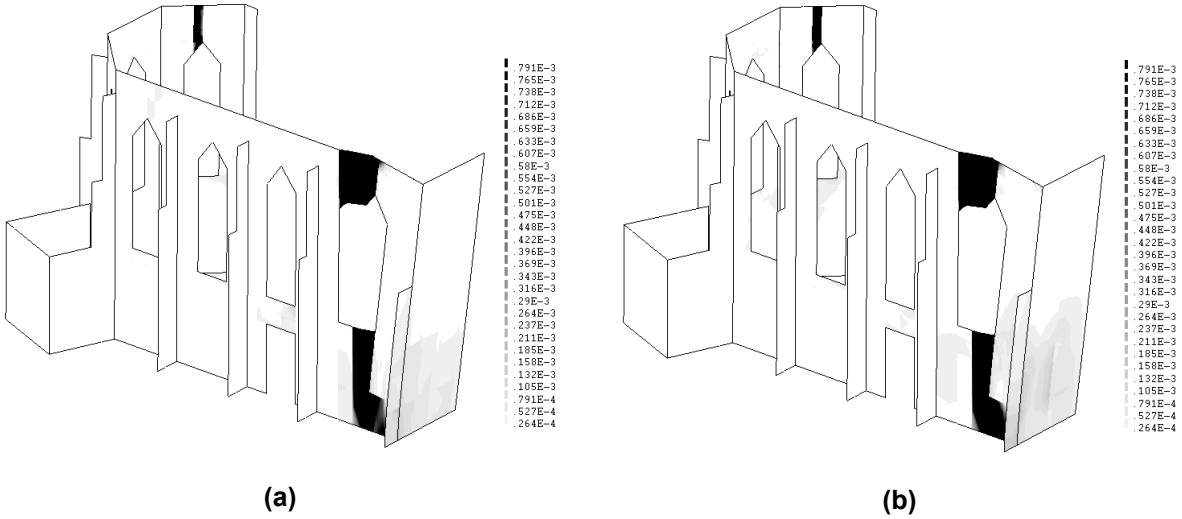

Figure 6.41. Principal tensile strains at stage (2) of the capacity curve calculated at (a) bottom and (b) top surfaces of the shell elements for pushover in –X'direction

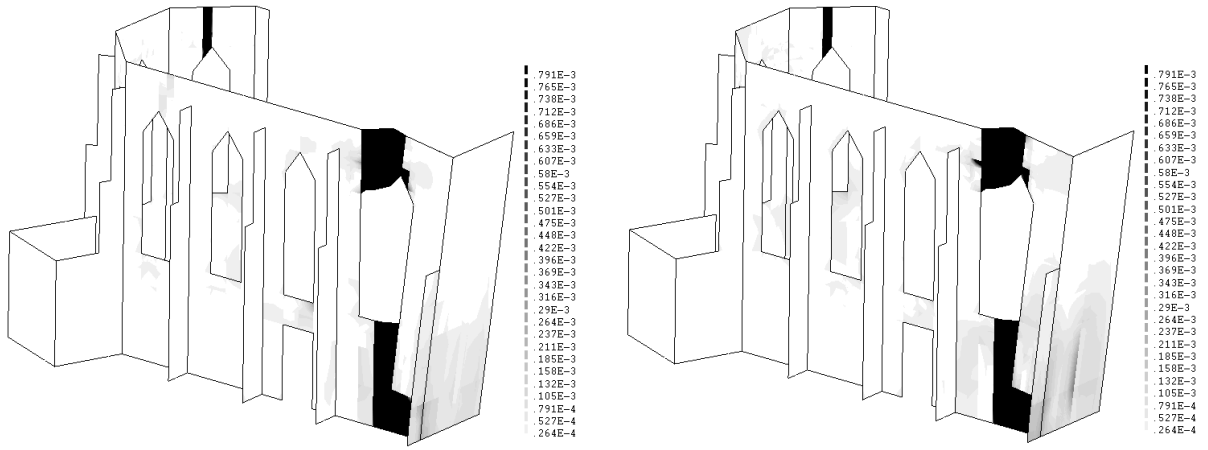

Figure 6.42. Principal tensile strains at stage (3) of the capacity curve calculated at (a) bottom and (b) top surfaces of the shell elements for pushover in –X' direction

6.7.4 Pushover analysis in Y' direction

The direction of the application of the load is shown in Figure 6.43-b. The node with the maximum displacement was node 3005 (see Figure 6.43-c) and it was selected to plot the capacity curve of the structure for this analysis which is shown in Figure 6.43-a. The lowest softening peak occurs at 0.13g which indicates the maximum capacity of the structure; anyway the path of the curve seems to be stabilized when the structure reaches a value of about 0.19g. This capacity is rather high than the capacity obtained for the pushover analysis in the global directions. Two different load stages were selected to calculate the damage pattern in terms of principal tensile strains and they were plotted.

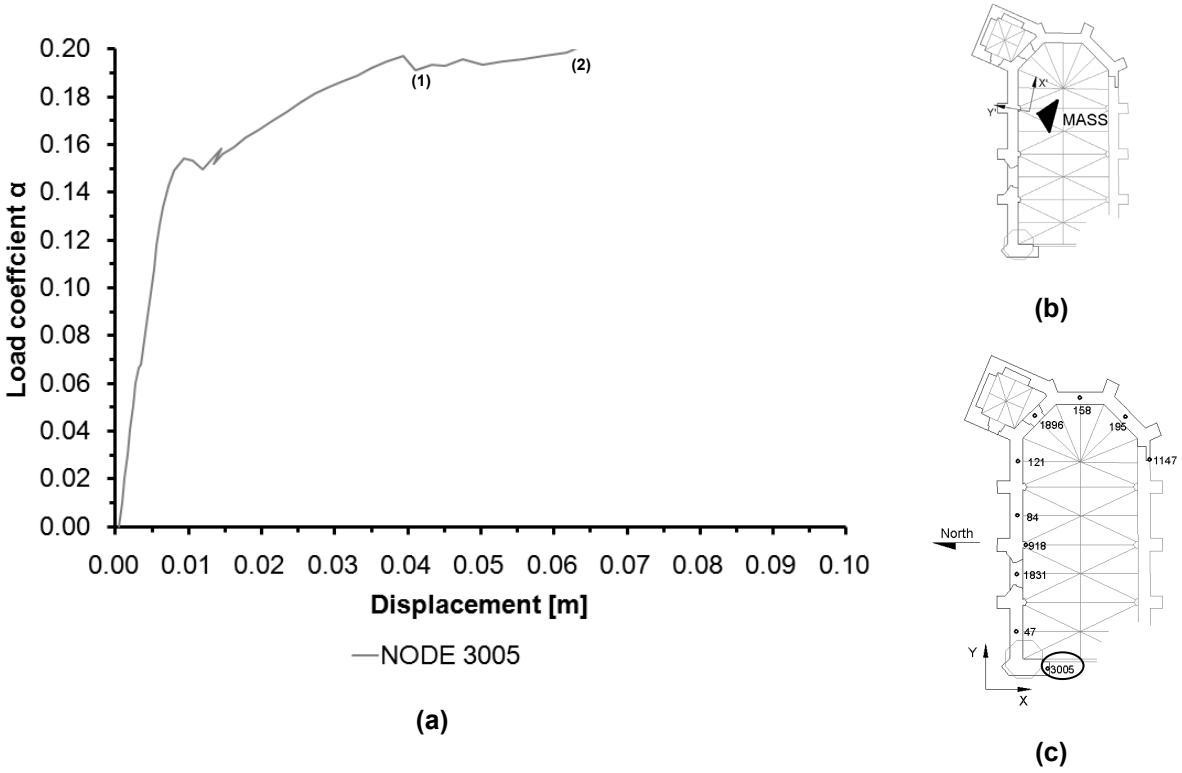

Figure 6.43. (a) Capacity curve of pushover analysis in Y' direction, (b) applied load direction and (c) selected control point

The damages regions at stages (1) and (2) are the same; above the first window to the right in the North façade and in the lower part of the West façade. The only difference is the increase of extension between the two load stages.

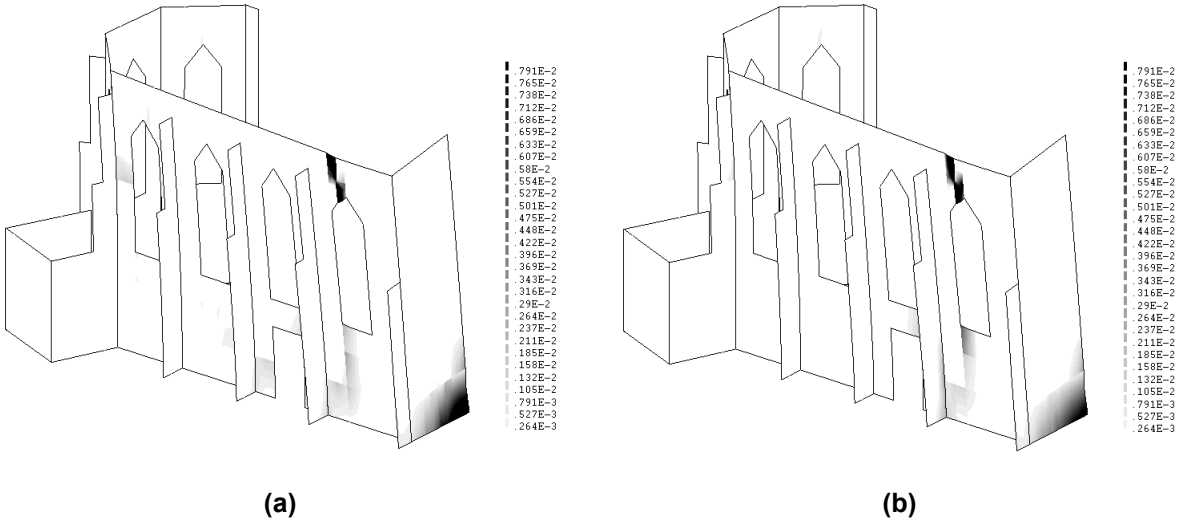

Figure 6.44. Principal tensile strains at stage (1) of the capacity curve calculated at (a) bottom and (b) top surfaces of the shell elements for pushover in Y' direction

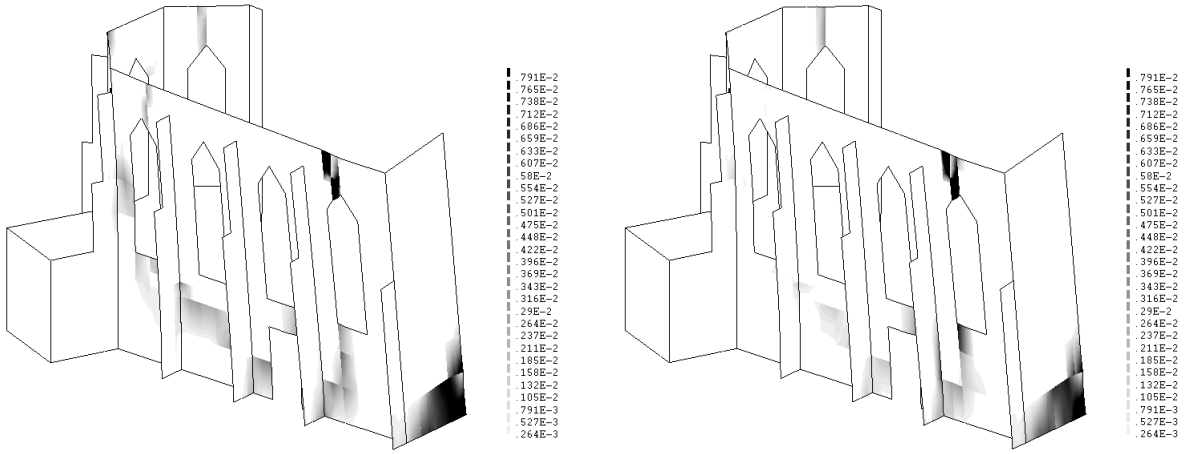

Figure 6.45. Principal tensile strains at stage (2) of the capacity curve calculated at (a) bottom and (b) top surfaces of the shell elements for pushover in Y' direction

6.7.5 Pushover analysis in –Y' direction

The direction of the application of the load is shown in Figure 6.46-b. The node with the maximum displacement was node 1831 (see Figure 6.46-c) and it was selected to plot the capacity curve of the structure for this analysis which is shown in Figure 6.46-a. The lowest softening peak occurs at 0.11g which indicates the maximum capacity of the structure; anyway the path of the curve seems to be stabilized when the structure reaches a value of about 0.14g. This capacity is similar to the capacity obtained for the pushover analysis in the global directions. Two different load stages were selected to calculate the damage pattern in terms of principal tensile strains and they were plotted.

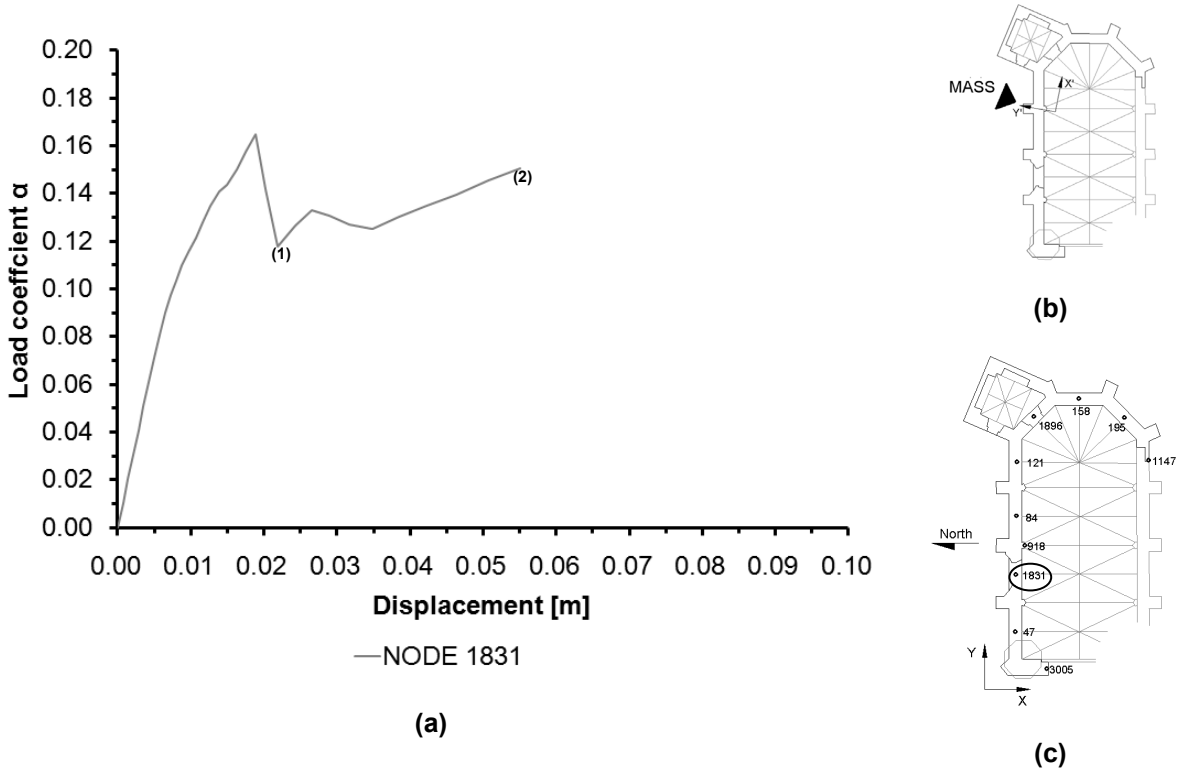

Figure 6.46. (a) Capacity curve of Pushover analysis in –Y' direction, (b) applied load direction and (c) selected control point

In this case the damage occurs at along the upper part of the connection between the West and the North facades, in the lower corner of that connection and above the first two windows to the right in the North façade. The difference between both stages is the intensity of the damage (see Figure 6.47. and Figure 6.48).

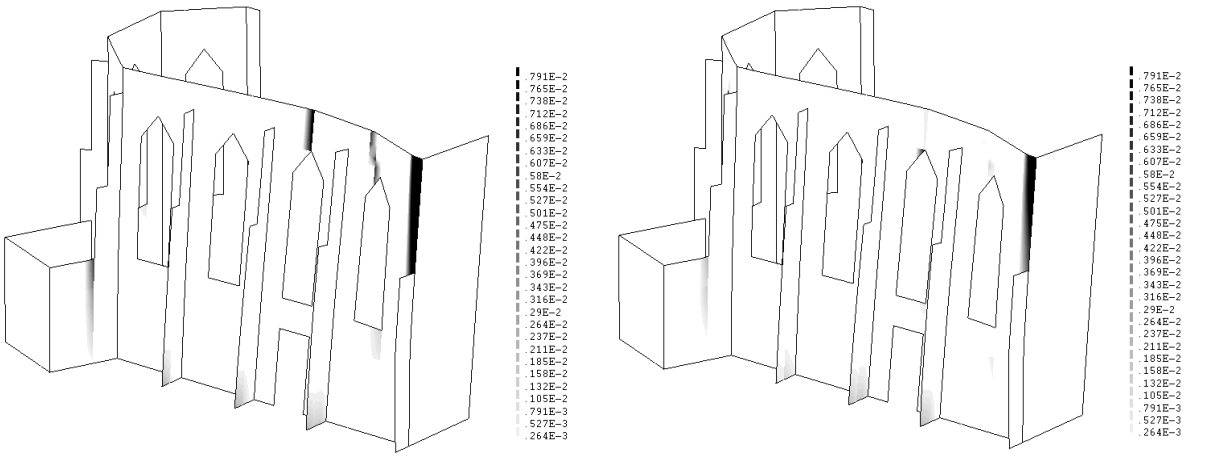

Figure 6.47. Principal tensile strains at stage (1) of the capacity curve calculated at (a) bottom and (b) top surfaces of the shell elements for pushover in –Y' direction

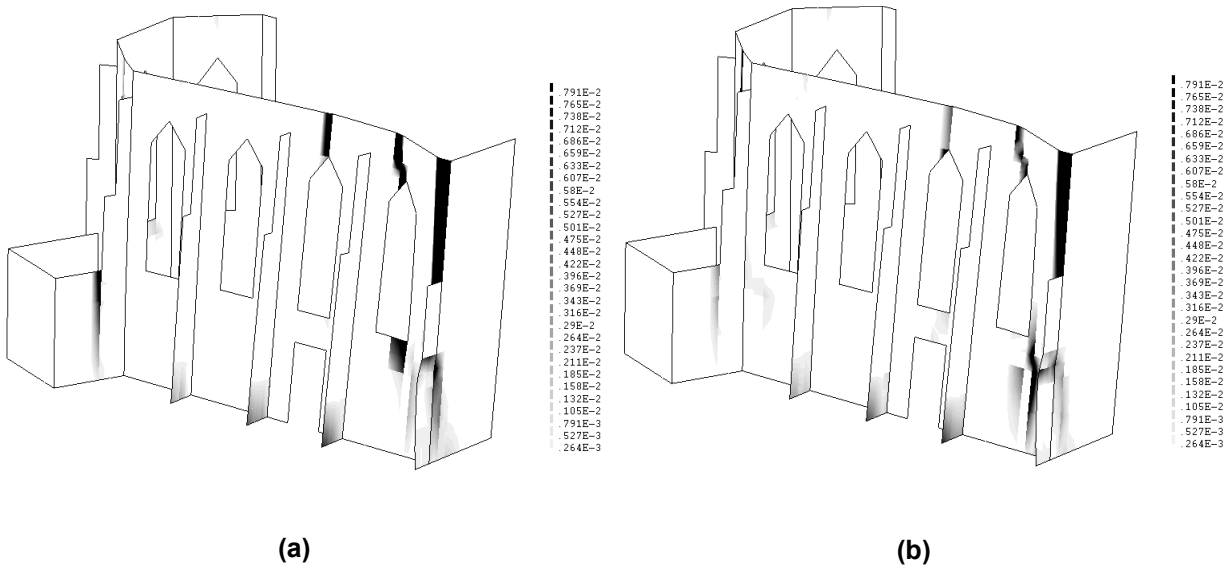

Figure 6.48. Principal tensile strains at stage (2) of the capacity curve calculated at (a) bottom and (b) top surfaces of the shell elements for pushover in –Y' direction

7. NON-LINEAR TIME HISTORY (DYNAMIC) ANALYSES

7.1 INTRODUCTION

The earthquake is reshown by means of ground motion parameters which are fundamental to describe the important characteristics of strong motion in a quantitative form. Therefore, for engineering purposes, the most significant characteristics of earthquake motion are: amplitude, frequency content and duration of motion, which are described by a time history of any of displacement, velocity or acceleration. The acceleration time history representation of the earthquake shows a significant proportion of relatively high frequencies, thus is most common to apply for describe the ground motion (Oliveira, 2008-2009). However, in code standard recommendations such as (EN 1998-1, 2004) is common to adopt the representation of the seismic action by means of the elastic response spectrum because it is a spectral representation of the peak response of single degree of freedom system with a given common damping ξ and natural periods T_n to a given seismic input motion. Thus, for a given input motion, it is possible to obtain several response spectra associated with different values of damping adopted (Mendes & Lourenço, 2008); which represent the response of an infinitive number of structures.

According to (EN 1998-1, 2004) the reference method for determining the seismic effects on the structure is the modal response spectrum analysis, using a linear-elastic model, especially for seismic design of new structures. In order to take into account the non-linear response of the structure (energy dissipation), a reduction factor is applied to the response of the structure (known as the behavior factor) and the obtained design forces are smaller than those corresponding to a linear elastic response (Oliveira, 2008-2009), however the application of this method may give conservative results but it is fast (in terms of computational cost). Nevertheless, it is also possible to apply non-linear methods such as dynamic analysis (also known as non-linear time history analysis) which should be properly substantiated with respect to the seismic input, the constitutive models used, the method of interpreting the results and the requirements to be met (EN 1998-1, 2004). Hereby for historical constructions which are cases out of the range of the (EN 1998-1, 2004) standards, this method is suitable by defining a proper seismic demand based on the real capacity to fulfill which should be less than the standards' requirements ((EN 1998-1, 2004) elastic response spectrum) and may be estimated in previous (linear and non-linear) analyses with less computer cost such as limit analysis and pushover analysis (Mendes & Lourenço, 2008); not to forget the proper application of the constitutive law of the material.

Hereby the structure was analyzed using Finite Element non-linear dynamic analysis where equilibrium and compatibility should be assessed to the structure in each time step following the equation of motion (see Equation 7.1). Meaning that for an external input that varies along time, the response of the structure (displacement, velocity and acceleration) will be also variable in time.

As a first step the horizontal seismic action was determined by means of two artificial accelerograms which are orthogonal and have independent components (EN 1998-1, 2004). These accelerograms were generated using the software SIMQKE_GR (Gelfi, 2006) and using as input, the parameters of the elastic response spectrum (type 1) defined by Cyprus National annex to Eurocode 8 (CYS EN 1998-1:2005, 2007) and the recommendations shown in section 3.2.3.1.2 in (EN 1998-1, 2004).

$$m \cdot \ddot{u}(t) + c \cdot \dot{u}(t) + k \cdot u(t) = p(t) \qquad 7.1$$

Where: m: is the mass matrix of the structure

$\ddot{u}(t)$: is the acceleration vector of the structure for time t

c: is the damping matrix of the structure

$\dot{u}(t)$: is the velocity vector of the structure for time t

k: is the stiffness matrix of the structure

$u(t)$: is the displacement vector of the structure for time t

$p(t)$: is the external applied dynamic force vector for time t

The constitutive model for the masonry and its non-linear properties (shown in Section 6.2) were also used for this task; in addition the damping ratio was defined using Rayleigh's formulation in order to compute the damping matrix. Then the non-linear dynamic analysis was performed using the finite element method with (DIANA, 2008) software. For this analysis, the Hilber-Hughes-Taylor time integration method was used and the iteration method applied was Regular Newton-Raphson in which the tangential stiffness matrix is computed before each iteration (see Section 6.4). The convergence criterion applied to assess equilibrium during the iteration process was the internal energy with a tolerance equal to 10^{-3}.

The obtained results were plotted in terms of Load coefficient (see Equation 6.1) and total displacement for each global direction (X and Y); the selected points were the same as those selected to plot the capacity curve of the structure in the pushover analyses (see Section 6.5); however the results obtained for each node from the selected set (see Figure 6.1-a) were compared to assure that the highest displacement was obtained for each direction. At the end, a comparison between the results of the kinematic analysis, pushover analysis and dynamic analysis, in terms of seismic response is done.

7.2 ARTIFICAL ACCELEROGRAMS

Two uncorrelated artificial accelerograms were defined in order to represent each seismic event; one accelerogram per each horizontal orthogonal direction. They were generated based on the elastic response spectra given in Section 3.2.2.2 of (EN 1998-1, 2004) (see Figure 7.1 and Equations 7.2 to

7.6) for 5% viscous damping ($\xi = 5\%$) which probability of exceedance is 10% and the return period is 475 years. The duration of the accelerograms shall be consistent with the magnitude and other relevant features of the seismic event such as PGA, but due to lack of site specific data, the adopted duration T_S of the stationary part of the accelerogram was 10 s (EN 1998-1, 2004) and for the transition parts a duration of 5 s was, obtaining total time duration of 20 s.

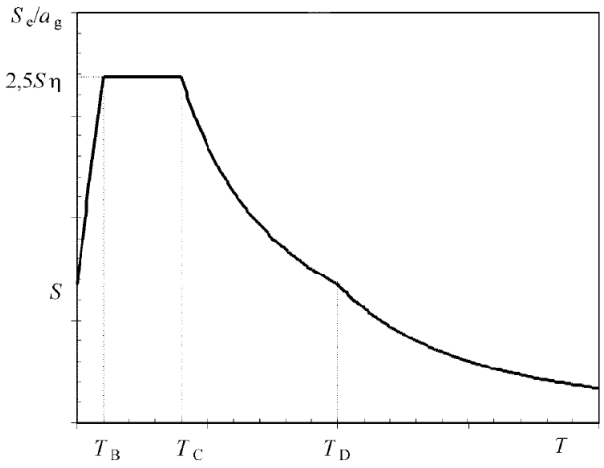

Figure 7.1. Shape of the elastic response spectrum defined in (EN 1998-1, 2004)

$$0 \le T \le T_B : \; S_e(T) = a_g \cdot S \cdot \left[1 + \frac{T}{T_B} \cdot (\eta \cdot 2.5 - 1)\right] \quad 7.2$$

$$T_B \le T \le T_C : \; S_e(T) = a_g \cdot S \cdot \eta \cdot 2.5 \quad 7.3$$

$$T_C \le T \le T_D : \; S_e(T) = a_g \cdot S \cdot \eta \cdot 2.5 \cdot \left[\frac{T_C}{T}\right] \quad 7.4$$

$$T_D \le T \le 4s : \; S_e(T) = a_g \cdot S \cdot \eta \cdot 2.5 \cdot \left[\frac{T_C \cdot T_D}{T^2}\right] \quad 7.5$$

$$\eta = \sqrt{10/(5+\xi)} \ge 0.55 \quad 7.6$$

Where:

$S_e(T)$: is the elastic response spectrum

T: is the vibration period of a linear single-degree-of-freedom system

a_g: is the design ground acceleration on type A ground

T_B: is the lower limit of the period of the constant spectral acceleration branch

T_C: is the upper limit of the period of the constant spectral acceleration branch

T_D: is the value defining the beginning of the constant displacement response range

S: is the soil factor

η: is the damping correction factor ($\eta = 1$ for 5% viscous damping)

The values for calculate the elastic response spectrum (Equations 7.2 to 7.6) were obtained from the Cyprus National annex to Eurocode 8, which is shown in (CYS EN 1998-1:2005, 2007), and the parameters are reported in Figure 7.2., where the ground type E parameters were selected according to the geological conditions of Famagusta shown in Section 2.2.3 (see Figure 2.7). Besides, it was also necessary to obtain the peak ground acceleration for Famagusta a_g which was previously obtained from the seismic hazard map shown in Figure 2.6 and its value is 0.25 g.

Ground Type	S	T_B (s)	T_C (s)	T_D (s)
A	1,0	0,15	0,4	2,0
B	1,2	0,15	0,5	2,0
C	1,15	0,20	0,6	2,0
D	1,35	0,20	0,8	2,0
E	1,4	0,15	0,5	2,0

Figure 7.2. Values of the parameters that describe elastic response spectrum type1 (CYS EN 1998-1:2005, 2007)

The above mentioned values were replaced in Equations 7.2 to 7.6 and the obtained response spectrum for Famagusta and ground conditions Type E is shown in Figure 7.3.

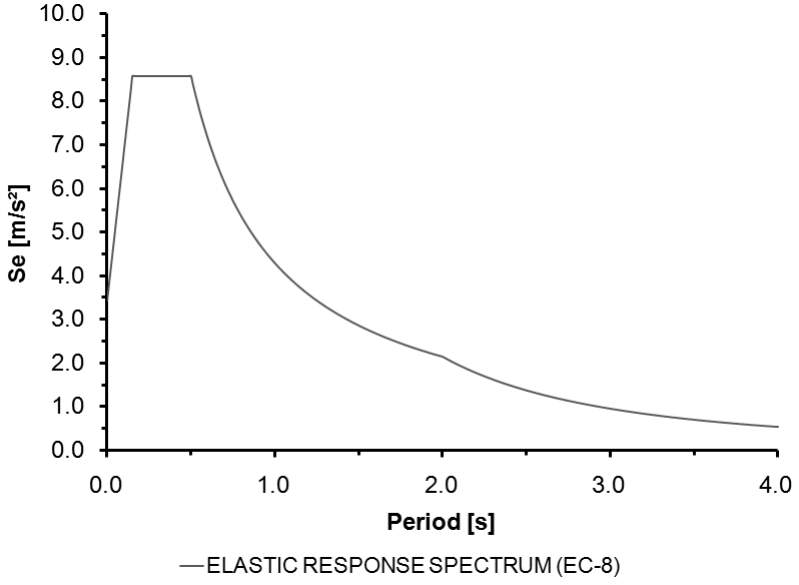

Figure 7.3. Elastic response spectrum for Famagusta and ground conditions type E

This response spectrum was used to calculate the two artificial accelerograms using the software SIMQKE_GR (Gelfi, 2006) which can be obtained from the same response spectrum but they must be uncorrelated (EN 1998-1, 2004). Also a base line correction filter was applied using SeismoSignal (Seismosoft, 2004), in order to force the time-history of the displacements to start and end with a value of 0 meters.

As it was discussed (see Section 7.1) the proper seismic demand may be estimated from previous analysis in order to fulfill the structure real capacity. Therefore, the results obtained from pushover analyses (see Chapter 6) were used and the maximum Load coefficient that structure is able to bear is 0.03 g and it happens when the horizontal load pattern is proportional to the 3rd mode configuration. Hereby the artificial accelerograms were scaled in order to reach maximum peak ground acceleration a_g equal to 0.05 g (Earthquake 1) and 0.06 g (Earthquake 2). The time-history of the acceleration and displacement are shown in Figure 7.4 (Earthquake 1) and Figure 7.5 (Earthquake 2) and the elastic response spectrum for each Earthquake is shown in Figure 7.6.

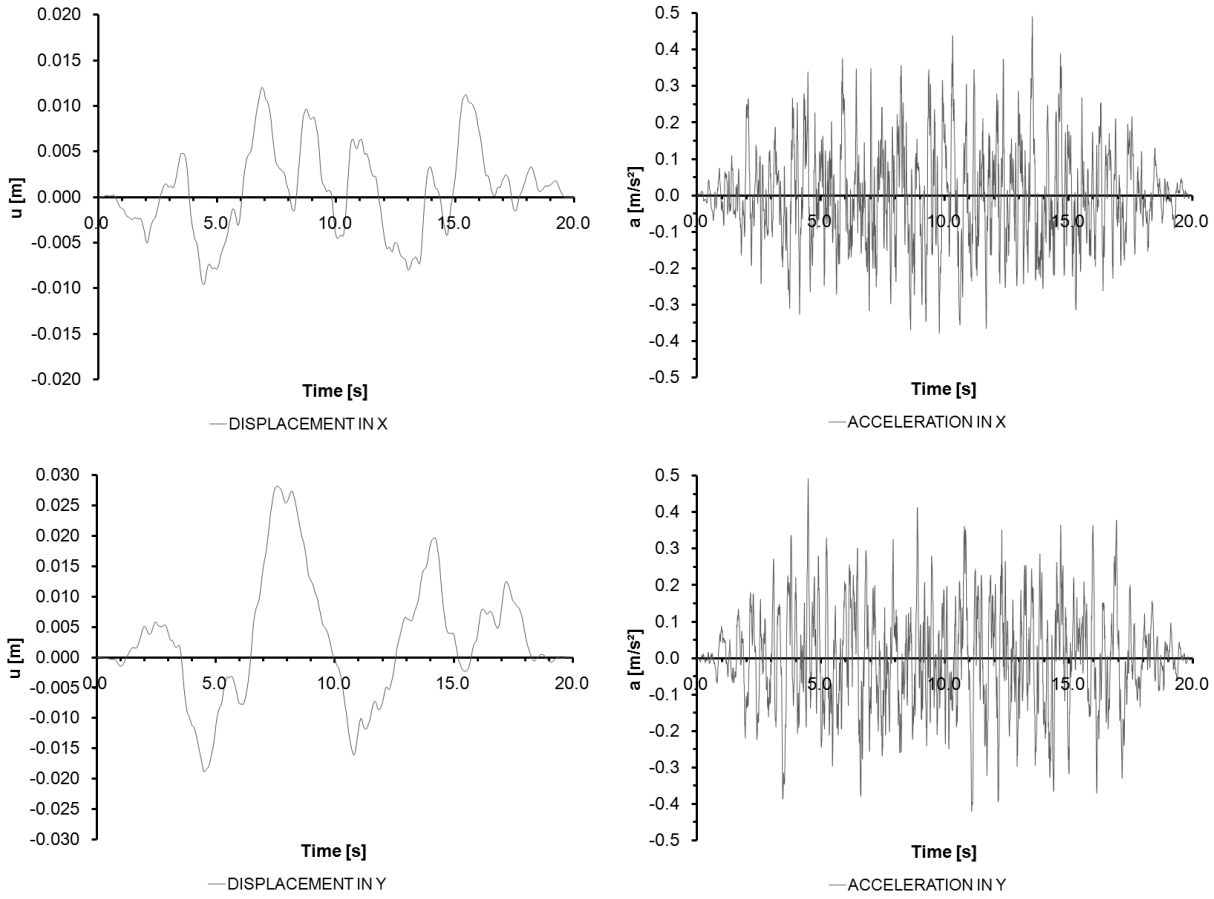

Figure 7.4. Earthquake 1 artificial accelerograms (in each global direction) with the applied time history of displacements

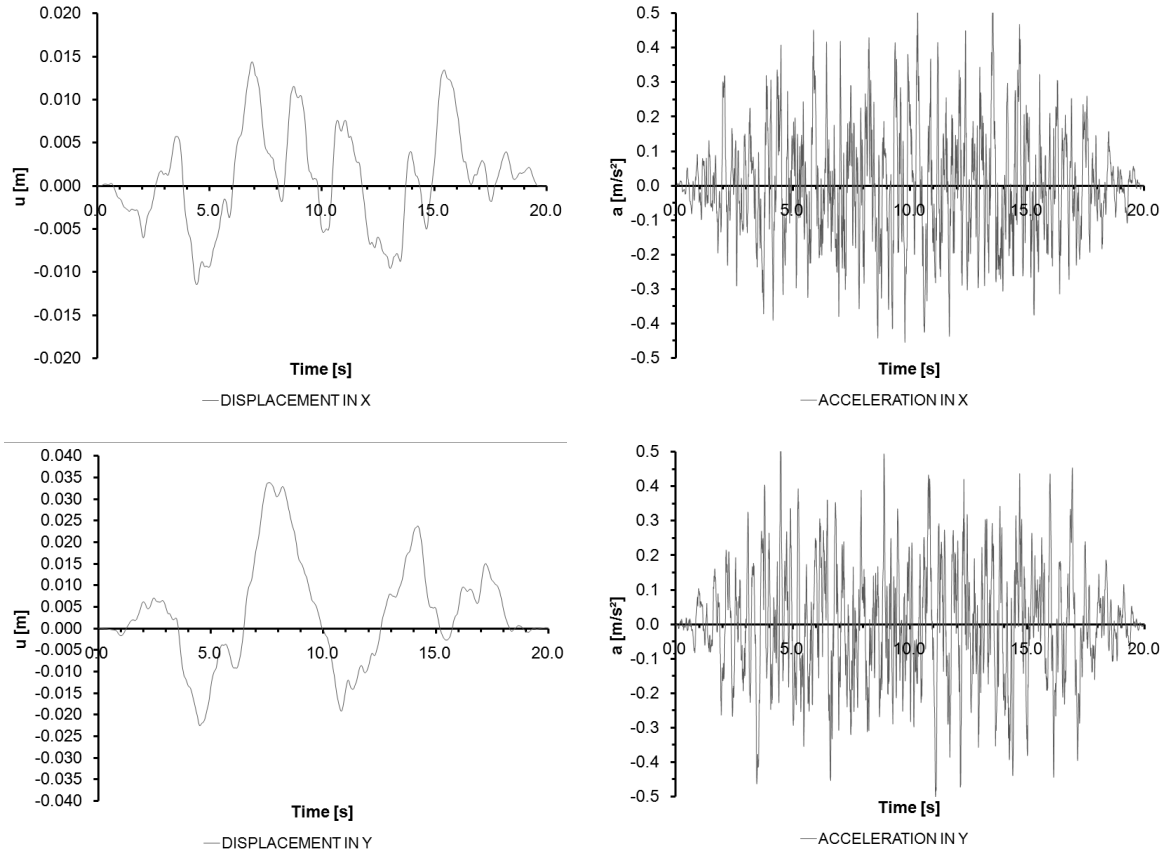

Figure 7.5. Earthquake 2 artificial accelerograms (in each global direction) with the applied time history of displacements

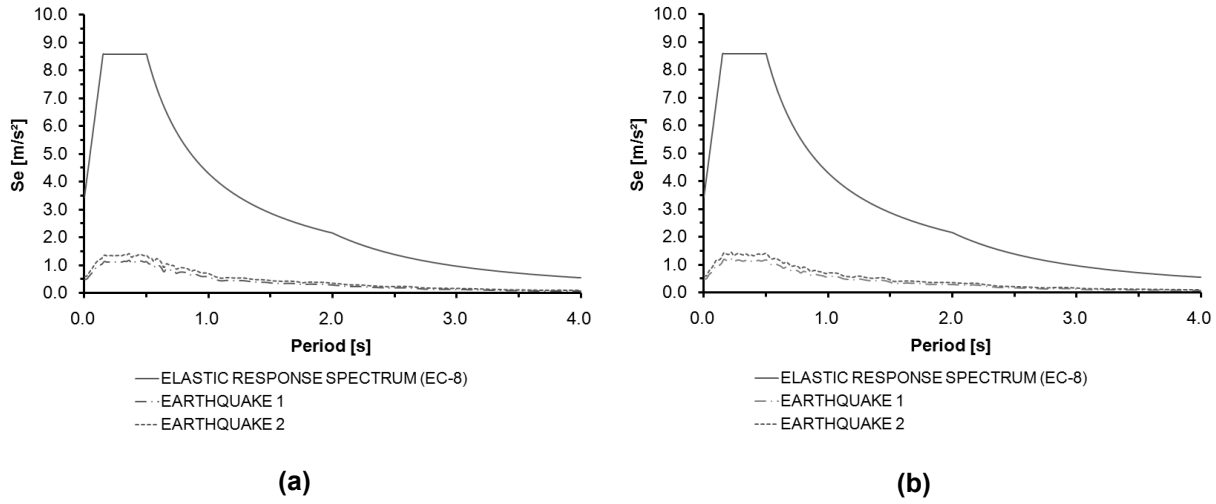

Figure 7.6. Elastic response spectrum: (a) in X direction and (b) in Y direction

7.3 MATERIAL DAMPING

The classical damping is an attempt to idealize the dissipation of energy in a structure, without damping the structure simple maintains its vibration state when subjected to dynamic excitation. There is one procedure described in (Chopra A. K., 2000) to determine Rayleigh damping (see Equation 7.7) as a linear combination of mass matrix and stiffness matrix. There are several inconvenient when the damping is assumed linear proportional to either the mass matrix or the stiffness matrix because the modal damping ratios variations are not consistent with the natural frequencies that they represent; hereby this procedure is consistent with experimental data (Chopra A. K., 2000).

$$c = a_0 \cdot m + a_1 \cdot k \qquad 7.7$$

Where:

c: is the damping matrix of the structure

a_0: is the first Rayleigh coefficient

m: is the mass matrix of the structure

a_1: is the second Rayleigh coefficient

k: is the stiffness matrix of the structure

In order to obtain the two Rayleigh coefficients a_0 and a_1 for a given damping ratio ξ it is necessary to solve a system of two equations which gives as result Equations 7.8 and 7.9.

$$a_0 = \xi \cdot \frac{2 \cdot \omega_i \cdot \omega_j}{\omega_i + \omega_j} \qquad 7.8$$

$$a_1 = \xi \cdot \frac{2}{\omega_i + \omega_j} \qquad 7.9$$

Where:

ω_i: is the angular frequency of the *i-th* mode

ω_i: is the angular frequency of the *j-th* mode

ξ: is the damping ratio of the *i-th* and *j-th* modes

In order to apply this procedure the modes *i* and *j* should be chosen to ensure reasonable values for the damping ratios in all the modes that significantly contribute to the structure response (Chopra A. K., 2000). After find Rayleigh coefficients is possible to calculate the damping ratio for the rest of the modes applying the Equation 7.10.

$$\xi_n = \frac{a_o}{2} \cdot \frac{1}{\omega_n} + \frac{a_1}{2} \cdot \omega_n \qquad 7.10$$

Where:

ω_n: is the angular frequency of the *n-th* mode

Therefore in order to estimate Rayleigh damping coefficients, which will be the input of material damping model in the numerical analyses, mode 1 and 31 were chosen as the *i-th* and *j-th* modes (2.43 Hz and 21.86Hz), despite the fact that their cumulative mass participation factors is lower than 90% (see Table 7.1). It was seen that after damping ratio calculation, the results are reliable for expected damping ratios common in this kind of structures. It is important to remark that the experimental results of damping estimation were disregarded because according to (Lourenço & Ramos, 2008) the obtained damping ratio (1.26%) is rather low due to the used of ambient vibrations to excite the structure, thus a damping ratio of 5% was adopted for the selected modes and the damping coefficient distribution along the modes is shown in Figure 7.7. Finally, the obtained values for Rayleigh coefficients were 1.37432 and 0.00065.

Mode	Frequency [Hz]	MASS PART X [%]	CUM. [%]	MASS PART Y [%]	CUM. [%]
1	2.43	32.49	32.49	0.01	0.01
2	2.82	0.00	32.49	9.05	9.06
3	3.19	5.47	37.97	12.34	21.41
4	3.95	1.21	39.17	7.83	29.24
5	4.98	13.45	52.63	8.55	37.79
6	5.29	2.96	55.59	3.41	41.20
7	5.89	0.86	56.45	14.65	55.85
8	7.17	0.11	56.56	0.24	56.09
9	8.69	6.69	63.24	0.38	56.47
10	9.25	1.89	65.14	0.78	57.25
11	9.63	0.34	65.47	0.75	58.00
12	10.12	0.32	65.79	3.68	61.68
13	11.31	0.00	65.79	0.07	61.75
14	12.76	0.00	65.80	0.17	61.92
15	13.77	1.06	66.85	2.99	64.91
16	14.49	2.61	69.46	0.01	64.92
17	15.01	0.21	69.67	0.28	65.20
18	15.73	0.41	70.08	1.34	66.54
19	16.62	0.03	70.11	0.00	66.54
20	16.94	0.16	70.27	0.44	66.98
21	17.22	0.03	70.31	0.00	66.98
22	17.74	1.16	71.47	3.86	70.84
23	18.25	0.30	71.76	0.00	70.84
24	19.42	4.52	76.28	0.03	70.88

25	19.58	1.59	77.88	0.00	70.88
26	20.13	0.01	77.88	0.00	70.88
27	20.28	0.72	78.61	2.27	73.15
28	20.49	0.02	78.63	1.53	74.68
29	21.03	2.23	80.86	2.33	77.01
30	21.53	0.49	81.35	0.04	77.05
31	21.86	0.00	**81.35**	4.69	**81.74**

Table 7.1. Contribution of vibration modes to mass excitation in each direction

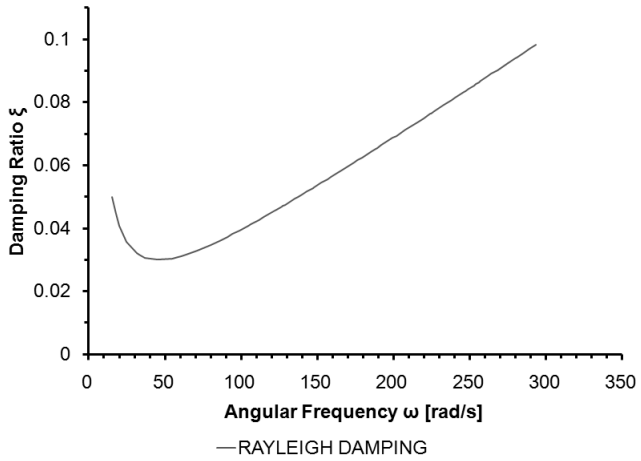

Figure 7.7. Rayleigh damping distribution along the modes for coefficients equal to 1.37432 and 0.00065

7.4 TIME INTEGRATION METHOD

In order to find the solution of the equation of motion (see Equation 7.1) when the excitation varies arbitrarily with time it is necessary to apply numerical time-stepping methods for find the integral of differential equations. The applied load $p(t)$ is given by a set of discrete values $p(t_i)$ which distribution is determined by the selection of time interval Δt_i which is usually constant. The response of the structure is determined at that discrete time instant t_i where all the values are known, then using numerical procedures, the response of the structure at time instant t_{i+1} is found. This procedure is approximate and it should assure convergence, stability and accuracy. But there are two different types: explicit and implicit methods. Using explicit methods, all unknown parameters can be computed without need to solve the equation of motion but the solution becomes unstable at largest time steps. In contrast, using the implicit methods all the unknowns can be computed by solving the equation of motions and the solution can be unconditionally stable if the control parameter as properly chosen (Oliveira, 2008-2009).

Therefore, the Hilber-Hughes-Taylor (HHT) method (also known as α method) was chosen. It is a implicit integration method (a generalization of Newmark's method) that eliminates the influence of non-realistic modes (higher frequency oscillations) by introducing numerical damping of higher frequencies; it is stable and has second order convergence. The solution for the response parameters in each time step is given by Equations 7.11 and 7.12.

$$\dot{u}_{t+\Delta t} = \dot{u}_t + [(1-\gamma)\cdot \ddot{u}_t + \gamma \cdot \ddot{u}_{t+\Delta t}] \quad 7.11$$

$$u_{t+\Delta t} = u_t + \dot{u}_t \cdot \Delta t + \left[\left(\frac{1}{2} - \beta\right)\cdot \ddot{u}_t + \beta \cdot \ddot{u}_{t+\Delta t}\right]\cdot \Delta t^2 \quad 7.12$$

Where: Δt: is the time step increment

$\ddot{u}_t$: is the acceleration vector of the structure for time t

$\dot{u}_t$: is the velocity vector of the structure for time t

u_t: is the displacement vector of the structure for time t

$\ddot{u}_{t+\Delta t}$: is the acceleration vector of the structure for time $t + \Delta t$

$\dot{u}_{t+\Delta t}$: is the velocity vector of the structure for time $t + \Delta t$

$u_{t+\Delta t}$: is the displacement vector of the structure for time $t + \Delta t$

The parameters α, β and γ control the integration scheme and they should follow Equations 7.13, 7.14 and 7.15 in order to bring unconditional stability and second order accuracy. For this particular case α was made equal to -0.1 following recommendations shown in (DIANA, 2008).

$$\gamma = \frac{1}{2}\cdot(1-2\alpha) \quad 7.13$$

$$\beta = \frac{1}{4}\cdot(1-\alpha)^2 \quad 7.14$$

$$-0.3 \leq \alpha \leq 0 \quad 7.15$$

The equation of motion (see Equation 7.1) is transformed into the Equation 7.16 during the application of the method.

$$m\cdot\ddot{u}_{t+\Delta t} + (1+\alpha)\cdot c\cdot\dot{u}_{t+\Delta t} - \alpha\cdot c\cdot\dot{u}_t + (1+\alpha)\cdot f^{int}_{t+\Delta t} - \alpha\cdot f^{int}_t = (1+\alpha)\cdot p(t+\Delta t) + \alpha\cdot p(t)\cdot \quad 7.16$$

Where:

The parameters have the same meaning as that shown in previous Equations (see Equation 7.1 and Equations 7.11 to 7.15)

f^{int}_t: is the vector with internal forces ($f = k\cdot u$) for time t

$f^{int}_{t+\Delta t}$: is the vector with internal forces for time $t + \Delta t$

As it was abovementioned the selection of the correct time increment Δt is fundamental for the correct dynamic response representation. Therefore, two different criteria were taken into account in order to define this parameter: (i) the time increment should be small enough in comparison with the total duration of the accelerogram (see Equation 7.17) (DIANA, 2008), and (ii) in order to guarantee the contribution of the higher modes with 5% of error, 20 time increments should be taken into account for the smaller period T_i (see Equation 7.18) (Mendes & Lourenço, 2008).

$$\Delta t \ll t \tag{7.17}$$

$$\Delta t = \frac{1}{20} T_i \tag{7.18}$$

In order to apply criterion number (ii), the small period which fulfils the requirements exposed in (EN 1998-1, 2004) (cumulative mass participation factor higher or equal to 90% in all directions) is 0.0227s by replacing this value in Equation 7.18 the obtained time increment Δt is of 0.001137 s, which gives 17596 number of time steps (for accelerogram duration of 20 s); this huge number of time steps require high computer calculation time, hereby this criteria was disregarded.

Applying criterion number (i), a time step equal to 0.004 s was defined which is much smaller than 20 s, therefore 5000 time steps were required to accomplish each non-linear time history analysis and each of them took 3.0 days in a Pentium(R) D CPU 3.40 GHz with 1.0 GB de RAM (DDR2 - 667 MHz).

7.5 RESULTS OF THE ANALYSES

Two different dynamic analyses were performed to the structure with different values of the PGA; the Earthquake 1 was defined for a maximum peak ground acceleration of 0.05g and the Earthquake 2 was defined for a maximum peak ground acceleration of 0.06g. It is important to remark that two additional earthquakes were defined for a PGA of 0.07g and 0.10g, but the analysis had several convergence problems. The first attempt to solve the problem was to increase the number of time steps to 17596 by applying the criterion (ii) exposed in Section 7.4, but the convergence problem appeared again. Then, the tensile fracture energy was incremented in 5 times the base value, but still the analysis did not converge.

7.5.1 Earthquake 1 (Maximum PGA equal to 0.05g)

During the dynamic analysis, the damage pattern along the time steps coincide with the damage patterns found in the pushover analyses. The evolution of damage along the time steps is shown in Figure 7.8 and the maximum damaged pattern found along the time steps is shown in Figure 7.9. in which is clear the presence of three damages regions. One is located above the Apse window, another one is located above the first window to the right in the North façade and the last region is located in below the same window and it seems that the maximum damage conditions are not enough

to cause the collapse of the structure; and possible they are local failures. It is important to highlight that during the application of the dynamic load the cracks that appear among the structure may open and close in each time step. The position of the damaged regions coincide with the assumed position of some plastic hinges assumed in the kinematic analysis of the collapse mechanisms, but there are not enough number of hinges to cause the collapse of the structure according to the collapse mechanism configuration (see Chapter 3).

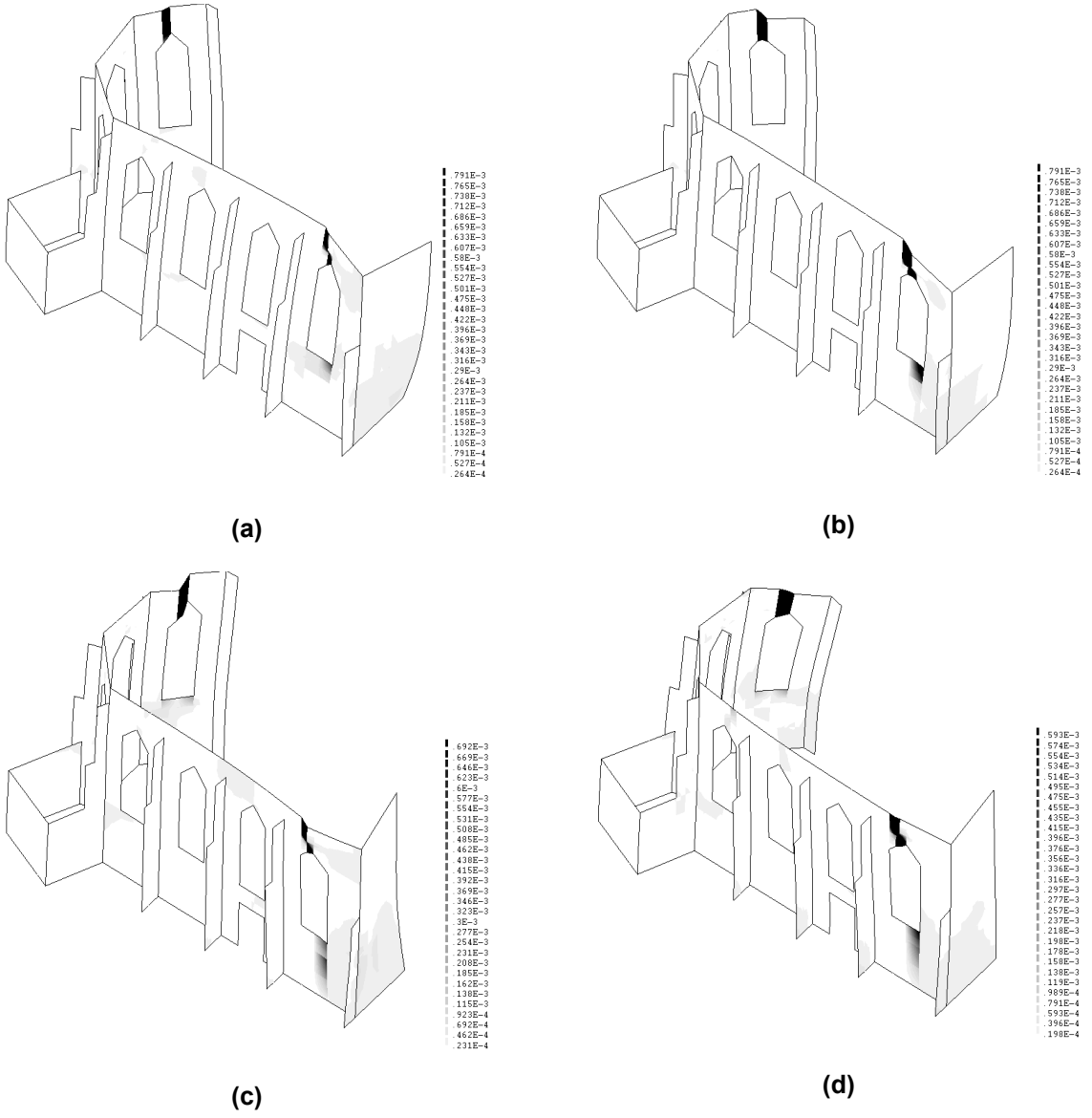

Figure 7.8. Principal tensile strains distribution (damage progress) along different time steps: (a) 4.96s, (b) 7.46s, (c) 12.50s and (d) 15.00s for the Earthquake 1

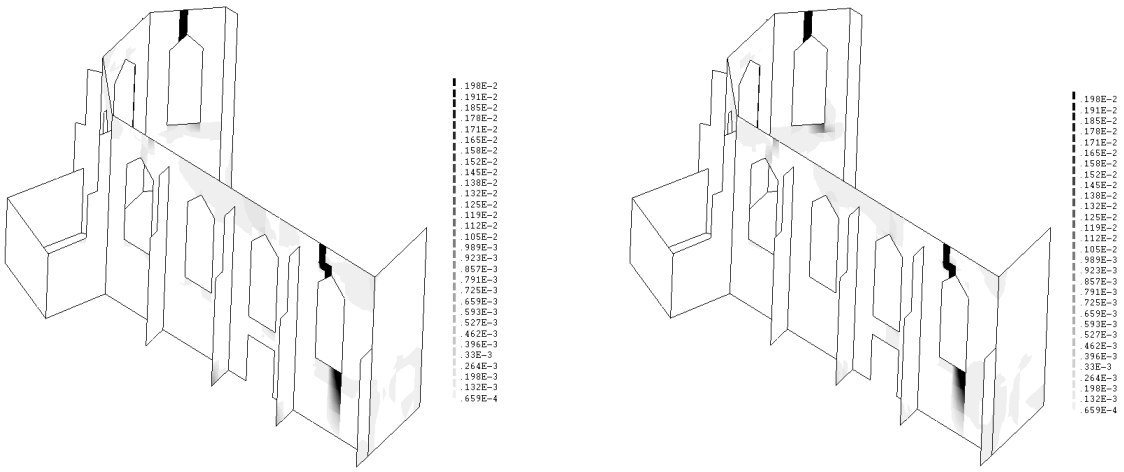

Figure 7.9. Output of the scan of the maximum principal tensile strains along all the time steps for Earthquake 1 calculated for (a) bottom and (b) top surfaces of shell elements

The evolution of the Load coefficient along the time steps is shown in Figure 7.10 for X direction and in Figure 7.11 for Y direction. In X direction node 918 and node 1831 were selected to plot the figures, and a maximum Load coefficient of 0.06g was reached and about 0.01m of maximum displacement. In Y direction, the figures were plotted in nodes 195 and 3005 and the maximum Load coefficient obtained for this direction was also 0.06g, the maximum displacement was about 0.012m. From these results it is possible to probe that the structure is safe when a maximum PGA of 0.05g is applied, and still the displacements on the structure are small.

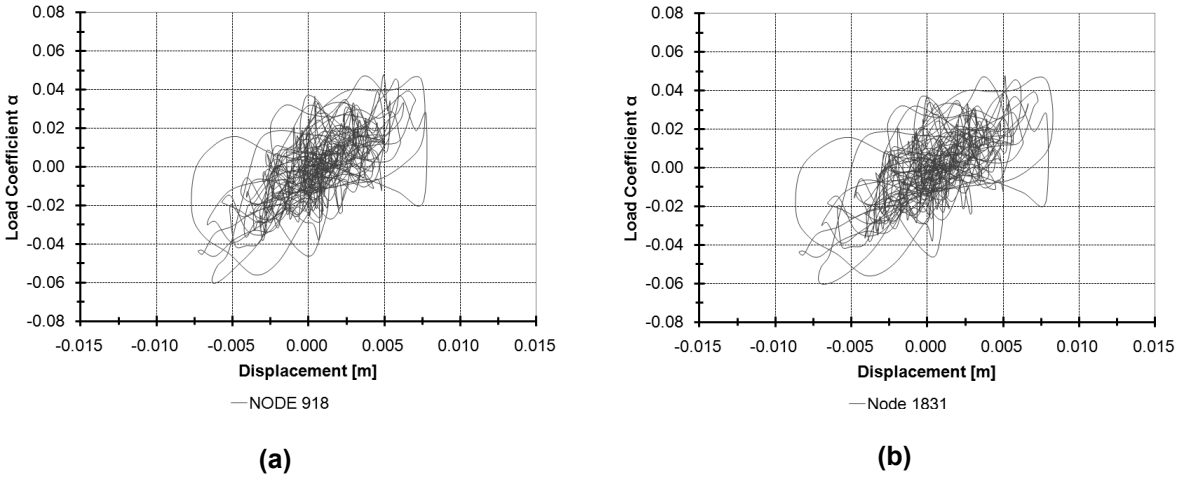

Figure 7.10. Load coefficient evolution in X direction along time for Earthquake 1 in (a) node 918 and (b) node 1831

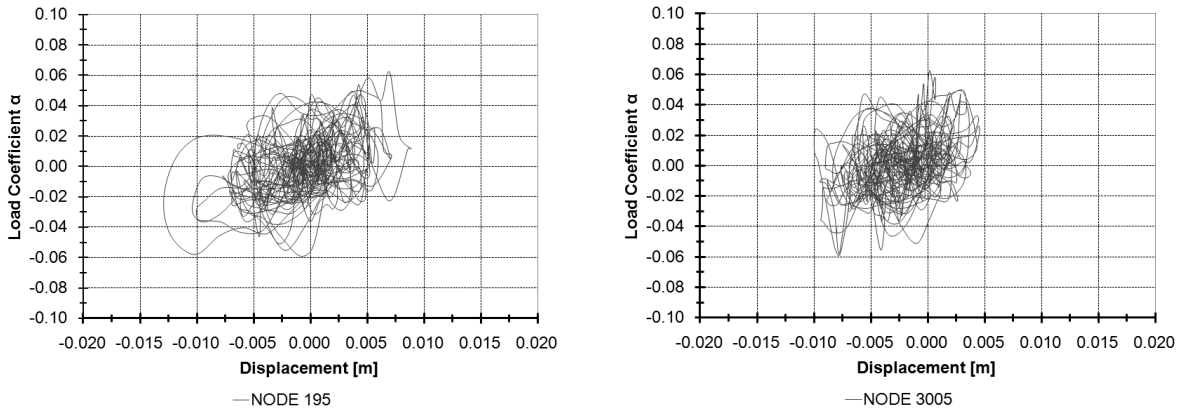

(a) **(b)**

Figure 7.11. Load coefficient evolution in Y direction along time for Earthquake 1 in (a) node 195 and (b) node 3005

7.5.2 Earthquake 2 (Maximum PGA 0.06g)

The damage pattern along the time steps was plotted over each time step founding that the intensity of the damage is increase as that from the damage conditions obtained from the previous dynamic analysis; some time steps were selected to plot the damage and they are shown in Figure 7.12. In this analysis is possible that the cracks open and close along the different time steps, hereby it was necessary to perform a scan through all the time steps finding the maximum damage conditions of the structure (see Figure 7.13). The damage pattern found in the structure coincides with the damage patterns found in the pushover analyses, and with the damage pattern found in the previous analysis (Earthquake 1). Two new damage regions appeared in the structure, one is located in the first widow to the left in the North façade and the other one is located in the lower part of right window in the Apse. Still, the maximum damage conditions are not enough to cause the collapse of the structure; and they are local failures. The position of the damaged regions also, coincide with the assumed position of the plastic hinges assumed in the kinematic analysis of the collapse mechanisms, but there are not enough number of hinges to develop the collapse mechanism analyzed in Chapter 3.

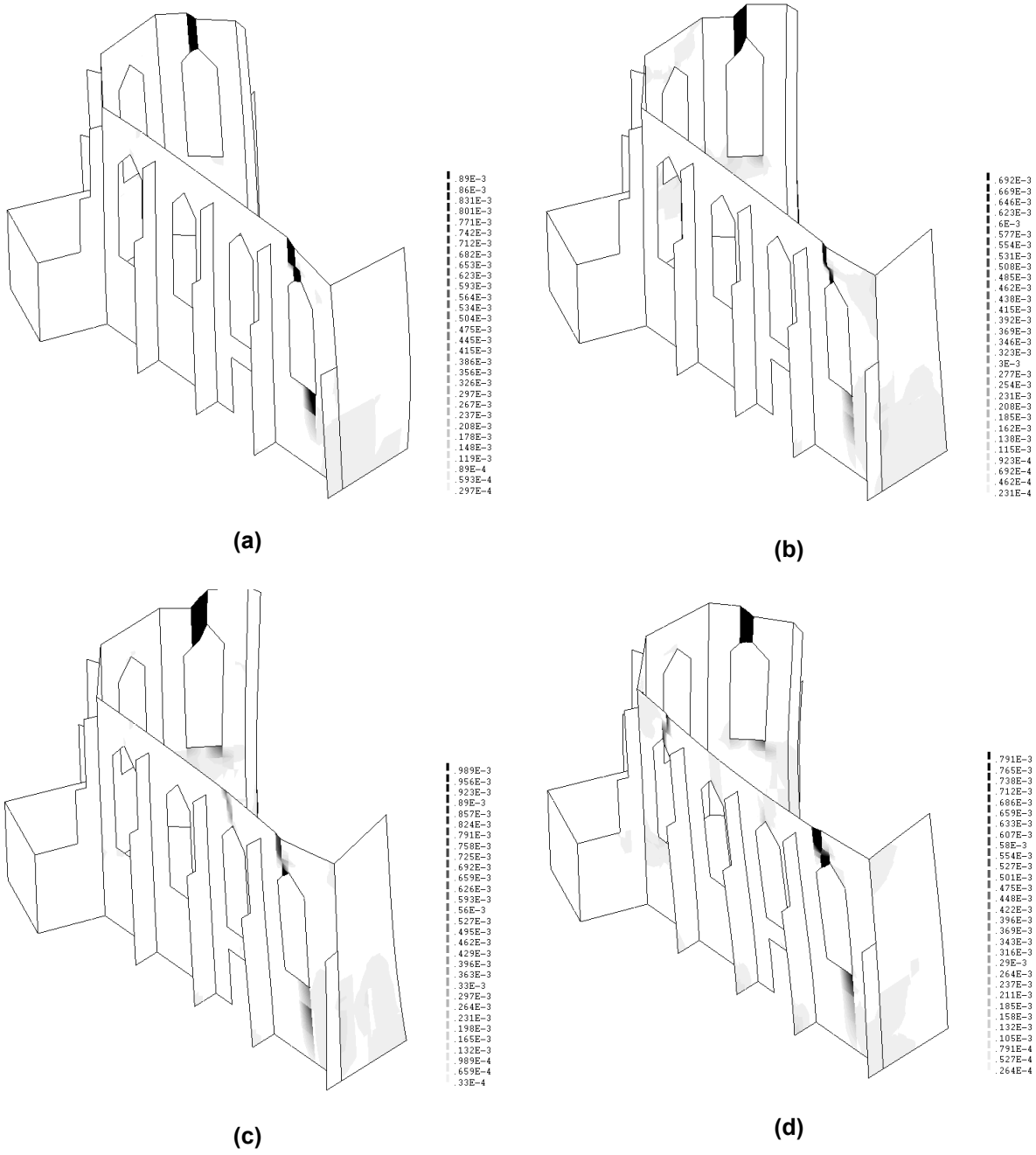

Figure 7.12. Principal tensile strains distribution (damage progress) along different time steps: (a) 7.46s, (b) 9.96s, (c) 12.50s and (d) 15.00s for the Earthquake 2

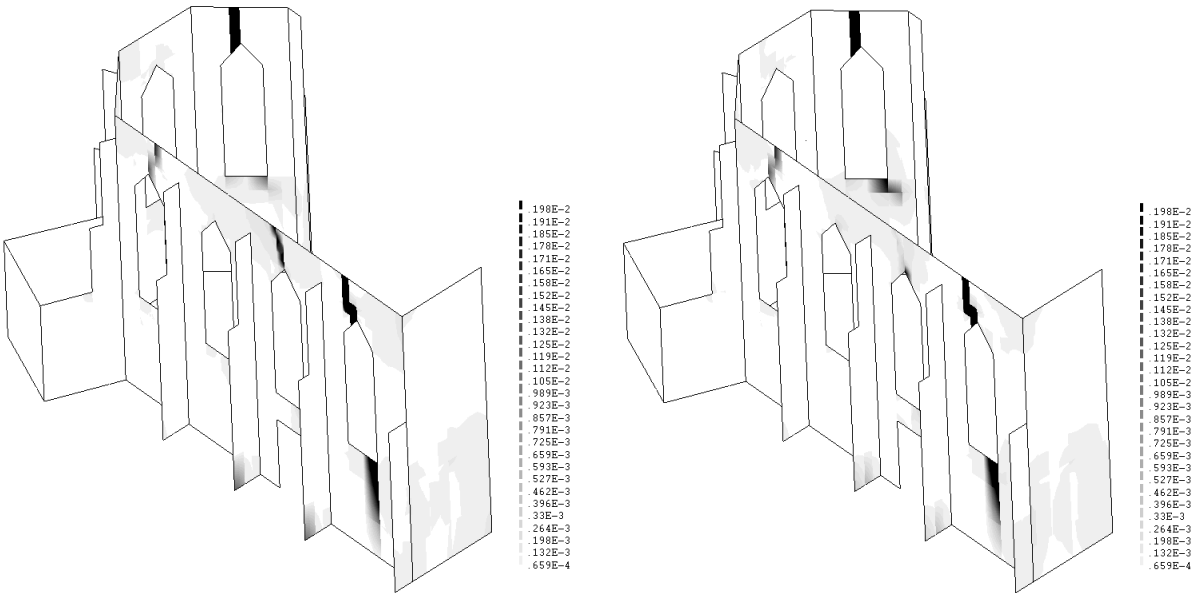

Figure 7.13. Output of the scan of the maximum principal tensile strains along all the time steps for Earthquake 2 calculated for (a) bottom and (b) top surfaces of shell elements

The evolution of the Load coefficient along the time steps is shown in Figure 7.14 and Figure 7.15 for X and Y directions respectively. The same nodes as those selected for the previous analysis in both directions were used to plot the response of the structure. A maximum Load coefficient of 0.07g was found in X direction and in Y direction it was about 0.08g. The maximum displacements found were about 0.01m in X direction and 0.017m in Y direction, but still those displacements are small to think about a possible collapse of the structure. From these results it is possible to probe that the structure is safe when a maximum PGA of 0.06g is applied, and still the displacements on the structure are small.

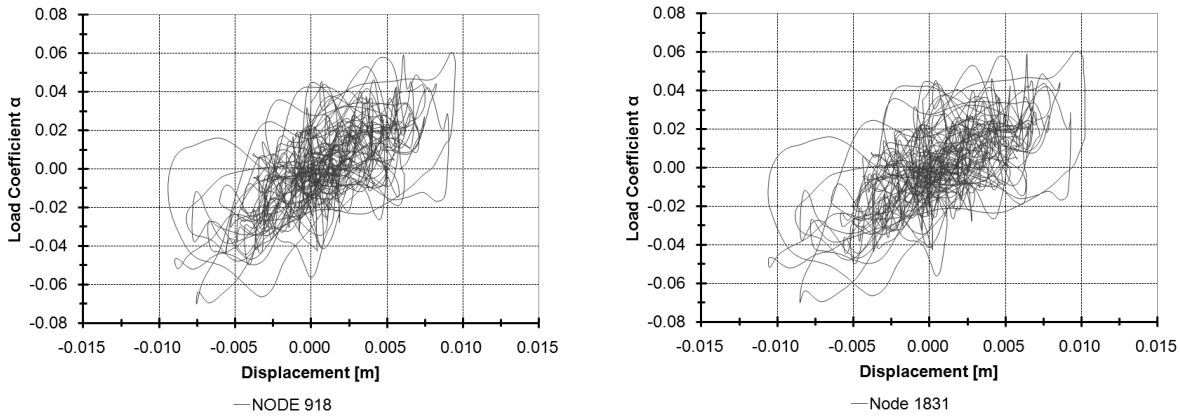

(a) **(b)**

Figure 7.14. Load coefficient evolution in X direction along time for Earthquake 2 in (a) node 918 and (b) node 1831

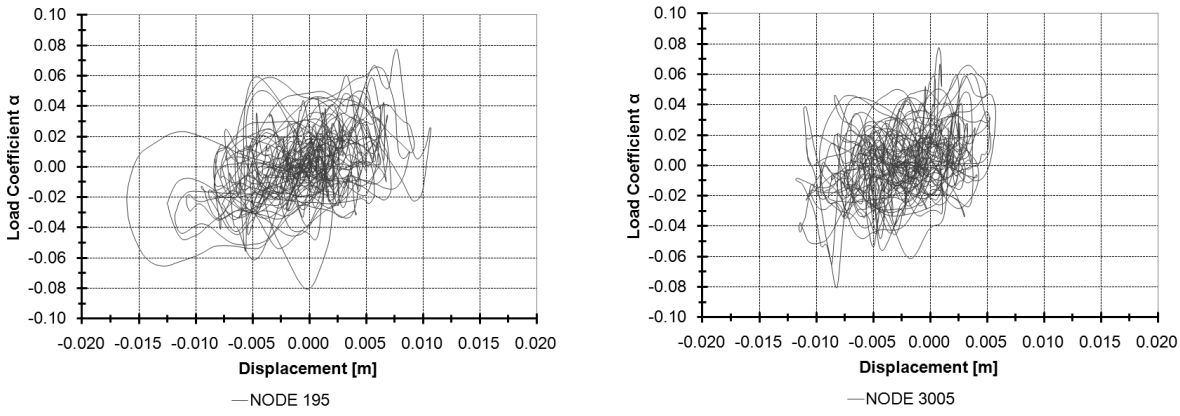

(a) **(b)**

Figure 7.15. Load coefficient evolution in Y direction along time for Earthquake 2 in (a) node 195 and (b) node 3005

8. CONCLUSIONS

A detailed study of the stability of Saint George of the Latins church under gravity loading and earthquake loading was carried out using different level of approach to the problem. First, a simple mechanical approach was used by the application of kinematic analysis of collapse mechanism. Then a non-linear static approach was applied using calibrated finite element models to perform classic pushover analyses. Finally a non-linear dynamic approach was applied using advanced numerical modeling with time integration. The safety of the structure was assessed with the three different approaches and it was possible to conclude the following ideas:

- When the safety of the structure was assessed by kinematic analysis of collapse mechanism, the obtained values are absolute lower bounds of the solution. This is justified by the application of simplified mechanical models which do not take into account the contribution of three dimensional mechanisms as the horizontal bending of the macro-elements. Nevertheless, the obtained results were validated with both, pushover and dynamic analyses, finding that the assumed mechanisms based on the damage patterns found in the visual inspection works (Lourenço & Ramos, 2008) are realistic. In most of the numerical analyses, the most frequent damage patterns found was compromising the stability of the North and the West facades by the formation of plastic hinges in similar places as those assumed for the different collapse mechanism.

- The safety assessment by kinematic analysis of collapse mechanism gave the result that the structure is safe until a horizontal load coefficient of 0.097g is applied in X direction and of 0.109 in Y direction. This means that when the structure is subjected to horizontal acceleration equal or higher than 0.10g, those collapse mechanisms (in the North and West façades) will be activate and the collapse process will begin until spend all the ductility. The ductility obtained from the displacement based analysis, is rather high and it should be limited by previous local failures during the collapse process, therefore those maximum displacements should not be reliable.

- The inclusion of damage patterns reported in the visual inspection works (Lourenço & Ramos, 2008) by means of using a smaller thickness in some elements located inside “damage” regions was very useful to update the numerical model with the present damage conditions of the structure. It was proved that the dynamic behavior of the structure is very sensitive to the structure damage state by obtaining rather low errors in the frequencies estimation (1.29%) and acceptable MAC values, in average 65%.

- During the model updating process it was possible to demonstrate that the apse of the church has strong influence in the dynamic response of the structure. The model updating process was improved by removing the modes that have mass participation of the Apse and comparing modes with similar deformed shape. This was also possible due to the lack of

information on the dynamic response of the apse because the points in which dynamic response was measured are located in the buttresses of the North façade.

- Highly non-linear behavior was found in all the pushover analyses characterized by a saw-tooth behavior. This behavior is possibly caused by a combination of numerical and physical aspects. Regarding the numerical aspects, the relative coarseness in the mesh located in the elements that represent the damage conditions in the structure may affect the convergence of the solution when non-linear analysis are performed because up to a certain number of elements the solution may be unstable. Also the number of integration points both in plane and in the thickness directions plays an important role for the accuracy of the results because a higher number of integration points allow a smoother variation of stresses and strains but also require highly computer cost. The tolerance criterion used in the iteration process may affect the convergence by a cumulative loosing of accuracy through the analysis development. Regarding physical aspects, the Total Strain Fixed Crack model which was use for modeling the non-linear behavior of the masonry, defines the damage criteria based on fracture energy; hereby this parameter may influence the results up to a certain limit. Another reason could be that the structure presents local damages so that the convergence criterion is hardly reach due to the loss of capacity in those specific areas.
- When the safety of the structure was assessed by performing pushover analyses with a horizontal load pattern proportional to the mass regardless the height applied in the global directions, the lowest softening peak found was about 0.03g. But this may be correlated to a local failure of the structure, therefore the maximum capacity (which is the minimum load factor within all the analyses) obtained was about 0.11g, which occurs when the load is applied in –Y direction. This value coincides with the value obtained from the safety assessment by limit analysis. In most of the cases the damage pattern represents the distribution of the assumed plastic hinges for the definition of the collapse mechanisms.
- When the safety of the structure was assessed by performing pushover analyses with a modal pattern proportional to lateral forces consistent with the lateral force distribution determined in the modal response analysis, the lowest softening peak obtained was about 0.02g. But the capacity of the structure was affected by the appearance of local damage conditions, therefore the structure had problems in convergence of the solution but at the end a maximum capacity of 0.03g was obtained, and it occurs when the modal pattern configuration is proportional to the 3rd mode configuration. This result is very small, and its validity is in doubt because when the dynamic analysis was performed a higher capacity was obtained. A possible influence of the punctual masses that represents the tower (due to the large deformation of that corner) may explain this phenomenon. Anyhow, the damage pattern obtained from the analysis in which the modal pattern configuration is proportional to the 1st mode clearly approaches to the plastic hinges distribution assumed for the collapse mechanism of the North façade.

- When the safety of the structure was assessed by performing pushover analyses with a horizontal load pattern proportional to the mass regardless the height applied in the principal axes directions, the lowest obtained softening peak was about 0.03g when the application of the load is –X'; it can be explained by local failure. When the structure capacity seen to be stabilized, the structure reached a maximum load coefficient of about 0.08g (it is the minimum among the analyses). This value is lower than the values of the previous analysis but still is close to them. The obtained damage pattern distribution was similar as that obtained from the previous pushover analyses.
- When the stability assessment of the structure was performed by means of non-linear dynamic analyses applying seismic forces with PGAs equal to 0.05g and 0.06g, the obtained maximum load coefficient was ranging between 0.06g and 0.08g. But the maximum displacement that the structure reached among the analyses was of 0.017m, which seems to be small to assure that structure reaches its maximum ductility level. The obtained damage pattern distribution validates the damage distribution obtained in the pushover analyses and the plastic hinges distribution assumed for the limit analysis of the collapse mechanism, but according to the obtained damage intensity, the structure still is far from collapse if compare to the levels obtained for pushover analyses. However it is important to highlight that according to the experience reported in (Mendes & Lourenço, 2008) for historical masonry "Gaioleiro" buildings, the capacity estimation by dynamic analyses is similar to the capacity obtained from applying pushover analyses with modal pattern proportional to lateral forces consistent with the lateral force distribution determined in the modal response analysis. Hereby without knowing the real capacity of the structure by means of dynamic analysis, the pushover results should be carefully used when a seismic stability assessment is done.
- The applied seismic demand (0.05g and 0.06g) was much lower than the recommended demand from the Cyprus national annex (CYS EN 1998-1:2005, 2007), which is about 0.35g. Therefore it is only possible to assess that the structure is stable under this seismic demand, but there are some uncertainties if higher peak ground accelerations are applied to the structure. During the seismic assessment of the structure by means of dynamic analysis, two higher PGA values were applied (0.07g and 0.10g) but the analyses had several convergence problems which were trying to solve by different approaches but none of them work (see Section 7.5).
- It is important to highlight the different levels of approach used to assess the seismic stability of the structure. The simple approach is the limit analysis of collapse mechanisms which are defined by means of the present damage conditions, construction typologies, material distribution, etc. and they can bring some information about horizontal loading capacity. The next approach, the pushover analyses, besides giving information about capacity and performance, they can give a close approximation of the real damage pattern when the

structure is subjected to seismic loads, and also they can validate the assumptions made in the limit analysis of the collapse mechanism regarding plastic hinges distribution. The final and more complex approach, dynamic analysis, gives the better approximation to the solution of the problem but takes high computer and time effort. The stability assessment is made by the obtaining the cyclic behavior of the structure in terms of load coefficient and displacement variation through the time; which also gives some information about the structure's ductility. The damage pattern can also be obtained as the maximum value among all the time steps. Amplifications in the acceleration, displacement distribution along height, drifts and curvatures may be obtained for several alignments and parts of the structure. All these results will validate the results of the previous levels of approach and will be the last word when assesses seismic stability; therefore it is required to be extremely careful with the integration scheme, the time integration method, the definition of the constitutive law and the needed results to be obtained. It is also important to highlight the importance of the previous approaches to define a seismic demand in accordance to previous estimations of the structure capacity because it is not feasible to carry out numerical analyses that at the end will have convergence problems.

According to the obtained results and the given conclusions, some recommendations on further works are given in order to have a possible better approach and understating of the problem.

- A new dynamic identification test is recommended using more DOFs in order to measure the response of the apse region and determine its influence in the modal response of the structure.
- A simple geotechnical prospection should be done in order to characterize the soil and obtain the required mechanical properties needed for assess the bearing capacity. This information may be also used along a range which can be used as an input of the modal updating process.
- A more detailed inspection is recommended in order to characterize the material distribution within the structure, namely sonic tests. This information may give a better approach in the distribution of material properties using for the calibration of the numerical model.
- More complex collapse mechanisms, namely 3D, should be used in order to take into account the bending of the horizontal strips or the horizontal arch effect. For the definition of these mechanisms, the results reported in this thesis may be used and the results should be compared with the obtained results from pushover analyses similar to the assumed mechanism.
- In order to determine the numerical influence in the saw-tooth behavior found during the pushover analysis parametrical analyses are recommended. As a first approach finer meshes should be used in the regions in which damage was modeled varying element size. Another approach may be to use different integrations schemes in plane and in thickness direction

making several combinations between plan and thickness points. Another parameter that may be varied is the tolerance of the convergence, to decide whether this parameter is low or high, and which will be the optimal parameter. As a final approach the tensile fracture energy may be varied in order to find the influence of this parameter in the stability and convergence of the analyses.

- A preliminary numerical model using cubic elements should be built in order to, whether validate or reject, the use of a numerical model composed by curved shell elements (as the model used in this work). Special care should be taken when making the comparison between the stiffness along the connections between two orthogonal walls; walls of the facades and buttresses and the connection between the North façade and the West façade.
- After the numerical model has been adjusted, by parametrical analysis, new dynamic analyses should be performed varying the seismic demand. The starting value for the PGA may be 0.07g, and if the analysis converges, the demand may be increased gradually in order to find the real capacity of the structure.

9. REFERENCES

Avorio, A., Borri, A., & Corradi, M. (2002). *Ricerche per la Ricostruzione. Iniziative di Carattere Tecnico e Scientifico a Supporto della Ricostruzione .* Roma: Regione dell'Umbria: DEI.

Bernardini, A., Gori, R., & Modena, C. (1988). *Valutazioni di Resistenza di Nuclei di Edifici in Muratura per Analisi di Vulnerabilitá Sismica-Internal Report 2/88.* University of Padova, Istituto di Scienza e Tecnica delle Construzioni.

Casarotti, C., & Pinho, R. (2007). An adaptive spectrum method for assessment of bridges subjected to earthquake action. *Bulletin of Earthquake Engineering* (3), 377-390.

Cervera, M. (2008-2009). Finite Element Approaches to Tensile Fracture. *SA2 Lectures.* Barcelona: Advanced Master in Structural Analysis of Historical Constructions and Monuments.

Chiumenti, M., & Cervera, M. (2008-2009). FEM Convergence Requirements. *SA2 Lectures.* Barcelona: Advanced Master in Structural Analysis of Historical Constructions and Monuments.

Chiumenti, M., Cervera, M., Kabele, P., & Roca, P. (2008-2009). Non Linear Solid Mechanics Overview. *SA2 Lectures.* Barcelona: Advanced Master in Structural Analysis of Historical Constructions and Monuments.

Chopra, A. K. (2000). *Dynamic of structures – Theory and applications to earthquake engineering.* Prentice Hall.

Chopra, A. K., & Goel, R. K. (2002). A modal pushover analysis procedure for estimating seismic. *Earthquake Engineering and Structural Dynamics* (21), 561-582.

CYS EN 1998-1:2005. (2007). *NATIONAL ANNEX TO Eurocode 8: Design of structures for earthquake resistance – General rules, seismic actions and rules for buildings.*

DIANA. (2008). DIsplacement method ANAlyser. *CD-ROM , Release 9.3*. Netherlands.

Doebling, S., C.R., F., & Prime, M. (1998). A Summary review of vibration-based damage identification methods. *The Shock and Vibration Digest , 2* (30), 91-105.

Douglas, B. M., & Reid, W. H. (1982). Dynamic tests and system identification of bridges. *Structural Division, ASCE , 108*, 2295-2313.

EN 1998-1. (2004). *Eurocode 8: Design of structures for earthquake resistance – General rules, seismic actions and rules for buildings.*

Enlart, C. (1913). *Gothic Art and the Renaissance in Cyprus.* (S. D. Hunt, Ed.) Trigraph Ltd.
Franchetti, P. (2008-2009). Damage and Collapsing Mechanism in Existing (Particulary Historical) Structure. *SA3 Lectures.* Barcelona: dvanced Master in Structural Analysis of Historical Constructions and Monuments.

GAMS. (1998). The General Algebraic Modeling System. *CD-ROM* . USA.

Gelfi, P. (2006). SIMQKE_GR – Artificial earthquakes compatible with response spectra. Italy: University of Brescia.

Giuffrè, A. (1993). *Sicurezza e conservazione dei centri storici. Il caso Ortigia.* Bari: Laterza.

Google. (2009). *Google Maps*. Retrieved April 22, 2009, from http://maps.google.com/

Heyman, J. (1966). The Stone Skeleton. *International Journal of Solids and Structures* , 270-279.

Kell, C. F. (1982). Medieval and Other Buildings in the Island of Cyprus (VI). *Transactions of The Royal Institute of British Arquitects* .

Kythreoti, S., & Pilakoutas, K. (2000, July 6-9). *Proceedings of the EuroConference on Global Change and Catastrophe Risk Management: Earthquake Risks in Europe*. (IIASA

Laxenburg, Austria) Retrieved April 15, 2009, from http://www.iiasa.ac.at/Research/RMS/july2000/Papers/stella.col.1107.pdf

Lourenço, P. B., & Ramos, L. F. (2008). *Preliminary Report on the Inspection on Three Famagusta Churches.* Guimarães: Universidade de Minho.

Lourenço, P., Krakowiak, K., Fernandes, F., & Ramos, L. (2007). Failure analysis of Monastery of Jerónimos, Lisbon: How to learn from sophisticated numerical models. *Engineering Failure Analysis* (14), 280-300.

Mendes, N. A., & Lourenço, P. B. (2008). Reduction of the seismic vulnerability of ancient buildings (Portuguese). *Activity report of project POCI/ECM/61671/2004, FCT* , Available from www.civil.uminho.pt/masonry.

Mendes, N., & Lourenço, P. B. (2008). Seismic Assessment of masonry "Gaioleiro" Buildings in Lisbon, Portugal. *Journal of Earthquake Engineering* , Submited for possible publication.

Miller, A. M. (1735). *Peregrinus in Jerusalem.* Cultural Foundation of the Bank of Cyprus.

Municipality of Famagusta. (2009). *The history of Famagusta*. Retrieved April 20, 2009, from http://www.famagusta.org.cy/istoria-en/default-en.asp

O. P. C. M. 3431. (2005). *Ordinance of the Prime Minister.* 3rd of May.

Oliveira, D. (2008-2009). Seismic Behavior and Structural Dynamics. *SA3 Lectures.* Barcelona: Advanced Master in Structural Analysis of Historical Constructions and Monuments.

Ramos, L. F. (2007). *Damage identification on masonry structures based on vibration signatures (PhD thesis).* Guimaraes, Portugal: University of Minho.

Republic of Cyprus, Ministry of Finance. (2006). *Goverment Web Portal*. Retrieved April 28, 2009, from http://www.cyprus.gov.cy

Roca, P. (2008-2009). Ancient Rules and Classical Approaches- Part 1. *SA1 Lectures.* Barcelona: Advanced Master in Structural Analysis of Historical Constructions and Monuments.

Roca, P., & Kabele, P. (2008-2009). Purpose and Posibilities of Structural Analysis. *SA1 Lectures.* Barcelona: Advanced Master in Structural Analysis of Historical Constructions and Monuments.

Roca, P., & Lourenço, P. B. (2008-2009). Introduction to Masonry Mechanics and Modeling Techniques. *SA2 Lectures.* Barcelona: Advanced Master in Structural Analysis of Historical Constructions and Monuments.

Seismosoft. (2004). SeismoSignal - A computer program for signal processing of strong-motion data.

Supporting Activities that Value the enviroment. (2008). *Famagusta Cultural Heritage Project*. Retrieved April 15, 2009, from http://www.save-cyprusheritage.com

Unit of Environmental Studies. (2004). *Cyprus geological heritage educational tool*. (Research & Development Center -Intercollege) Retrieved April 14, 2009, from http://www.cyprusgeology.org/english/index.htm

Valluzzi, M. R., Cardani, G., Binda, L., & Modena, C. (2004). Seismic Vulnerability Methods for Masonry Buildings in Historical Centres: Validation and Application for Prediction analyses and Intervention Proposals. *13th World Conference on Earthquake Engineering. August 1-6, 2004.* Vancouver, Canada.

Walsh, M. J. (2007). Famagusta 2007: An appeal for International Cooperation. Famagusta: Eastern Mediterranean University.